Characterization and modeling of the thermo-mechanical behavior of a Ti-6Al-4V alloy under dynamic complex loading

Miguel Ruiz de Sotto

To cite this version:

Miguel Ruiz de Sotto. Characterization and modeling of the thermo-mechanical behavior of a Ti-6Al-4V alloy under dynamic complex loading. Mechanics of materials [physics.class-ph]. Université de Toulouse, Institut Supérieur de l'Aeronautique et de l'Espace, 2020. English. NNT : . tel-03023834

HAL Id: tel-03023834
https://hal.science/tel-03023834v1

Submitted on 25 Nov 2020

Université Fédérale
Toulouse Midi-Pyrénées

THÈSE

En vue de l'obtention du

DOCTORAT DE L'UNIVERSITÉ DE TOULOUSE

Délivré par:
Institut Supérieur de l'Aéronautique et de l'Espace

Présentée et soutenue par :
Miguel RUIZ DE SOTTO

le mercredi 5 février 2020

Titre :
Characterization and modeling of the thermo-mechanical behavior of a Ti-6Al-4V alloy under dynamic complex loading

Caractérisation et modélisation du comportement thermo-mécanique d'un alliage de titane Ti-6Al-4V sous chargement dynamique complexe

---

École doctorale et discipline ou spécialité :
ED MEGEP : Génie mécanique, mécanique des matériaux

Unité de recherche :
Institut Clément Ader, CNRS UMR 5312
Laboratoire de Mécanique des Solides, CNRS UMR 7649

Directeur/trice(s) de Thèse :

Patrice LONGÈRE	ISAE-SUPAERO	Directeur
Véronique DOQUET	Ecole Polytechnique	Co-Directrice

Jury :

Jacques BESSON	Mines ParisTech	Rapporteur
Anne-Marie HABRAKEN	Université de Liège	Rapporteure
Pierre-Yves MANACH	Université de Bretagne Sud	Président
Jessica PAPASIDERO	Safran Aircraft Engines	Encadrante
Han ZHAO	Sorbonne Université	Examinateur

Abstract

During the aircraft engine certification, various components are tested against ballistic phenomena. The engine fan must accordingly resist bird strike and blade loss without compromising the whole engine thrust performance. Fan blades, and particularly their leading edge, undergo large deformation under high strain rate, non-proportional loading paths and plastic dissipation induced self-heating. Due to their high specific mechanical properties, Ti-6Al-4V titanium alloys are promising candidates for fan multi-component blade leading edge. In this work, an experimental campaign has been carried out on a cold rolled Ti-6Al-4V alloy comprising tension, compression and shear tests performed at various temperatures and (low and high) strain rates, under monotonic and alternated loading paths. Based on these results, a constitutive model has been developed accounting for the combined effects of orthotropy, strength differential, nonlinear kinematic and isotropic hardenings, strain rate hardening as well as thermal softening. Material constants have been identified using Zset software. The model has been implemented as user material (Fortran) subroutine into the commercial finite element computation code LS-DYNA. The performances of the numerical model have then been estimated by conducting numerical simulations considering a volume element under various loading paths as well as the specimens used for the experimental campaign.

Résumé

Lors de la certification des moteurs d'avion, certains composants sont testés vis-à-vis de phénomènes balistiques. La soufflante doit ainsi résister à l'ingestion d'oiseaux et à la perte d'aubes sans compromettre les performances globales du réacteur. Les aubes de soufflante, et particulièrement leur bord d'attaque, subissent des déformations élevées à grande vitesse, des chargements non proportionnels et un auto-échauffement induit par la dissipation plastique. Compte tenu de leurs bonnes propriétés mécaniques spécifiques, les alliages de titane Ti-6Al-4V sont considérés comme des candidats prometteurs pour le bord d'attaque d'aubes de soufflante multi-composants. Dans ce travail, une campagne expérimentale a été menée sur un alliage de Ti-6Al-4V laminé comprenant des essais de traction, compression et cisaillement à plusieurs températures et vitesses de déformation (lentes et rapides), sous des trajets de chargements monotones et alternés. A partir des résultats obtenus, un modèle constitutif a été développé rendant compte des effets combinés de l'orthotropie, de l'asymétrie traction-compression, des écrouissages cinématique et isotrope non linéaires, de la vitesse et de l'adoucissement thermique. Les constantes ont été identifiées au moyen du logiciel Zset. Le modèle a ensuite été implémenté en tant que procédure matériau utilisateur (Fortran) dans le code de calculs commercial par élément finis LS-DYNA. Les performances du modèle numérique ont alors été évaluées en menant des simulations numériques sur un élément de volume soumis à différents trajets de chargement ainsi que sur des éprouvettes utilisées pour la campagne expérimentale.

Acknowledgments

I would like to start first and foremost by thanking my PhD advisors. To Jessica, for all the helpful support and the encouragement. To Véronique for all the enthusiasm and wise advice given during my stay in LMS. And to Patrice, for the endless conversations and valuable support.

I profoundly thank the jury members for the thorough examination of this work.

I thank Safran Aircraft Engines and the Association Nationale Recherche Technologie for the funding of this thesis. Likewise, I would like to express my gratitude to the Institut Clément Ader and the Laboratory of Solid Mechanics for the participation in this enterprise.

I thank all the technicians of the Institut Clément Ader for their skillful support, the researchers for their valuable advice and the PhD students: the old ones for their experience and the young ones for their fresh motivation for research. I thank especially my office mates, Hannah and Yohan, for their continued patience. In short, I thank the friendly environment of the laboratory that contributed to the quality of this work.

I thank all the community of the LMS, be it engineers, technicians and students for all the help received. A special mention for Gerard Gary et Philippe Chevallier for the priceless knowledge and advice given.

Lastly, I want to express my gratitude to all my friends and family for the immeasurable support during these three years. This work could not have been possible without their constant encouragement.

Miguel Ruiz de Sotto

Contents

Introduction

General context

The reduction of aircraft polluting gas emissions and fuel consumption aiming at reducing the environmental impact and the transportation costs has been one of the main challenges in the aeronautical industry for the past few years. In order to achieve that, the aerodynamic performance, the combustion efficiency and the aircraft weight-reduction are addressed. Concerning the latter, the choice of structural materials becomes a critical factor as their mechanical properties must ensure a correct functioning of the airplane without increasing its overall weight nor compromising the safety standards.

The engine can count for an important fraction of the total weight of an aircraft. The current structural design approach consists in assembling multicomponents parts composed of different materials in order to optimize the overall mechanical properties-to-weight ratios. The LEAP, for Leading Edge Aviation Propulsion, is an aircraft engine developed in this context by Safran Aircraft Engines and General Electric. One notable example is its fan blade architecture comprising three different materials: a carbon fiber woven composite constitutes the main body of the blade, a titanium alloy, the leading edge, and a structural glue the connection between the previous two materials.

During the certification of aircraft engines regarding accidental events, real scale ballistic tests including bird strike or fan blade loss must be passed without compromising the engine performance. During such tests the fan blades undergo large deformation, high strain rate, non-proportional multi-axial loading, load reversals and self-heating, potentially leading to fracture. Although the experimental optimisation of the structure vis-à-vis these conditions by real rests has for long been an option, the related costs and time is considerable. A numerical simulation-aided design of impact-resistant fan blades is thus preferable, but demands a reliable constitutive model to account for all the mechanical and thermal aspects of ballistic events-induced loadings. This work focuses on a Ti-6Al-4V titanium alloy known for its high strength-to-weight ratio and good toughness [1] and accordingly considered as a promising candidate for the leading edge of multicomponent fan blades.

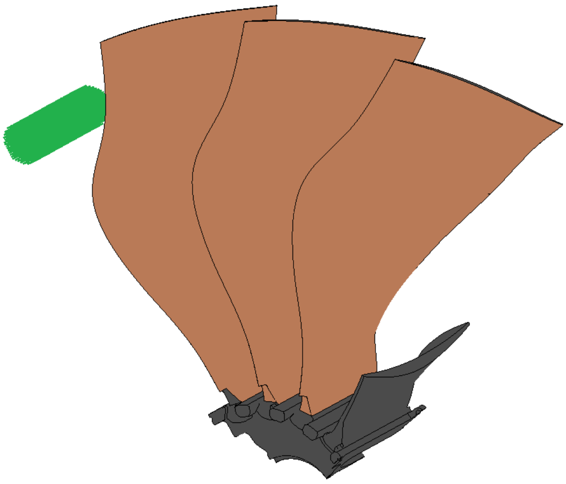

Figure 1: Finite Element Model of the bird strike problem.

Typical impact simulation on a fan blade leading edge

The work here described has been achieved in the context of a *Convention Industrielle de Formation par la Recherche* (CIFRE) partly funded by the *Association Nationale Recherche Technologie* (ANRT). It focuses mainly on the fan design vis-à-vis the bird strike problem. Low fidelity numerical simulations are performed to analyze the behavior of the structure and the materials involved at the macroscopic level when impacted by a projectile (see Figure 1). The aim is to get order of magnitudes in terms of loading path, strain and strain rate. The main materials to be considered in this simulation are the Ti-6Al-4V alloy in the leading edge, the composite material shaping the blade, the structural glue joining both pieces and the gelatin-like projectile impacting the structure at an approximated speed of $v \simeq 10^2\,\mathrm{m/s}$ with the fan rotating at $\omega \simeq 4000\,\mathrm{rpm}$. Regarding the titanium alloy, object of the following study, tentative simple elasto-plastic law and experimental hardening curves at various rates are used.

Figure 2a shows a schematic view of a fan blade used in the simulation. The leading edge, colored in light blue, receives the impact load and protects the main piece (the grey colored composite blade). Several scenarios can be considered with different impact locations. The history of the equivalent plastic strain at various points located along a line near the impact area are computed and compared in Figure 2b. The evolution computed in the elements with the highest plastic strain and the highest plastic strain rate are highlighted in color (the rest of the elements are plotted in grey to denote the high variability with no correlation with the position). An important plastic strain gradient is observed along the line following the leading edge. The maximum value is around $17\,\%$ and is reached within a few milliseconds, which denotes a high strain rate.

Regarding the stress triaxiality ratio χ (shown in Figure 3a), a rather erratic oscillatory behavior is found. The evolution computed in the elements with the highest plastic strain and the highest plastic strain rate are highlighted. In most of the elements, sudden changes of triaxiality from very negative values (down to $\chi \simeq -1$) to very positive ones (up to $\chi \simeq +1$) are observed and vice versa, due to reversed bending of the blade. As for the plastic strain rate, a wide range is visible with values reaching $5 \times 10^3\,\mathrm{s}^{-1}$ and

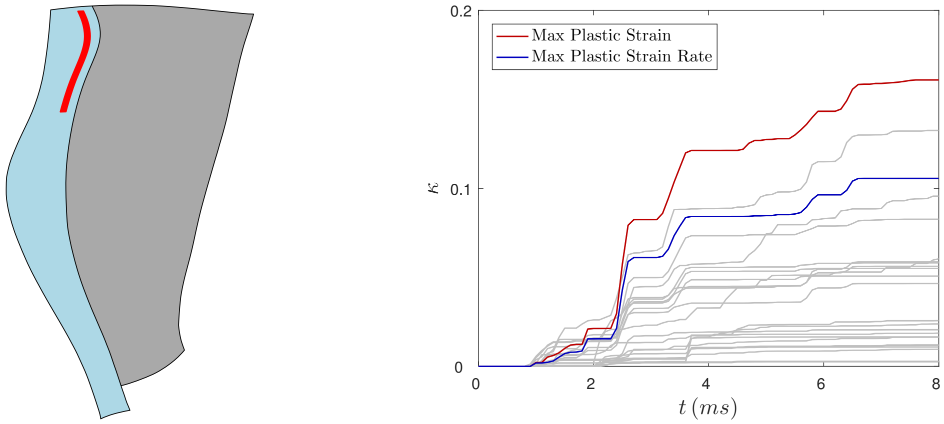

(a) Fan blade post-processing

(b) History of plastic deformation

Figure 2: Simulation and analysis of the bird strike problem. The plastic deformation curves correspond to the elements along the red line shown in the fan blade leading edge.

more (see Figure 3b). This implies an adiabatic behavior with a probable self-heating of the material which can alter the mechanical properties (by thermal softening). As a rough approximation, the temperature increase can be estimated from the plastic work dissipation to be $\Delta T \simeq 150\,°\mathrm{C}$

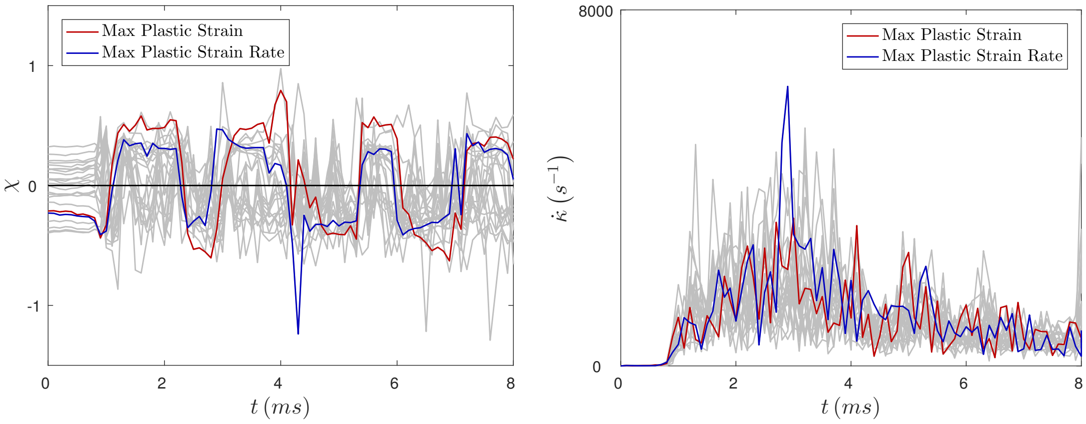

(a) Stress Triaxiality Ratio χ

(b) Equivalent plastic Strain Rate $\dot{\kappa}$

Figure 3: History of the stress triaxiality ratio χ and equivalent plastic strain rate $\dot{\kappa}$.

Finally, the equivalent plastic strain κ is plotted vs. the stress triaxiality ratio χ in Figure 4. A non-proportional loading is observed from these curves. Most of the changes in the stress triaxiality occur in the elastic regime (no plastic evolution is observed). However, a few trajectories show the evolution of the plastic strain during the stress triaxiality reversal.

This preliminary analysis indicates the typical loading conditions that the Ti-6Al-4V made part is expected to undergo during a ballistic phenomenon. Plastic flow up to relatively large strain should occur in a wide range of strain rates, temperatures and stress triaxiality ratios during the non-proportional loading. These conditions are expected to have a strong impact on the viscoplastic behavior of the material and further fan blade.

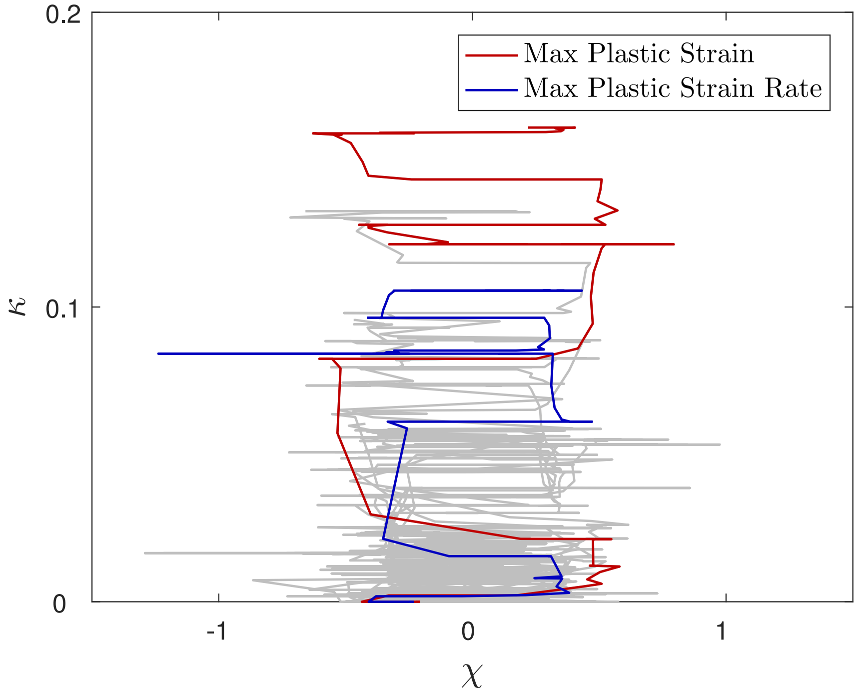

Figure 4: Equivalent plastic strain κ vs. stress triaxiality ratio χ in the fan blade after the impact.

Scientific and industrial challenges

In this work, both scientific objectives and industrial requirements have to be met.

Scientific objectives

It will be shown in Chapter 2 that models taking into account some of the above-mentioned aspects, e.g. rate, temperature and loading path-dependence, exist in the literature for Ti-6Al-4V titanium alloys but that none takes all these aspects into account. A more complete model has to be formulated and identified. For that purpose, a thorough experimental characterization of the mechanical behavior of a Ti-6Al-4V grade needs to be made in representative loading conditions. The experimental campaign has to cover the conditions seen in the above simulation: (i) a wide stress triaxiality range (negative $\chi \simeq -1$, nil $\chi \simeq 0$ and positive $\chi \simeq 1$), (ii) high strain rates ($\dot{\kappa} \simeq 5 \times 10^3\,\mathrm{s}^{-1}$), (iii) large strain ($\varepsilon \simeq 20\,\% - 30\,\%$), (iv) high temperature rise ($\Delta T \simeq 150\,°\mathrm{C}$) and (v) non proportional loading (see Figure 4).

Since the new constitutive model will be used in complex structural simulations, a phenomenological approach is found more suitable than a microstructure-based one. The integration of the non-linear equations constituting the model into an industrial Finite Element software will have to be finalized and the effect of the mesh size, the time increment or the element type on the model assessed.

Industrial requirements

The correct simulation and prediction of the bird strike onto a fan blade is aimed. The purpose of this work is to provide with a material model able to describe the mechanical behavior of a class of titanium alloy under complex conditions.

The LS-DYNA Finite Element commercial software is currently being used for the bird strike problem in the partner company. Hence, the numerical model should be accordingly coded in a subroutine that can be implemented in this software. In addition, simplicity of the modeling is looked for so it can be easily employed in the design office.

Last, the material constitutive model must be compatible with the features of the current Finite Element Model, i.e. explicit time integration, element type or mesh size.

General overview of the report

The present work is divided in three chapters, each one focusing on a major aspect of the modeling of titanium alloys: experimental, constitutive and numerical. The first chapter includes an extensive mechanical characterization as well as numerous microscopic observations of damage and fracture mechanisms that can help to explain the overall behavior.

In the second chapter, a constitutive model built in the irreversible thermodynamics framework is presented. Some key aspects such as anisotropy, strain and strain rate hardening, and thermal softening are here considered justified by experimental evidence from the first chapter. A calibration of the material constants is done to assess the suitability of the model for the present material.

Last, the numerical performance of the constitutive model is evaluated. An explicit approach for the integration of the rate equations is followed. Simulations at the RVE scale and the specimen scale are carried out to assess the capability for reproducing the experiments.

Some conclusions about the efficiency and limitations of the model as well as some future work are drawn at the end of this work.

CHAPTER 1

Characterization of a Ti-6Al-4V alloy

Abstract

After a characterization of its microstructure, an extensive study of the mechanical behavior of the Ti-6Al-4V titanium alloy under consideration is summarized in this chapter. Different loading conditions with various strain rates, stress triaxiality ratios, temperatures, loading paths including load reversals are applied on various sample geometries cut in various directions of a cold-rolled plate, and a large experimental database is obtained for further modeling. In addition, microscopic observations are reported showing the different deformation and damage mechanisms produced inside the material together with the type of fracture.

Contents

1.1 Introduction

This chapter summarizes the results of an extensive experimental campaign of characterization under a wide range of strain, strain rate, stress triaxiality ratio, temperature and loading path of the Ti-6Al-4V alloy under consideration. A general review on the various forms of the Ti-6Al-4V alloy is briefly reported followed by the presentation of the grade under consideration. Next, the experimental procedure, consisting of the different specimen geometries as well as the experimental set-ups, is shown. The low strain rate (quasi static) tests are performed by using conventional tension-compression testing machines and the high strain rate (dynamic) tests by means of compression and tension split Hopkinson pressure bar (SHPB)-type set-ups. Afterwards, the main results of the experimental characterization are presented[1]. First, the apparent effects of the loading conditions on the material response are shown. Secondly, a thorough analysis of the results is done to extract the different contributions to the mechanical behavior, namely anisotropy, strain and strain rate hardening and thermal softening. Finally, a compilation of microscopic observations is shown aiming at explaining the deformation mechanisms, the damage mechanisms and the features characterizing the rupture of the material.

1.2 Ti-6Al-4V alloy

This section aims at providing a dedicated literature review and presenting the current material under consideration.

1.2.1 Elements from the literature about Ti-6Al-4V alloys

A brief review of the literature in relation with the applications of the present study is conducted in the following. In particular, some key aspects of the micro and macro mechanical behavior of the Ti-6Al-4V are here summarized followed by the presentation of the material used in this work. The reader can refer to [1–3] for a more extensive review on titanium.

1.2.1.1 Microstructure and deformation mechanisms

Ti-6Al-4V is a "quasi-α" titanium alloy containing 6 % aluminum, an α-stabilizing element, and 4 % vanadium, a β-stabilizing element. This leads to a dual-phase microstructure, with a large fraction of α phase, with an hexagonal close packed (HCP) crystallography, and a smaller fraction of β phase, with a body centered cubic (BCC) crystallography. Figure 1.1, extracted from Titanium and titanium alloys [2], shows the phase diagram of a Ti-6Al alloy as a function of the content in vanadium. For a range of concentration between 2 % and 16 % in vanadium content, both phases coexist for temperatures below the so called β transus. Above this temperature, only the β phase is present.

Now, the alloying elements are not the only factor affecting the microstructure of the material. As seen in Zheng et al. [4], different microstructures can be obtained by submit-

---

[1] For confidentiality reasons, the stress values determined in the following are normalized, viz. $\tilde{\sigma} = \sigma/\sigma_{RD_0}$, where σ_{RD_0} is the yield stress at 0.2 % of plastic strain along the rolling direction at room temperature and $\dot{\varepsilon} \simeq 10^{-3}\,\mathrm{s}^{-1}$. Likewise, the force is normalized with respect to the reference stress just mentioned and the initial cross section A of the specimen as $\tilde{F} = F/\left(A \cdot \sigma_{RD_0}\right)$.

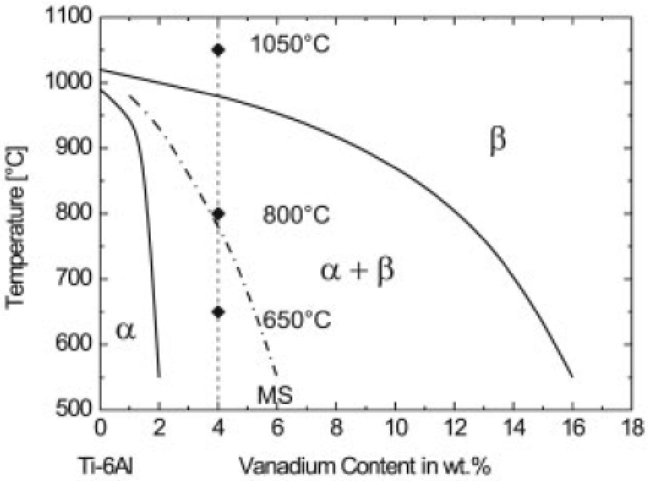

Figure 1.1: Phase diagram for a Ti-6Al-V alloy. After Titanium and titanium alloys [2].

ting them to different heat treatments which have a significant effect on the mechanical properties of the alloy, as expected. Figure 1.2 shows some examples of microstructures that can be obtained from various quenching speeds from above or below the transus line, among which the bimodal form considered here, consisting of relatively “soft” primary α phase nodules within a harder β matrix containing tiny secondary α laths. It is noteworthy the α-colony structure also known as "macrozones" obtained from quenching from a microsctructure composed of the so called prior β grains [5].

Both dislocation glide and mechanical twinning are activated in Ti-6Al-4V upon plastic deformation, as reported by Prakash and Coghe et al [6 ; 7]. Since Taylor [8], it was established that five independent slip systems are necessary to accommodate an homogeneous deformation without any crack. In HCP structures, the basal and prismatic slip systems, as well as the $\langle a\rangle$ pyramidal slip, offer only four independent modes. In order to obtain five independent systems, the activation of $\langle c+a\rangle$ pyramidal slip system is necessary. However, twin systems have been proven to accommodate the deformation along the $\langle c\rangle$ axis as an alternative to the $\langle c+a\rangle$ slip [9].

Regarding the slip systems in the α phase, they can be summarized in five families, namely the (i) basal $\langle a\rangle$, (ii) prismatic $\langle a\rangle$, (iii) pyramidal $\langle a\rangle$, (iv) first order pyramidal $\langle c+a\rangle$ and (v) second order pyramidal $\langle c+a\rangle$ with a total of 30 possible slip systems [10] (see Figure 1.3). As seen in Mayeur and McDowell [11], based on a comparison of different sources, at room temperature, the basal and prismatic systems have the lowest Critical Resolved Shear Stress (CRSS) and hence they are more likely to activate. The pyramidal $\langle a\rangle$ has a comparatively higher CRSS, and the pyramidal $\langle c+a\rangle$ a much higher one, up to 15 times the CRSS of the prismatic slip. Nonetheless, the temperature, strain rate and the grain size [12] are also important factors in the predictability of the activated slip systems.

Several twinning systems can theoretically operate on HCP structures, and in particular in titanium alloys as shown in Partridge [13]. Even though it becomes less likely with an increase in the aluminum content [14], twinning (mostly of the tension $\{10\bar{1}2\}(\bar{1}011)$ type) can still be an active deformation system (specially at high strain rates [7]). Prakash et al. [6] go further and speculate that the scarce reports of twinning in Ti-6Al-4V may

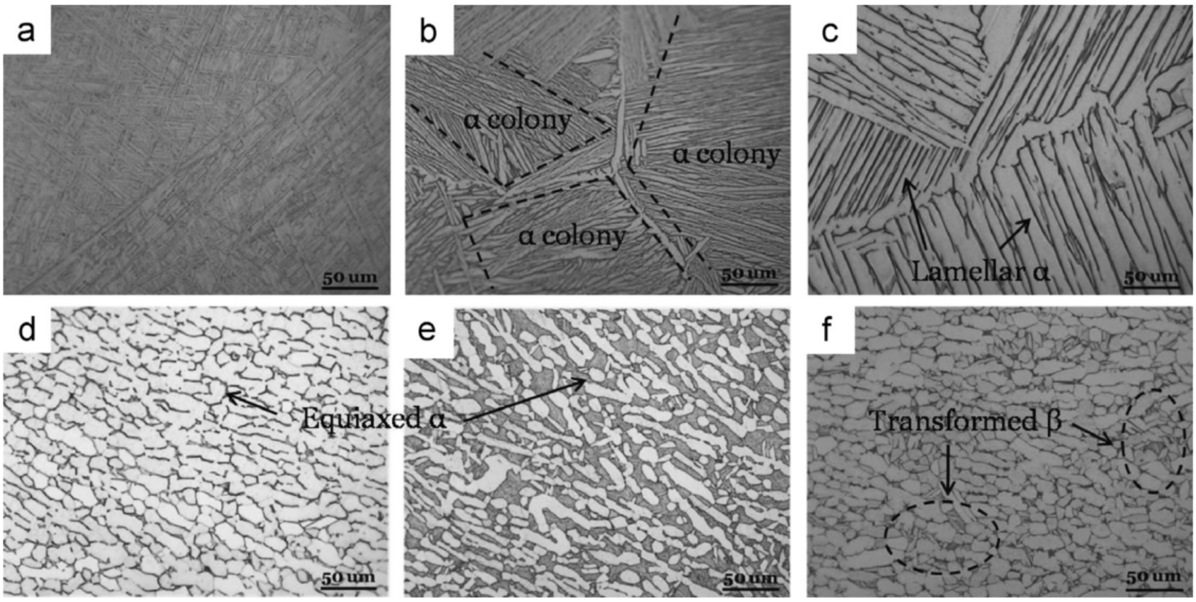

Figure 1.2: Several microstructure types of a Ti-6Al-4V obtained with different heat treatments: lamellar microstructure obtained with water quenching (a), air (b) and furnace (c) cooling from above the β transus line, equiaxed structure obtained with furnace cooling from below the transus temperature (d) and bimodal structure with water quenching (e) and air cooling (f) from below the transus temperature. After Zheng et al. [4].

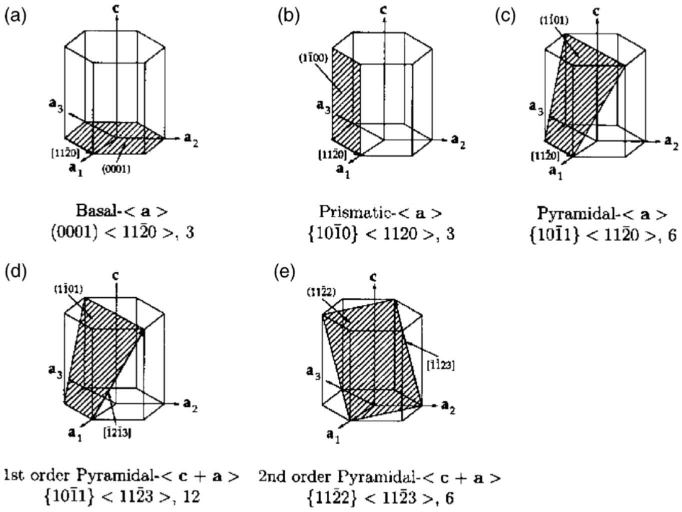

Figure 1.3: Schematic depiction of the slip systems in an HCP structure. After Hasija et al. [10].

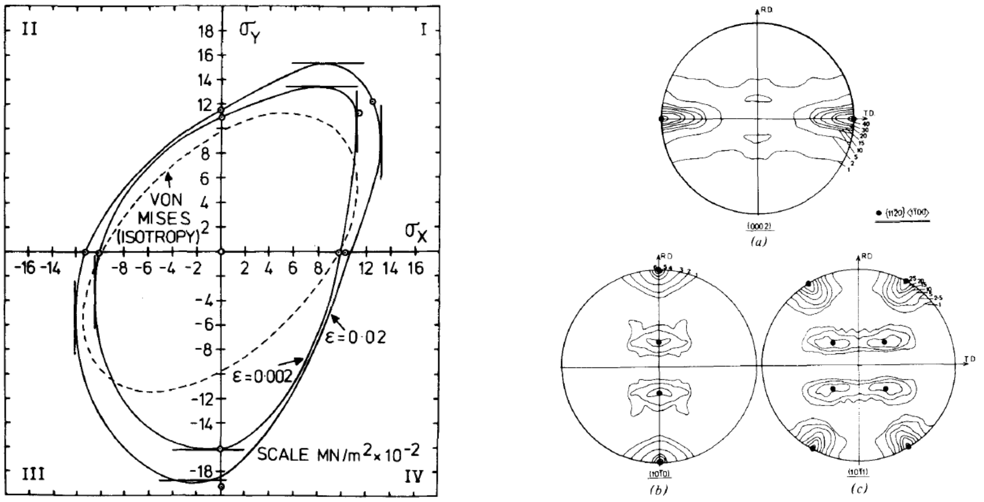

(a) Yield Loci

(b) Pole Figures

Figure 1.4: Yield loci and texture of a Ti-6Al-4V alloy. After Lowden and Hutchinson [15].

be due to the difficulty in distinguishing entirely twinned grains from unrotated ones.

From a macroscopic point of view, cold rolled plates of a Ti-6Al-4V titanium alloy usually exhibit a strong texture [15 ; 16]. As reported in Lee et al. [17], primary α grains usually tend to rotate so that their $\langle 0001 \rangle$ direction becomes perpendicular to the rolling direction. Furthermore, the slip and twinning systems involved during deformation can be related to the type of texture present in the material as done by Zaefferer for several titanium alloys [18].

1.2.1.2 Mechanical behavior

Figure 1.4 shows the yield loci of a textured Ti-6Al-4V. In addition to the texture-induced orthotropic behavior, a strength differential between tension and compression is observed. This feature has been also found in other Ti-6Al-4V alloys (see [16 ; 19 ; 20]) as well as in other HCP materials, such as high purity α-titanium [21], Magnesium [22 ; 23] or Molybdenum [24]. As pointed out by Lowden and Hutchinson [15], the strength differential is generally ascribed to the different activation of $\langle c + a \rangle \{11\bar{2}2\} \langle 11\bar{2}3 \rangle$ slip systems which are dependent on the direction and sensitive to the hydrostatic pressure. Observations made by Jones and Hutchinson [25] later proved a big difference in the CRSS for this slip system as well a volume dilatation necessary to move the $< c + a >$ dislocation, hence the pressure dependence. Additionally, the asymmetry has also been associated to mechanical twinning, whose activation depends on the loading direction [6 ; 26].

As seen in Figure 1.5a, extracted from Tancogne-Dejean et al. [27] for a Ti-6Al-4V alloy made through additive layer manufacturing (ALM), an orthotropic behavior induced by the material deposition direction can generally be observed with a significantly different yield strength along the rolling, transverse and normal directions of the plate.

Additionnaly, Figure 1.5b, from Tuninetti et al. [19], shows that the orthotropy measured in a Ti-6Al-4V alloy ingot is combined with an important strength asymmetry between tension and compression.

Regarding the hardening capability, three important aspects are to be considered: strain hardening, strain rate hardening and thermal softening that can potentially ap-

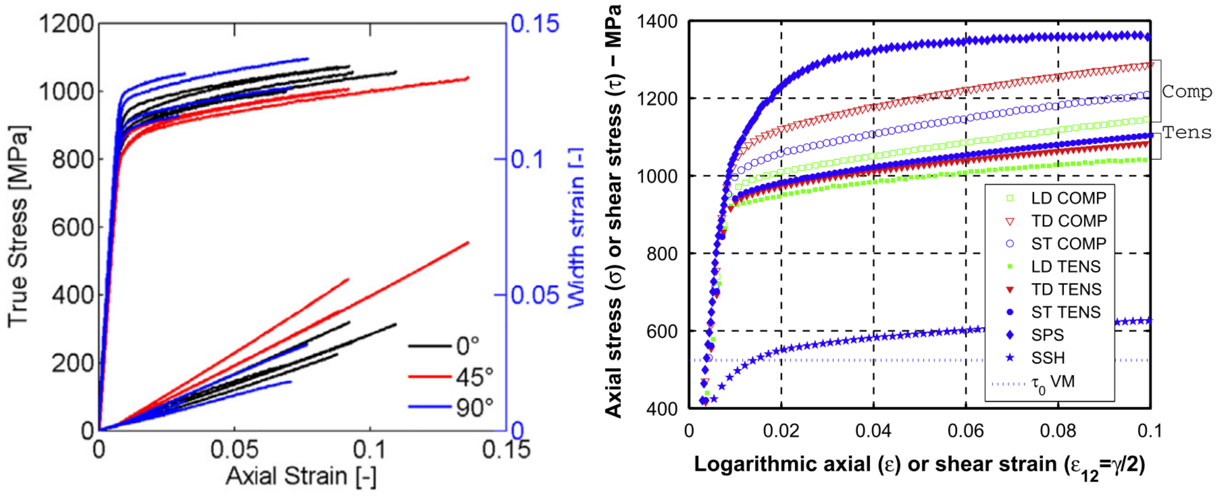

(a) Tancogne-Dejean et al. [27]

(b) Tuninetti et al. [19]

Figure 1.5: Anisotropic behavior of Ti-6Al-4V alloys. On the left, orthotropy measured along three different directions after additive manufacturing. On the right, orthotropy and strength differential from a Ti-6Al-4V ingot (LD for longitudinal, TD for transverse and ST for short transverse direction, SPS for plane strain and SSH for simple shear).

pear. Concerning the former, the Bauschinger effect on the mechanical behavior of metals has been extensively studied, e.g. in Zhonghua and Gu [28 ; 29] for dual-phase steel or Helbert et al. [30] for titanium alloys. Since ballistic events on fan blades induce load reversals, it is crucial to take kinematic hardening into account in the constitutive modeling.

Strain rate sensitivity

The behavior of titanium alloys is strongly strain rate-dependent, see e.g. Minaar and Zhou [31] and Longère [32] in Figure 1.6 or Tuninetti and Habraken [33]). The mentioned works analyzed the strain rate dependence for loading rates comprising both the quasi-static ($10^{-3}\,s^{-1}$) and the dynamic regime (up to $2 \times 10^{3}\,s^{-1}$).

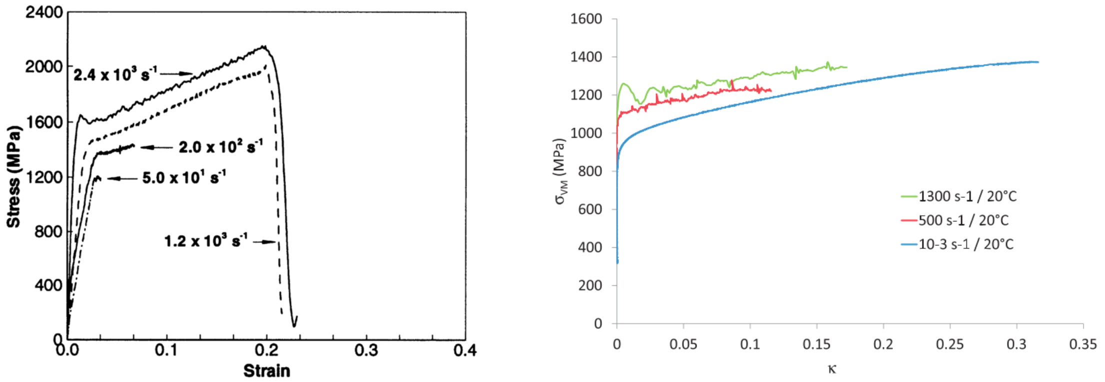

(a) Minaar and Zhou [31]
Tension

(b) Longère [32]
Compression

Figure 1.6: Strain rate dependence under tension and compression on Ti-6Al-4V alloys.

Temperature sensitivity

The strong temperature-dependence of Ti-6Al-4V titanium alloys behavior is also well-known, see e.g. Seo et al. [34] and Longère [32] in Figure 1.7. Therefore, a thermal softening function is generally considered to describe the decrease of the yield stress with increasing temperature. In addition, due to its low heat capacity, a significant self-heating-induced temperature rise may occur under adiabatic conditions at high loading rates [35 ; 36]. Consequently, a competition between strain and strain rate hardening, thermal softening and potential Dynamic Recrystalization (DRX) takes place along the deformation process, potentially leading to material instability and further strain localization under adiabatic shear banding, see e.g. Longère and Dragon [37].

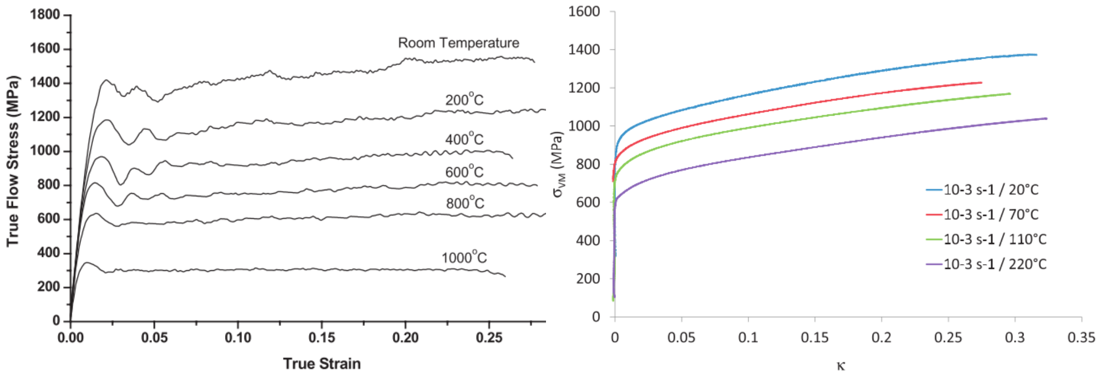

(a) Seo et al. [34]
Tension

(b) Longère [32]
Compression

Figure 1.7: Temperature dependence under tension and compression on Ti-6Al-4V alloys.

Worth noting are the works of Tuninetti and Habraken [33] where the strain rate sensitivity of a Ti-6Al-4V alloy was found to be dependent (through the material constant related to strain rate) on temperature but not in a monotonic way (see Figure 1.8).

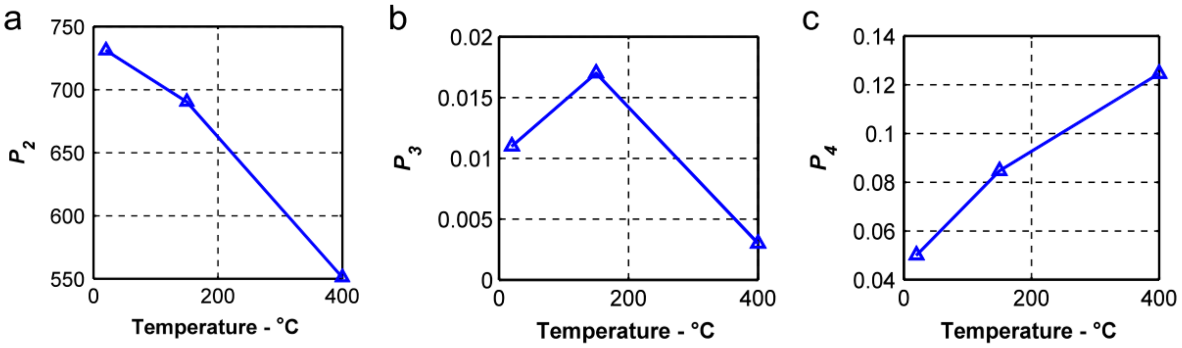

Figure 1.8: Variation of the isotropic hardening material constants with the temperature. (a) P2 related to strength, (b) P3 related to strain rate sensitivity and (c) P4 related to hardening : $\sigma_y = exp\left(-P_1\varepsilon\right)\sqrt{3}P_2\left(\sqrt{3}\dot{\varepsilon}\right)^{P_3}\varepsilon^{P_4}$. After Tuninetti and Habraken [33].

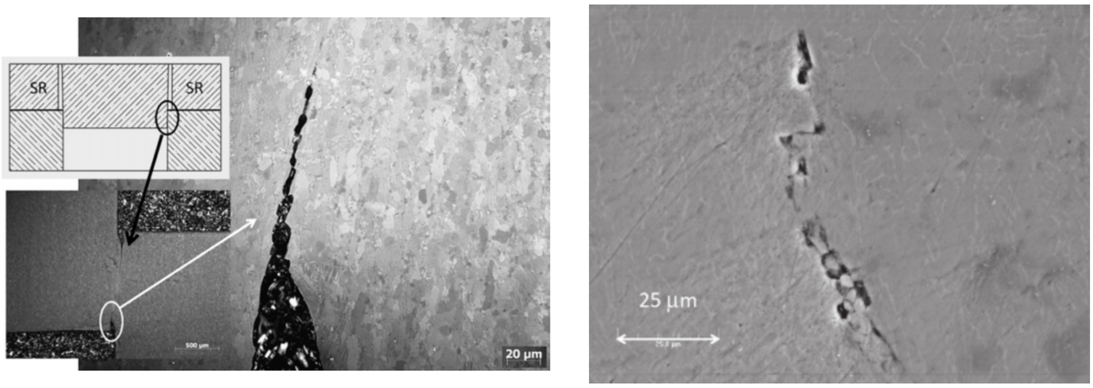

(a) Peirs et al. [38]

(b) Longère and Dragon [37]

Figure 1.9: Rupture induced by diffused damage in hat-shaped specimens of Ti-6Al-4V alloys.

1.2.1.3 Damage and fracture

Ductile damage usually occurs under positive stress triaxiality by void initiation, growth and coalescence until ultimate failure. In some cases, e.g. under low stress triaxiality and high strain rates involving adiabatic conditions, it may be preceded by shear localization. Ductile damage and dynamic shear localization in Ti-6Al-4V have been the subject of many works in literature for decades.

The first scenario involves the nucleation, growth and coalescence of cavities spread throughout the material. Experiments on hat-shaped specimens involving negative stress triaxialities have evidenced fracture by coalescence of diffuse damage (see Figures 1.9a from [38] and 1.9b from [37]). For these cases, damage is considered to have appeared from excessive rotation and deformation of grains submitted to shear stresses which yield the characteristic zig-zag crack paths depicted in the Figures.

These cavities are usually nucleated on the α/β interface as well as α grain boundaries as plastic strain incompatibilities develop [39 ; 40]. However, damage has been found to appear within an α grain as temperature is increased [41] or in matrix-twin interfaces [42].

The second scenario often takes place in the form of adiabatic shear bands (ASBs)(see [38 ; 43]). Under these conditions, the elevated strain rate impeding heat transfer combined with the softening due to temperature contributes to the localization of high deformation within a narrow band. These conditions can be generally considered a precursor for damage and final failure. As seen in Zhang et al. [44] the appearance of ASBs is dependent on the local texture that is: on the relative misorientation of neighboring grains. In addition, they measured temperature rises of up to 150 °C. Furthermore, high testing temperatures can also promote shear banding, even at low strain rates, at sufficiently large strains [45]. In the works of Lee and Lin, failure in compression specimens was achieved by a crack formation within a shear band, with no significant sensitivity on the loading rate [43]. Further works from Lee and Lin showed diffuse damage in the shape of cavities formed within the shear band after it had formed [46].

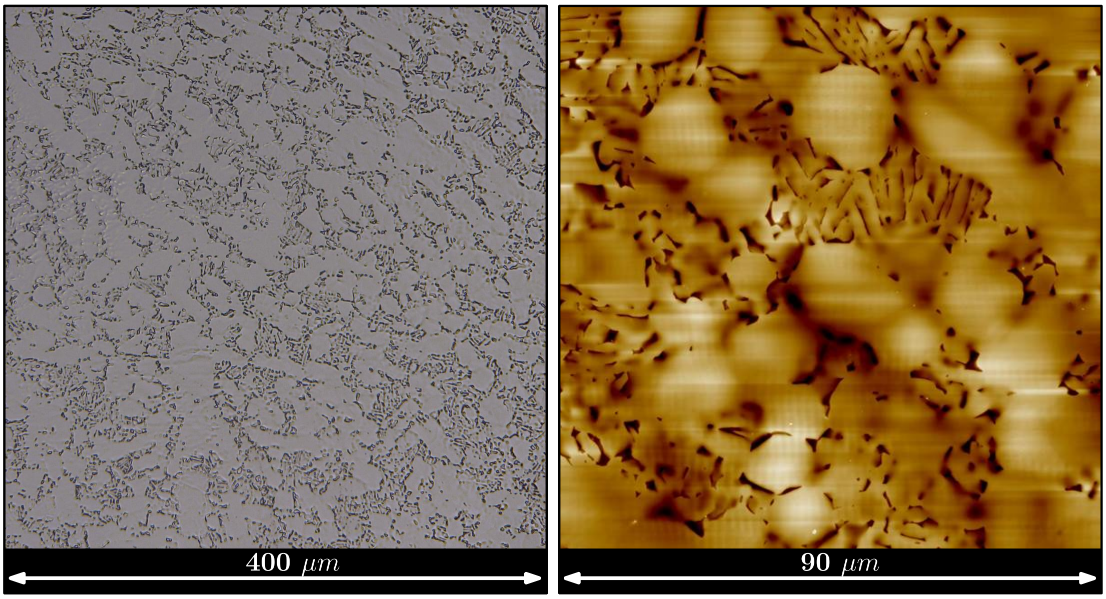

(a) Optical Microscopy (b) Atomic Force Microscopy

Figure 1.10: As received microstructure of the Ti-6Al-4V.

1.2.2 The Ti-6Al-4V under consideration

The material under consideration is provided in the form of a 16 mm-thick cold-rolled sheet of a Ti-6Al-4V alloy. The bimodal microstructure is observable after mechanical polishing down to 3 µm followed by electro-polishing with Struers A3 electrolyte solution and a tension of 20V. The size of the equiaxed α phase nodules ranges from a few microns up to 30 µm (see Figure 1.10). The more scarce β phase corresponds to the dark looking matrix surrounding the nodules, which also comprises some secondary lamellar α.

Figure 1.11 shows an orientation map for the α phase issued from an EBSD (*Electron Back-Scatter Diffraction*) analysis of the sheet. The observed zone of approximately 3 mm^2 presents clearly differentiated zones with different orientations. These “macrozones” are inherited from the orientation of the prior β grains formed during previous thermomechanical treatments of the alloy [5], and it produces some scatter in the experimental results since the scale of these zones approaches that of the specimens tested. The pole figures associated to the observed area shows a relatively strong local anisotropy. However, they do not correspond neither with the tendency showed in Lowden and Hutchinson [15] for a similar alloy nor to the different textures presented by Zaefferer [18].

The Figure 1.12, 1.13 and 1.14 presents additional EBSD measurements on other samples. The presence of macrozones keep producing strong local textured zones. The pole figures show no clear common relationship which would imply that the local anisotropy due to these macrozones is stronger than any global texture induced by sheet rolling.

In addition to the local field maps, X-ray diffraction measurements at the specimen scale were carried out. The pole figures from such observations reveal a weak average global texture (Figure 1.15a) as compared with the local macrozones. Regarding the basal plane or direction $< 0001 >$ (first pole figure), there is a tendency towards the transverse direction. However, a non negligible fraction of c-axes are also aligned along the rolling direction. As for the $< 10\bar{1}0 >$ (second pole figure), no clear pattern is deduced from the pole figures. When compared with the study done by Lee et al. [17]

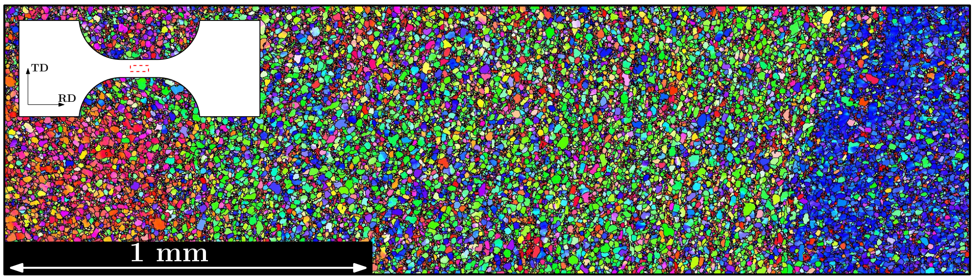

(a) Crystal orientation map

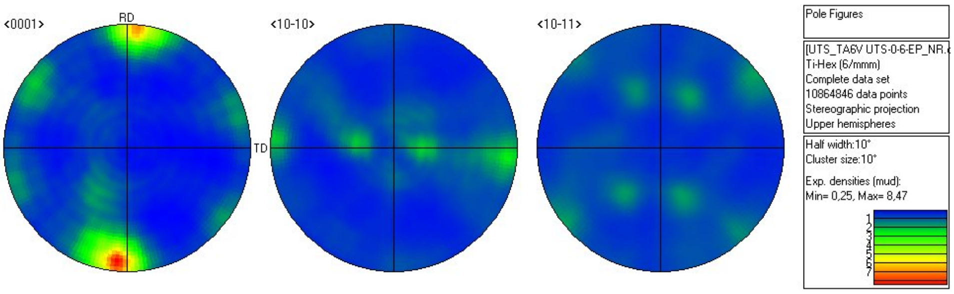

(b) Pole figures

Figure 1.11: EBSD mapping of α phase crystals orientation on a smooth flat tension specimen before loading (i).

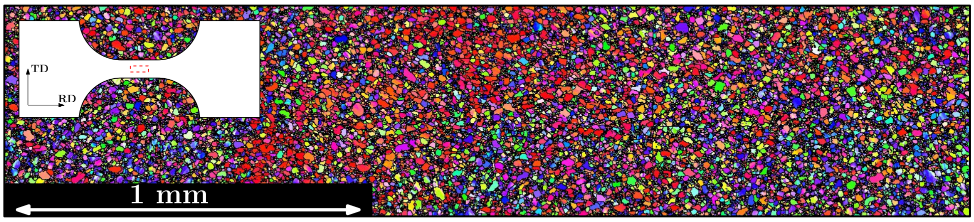

(a) Crystal orientation map

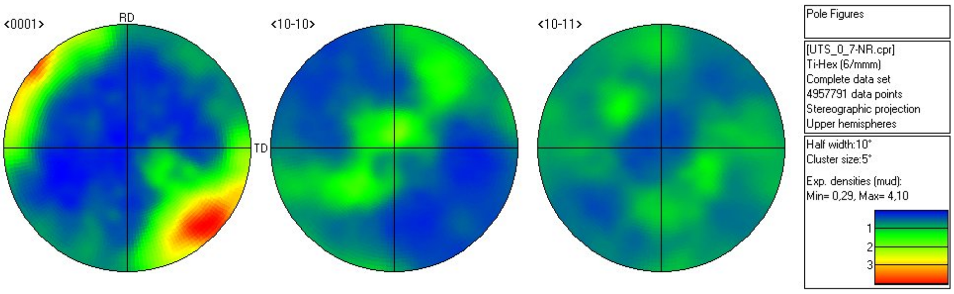

(b) Pole figures

Figure 1.12: EBSD mapping of α phase crystals orientation on a tension specimen before loading (ii).

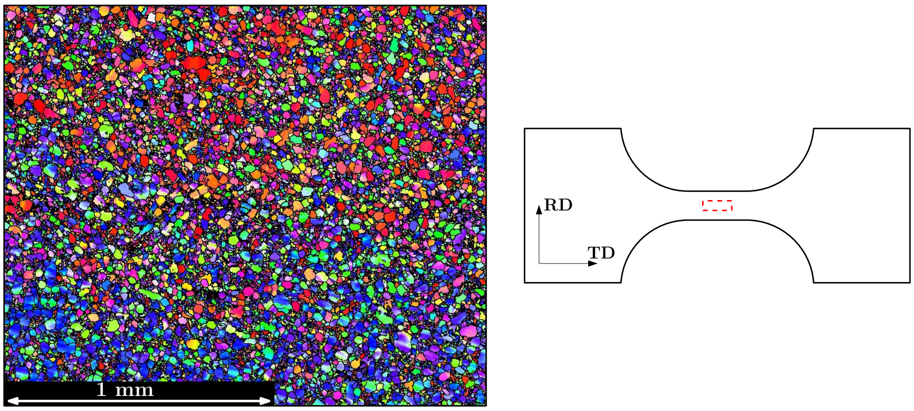

(a) Crystal orientation map

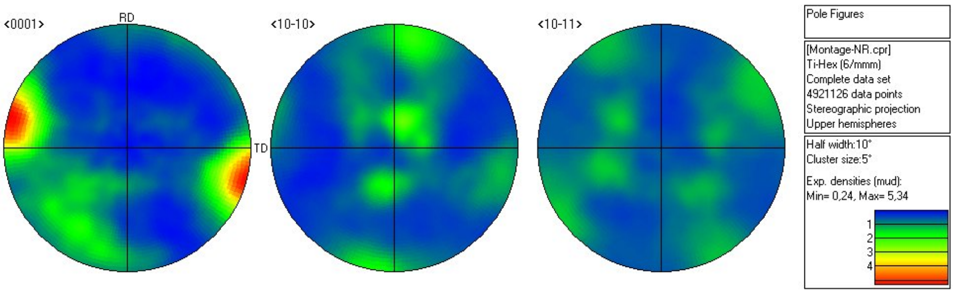

(b) Pole figures

Figure 1.13: EBSD mapping of α phase crystals orientation on a tension specimen before loading (iii).

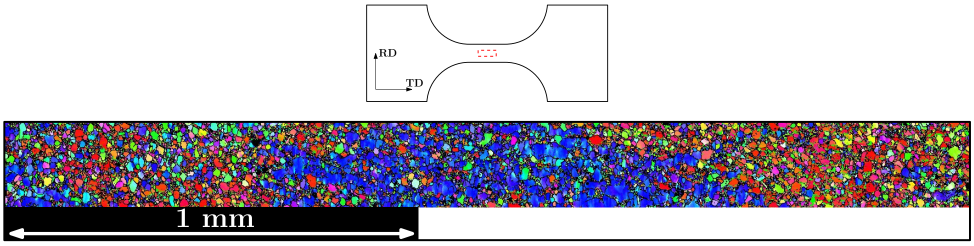

(a) Crystal orientation map

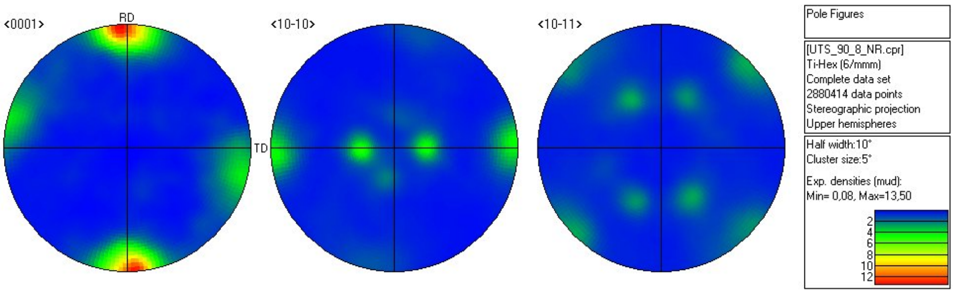

(b) Pole figures

Figure 1.14: EBSD mapping of α phase crystals orientation on a tension specimen before loading (iv).

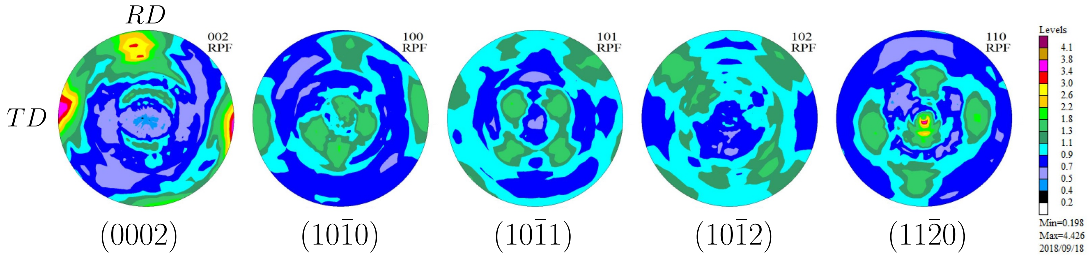

(a) Pole figures

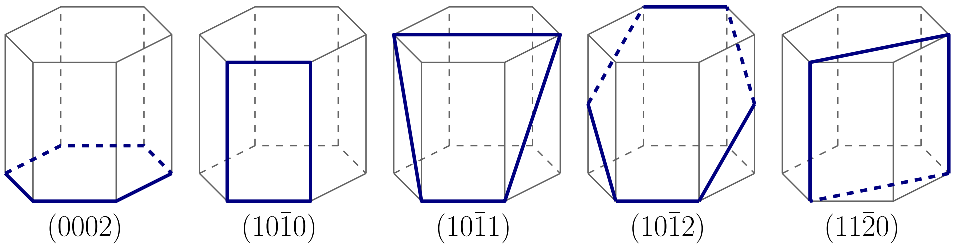

(b) Related crystallographic systems

Figure 1.15: Pole figures obtained by X-ray diffraction over large areas.

who reported an important fraction of <c> axes aligned towards the transverse direction and the $< 10\bar{1}0 >$ preferentially oriented along the rolling direction, the current material does not follow this pattern. Lowden and Hutchinson also presented a strong textured Ti-6Al-4V with the c-axis oriented along the normal and tranverse direction (depending on the amount of rolling imposed) [15].

1.3 Experimental procedure

The specimen geometries as well as the experimental set-ups employed are here presented.

1.3.1 Test specimens

Various types of specimens have been machined along four directions: the rolling RD, transverse TD and normal ND direction, as well as a diagonal directions DD in the RD-TD plane pointing 45° with respect to the rolling direction as shown in Figure 1.16.

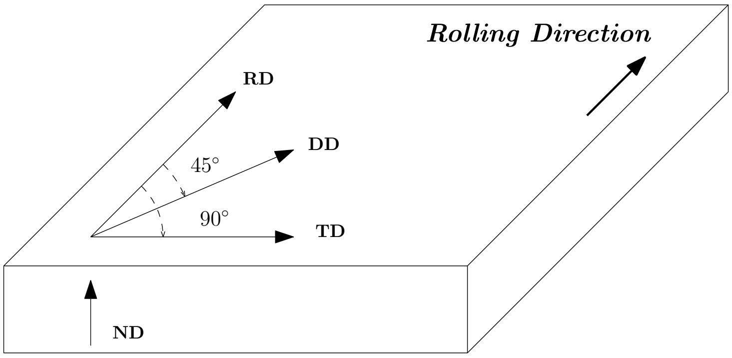

Figure 1.16: Orientations considered for the machining of the specimens.

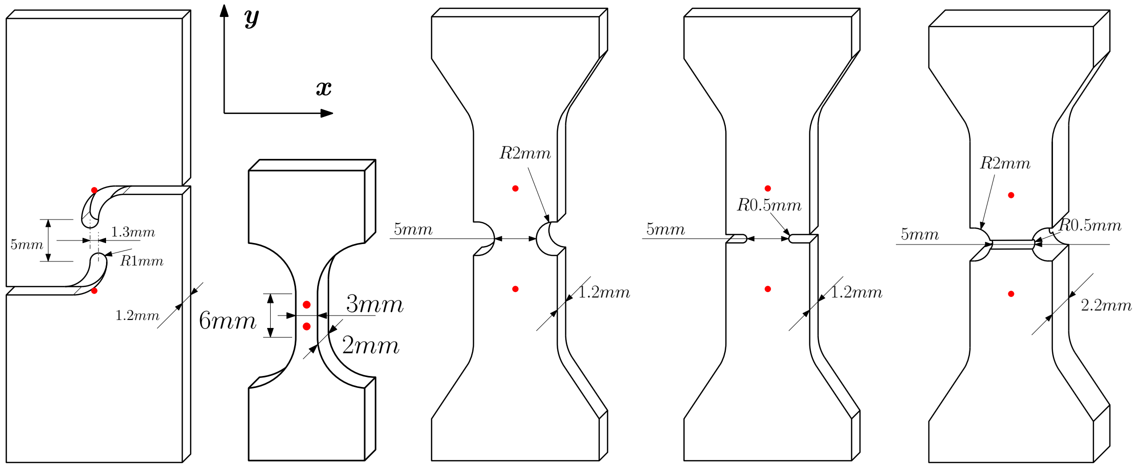

$\chi \simeq 0$ (a) Shear

$\chi \simeq 1/3$ (b) Smooth

$\chi \simeq 1/2$ (c) $R = 2\,\text{mm}$

$\chi \simeq 2/3$ (d) $R = 0.5\,\text{mm}$

$\chi \simeq 1$ (e) $R = 2\text{x}0.5\,\text{mm}^2$

Figure 1.17: Flat specimen geometries used to cover the triaxiality range $\chi \in [0, 1]$. Red dots indicate the position of the two points for the extensometer.

The geometries of the specimens have been designed to investigate a wide range of stress triaxiality ratio (STR) χ defined as

$$\chi = -\frac{p}{q} \quad \text{with} \quad p = -\frac{trace(\underline{\underline{\sigma}})}{3} \quad \& \quad q = \sqrt{\frac{3}{2}\underline{\underline{s}} : \underline{\underline{s}}} \tag{1.1}$$

where $\underline{\underline{s}}$ is the stress deviator of the Cauchy stress tensor $\underline{\underline{\sigma}}$ so that $\underline{\underline{s}} = \underline{\underline{\sigma}} + p\underline{\underline{I}}$.

In Figure 1.17 are drawn the specimens allowing for obtaining positive and nil χ, in Figure 1.18 the specimens allowing for negative χ and in Figure 1.19 the specimens for alternate loading. The χ indicated in Figures 1.17 and 1.18 are average values obtained from preliminary Finite Element simulations.

The dimensions of the smooth tension specimen ($\chi = 1/3$) are $2\,\text{mm} \times 3\,\text{mm} \times 6\,\text{mm}$ (thickness x width x gauge length). A shorter specimen is used for the normal direction along which the length is limited by the sheet thickness. Its cross section remains the same, but the gauge length is reduced to 4 mm.

Furthermore, three types of notched specimens are investigated with an increasing level of χ achieved: two with lateral notch radii of 2 mm and 0.5 mm to provide a $\chi \simeq 1/2 - 2/3$ and a specimen notched both in width and thickness to get a triaxiality close to 1.

Moreover, in order to get an average χ close to 0, a half-smiley type tension-induced shear specimen geometry desgined by Roth and Mohr [47] is used. The notches are machined with a constant radius which is suited for medium ductility materials. The two notches are separated by a slight offset which avoids too severe tension stresses on the border when largely deformed and favor pure shear loading in the zone of interest, as also done with Peirs's shear specimen [48]. An alternative technique to carry out shear tests can be found in Thuillier and Manach [49].

In Figure 1.18, three types of compression specimens are used: cylinders with dimensions of $8\,\text{mm} \times 7\,\text{mm}$ (height x diameter) and hat-shaped specimens using Couque [50] and Meyers [51] designs ($\chi \simeq -1/2$ and $\chi \simeq -1/5$ respectively)

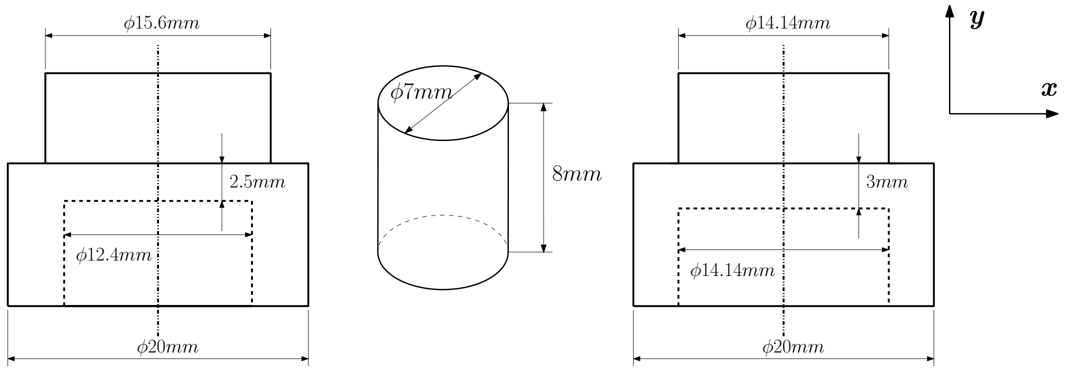

$\chi \simeq -1/2$ (a) Couque [50]

$\chi \simeq -1/3$ (b) Simple Compression

$\chi \simeq -1/5$ (c) Meyers [51]

Figure 1.18: Axisymmetric specimen geometries used to cover the stress triaxiality range $\chi \in [-1/2, -1/5]$.

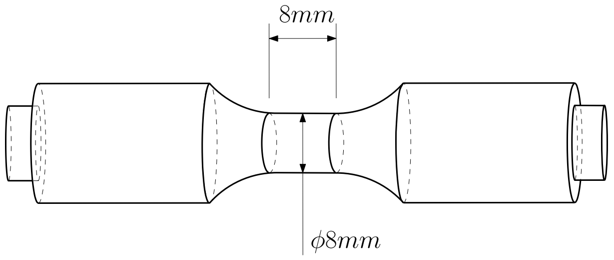

Figure 1.19: Cylindrical specimen for alternated tension-compression uniaxial tests at $\chi \simeq \pm 1/3$.

In an intermediate category, a cylindrical specimen of a radius of 8 mm and a gauge length of 8 mm is employed for cyclic tests (see Figure 1.19). These tests aim to study the kinematic hardening and to check if the potential differences between the tension and compression response of the material in terms of yield stress or viscosity using the previously mentioned geometries are retrieved when a single geometry and test setup is used for both loadings.

1.3.2 Experimental set-ups and procedures

Both the quasi-static and dynamic regimes are investigated in the experimental campaign with the objective of capturing any viscous effect. The same strain and stress definition are used for both types of tests when it comes to characterize the material.

The loading direction-related component of ε of the logarithmic strain tensor $\underline{\underline{\varepsilon}}$ is defined as $\varepsilon = ln\left(1 + \varepsilon_N\right)$, where $\varepsilon_N = \frac{\Delta l}{l_0}$ is the nominal strain with Δl the gauge length elongation given by the extensometer and l_0 the initial gauge length. Under the small strain assumption tentatively adopted here, the strain ε is partitioned into elastic ε^e and plastic ε^p contributions, i.e. $\varepsilon = \varepsilon^e + \varepsilon^p$, for the uniaxial tests (this assumption is discussed later on in the following section dedicated to constitutive modeling, see section 2.3.1). The corresponding Cauchy stress component σ is given as $(F/A_0) \cdot (1 + \varepsilon_N)$, where F is the load and A_0 the initial cross-section area.

1.3.2.1 Low Strain Rate

A series of displacement-controlled quasi-static tests are performed along different orientations under tension or compression loading with strain rates ranging from $|\dot{\varepsilon}| \simeq 10^{-4}\,\mathrm{s}^{-1}$ to $10^{-1}\,\mathrm{s}^{-1}$ using either an Instron electromechanical press or a MTS servohydraulic machine.

The load is measured by load cells of 10 kN or 100 kN depending on the size of the specimens.

Table 1.1 summarizes the different measurement techniques used during the experimental campaign.

Table 1.1: Summary of the different measurement techniques employed during the experimental campaign.

	Quasi-Static		Dynamic
Loading	$T = 25\,°\mathrm{C}$	$T > 25\,°\mathrm{C}$	$T = 25\,°\mathrm{C}$
Smooth Tension	Marker tracking	Marker tracking	DIC
Smooth Tension (Normal Direction)	DIC	DIC	-
Smooth Compression	Extensometer	Marker tracking	Strain Gages
Notched & Shear	Extensometer & DIC	-	DIC
Hat-shaped	Extensometer	-	-

In the case of compression tests at room temperature, an axial clip-on extensometer with 12.5 mm gauge length and +/- 5 mm displacement range is mounted on the rigid plates compressing the sample. Some grease is applied as lubricant on the samples surface in order to minimize the barreling effect.

During tension tests as well as under cyclic loadings (and uniaxial compression at high temperature) the deformation is measured by tracking marker points on the sample surface. For the smooth specimens, four points were measured to calculate the axial as well as the transverse strain so that the Lankford coefficient can be estimated. According to the definition given by Hill [52], the width to thickness ratio of the strain rate is denoted as the anisotropy ratio. By assuming an isochoric plastic deformation and assuming a negligible elastic strain, the Lankford coefficients can be expressed as

$$r_\theta = \frac{\dot{\varepsilon}^p_{transverse}}{\dot{\varepsilon}^p_{normal}} \simeq -\frac{\varepsilon_{transverse}}{\varepsilon_{transverse} + \varepsilon_{axial}} \tag{1.2}$$

where $r_\theta = 1$ for an isotropic material.

The notched and shear samples used a clip-on mechanical extensometer of initial gauge length of 12 mm to measure the nominal strain.

For high temperature tests, an oven reaching temperatures of up to 350 °C is employed. The temperature of the sample is controlled by a thermocouple and does not fluctuate by more than 2 °C around the setpoint during the whole mechanical test.

1.3.2.2 High Strain Rate

Split-Hopkinson pressure bar (SHPB) set-ups are used for compression and tension tests at high strain rates of up to $|\dot{\varepsilon}| \simeq 1.5 \times 10^3\,\mathrm{s}^{-1}$, at room temperature (see [53–56]). For tension tests, the load-inversion device designed by Dunand et al. [57] and extended by Roth et al. [58] is used. In order to obtain the desired high loading rate, the tension specimen is $1.2\,\mathrm{mm} \times 3\,\mathrm{mm} \times 10\,\mathrm{mm}$ (thickness x width x gauge length) and the compression specimen is $4.7\,\mathrm{mm} \times 5.4\,\mathrm{mm}$ (height x diameter).

According to the one-dimensional analysis of the wave propagation in compression, the specimen strain rate and load transferred to the specimen are measured via strain gauges glued on the input and output bars. In the case of tension dynamic tests, the force is still measured with a strain gauge on the output bar by using a one point measurement (see Zhou and Park [59]). The strain field in the sample is obtained by digital image correlation (DIC), based on images captured with a Phanton v7.3 high speed camera. A frame rate of up to $10^5\,\mathrm{Hz}$ with a resolution of $304 \times 64\,\mathrm{px}^2$ is employed to observe the zone of interest of $10 \times 3\,\mathrm{mm}^2$ covered with speckle painting using an airbrush. The VIC-2D software is used for DIC and the mean strain in the gauge length is measured using a virtual extensometer following the relative displacement of two points of the speckle. Figure 1.20 shows a schematic drawing of the experimental set-up.

(a) Set-up for compression

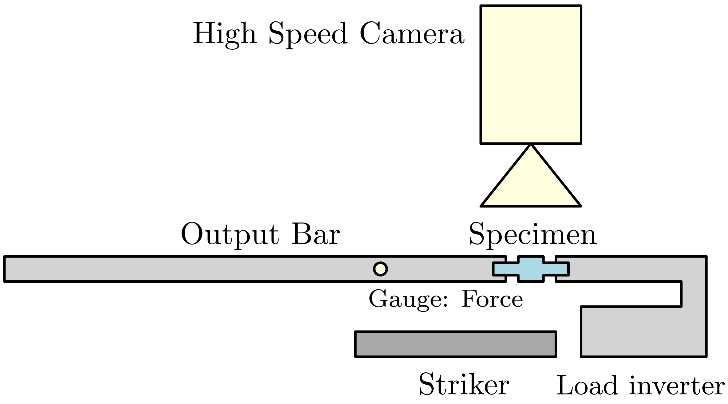

(b) Set-up for tension

Figure 1.20: Split-Hopkinson Pressure Bars (SHPB) set-ups used.

1.4 Experimental results

In a first approximation, the uniaxial component σ measured along the loading direction is assumed to be additively decomposed into a kinematic hardening contribution σ_{KH}, an isotropic hardening contribution σ_{IH} and a viscous contribution σ_v which a priori depend on a finite number of parameters, namely the orientation θ, the triaxiality χ, the temperature T, the accumulated plastic strain κ and the plastic strain rate $\dot{\kappa}$ (in this section, it is tentatively assumed $\kappa \simeq |\varepsilon^p|$ and $\dot{\kappa} \simeq |\dot{\varepsilon}^p|$ under monotonic uniaxial loading). The stress σ accordingly reads

$$|\sigma| \simeq \sigma_{KH}\left(\theta, \chi, \kappa, T\right) + \sigma_{IH}\left(\theta, \chi, T, \kappa\right) + \sigma_v\left(\dot{\kappa}, \theta, \chi, \kappa, T\right) \tag{1.3}$$

where the kinematic and isotropic hardening contributions are assumed to be rate independent. The aim is to identify each contribution.

In a first step, the dependence on the loading direction θ, loading path χ, temperature T and strain rate $\dot{\kappa}$ is quantified by an analysis of the total stress $(\sigma_{KH} + \sigma_{IH} + \sigma_v)$. For this purpose, monotonic, cyclic and relaxation loadings are employed. Secondly, the contributions of the rate independent stress $(\sigma_{KH} + \sigma_{IH})$ and the viscous stress (σ_v) are identified.

1.4.1 Monotonic loading

At least two samples per geometry and per direction were used for the tension and for the compression loadings.

1.4.1.1 Effect of the loading direction θ

Examples of quasi-static uniaxial tests performed along four directions are plotted in Figure 1.21. The highest yield stress is found along the transverse direction (which is consistent with the high fraction of c axes of the HCP phase in this direction on the pole figures in Fig.1.15a) followed by the rolling (along which a smaller, but non negligible fraction of c axes are aligned) and the diagonal direction, in both tension and compression (note the resemblance with Figure 1.5a). The normal direction (orthogonal to most c axes) has, accordingly, the lowest yield stress. The anisotropy is visibly more accentuated under compression loading (as also seen in Figure 1.5b).

1.4.1.2 Effect of loading sign $\chi = \pm 1/3$

As shown in Figure 1.21 for all directions and Figure 1.22 for the rolling direction in particular, a strong yield stress differential between tension and compression is observed. According to Figure 1.22, the yield stress in compression is higher than in tension by around 20 %. The hardening for both types of loading is strongly non linear at small plastic strain and tends to become linear at large plastic strain. The nonlinear part is more pronounced under compression loading while the linear part is (quasi) similar (same slope) under tension and compression loading. Similar results were found for the other directions (not shown here).

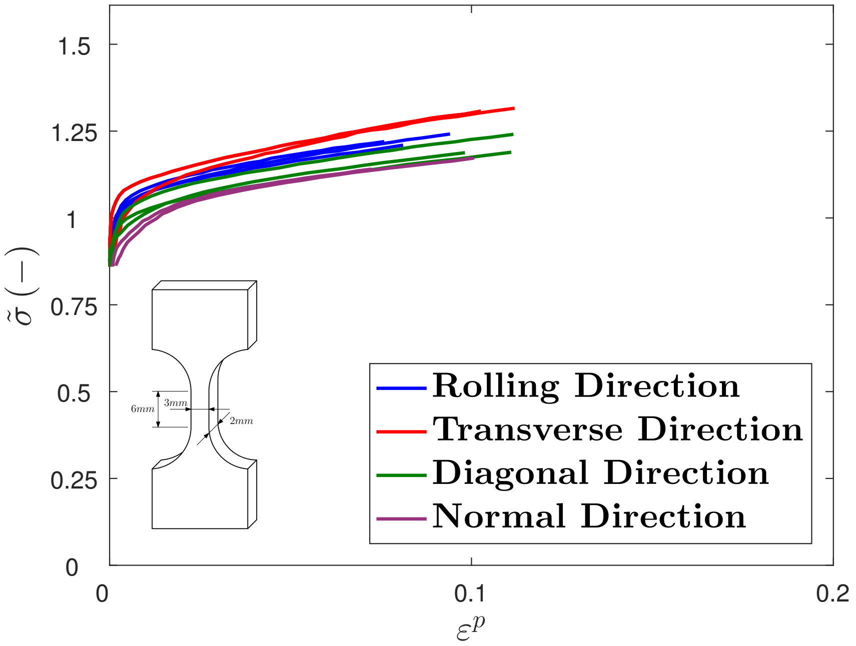

(a) Tension

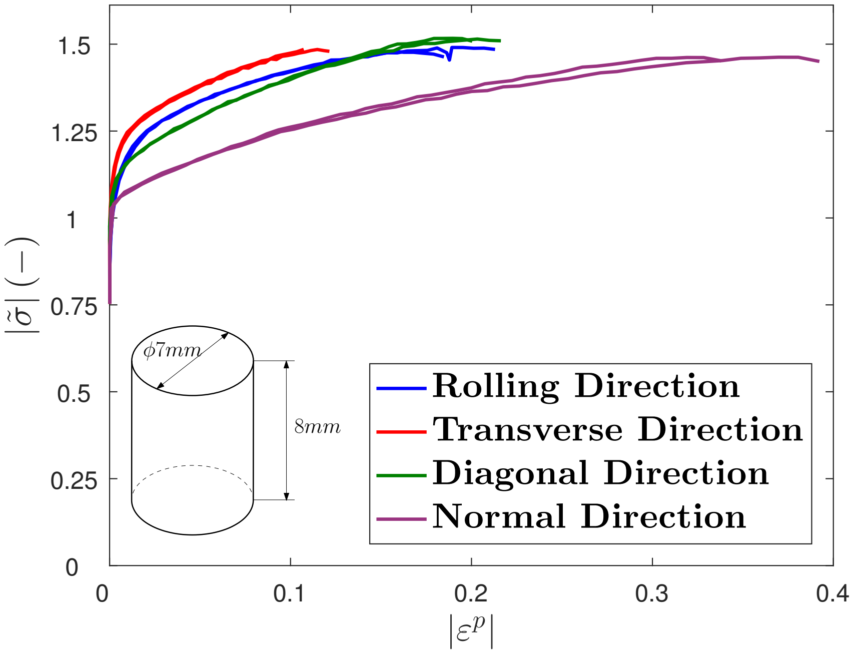

(b) Compression

Figure 1.21: Stress vs. plastic strain. Tension and compression. Influence of the direction. $|\dot{\varepsilon}| \simeq 10^{-3}\,\mathrm{s}^{-1}$ and $T = 25\,°\mathrm{C}$.

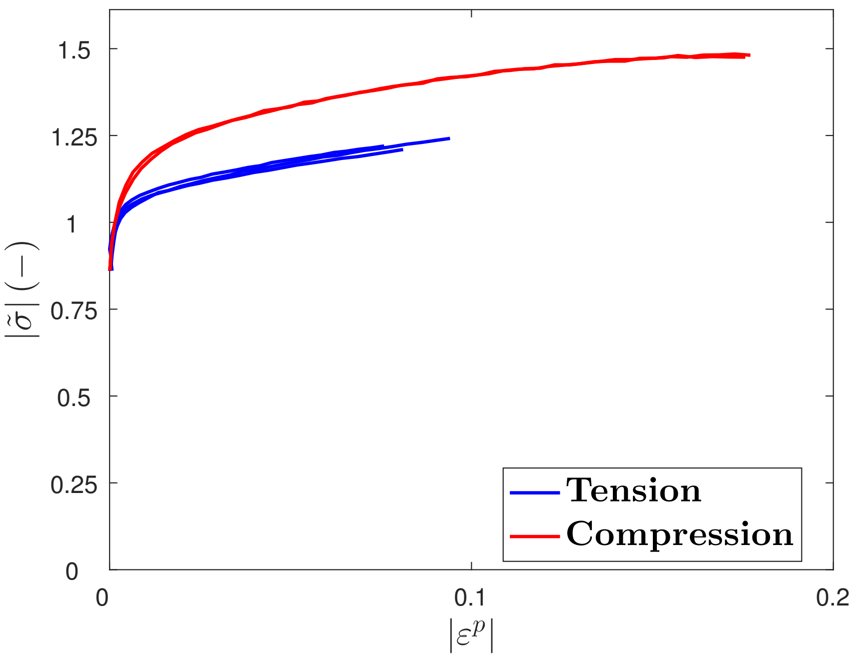

Figure 1.22: Stress vs. plastic strain. Tension-Compression superposition. $|\dot{\varepsilon}| \simeq 10^{-3}\,\mathrm{s}^{-1}$, $T = 25\,°\mathrm{C}$, Rolling direction RD.

1.4.1.3 Effect of the strain rate $\dot{\kappa}$

In Figure 1.23 are superimposed the results of uniaxial tension and compression tests carried out at various loading rates ranging from quasi-static to dynamic regimes. Strain rates of up to $10^3\,\mathrm{s}^{-1}$ were obtained. While the effect of the strain rate is not significant between $10^{-3}\,\mathrm{s}^{-1}$ and $10^{-2}\,\mathrm{s}^{-1}$, and even masked by the scatter from one specimen to the other, a clear shift can be noticed when going from the quasi-static to the dynamic range. It is noteworthy that due to notably inelastic self-heating at high strain rate, the specimen softens under adiabatic conditions. As a result, the hardening rate in the dynamic regime is apparently lower than in the quasi-static case. Equivalent isothermal stress-strain curves are shown later in Figure 1.41.

Figure 1.24 shows the apparent dependence of the yield stress on the plastic strain rate. A clear strain rate hardening can be seen. On a logarithmic scale, this viscous effect seems to follow a nonlinear trend for all the directions considered (especially in compression). The net viscous effect is sill to be analyzed in the next Section 1.4.1.4.

1.4.1.4 Effect of temperature T

Figure 1.25 shows the results of uniaxial tension and compression tests at various temperatures. While the yield stress decreases quasi-linearly as the temperature rises (see Figure 1.26), the hardening rate does not seem to be affected by the temperature under isothermal conditions.

The yield stress dependence on the temperature can have a strong impact on the consequences of self-heating at high loading rates. Indeed, the competition between thermal softening and strain rate hardening at high loading rates will determine the potential instability of the material, hence the importance of accounting for the dependence of the yield stress on temperature.

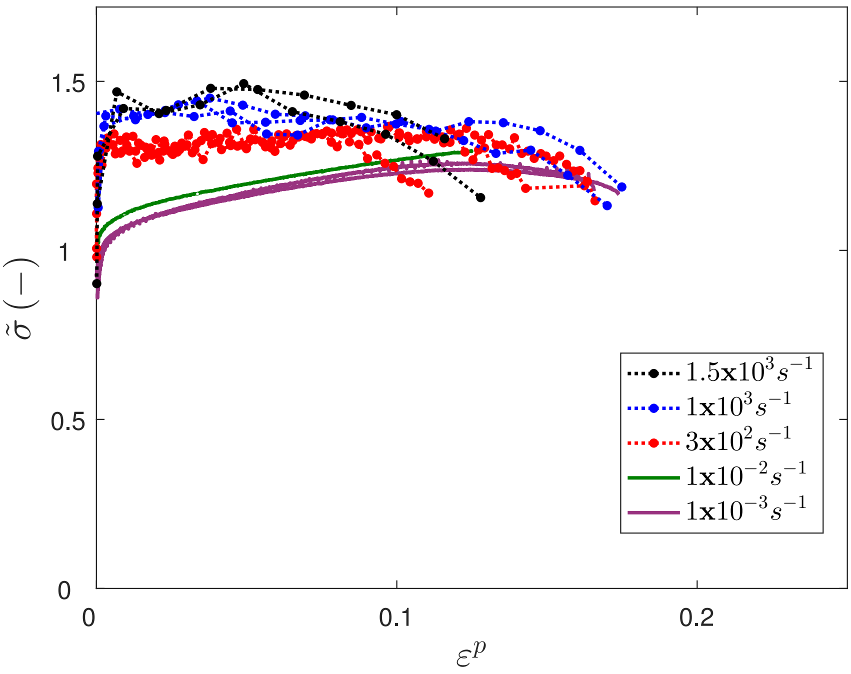

(a) Tension

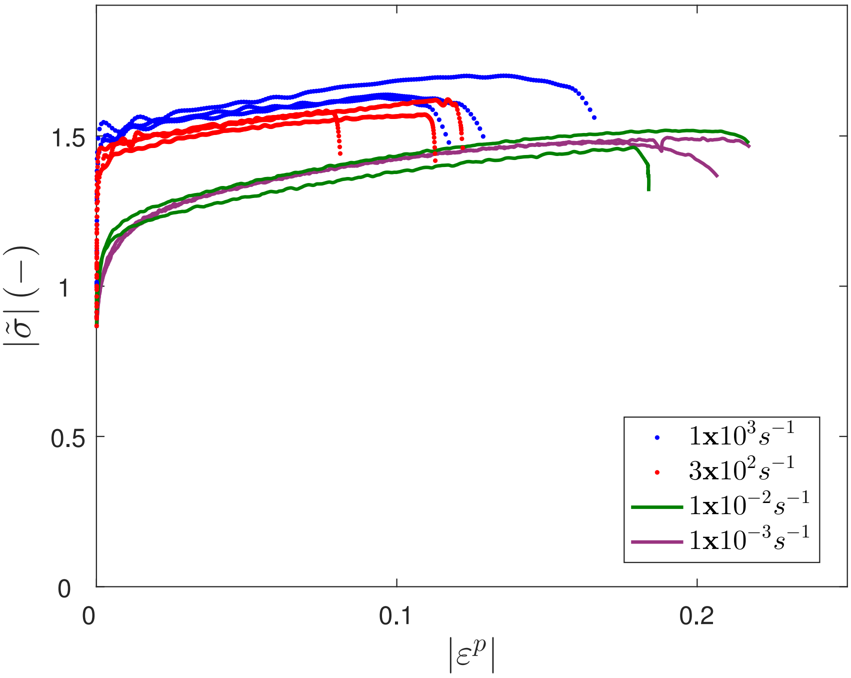

(b) Compression

Figure 1.23: Stress vs. plastic strain. Tension and compression. Influence of strain rate. $T = 25\,°\text{C}$, Rolling direction RD. The dots in the high strain rate tension curves correspond to the high speed camera recording shots.

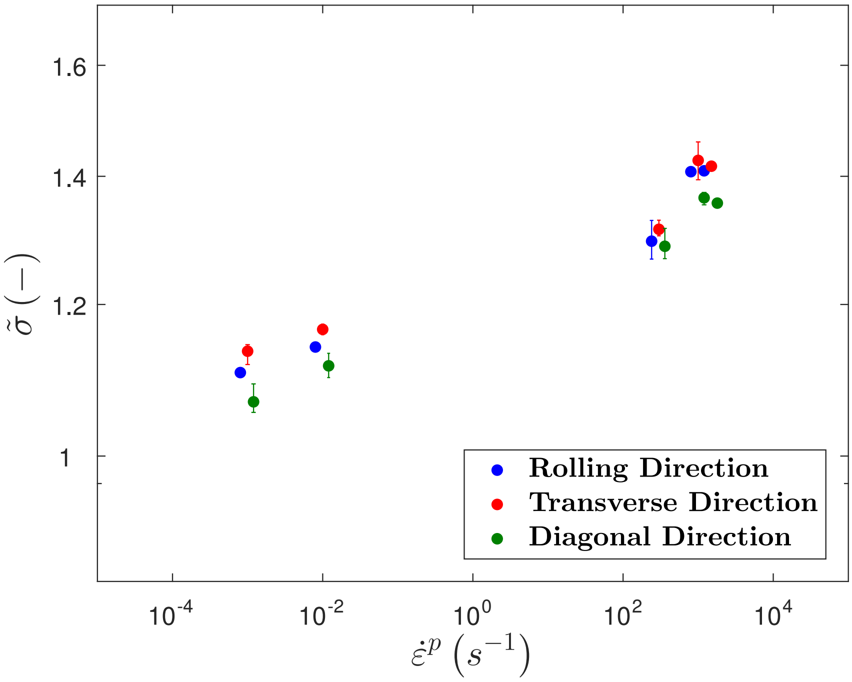

(a) Tension

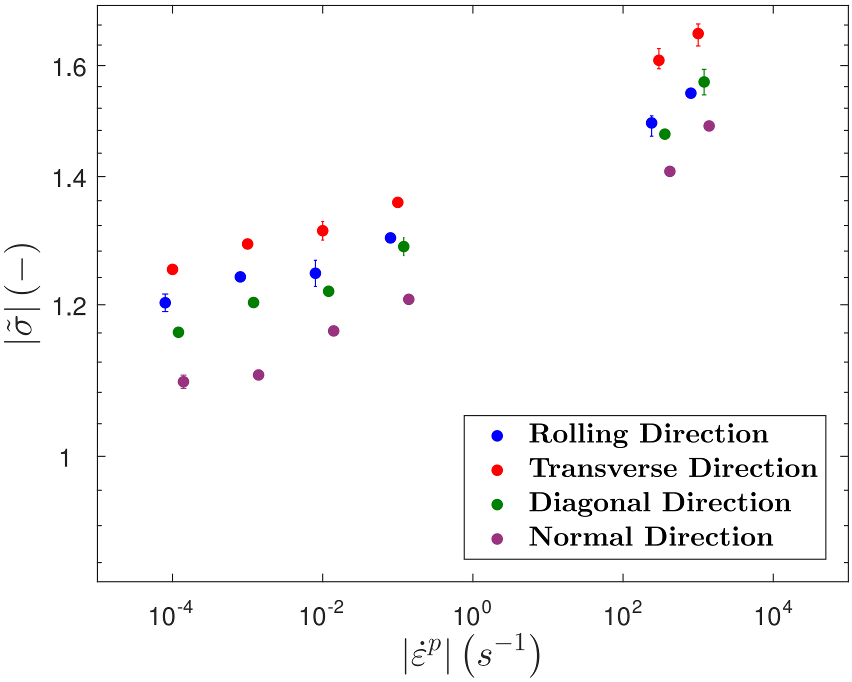

(b) Compression

Figure 1.24: Stress at 2 % plastic strain vs. plastic strain rate. Tension and compression. $T = 25\,°\mathrm{C}$. Self-heating induced softening is negligible at this strain amount.

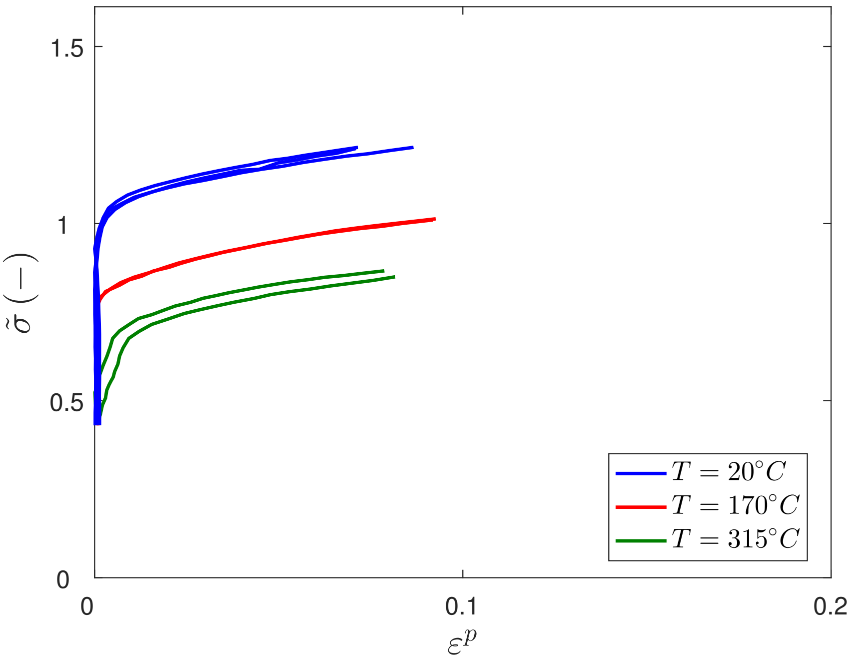

(a) Tension

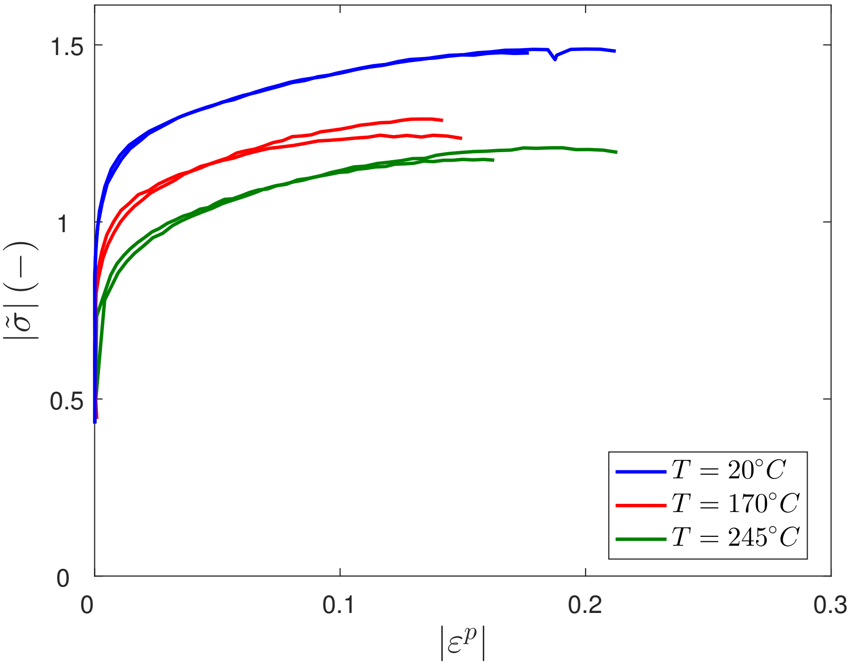

(b) Compression

Figure 1.25: Stress vs. plastic strain. Tension and compression. Influence of temperature. $|\dot{\varepsilon}| \simeq 10^{-3}\,\mathrm{s}^{-1}$, Rolling direction RD. Similar effects were observed for the other directions.

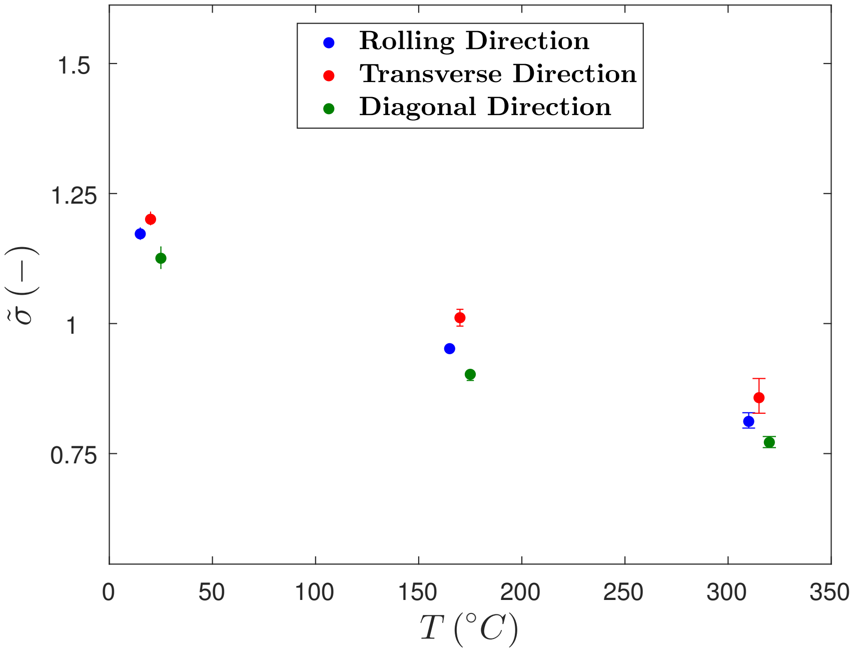

(a) Tension

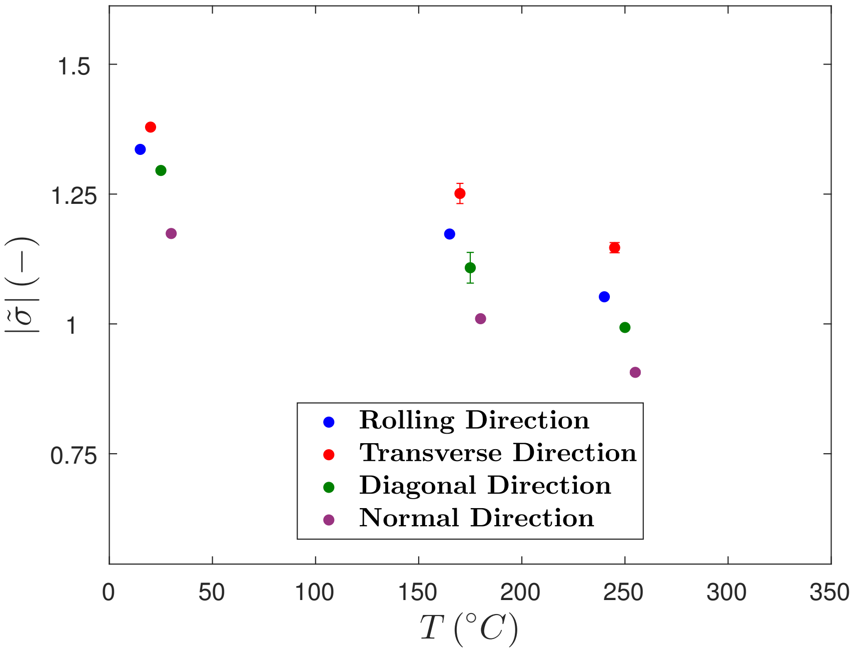

(b) Compression

Figure 1.26: Stress at 5 % plastic strain vs. temperature. Tension and compression. $|\dot{\varepsilon}| \simeq 10^{-3}\,\mathrm{s}^{-1}$.

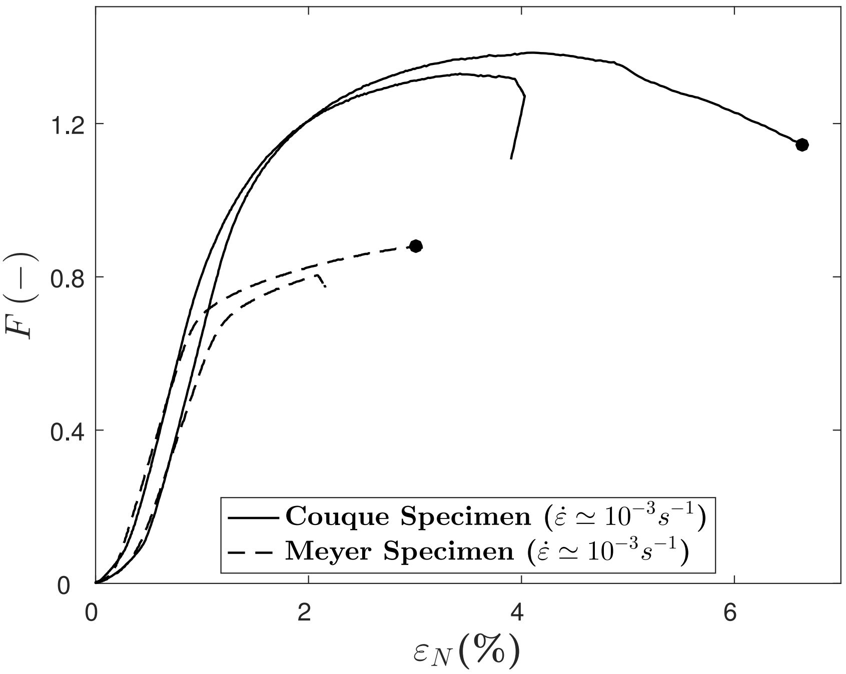

Figure 1.27: Force vs. nominal strain. Couque [50] and Meyers [51] hat-shaped specimens. Influence of stress triaxiality. $v = 8 \times 10^{-3}$ mm s, $T = 25\,°\mathrm{C}$ and Normal direction ND. Fracture of the specimens are denoted by a dot. The force is normalized with the cross-section area of the specimen (truncated cone) for comparison purposes.

1.4.1.5 Effect of stress triaxiality ratio χ

The following tests aimed at exploring the influence of the stress triaxiality ratio on the material response. They will provide with the experimental data used for the verification and validation of the model. First, the tests on hat-shaped compression specimens involving negative STR where carried out using the same set-up as for the uniaxial compression tests. Figure 1.27 shows the superimposed force vs. nominal strain curves for the Couque ($\chi \simeq -1/2$) and Meyers ($\chi \simeq -1/5$) specimens. As expected, the combined effects of shear and compression on the Couque sample produce a higher load as compared to the Meyers geometry. For each geometry, one test was carried out until rupture (marked as dots in Figure 1.27) and the other test was interrupted for later observations under the microscope. It is worth noting that the Meyers hat-shaped specimen presents a brutal rupture whereas in the Couque geometry, the final rupture is preceded by a slow decrease in the load.

Figure 1.28a shows the force vs. nominal strain for the flat notched tension specimens in Figure 1.17 ($\chi \in [1/2 - 1]$). The resistance and the ductility are highly dependent on the notch radii and resulting stress state, as expected. The highest force and lowest nominal strain at fracture are observed for the double notched specimen ($\chi \simeq 1.0$), while both single notched specimens exhibit the same peak load ($\chi \simeq 1/2 - 2/3$), but a lower fracture strain for the smallest notch radius. The experimental scatter is probably due to small deviations from the nominal specimens dimension and to the macrozones present in the material (see Figure 1.11).

A closer analysis of the final instants on some of these tension specimens has been carried out. Two measurement channels were used to record the signal from the mechanical extensometer: the main one at a sampling frequency of 10 Hz and a secondary one, manually triggered towards the end of the test, with a sampling frequency of 1 kHz. Figure 1.28b and 1.28c shows the load vs. nominal strain curves for the simple notched specimens of radii $R = 2$ mm and $R = 0.5$ mm. Using the low sampling frequency, damage-induced softening would hardly be detected, but when the high frequency sampling is used, a progressive drop in the stress is observed just before final failure. The 20 MPa stress drop, which is small compared to the average ≃1000 MPa flow stress, occurs within a strain range of less than 0.1 %, which is also quite small.

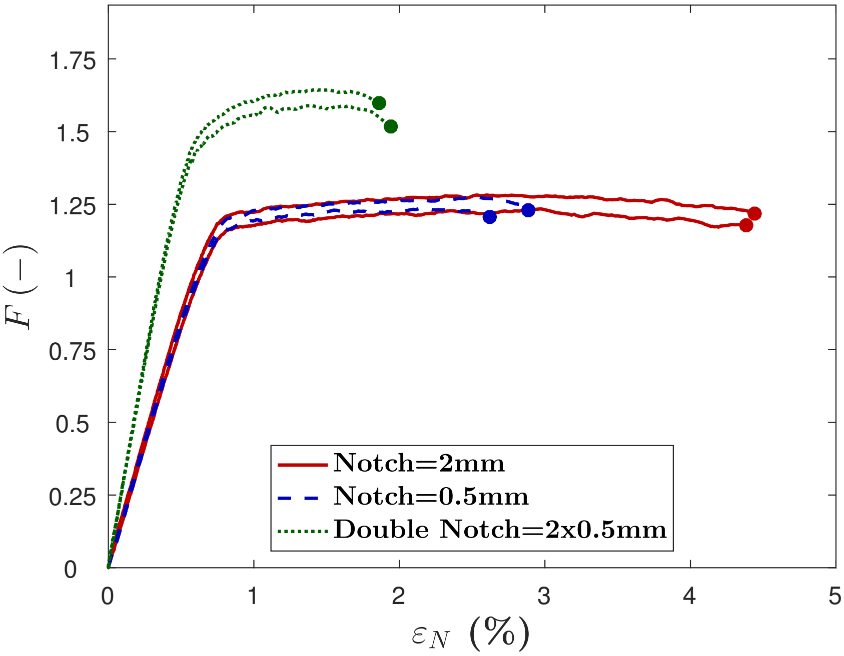

(a) Force vs. nominal strain

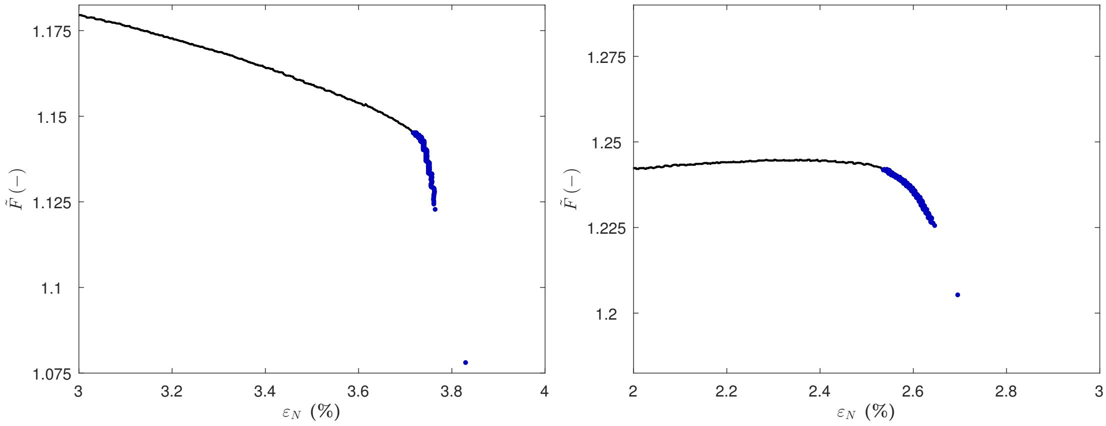

(b) $R = 2$ mm (zoom) (c) $R = 0.5$ mm (zoom)

Figure 1.28: Force vs. nominal strain. Flat notched tension specimens from Figures 1.17c, 1.17d and 1.17e. Influence of stress triaxiality. $v = 1.6 \times 10^{-3}$ mm/s, $T = 25$ °C and Transverse direction TD. Fracture of the specimens are denoted by a dot. The force is normalized with the cross-section area of the specimen for comparison purposes. Similar effects were obtained for the other directions.

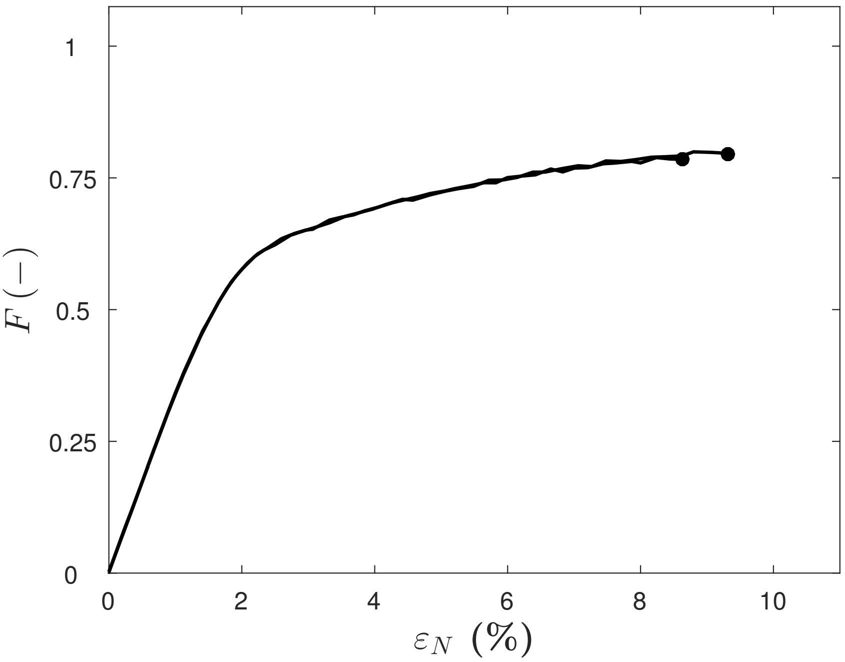

Figure 1.29: Force vs. nominal strain. Shear tension flat specimen from Figure 1.17a. Influence of stress triaxiality. $v = 1.6 \times 10^{-3}\,\mathrm{mm/s}$, $T = 25\,°\mathrm{C}$ and Transverse direction TD. Fracture of the specimens are denoted by a dot. The force is normalized with the cross-section area of the specimen for comparison purposes. No high frequency sampling measurements were done for this specimen.

Figure 1.29 shows the results for the tension-induced shear specimen (depicted in Figure 1.17a). A comparatively lower load and higher nominal strain at fracture is observed with respect to the other flat tension geometries. The experimental scatter is negligible.

1.4.2 Reversed loading

Kinematic hardening is quite common among dual-phase microstructures and can contribute to an important part of their hardening. In order to quantify the respective contributions of isotropic and kinematic hardening, tension-then-compression and compression-then-tension tests are carried out. These two different sequences also allow to verify that the strength differential deduced from separate tension and compression tests on different sample geometries is retrieved when a unique sample geometry and test setup is used. As an example, Figure 1.30 shows the recorded stress-strain loops during 2.5 tension-compression cycles along the rolling direction. As the loading is reversed, a precocious slow yield is observed. This effect might entail the presence of a strong non linear kinematic hardening. Furthermore, the increase in size between both cycles evidences the contribution of isotropic hardening.

Figure 1.31 shows the stress strain curves of a tension test with consecutive unloadings. The isotropic and kinematic components of the material hardening can be deduced from the stress for which the stress-strain curve during unloading departs from linearity by more than a given offset [60]. For example, with an offset of $\delta\varepsilon^p = 10^{-4}$, the kinematic hardening values were found to contribute about 30 %-60 % to the flow stress all along the deformation process (discussed later in Section 1.4.4.2).

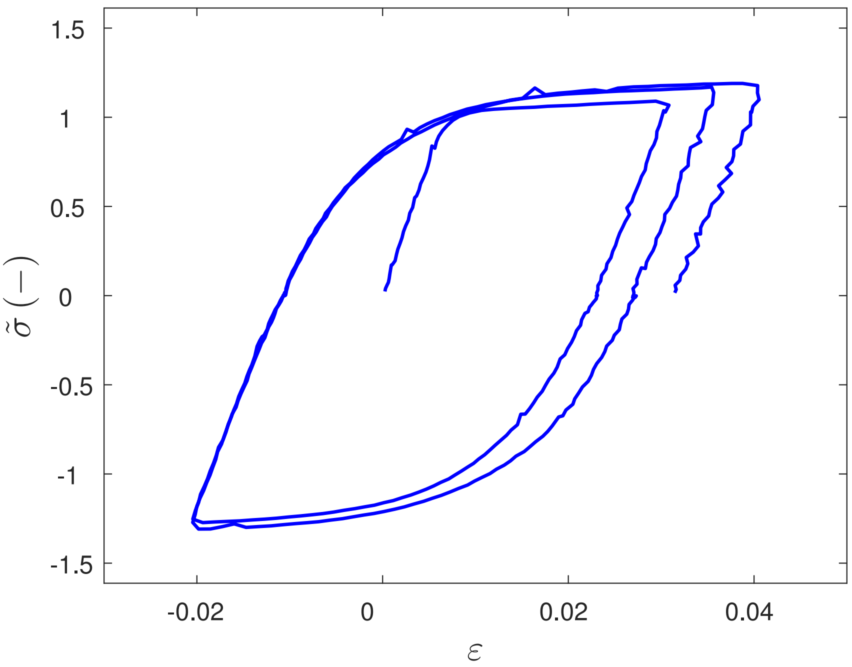

Figure 1.30: Stress vs. strain. Alternating tension-compression test. $|\dot{\varepsilon}| \simeq 5 \times 10^{-4}\,\mathrm{s}^{-1}$, $T = 25\,°\mathrm{C}$, Rolling direction RD.

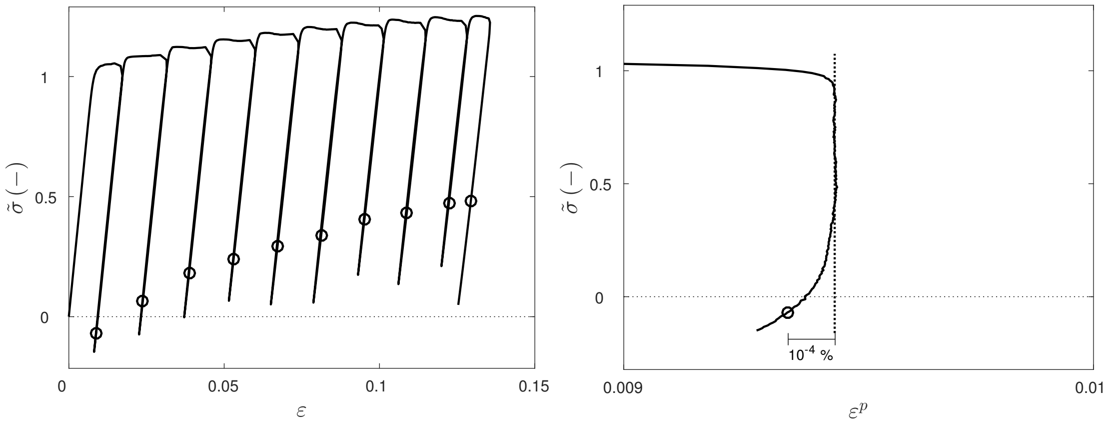

(a) Stress-strain curve (b) Criterion for the yield return limit

Figure 1.31: Stress vs. strain. Consecutive loadings and unloading on a cylindrical tension specimen. $\dot{\varepsilon} \simeq 5 \times 10^{-4}\,\mathrm{s}^{-1}$, $T = 25\,°\mathrm{C}$ and Rolling direction RD.

1.4.3 Multi-step relaxation loading

As deduced from tests carried out at different strain rates, a strain rate-induced overstress is present at room temperature, see Figure 1.23. A series of stress relaxation periods are therefore introduced during tension as well as compression tests, in order to extract the viscous component of the flow stress. The displacement-controlled tests are interrupted at selected strain amounts and the total deformation of the specimen remains constant. A drop in stress is recorded due to viscous relaxation and the test is resumed when the stress level has reached a steady state.

In Figure 1.32 are plotted the stress-strain curves obtained from the multi-step relaxation loading. The dotted lines are obtained by interpolation between the end-points of the relaxation periods and represent the rate independent part of the flow stress. By subtracting it from the total stress, the viscous component can be determined via (see Equation 1.3)

$$\sigma_v = |\sigma| - (\sigma_{KH} + \sigma_{IH}) \tag{1.4}$$

According to Figure 1.32, the viscous stress remains constant along the deformation in tension and compression. Furthermore, no effect of anisotropy is found in terms of the relaxed stress. Therefore, the viscous component is considered independent of the loading direction and of the strain. This enforces the previous simplification in Equation 1.3 of additive decomposition of the stress in a strain hardening and a viscous component.

Slight differences in viscous behavior in tension and in compression can be however noticed. To check if these differences are significant or an artifact due to the differences in testing devices and specimens geometries, the cylindrical specimens used for the reversed loading are employed to measure the relaxed stress both in tension and in compression. Figure 1.33 shows the results of a compression-tension test with two relaxation periods in tension and compression. The viscous stress, plotted in red, does not show a significant dependence on the loading direction.

Some works have reported a dependence of the strain rate sensitivity on temperature (although not in a monotonic way), see e.g. Tuninetti and Habraken [33] who found that the strain rate sensitivity is higher at $T = 150\,°\mathrm{C}$ than at room temperature, but lower at $T = 400\,°\mathrm{C}$ than at room temperature. Figure 1.34 compares the results of multi-step relaxation tests run on compression specimens at room temperature and $T = 170\,°\mathrm{C}$. As temperature is increased, the amount of relaxed stress becomes lower. This is mainly due to the overall decrease (by approximately 25 %) of the flow stress as temperature is increased while a 30 % drop in relaxed stress is observed. This could imply a temperature dependence of the strain rate sensitivity, as shown in the above mentioned publication.

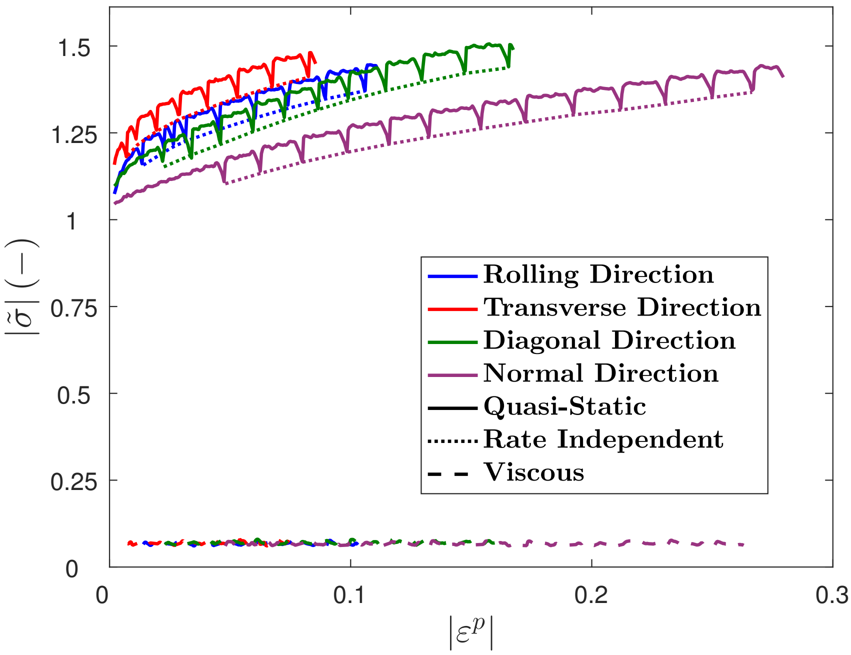

(a) Tension

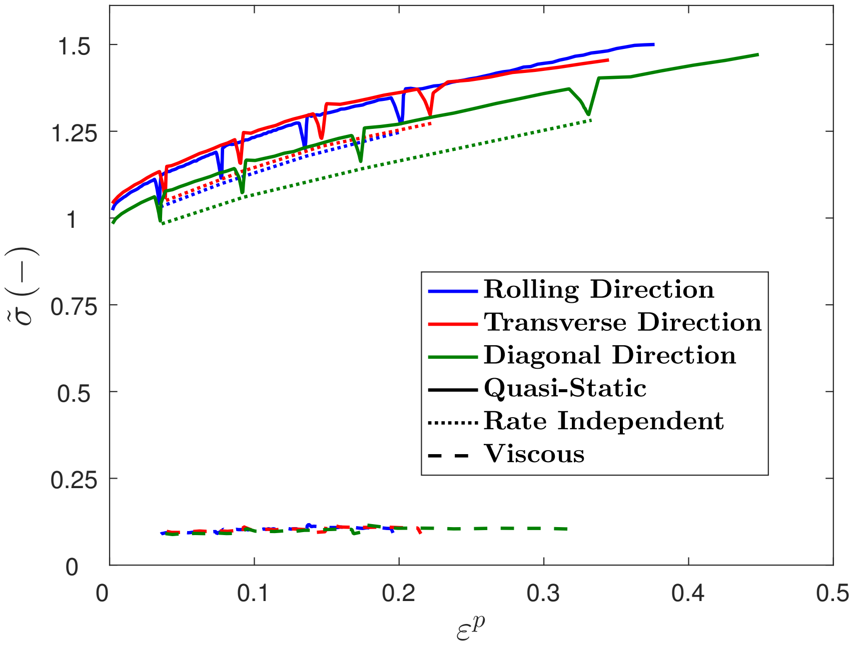

(b) Compression

Figure 1.32: Stress vs. plastic strain. Tension and compression. Multi-step relaxation. $|\dot{\varepsilon}| \simeq 5 \times 10^{-4}\,\mathrm{s}^{-1}$ and $T = 25\,°\mathrm{C}$. The drop in stress as the static state is achieved is defined as the strain rate induced overstress or viscous stress (plotted as a dashed line).

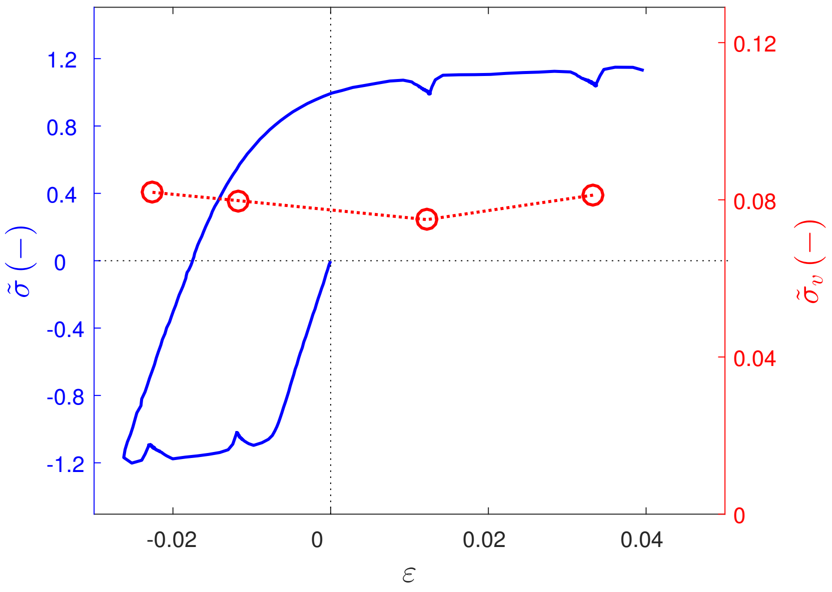

Figure 1.33: Stress vs. strain. Compression-tension test with four relaxation periods on a cylindrical specimen. $|\dot{\varepsilon}| \simeq 5 \times 10^{-4}\,\mathrm{s}^{-1}$, $T = 25\,°\mathrm{C}$ and Rolling direction RD. The viscous stress is plotted in red.

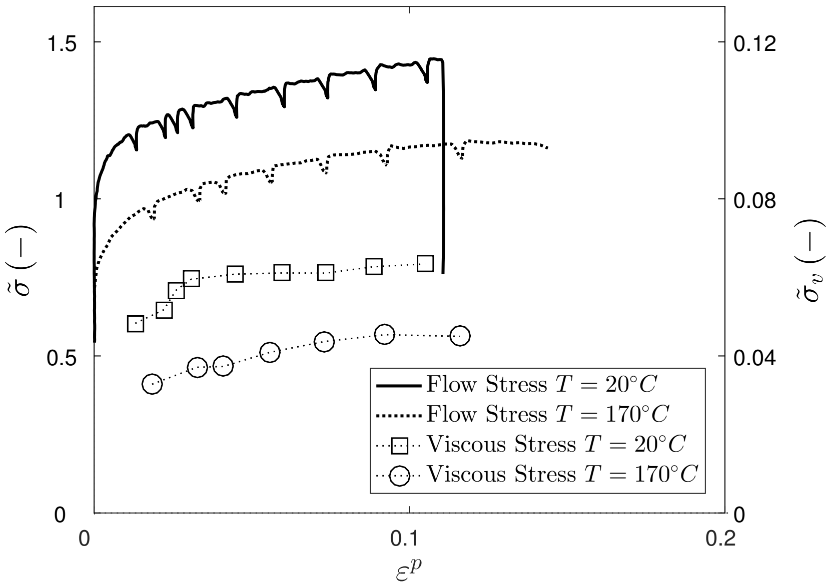

Figure 1.34: Stress vs. plastic strain. Multi-step relaxation under tension. $|\dot{\varepsilon}| \simeq 5 \times 10^{-4}\,\mathrm{s}^{-1}$ and Rolling direction RD.

1.4.4 Analysis and discussion

By extrapolating the steady-state curves (dotted lines) in Figure 1.32, the rate independent initial yield stress at room temperature can be estimated for each loading direction. It can then be subtracted from the flow stress at various strain rates so as to determine the viscous stress. Similarly, the viscous stress measured in the relaxation tests can be used to obtain the rate independent stress $\sigma_{KH} + \sigma_{IH} = \sigma - \sigma_v$ (see Equation 1.3).

In this section, the effects of anisotropy, strain hardening and temperature on the rate independent stress are herein studied. Likewise, the viscous stress is also analyzed.

1.4.4.1 Plastic anisotropy and Strength Differential

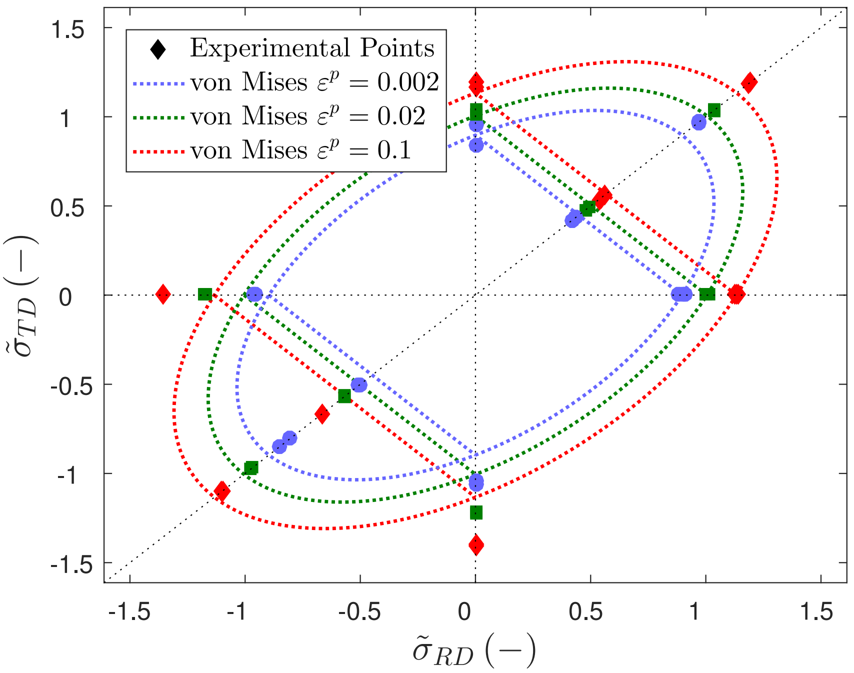

Figure 1.35: Yield locus in the $(\sigma_{RD}, \sigma_{TD})$ plane, after viscous component removal. $|\dot{\varepsilon}| \simeq 10^{-3}\,\mathrm{s}^{-1}$ and $T = 25\,°\mathrm{C}$. The loading in the normal direction is considered equivalent to the biaxial stress state. The diagonal direction implicitly includes a shear component not represented in the graph.

Figure 1.35 shows the yield surface in the TD-RD plane at various plastic strains with the viscous component removed. In the case of the diagonal direction, the Cauchy stress components with respect to the rolling and transverse axes are plotted. As for the normal direction, the equivalent biaxial state is used: assuming that the hydrostatic pressure does not play a role in plasticity, the stress tensor deviator for both types of loading are equal.

$$\begin{cases} \underline{\underline{\sigma}}_{ND} = \begin{bmatrix}0&0&0\\0&0&0\\0&0&\sigma\end{bmatrix} & \rightarrow \underline{\underline{s}}_{ND} = \begin{bmatrix}-\frac{1}{3}\sigma & 0 & 0\\ 0 & -\frac{1}{3}\sigma & 0\\ 0 & 0 & \frac{2}{3}\sigma\end{bmatrix} \quad \& \quad p\underline{\underline{I}} = \frac{1}{3}\sigma\underline{\underline{I}} \\ \underline{\underline{\sigma}}_{B} = \begin{bmatrix}-\sigma&0&0\\0&-\sigma&0\\0&0&0\end{bmatrix} & \rightarrow \underline{\underline{s}}_{B} = \begin{bmatrix}-\frac{1}{3}\sigma & 0 & 0\\ 0 & -\frac{1}{3}\sigma & 0\\ 0 & 0 & \frac{2}{3}\sigma\end{bmatrix} \quad \& \quad p\underline{\underline{I}} = -\frac{2}{3}\sigma\underline{\underline{I}} \end{cases} \tag{1.5}$$

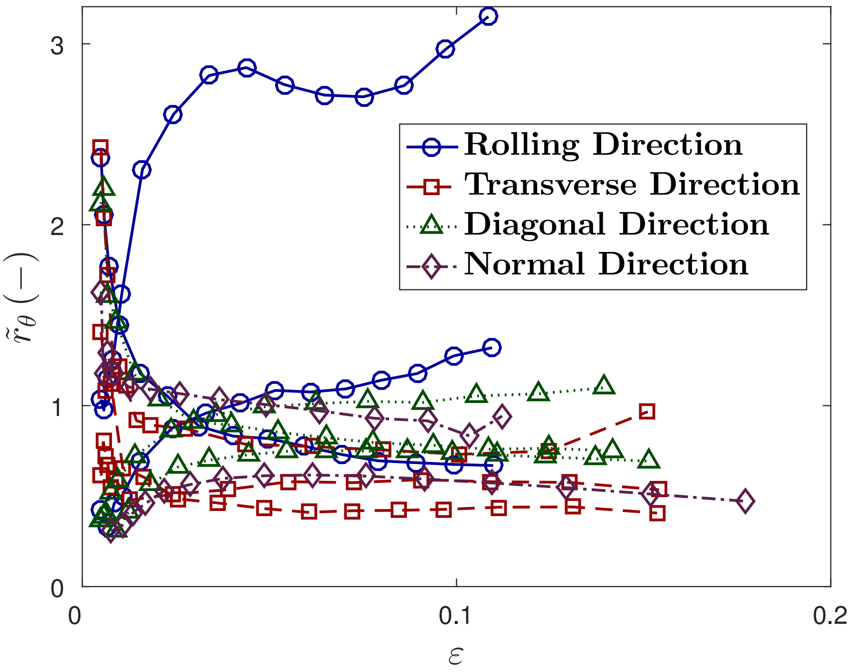

Figure 1.36: Lankford coefficients vs strain. $|\dot{\varepsilon}| \simeq 10^{-3}\,\mathrm{s}^{-1}$ and $T = 25\,°\mathrm{C}$.

For the sake of comparison, the von Mises yield surface passing through the yield stress along the rolling direction (in tension) is also plotted at the corresponding plastic strain to quantify the degree of anisotropy in Figure 1.35. According to the latter, Von Mises criterion clearly underestimates the yield stresses in compression (the compression under the normal direction is shown in the top right quadrant as a biaxial tension state). As for the orthotropy, differences are more subtle. The yield stress in the transverse direction tends to be underestimated whereas those in the normal and diagonal directions are overestimated. As the deformation increases, the misfit with von Mises criterion grows larger.

In addition, Figure 1.36 shows a comparison of the Lankford coefficients r_θ measured during the tension tests on smooth specimens. An important scatter is visible mainly due to the heterogeneity of the material and to measurement errors (highly dependent on the camera resolution as well as on the markers location). As a consequence, these experiments will not be used for the calibration, but they will be later on employed for verification purposes (see Section 3.4.2).

1.4.4.2 Strain Hardening

The first push-pull cycle from Figure 1.30 is reconsidered here after removing the viscous component, to highlight the respective contributions of the isotropic and the kinematic hardening. The compression part of the cycle has been inverted and is compared with the tension and compression monotonic stress-strain curves. As observed in Figure 1.37, a nonlinear kinematic hardening produces a progressive yielding during the load reversal. As the cyclic curve goes into compression, a permanent offset with respect to the monotonic compression appears, as a result of the Bauschinger effect.

The proportions of isotropic stress σ_{IH} and back stress σ_{KH} can be estimated from the effective stress (as defined in Helbert et al. [30]) plotted in Figure 1.31. The current

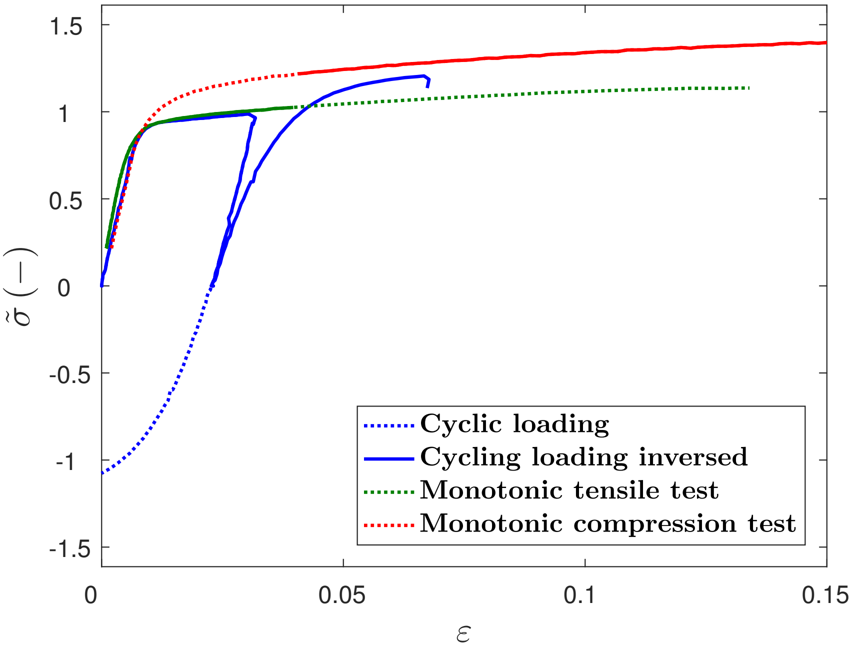

Figure 1.37: Strain vs. strain. Strain hardening comparison between the monotonic tests and the load reversal test. $|\dot{\varepsilon}| \simeq 10^{-3}\,\mathrm{s}^{-1}$ and $T = 25\,°\mathrm{C}$.

elastic domain is delimited by the maximum tension stress and the $\sigma_{reverse}$ at the onset of reversed plastic flow, defined with a fixed plastic offset of $\delta\varepsilon^p = 10^{-4}$. The isotropic and kinematic components are obtained as

$$\begin{cases} \sigma_{max} - \sigma_{reverse} = 2R \\ \sigma_{max} = R + X \end{cases} \rightarrow \begin{cases} R = \dfrac{1}{2}\left(\sigma_{max} - \sigma_{reverse}\right) \\ X = \dfrac{1}{2}\left(\sigma_{max} + \sigma_{reverse}\right) \end{cases} \tag{1.6}$$

Figure 1.38 shows the evolution of the hardening components with the total strain from the loading-unloading test presented in Figure 1.31. As the flow stress increases, the kinematic component (initially non-negligible) rises. On the other hand, the isotropic component tends to decrease with deformation (similar conclusions were observed in Helbert et al. [30]). Overall, a mixed hardening is observed in the material with a contribution of kinematic hardening ranging from 30 to 60 % of the flow stress. Note however, that the exact values depend on the plastic offset used to detect reverse plasticity although the global proportion remains almost unchanged.

In Figure 1.39 the Young's modulus has been measured during each load/unload segment and shows a slight but consistent decrease with the cumulated plastic strain. A similar effect (amplified by dwell periods) was observed at room temperature in Ti6242 alloy by Lefranc et al [40] who attributed it to nano-cavity nucleation at α/β interfaces. However, this effect will be neglected due to the small overall decrease of this parameter (less than 10 %).

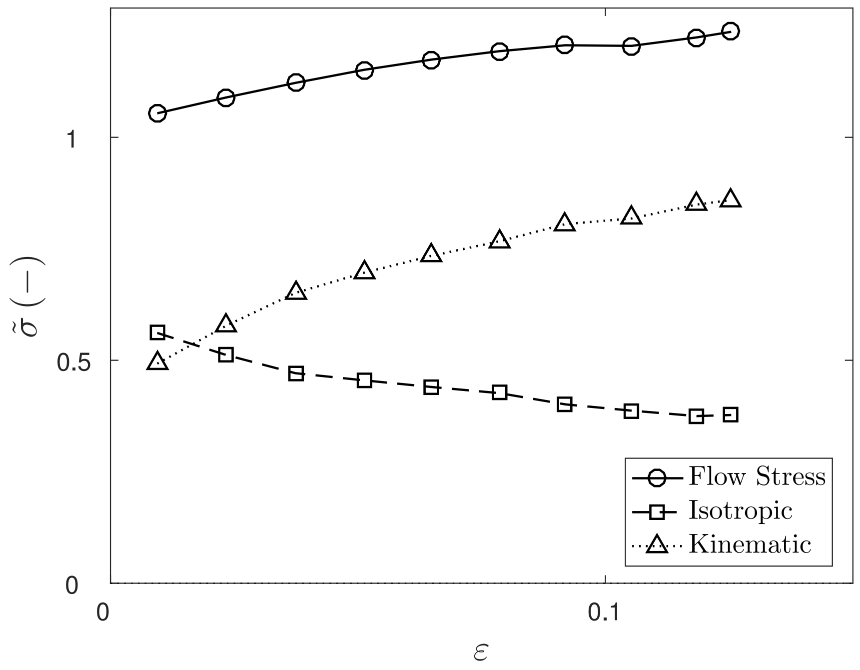

Figure 1.38: Stress vs. strain. Isotropic and kinematic contributions on specimen loaded in push-pull. $|\dot{\varepsilon}| \simeq 5 \times 10^{-4}\,\mathrm{s}^{-1}$, $T = 25\,°\mathrm{C}$ and Rolling direction RD. The elastic domain is determined with a deviation of $\delta\varepsilon^p = 10^{-4}$ from linearity.

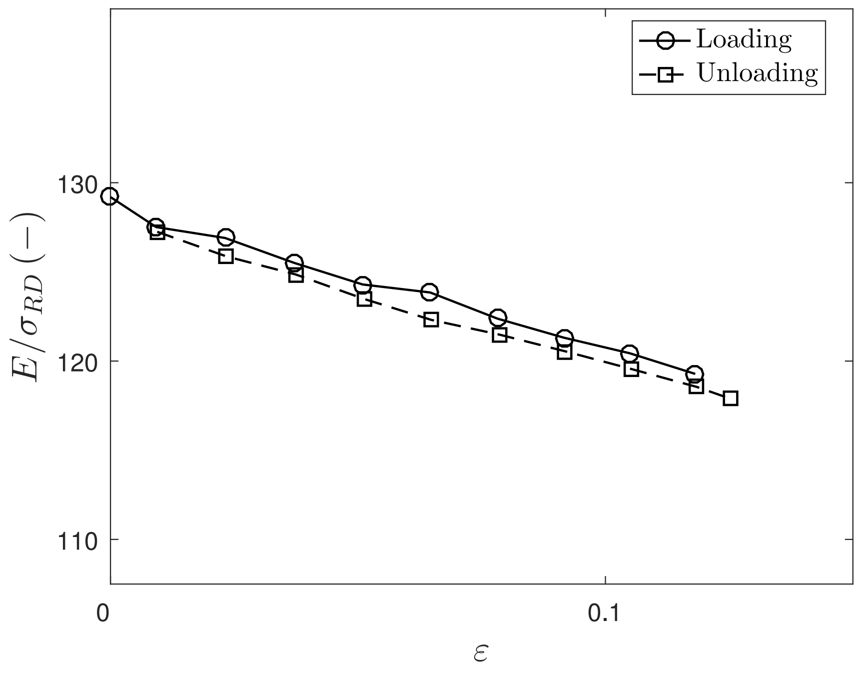

Figure 1.39: Young's modulus vs. strain. Young's modulus evolution on a specimen loaded in push-pull. $|\dot{\varepsilon}| \simeq 5 \times 10^{-4}\,\mathrm{s}^{-1}$, $T = 25\,°\mathrm{C}$ and Rolling direction RD.

1.4.4.3 Strain Rate Hardening

The viscous component from the curves in Figure 1.23 is plotted versus the strain rate in a logarithmic scale on Figure 1.40 for the tension and compression tests. The tension tests are subject to a higher scatter due to a more oscillatory response in the dynamic regime as well as the poor resolution in strain.

Figure 1.40 evidences the linear evolution of the viscous component with strain rate (in the log scale). The Norton-Perzyna law is accordingly suitable to reproduce the observed results [61 ; 62], it is expressed as

$$\sigma_v = Y_v \dot{\kappa}^{1/n_v} \tag{1.7}$$

1.4.4.4 Thermal Softening

As shown in Figure 1.25, the flow stress monotonically decreases with increasing temperature. Although the evolution of the flow stress with respect to temperature seems linear (see Figure 1.26), within the limited range of temperatures investigated, a linear extrapolation would predict negative stress values before the melting point. A power law is commonly used in the literature, and it ensures a positive stress until melting [32]:

$$\sigma \propto 1 - \langle \frac{T - T_{ref}}{T_m - T_{ref}} \rangle^{m_T} \tag{1.8}$$

where m_T is a material parameter, $T_m \simeq 1630\,°\mathrm{C}$ the melting point and $T_{ref} = 25\,°\mathrm{C}$ a reference temperature. The Macaulay brackets $\langle x \rangle = \max(0, x)$ are used.

Under low strain rate loading the conditions are isothermal, whereas under high strain rate loading, they are (quasi) adiabatic. As a consequence, the heat generated by plastic dissipation is not evacuated fast enough by conduction, leading to a local temperature rise. The material is then subject to thermal softening along the deformation process. Self-heating is usually estimated by considering that a fraction of the plastic work rate is converted into heat:

$$\Delta T \simeq \frac{\beta}{\rho c} \int_{\kappa} \sigma d\kappa \tag{1.9}$$

where ρ is the mass density and c is the heat capacity of the material. β represents the inelastic heat fraction also called Taylor-Quinney coefficient [63]. The latter is often assumed constant with values typically ranging between 0.8 and 1. Taking $\beta \simeq 0.9$ and integrating Equation 1.9 combined with the data from Figure 1.26, the drop related to temperature softening can be deduced.

Equivalent isothermal stress-strain curves may be obtained from adiabatic stress-strain curves by removing the self-heating induced thermal softening just calculated. By doing so, see Figure 1.41, strain hardening is retrieved on stress-strain curves at high strain rate. With this approach, the isothermal dynamic compression curves exhibit a similar strain hardening as the quasi-static ones.

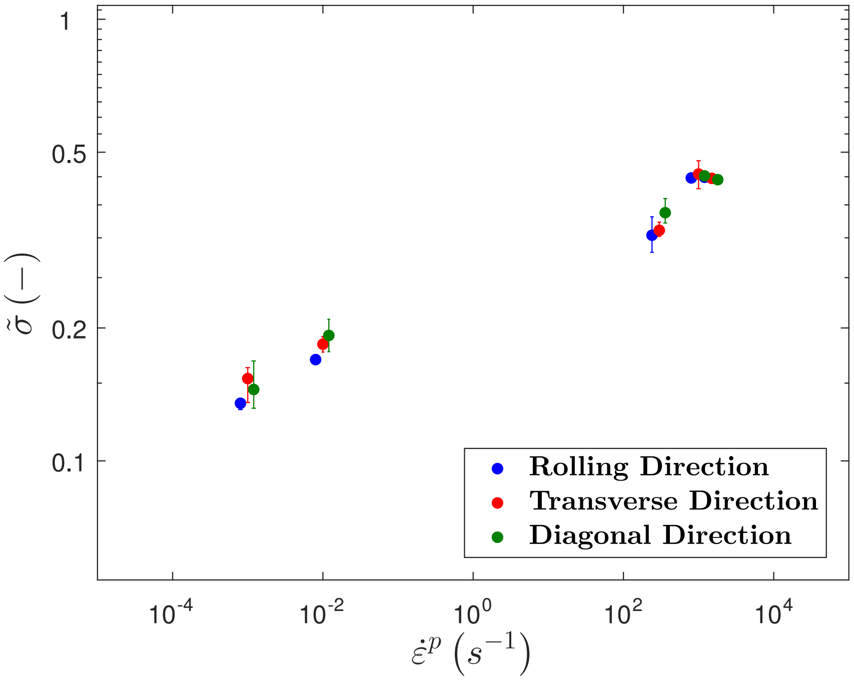

(a) Tension

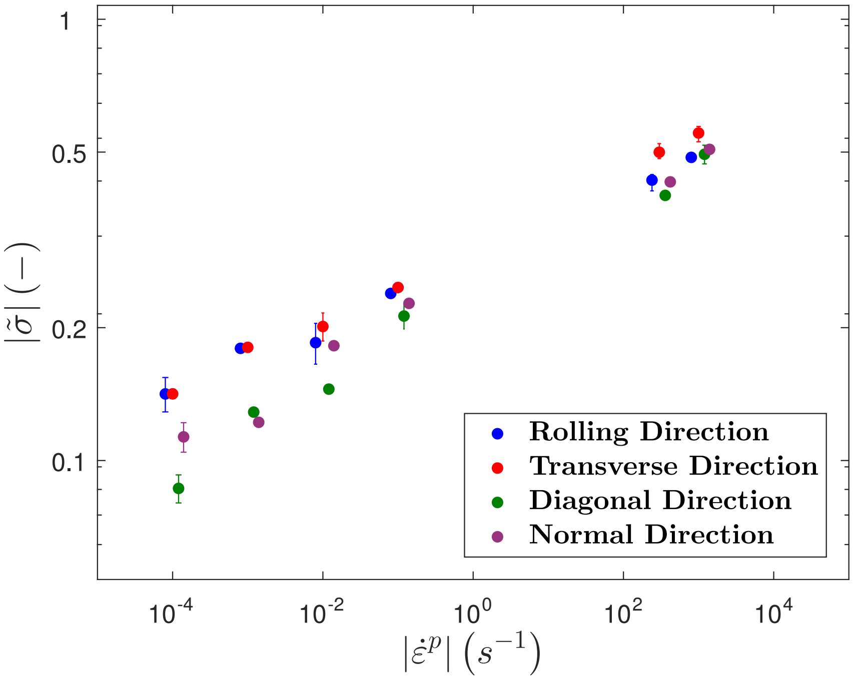

(b) Compression

Figure 1.40: Stress at 2 % of plastic strain vs. plastic strain rate. Tension and compression. $T = 25\,^{\circ}\mathrm{C}$. Self-heating softening can be negligible at this stage of deformation.

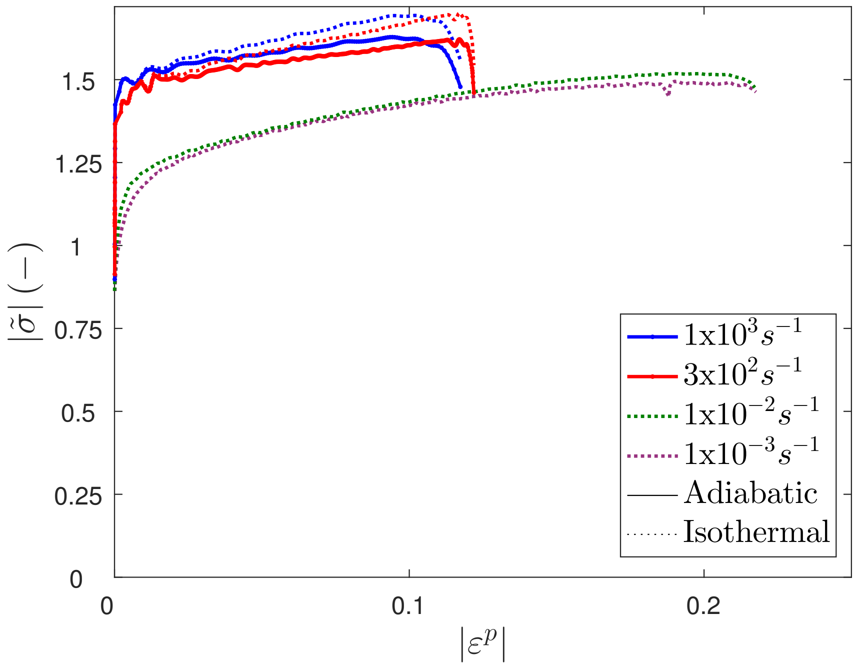

Figure 1.41: Stress vs. plastic strain. Isothermal quasi-static and dynamic compression curves (adiabatic and equivalent isothermal). $T = 25\,°\mathrm{C}$ and Rolling direction RD.

1.5 Observations of damage and fracture mechanisms

This section gathers microscopic observations of damage mechanisms and fracture surfaces done mainly by Optical Microscopy and Scanning Electron Microscopy (SEM).

1.5.1 Damage mechanisms

Post-mortem observations of fractured samples, as well as observations after interrupted tests are carried out to identify the mechanisms of damage leading to the final fracture. This section focuses only on micro-scale observations. For those observations, mechanical polishing with sandpaper followed by electro-polishing (using Struers A3 solution and a tension of 20V) or by ion polishing was performed on longitudinal sections of the samples.

Positive Stress Triaxiality

Figure 1.42 shows SEM post-mortem observations of smooth tension specimens broken at different temperatures and loading rates. The presence of voids is found near the fracture surface. They appear to nucleate mainly on interfaces between α and β phases (see Figure 1.42a) although a few very small cavities were found within α grains. This is consistent with the observations made by Helbert et al [39]. It is noteworthy that the loading rate does not seem to have a direct effect on void nucleation, and that voids are only formed near the fracture surface (Figure 1.42b). However, the void density seems to be higher after high temperature tests for which damage is observed further away from the fracture surface (see Figure 1.42c).

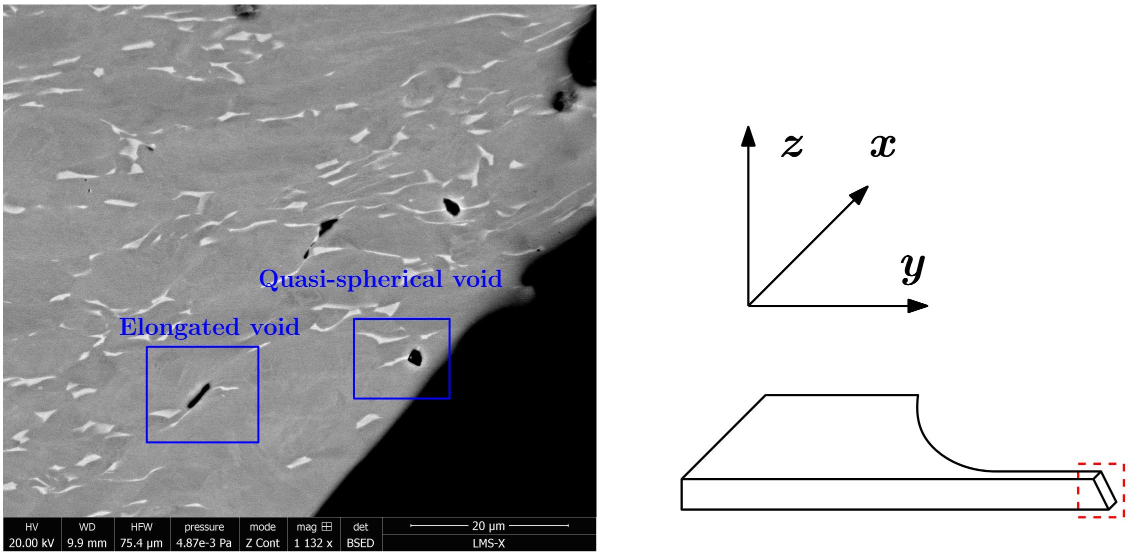

(a) $\varepsilon_f \simeq 15\,\%$, $\dot{\varepsilon} = 350\,\mathrm{s}^{-1}$, $T = 25\,°\mathrm{C}$
$y \equiv RD$

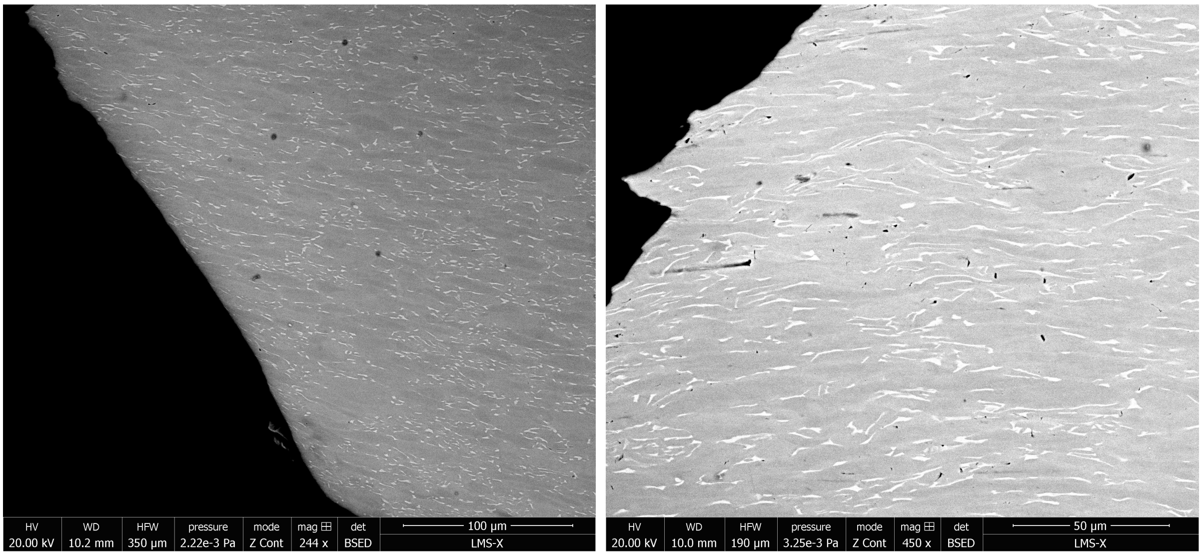

(b) $\varepsilon_f \simeq 15\,\%$, $\dot{\varepsilon} = 1500\,\mathrm{s}^{-1}$, $T = 25\,°\mathrm{C}$
$y \equiv DD$

(c) $\varepsilon_f \simeq 30\,\%$, $\dot{\varepsilon} = 1 \times 10^{-3}\,\mathrm{s}^{-1}$, $T = 315\,°\mathrm{C}$
$y \equiv DD$

Figure 1.42: SEM post-mortem observations of longitudinal sections of smooth tension specimens. See the corresponding tests in Figures 1.23 and 1.25.

The same type of observations is carried out on notched specimens, after fracture or before. Figure 1.43 summarizes the more remarkable results. Figure 1.43a shows a broken notched tension specimen. As in the smooth specimens, some cavities were found near the fracture surface. However, these cavities become scarcer when one moves away from the fracture surface, in spite of the considerably higher stress triaxiality ratio. In an attempt to determine at what stage the cavities were formed, a test on a notched tension specimen was interrupted just before fracture and a longitudinal section was observed 1.43b. The observations are made approximately at the mid-length of the sample. Some cavities are found near the free surfaces, indicating that, although it remains limited, diffuse damage takes place before fracture under high stress triaxiality ratios.

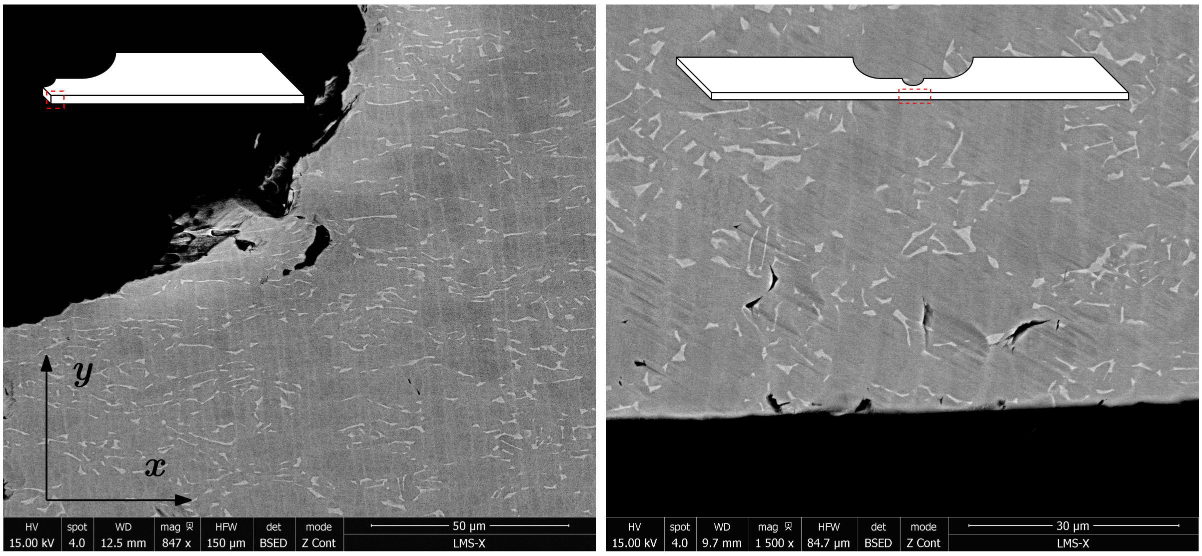

(a) Fractured $\varepsilon_f \simeq 3.8\,\%$, $\dot{\varepsilon} = 10^{-3}\,\mathrm{s}^{-1}$, $T = 25\,^{\circ}\mathrm{C}$, $x \equiv TD$ & $y \equiv RD$

(b) Non-broken $\varepsilon_i \simeq 3.3\,\%$, $\dot{\varepsilon} = 10^{-3}\,\mathrm{s}^{-1}$, $T = 25\,^{\circ}\mathrm{C}$, $x \equiv TD$ & $y \equiv RD$

Figure 1.43: SEM observations of longitudinal sections of flat notched tension specimens ($R = 2\,\mathrm{mm}$). See the corresponding tests in Figure 1.28a.

Figure 1.44 shows the fracture surface of a notched specimen (notch radius 2 mm). The surface is considerably uneven showing heterogeneities of all sizes. A closer look shows extremely dense clusters of more or less equiaxed dimples. These features suggest the nucleation, growth, and coalescence of voids favored by a high hydrostatic pressure. Furthermore, although no clear signs of the fracture initiation site are found, it can be speculated to be close to the center (expected maximum stress triaxiality) considering the large, uneven features around the middle, and the absence of directional features near the edges.

A similar observation is performed for the notched tension specimen of radius 0.5 mm (see Figure 1.45). For this sample, the heterogeneity of the surface seems comparatively smaller than for the larger notch radius. However, the same type of equiaxed dimples is retrieved. In this case, fracture seems to have been initiated near the notch tips where the surface roughness is sensibly larger. The reason behind this might be a larger plastic strain near there, combined with a sufficiently high stress triaxiality ratio. It can be speculated that the maximum χ is found away from the center-line. This hypothesis will be confirmed by the numerical simulations shown in Chapter 3.

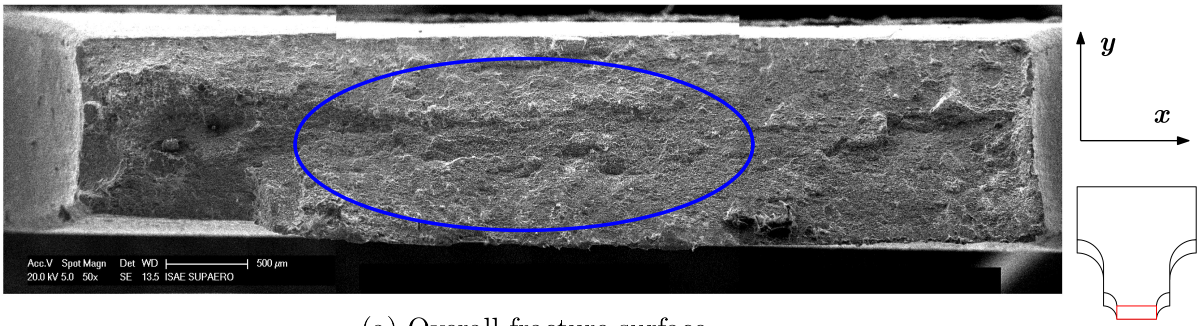

(a) Overall fracture surface

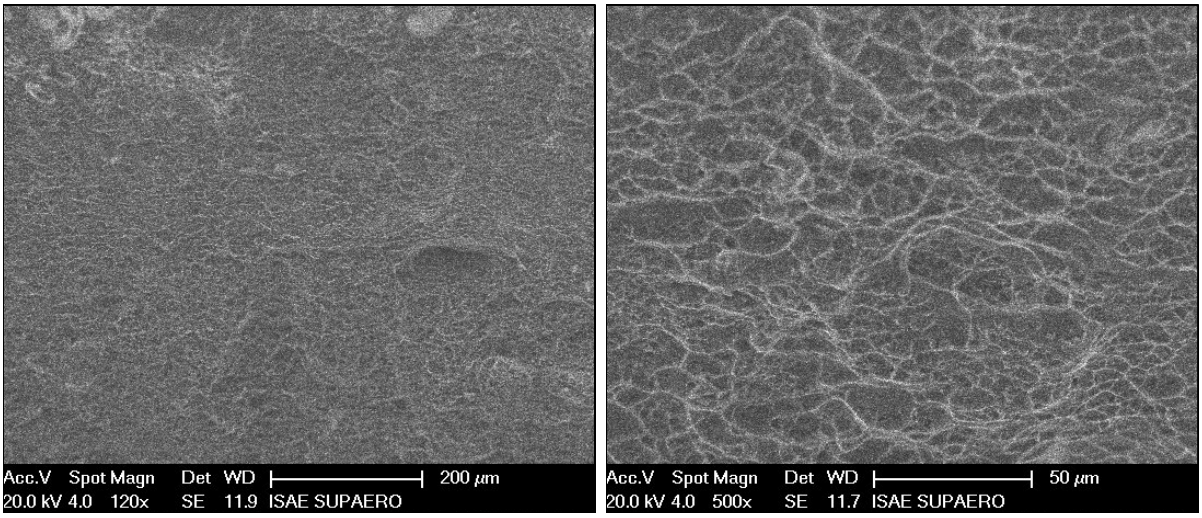

(b) Field width of 800 mm (c) Field width of 175 mm

Figure 1.44: SEM micrography on a flat notched specimen ($R = 2\,\mathrm{mm}$). $\varepsilon_f \simeq 3.8\,\%$, $\dot{\varepsilon} = 10^{-3}\,\mathrm{s}^{-1}$, $T = 25\,°\mathrm{C}$, $x \equiv RD$ & $y \equiv ND$. Blue ellipse: likely place of void initiation, i.e. in the specimen center. Zoom images taken in the center. See the corresponding tests in Figure 1.28a.

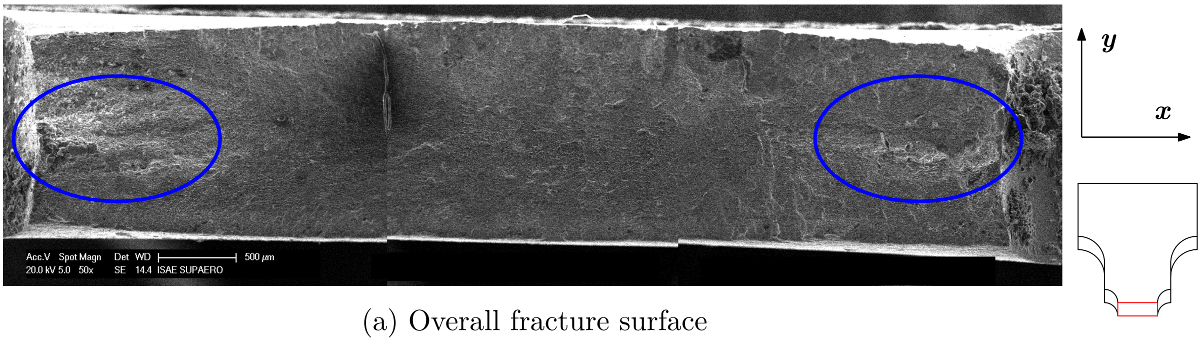

(a) Overall fracture surface

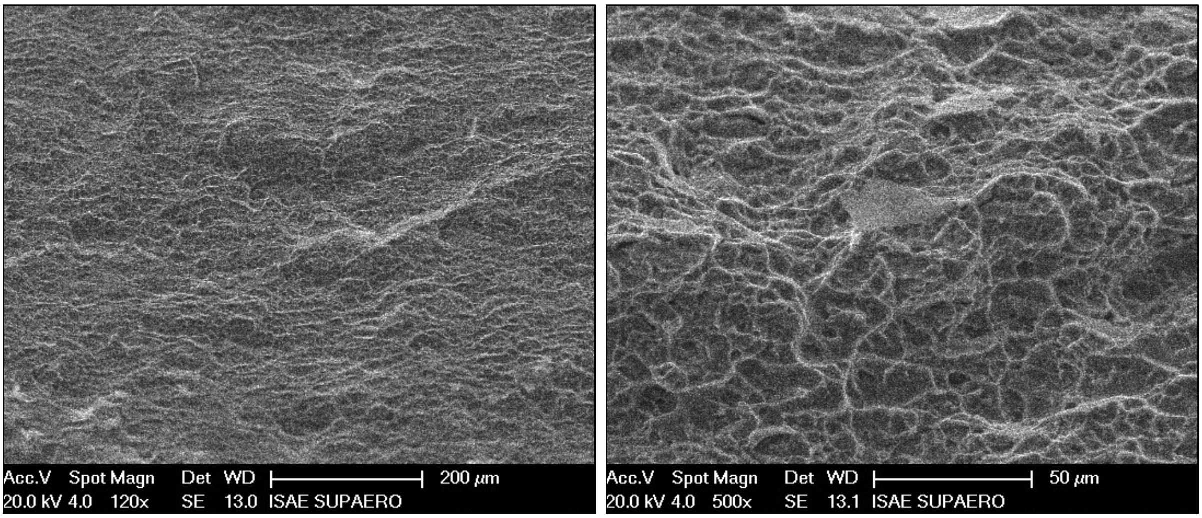

(b) Field width of 800 mm

(c) Field width of 175 mm

Figure 1.45: SEM micrography on a flat notched specimen ($R = 0.5\,\mathrm{mm}$). $\varepsilon_f \simeq 2.5\,\%$, $\dot{\varepsilon} = 10^{-3}\,\mathrm{s}^{-1}$, $T = 25\,^{\circ}\mathrm{C}$, $x \equiv RD$ & $y \equiv ND$. Blue ellipse: likely place of void initiation, i.e. from the notch tips. See the corresponding tests in Figure 1.28a.

Nil Stress Triaxiality

Regarding the tension-induced shear specimens, a substantial distribution of cavities or even microcracks was observed after an interrupted test (see Figure 1.46). This was somewhat unexpected, considering the rise of the critical equivalent plastic strain for cavity nucleation in Ti alloys reported at low hydrostatic pressure by Helbert et al [39].

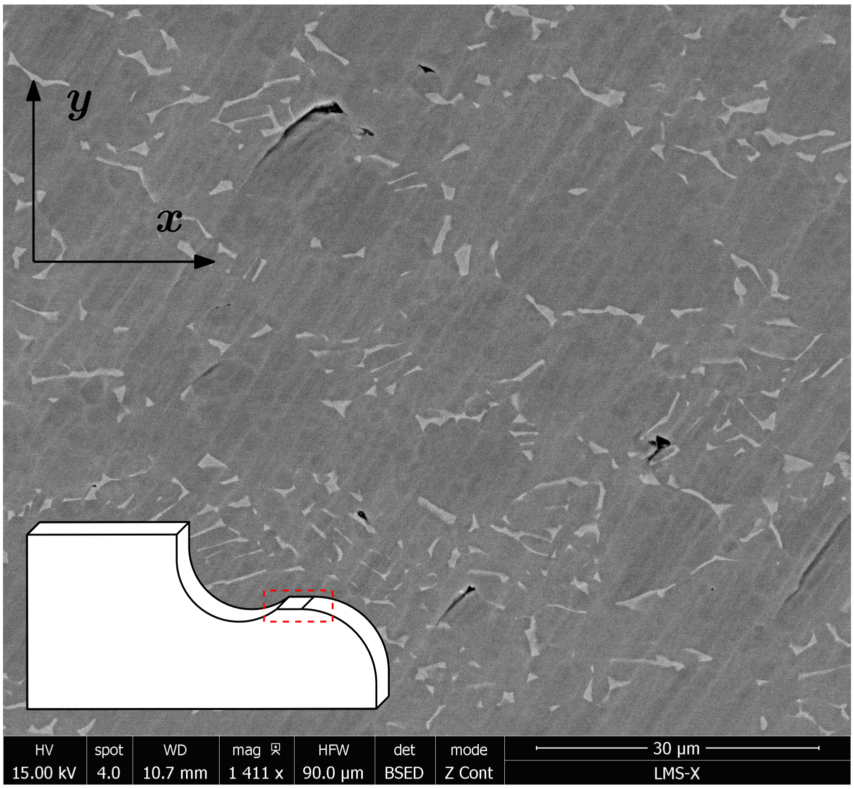

Figure 1.46: SEM observations of a longitudinal section of an interrupted flat tension-induced shear specimen. $\varepsilon_f \simeq 9\,\%$, $\dot{\varepsilon} = 10^{-3}\,\mathrm{s}^{-1}$, $T = 25\,°\mathrm{C}$, $x \equiv TD$ & $y \equiv RD$. See the corresponding tests in Figure 1.29.

Figure 1.47 shows the fracture surface of a tension-induced shear specimen. The features found are rather similar to those observed in the shear compression specimen. The fracture surface is heterogeneous, and exhibits clusters of elongated dimples surrounded by smooth, mated zones.

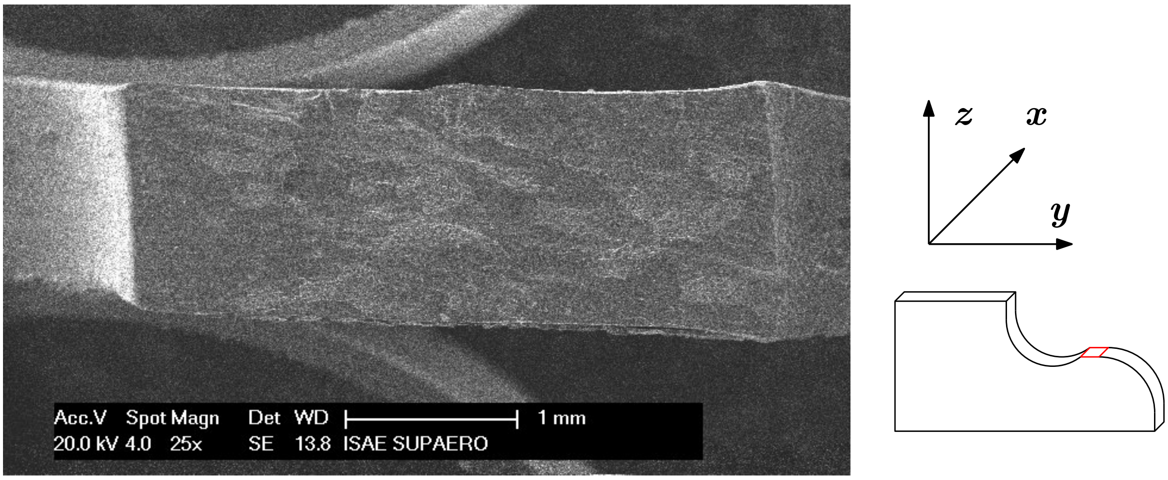

(a) Overall surface

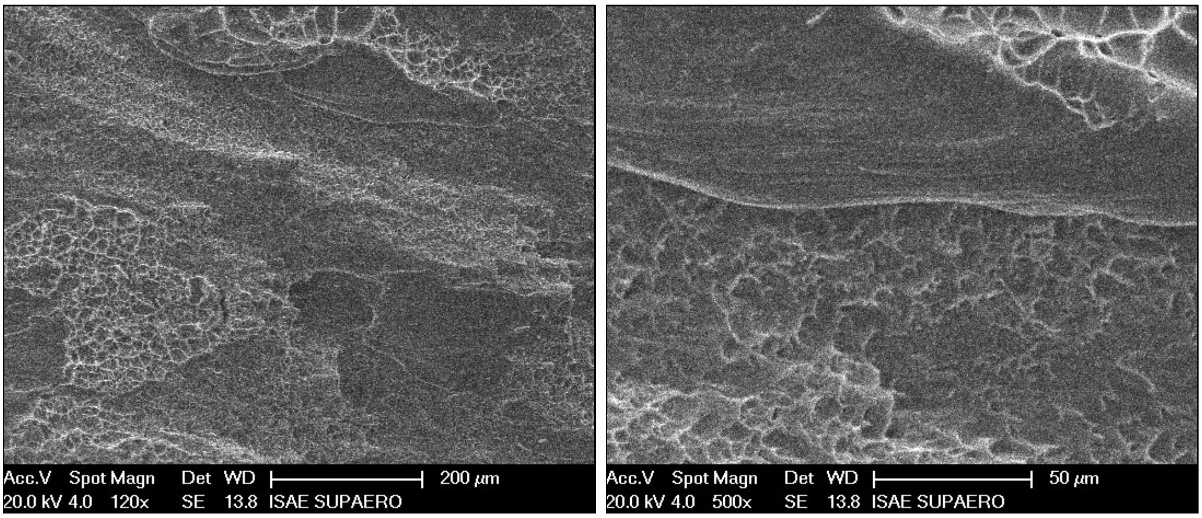

(b) Field width of 800 mm (c) Field width of 175 mm

Figure 1.47: SEM observations on a tension-induced shear specimen. $\varepsilon_f \simeq 9\,\%$, $\dot{\varepsilon} = 10^{-3}\,\mathrm{s}^{-1}$, $T = 25\,°\mathrm{C}$, $y \equiv TD$. Evidence of shear planes and dimple clusters. See the corresponding tests in Figure 1.29.

Negative Stress Triaxiality

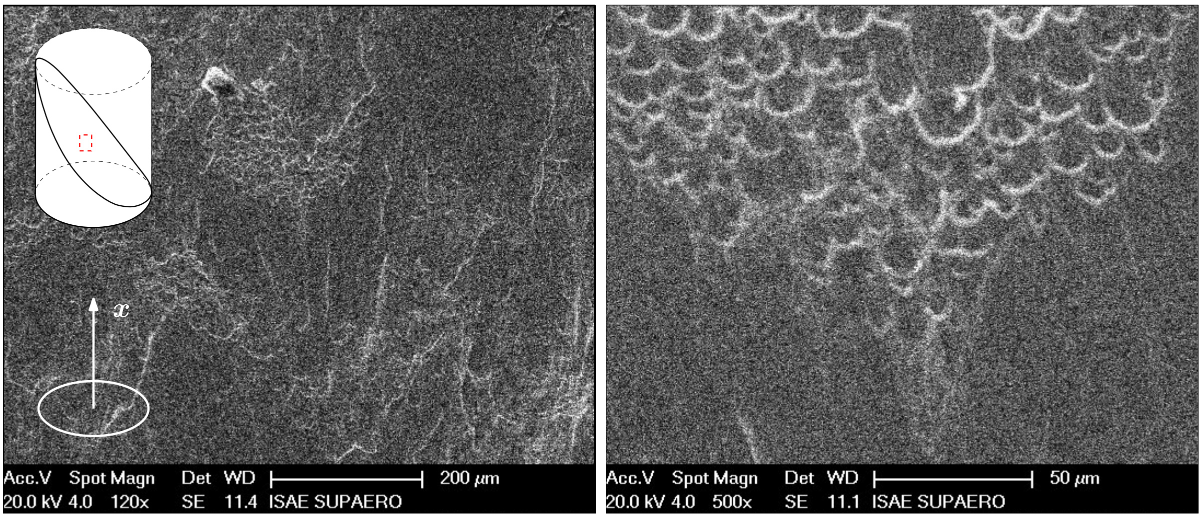

(a) Field Width of 500 µm (b) Field Width of 150 µm

Figure 1.48: SEM observations of the fracture surface of a compression specimen. $\varepsilon_f \simeq 17\,\%$, $\dot{\varepsilon} = 10^{-3}\,\mathrm{s}^{-1}$, $T = 25\,°\mathrm{C}$, $x \equiv TD$. Evidence of shear planes and dimple clusters. See the corresponding tests in Figure 1.21.

The fracture of compression specimens is sudden, precocious and localized in a 45° band. Figure 1.48 shows a SEM observation of such a fracture surface, which exhibits mated areas surrounding dimple clusters. In addition, the elongated shape of such dimples is a clear sign of large shear strain. These micrographies show a great resemblance with those presented in Lee and Lin [43].

Comparing all the micrographies here presented, one retrieves two different fracture mechanisms described by many authors: a shear-driven mechanism, under negative stress triaxialities (compression and shear loadings), and a cavity nucleation/growth and coalescence mechanism, typical of high positive triaxiality ratios. These two scenarios would entail the use of two different fracture criteria: one based on shear localization and another one strongly dependent on stress triaxiality (see an example of such criterion in Hooputra et al. [64]).

1.5.2 Final fracture

This section focuses on the macroscopic aspect of fracture, characterized by optical microscopy.

Positive Stress Triaxiality

Figure 1.49 presents the broken smooth tension specimens loaded along the rolling, transverse and diagonal directions at low strain rate and at room temperature. Both the front and side views are shown. For the three cases, the fracture surface is inclined into the thickness (see side views). Indeed, for both the rolling and transverse specimens, the fracture surface is inclined by 45°, while for the diagonal direction, it seems constituted with two bands inclined by +- 45°.

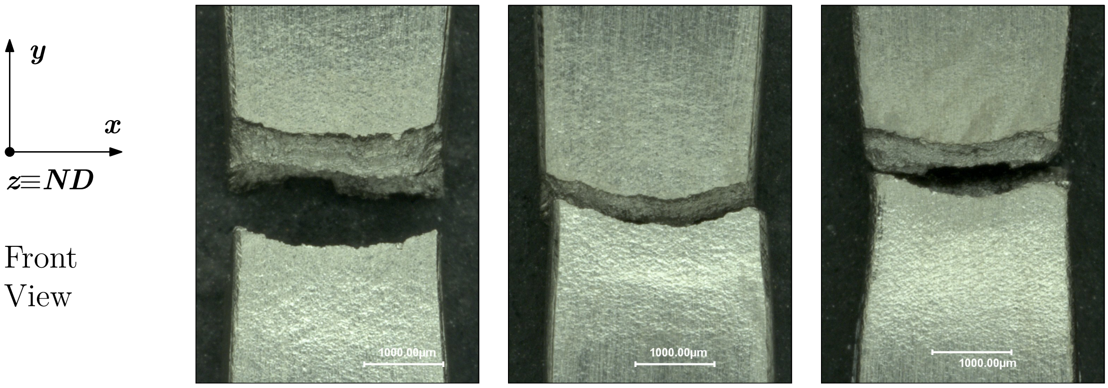

(a) $y \equiv RD$ (b) $y \equiv TD$ (c) $y \equiv DD$

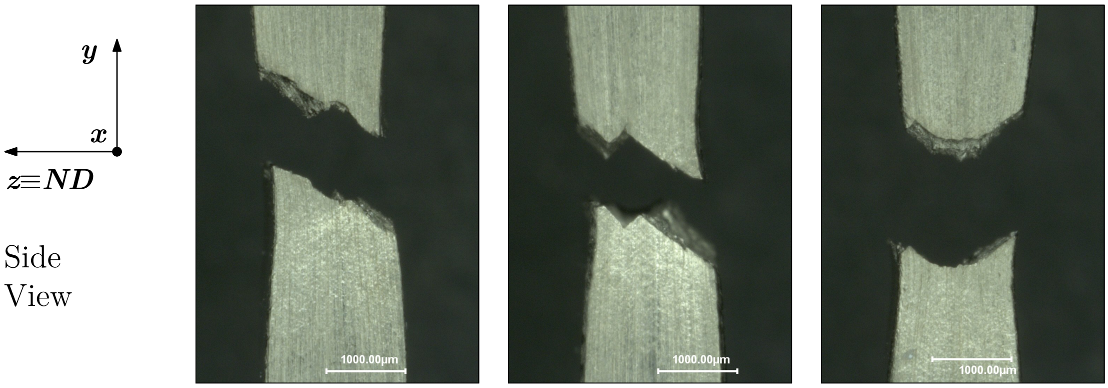

(d) $y \equiv RD$ (e) $y \equiv TD$ (f) $y \equiv DD$

Figure 1.49: Broken smooth flat tension specimens. $\dot{\varepsilon} = 10^{-3}\,\mathrm{s}^{-1}$ and $T = 25\,°\mathrm{C}$.

The same observations were done for specimens broken at $T = 315\,°\mathrm{C}$ (see Figure 1.50). At such temperature, fracture keeps taking place along a plane inclined into the thickness. Necking is qualitatively higher than at room temperature, and the fracture borders are considerably more deformed.

The samples broken at high loading rate are shown in Figures 1.51 and 1.52. No major differences were observed with respect to those broken at low loading rates and room temperature. Except for less tilted fracture at a loading rate of $\dot{\varepsilon} \simeq 1500\,\mathrm{s}^{-1}$ (Figure 1.52). However, this last remark might be purely fortuitous as fracture at $\dot{\varepsilon} \simeq 350\,\mathrm{s}^{-1}$ (Figure 1.52) is clearly tilted.

In Figure 1.53, a non broken specimen tested at high temperature and low loading rate is shown. The interest in this observation is the necking which is more pronounced in the thickness direction. This could be the reason why fracture is preferentially tilted along that dimension.

Low magnification observations of some fracture surfaces of smooth tension specimens are shown on Figure 1.54. Four loading conditions are compared: (i) ambient temperature and quasi-static loading rate, (ii) high temperature and quasi-static loading rate and (iii) ambient temperature and $\dot{\varepsilon} \simeq 350\,\mathrm{s}^{-1}$ and (iv) $\dot{\varepsilon} \simeq 1500\,\mathrm{s}^{-1}$. The four samples show some global similarities, most notably the seemingly uniform appearance along the width, as fracture seems to progress into the thickness direction. The specimen tested at high temperature in Figure 1.54b exhibits a rougher fracture surface, suggesting that temperature might favor diffuse damage instead of localization. For the specimens loaded

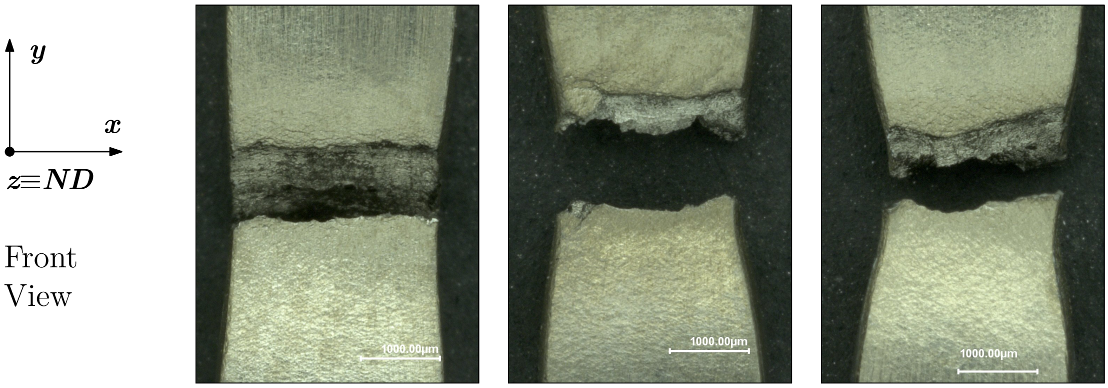

(a) $y \equiv RD$ (b) $y \equiv TD$ (c) $y \equiv DD$

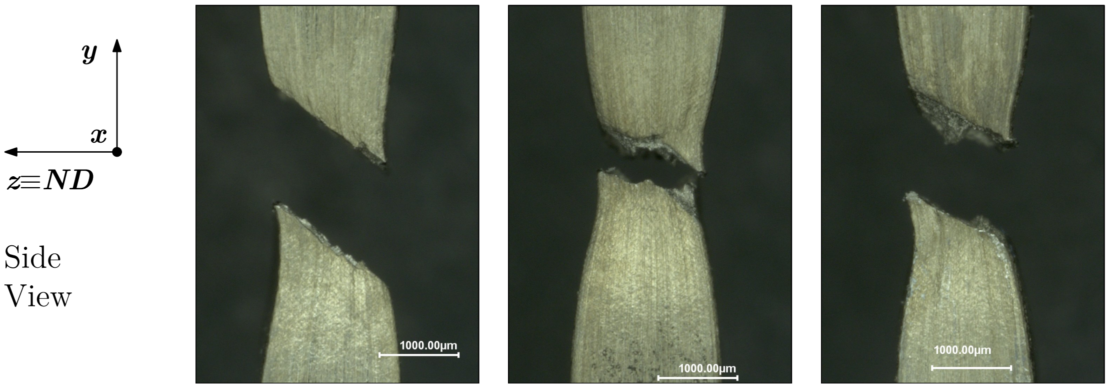

(d) $y \equiv RD$ (e) $y \equiv TD$ (f) $y \equiv DD$

Figure 1.50: Broken smooth flat tension specimens. $\dot{\varepsilon} = 10^{-3}\,\mathrm{s}^{-1}$ and $T = 315\,°\mathrm{C}$.

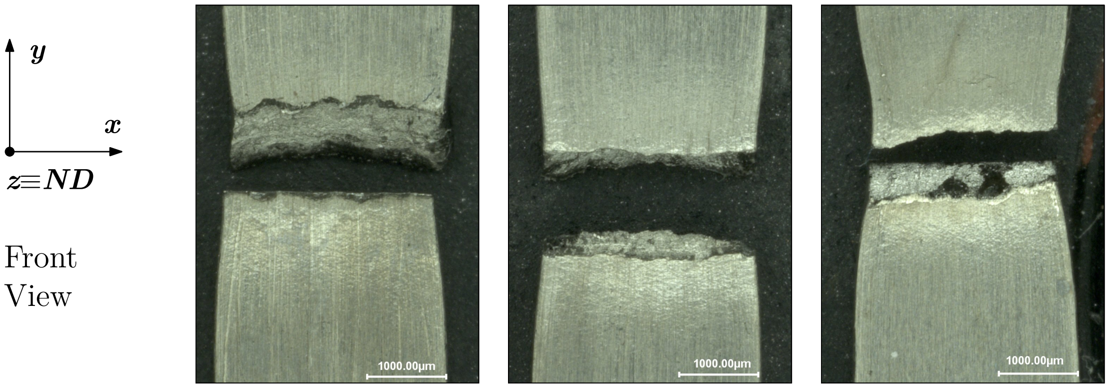

(a) $y \equiv RD$ (b) $y \equiv TD$ (c) $y \equiv DD$

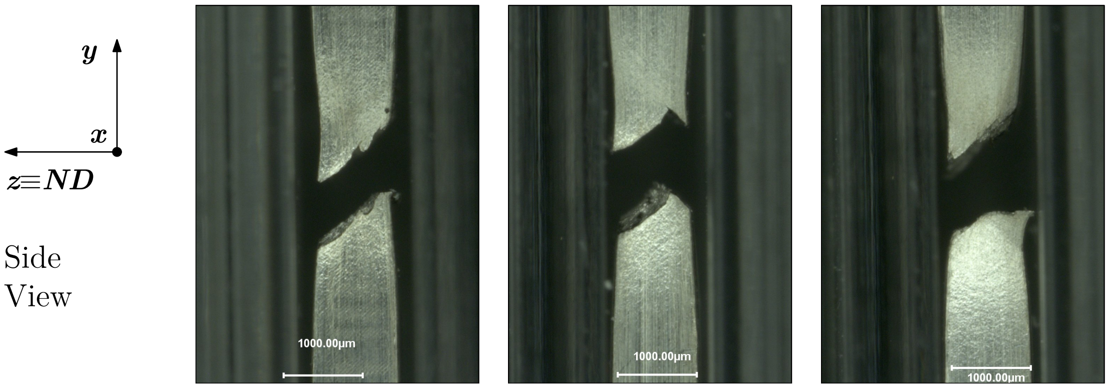

(d) $y \equiv RD$ (e) $y \equiv TD$ (f) $y \equiv DD$

Figure 1.51: Broken smooth flat tension specimens. $\dot{\varepsilon} = 350\,\mathrm{s}^{-1}$ and $T = 25\,°\mathrm{C}$.

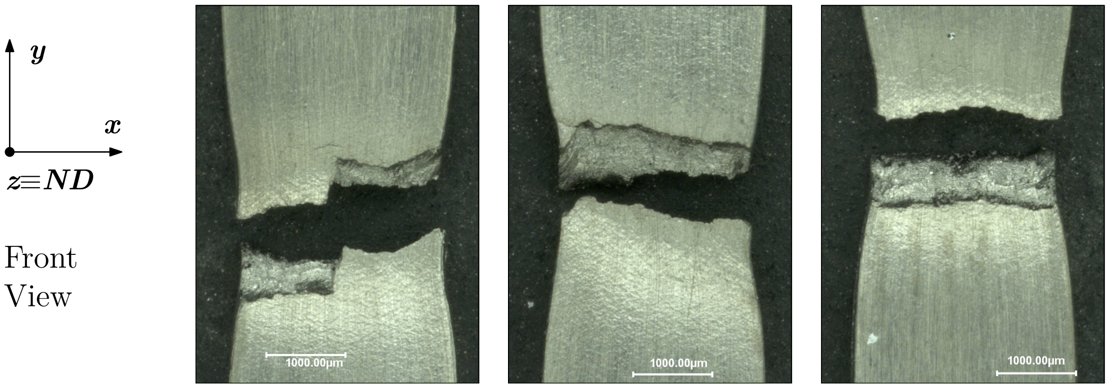

(a) $y \equiv RD$ (b) $y \equiv TD$ (c) $y \equiv DD$

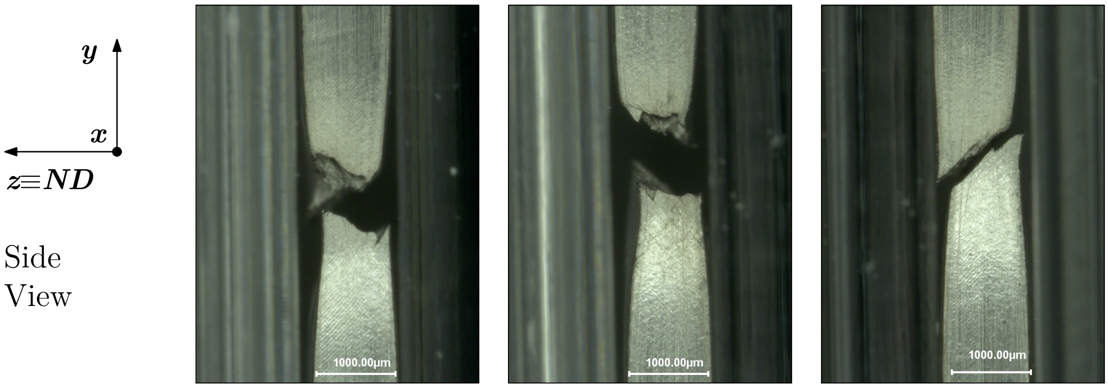

(d) $y \equiv RD$ (e) $y \equiv TD$ (f) $y \equiv DD$

Figure 1.52: Broken smooth flat tension specimens. $\dot{\varepsilon} = 1500\,\mathrm{s}^{-1}$ and $T = 25\,^{\circ}\mathrm{C}$.

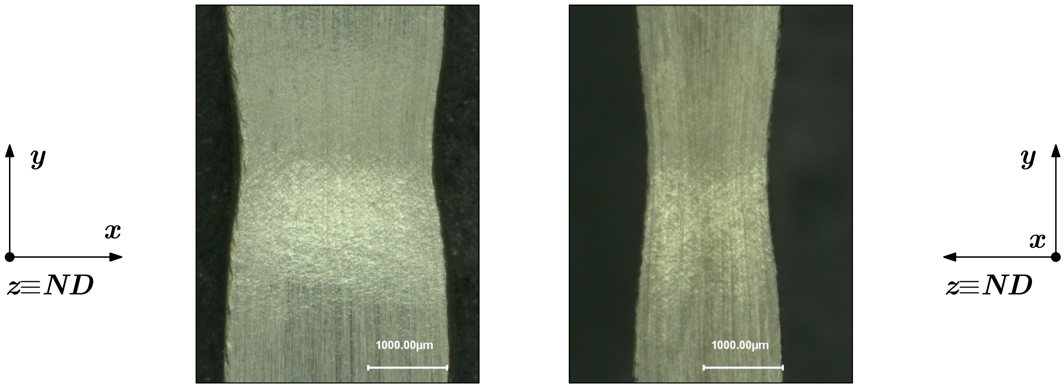

(a) Front view (b) Side view

Figure 1.53: Non-broken smooth flat tension specimens. $\dot{\varepsilon} = 10^{-3}\,\mathrm{s}^{-1}$, $T = 315\,^{\circ}\mathrm{C}$ and $y \equiv RD$.

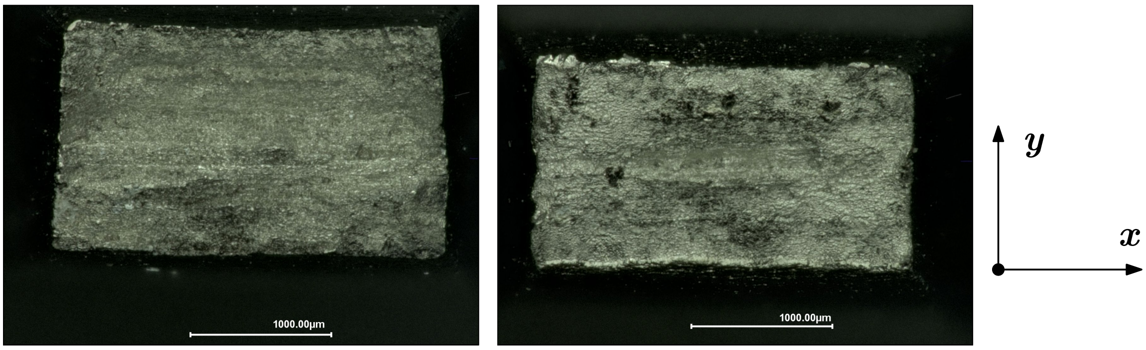

(a) $T \simeq 25\,^{\circ}\mathrm{C}$ & $\dot{\varepsilon} \simeq 10^{-3}\,\mathrm{s}^{-1}$ (b) $T \simeq 315\,^{\circ}\mathrm{C}$ & $\dot{\varepsilon} \simeq 10^{-3}\,\mathrm{s}^{-1}$

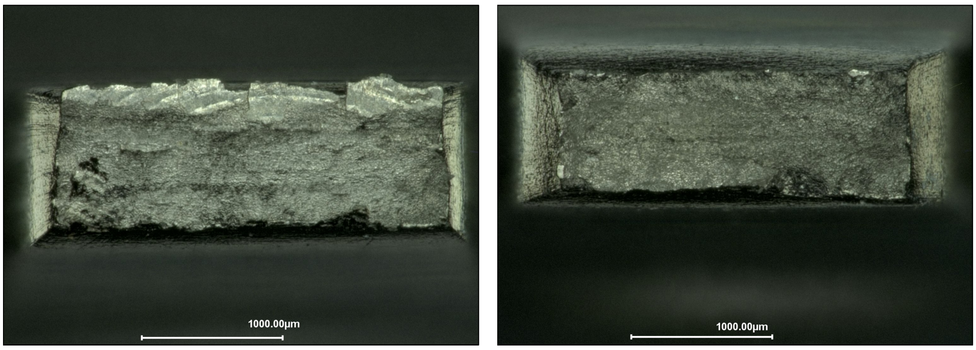

(c) $T \simeq 25\,^{\circ}\mathrm{C}$ & $\dot{\varepsilon} \simeq 350\,\mathrm{s}^{-1}$ (d) $T \simeq 25\,^{\circ}\mathrm{C}$ & $\dot{\varepsilon} \simeq 1500\,\mathrm{s}^{-1}$

Figure 1.54: Fracture surfaces of smooth flat tension specimens along the Rolling direction RD. $x \equiv TD$ and $y \equiv ND$.

at high strain rate, the patterns are harder to interpret. Although loading at $\dot{\varepsilon} \simeq 350\,\mathrm{s}^{-1}$ results in a rougher surface (see Figure 1.54c), the specimen tested at a higher rate ($\dot{\varepsilon} \simeq 1500\,\mathrm{s}^{-1}$ in Figure 1.54d) exhibits a similar fracture surface, if not smoother as the sample tested at ambient temperature and low strain rate in Figure 1.54a. Therefore, it is not clear whether a high loading rate favors localized damage leading to a smooth fracture surface along a localized shear band, or a more ductile fracture resulting from coalesced, initially diffuse damage.

Necking-related quantities of broken flat tension specimens were measured with respect to width, thickness and cross-section area for the three directions, different loading rates and temperatures. They are calculated as

$$\begin{cases} \eta_w = \dfrac{w_f - w_o}{w_o} \\ \eta_t = \dfrac{t_f - t_o}{t_o} \\ \eta_A = \dfrac{A_f - A_o}{A_o} \end{cases} \tag{1.10}$$

where w_f, w_o, t_f, t_o, A_f and A_o are shown in Figure 1.55.

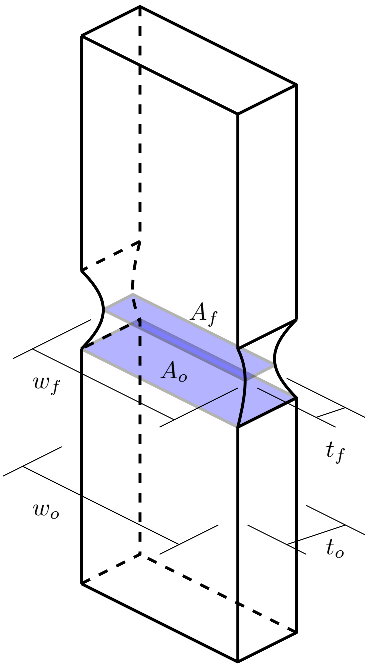

Figure 1.55: Schematic drawing of the necking in a smooth flat tension specimen.

In Figure 1.56, the main results are plotted and compared with respect to machining direction, strain rate and temperature. The diagonal direction presents the highest necking for all loading conditions except at the highest loading rate. The thickness reduction is more pronounced than the width reduction. Regarding loading rate, no clear tendency is appreciated, ductility seems to drop at $\dot{\varepsilon} \simeq 350\,\mathrm{s}^{-1}$ but to rise again at $\dot{\varepsilon} \simeq 1500\,\mathrm{s}^{-1}$, sometimes reaching higher values than in the quasi static regime. As for temperature, ductility seems to be slightly higher when the temperature is increased. By order of importance on ductility, it seems that the deformation direction (thickness as opposed to width) comes first, then the loading direction followed by the temperature, and last the loading rate for which no simple conclusion can be extracted.

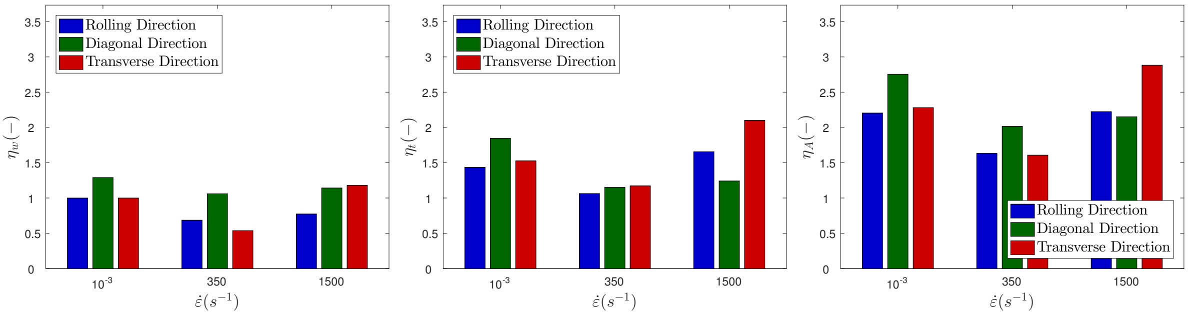

(a) Width (b) Thickness (c) Cross-section

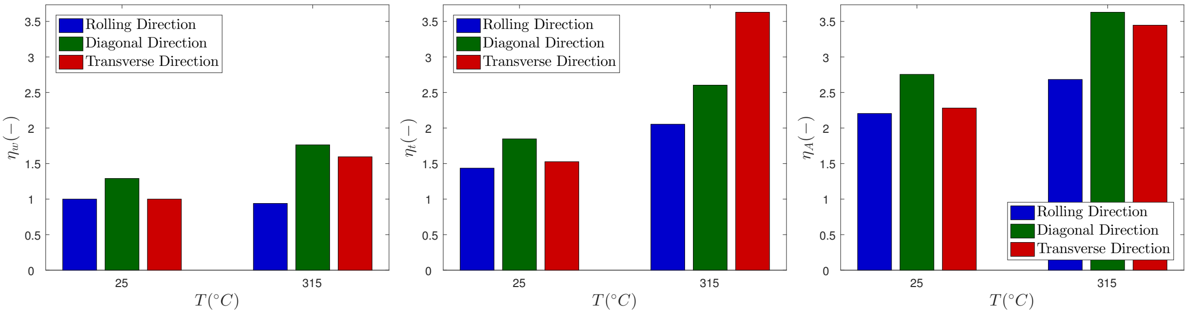

(d) Width (e) Thickness (f) Cross-section

Figure 1.56: Ductility comparison of the rolling, transverse and diagonal direction of a smooth flat tension specimen at various loading rates and temperatures. Values are normalized with respect to the case at $\varepsilon \simeq 10^{-3}\,\mathrm{s}^{-1}$, $T = 25\,°\mathrm{C}$ and Rolling Direction RD.

Concerning the notched tension specimens, fracture seems to be similar: it occurs along a plane tilted by 45° into the thickness (see Figure 1.57).

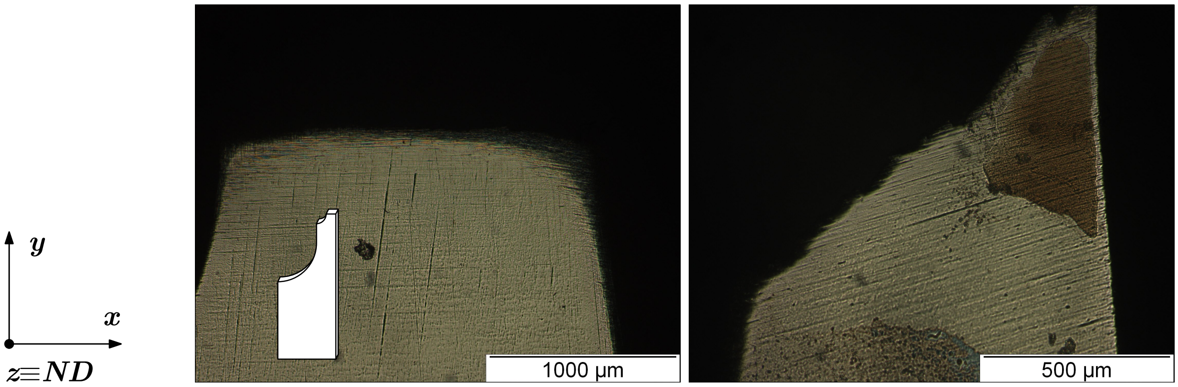

(a) $R = 2\,\mathrm{mm}$ (front view) (b) $R = 2\,\mathrm{mm}$ (side view)

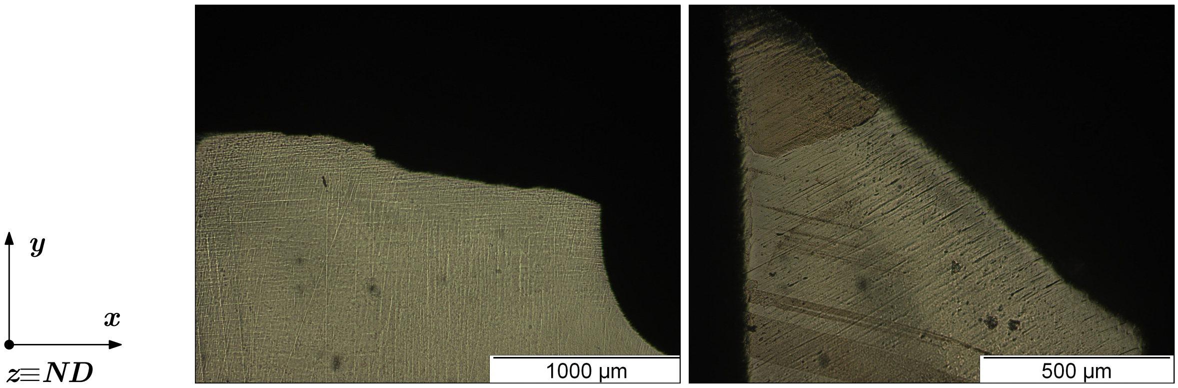

(c) $R = 0.5\,\mathrm{mm}$ (front view) (d) $R = 0.5\,\mathrm{mm}$ (side view)

Figure 1.57: Notched specimens loaded to fracture. $\dot{\varepsilon} \simeq 10^{-3}\,\mathrm{s}^{-1}$, $T = 25\,°\mathrm{C}$ and $y \equiv TD$.

Nil Stress Triaxiality

Fracture in a shear specimen is somewhat different. As seen in Figure 1.58, the fracture surface is flat and its plane is not tilted, neither in thickness nor in width.

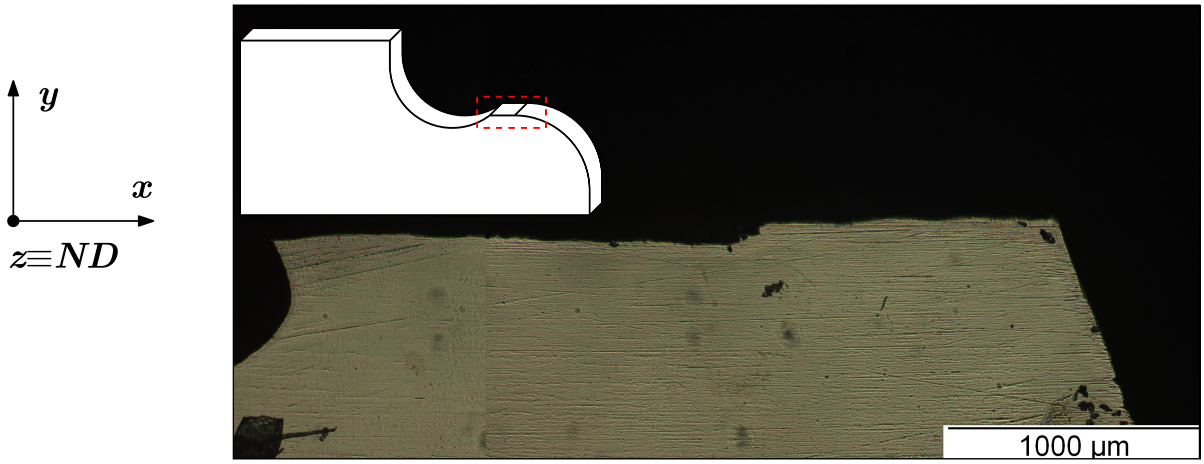

Figure 1.58: Tension-induced shear specimen loaded to fracture. $\dot{\varepsilon} \simeq 10^{-3}\,\mathrm{s}^{-1}$, $T = 25\,^{\circ}\mathrm{C}$ and $x \equiv TD$.

Negative Stress Triaxiality

Compression tests on hat-shaped specimens for which macro crack propagation had began were successfully stopped. In Figure 1.59, observations in the quasi-static and dynamic regime are shown. The macro cracks, initiated from the corners, propagated diagonally along a seemingly straight path. However, when zooming on the crack tip, a staircase-shaped trajectory appears, perhaps due to the coalescence of some diffuse damage nucleated under shear as shown in Figure 1.46. This particular crack shape has been observed in other Ti-6Al-4V alloys loaded under high strain rate conditions (see Dorothy and Longère [65], Longère and Dragon [37] and Peirs et al. [38]).

In the Meyers geometry, deformed under shear stress close to null stress triaxiality ratios, the crack propagation also nucleated from the corners of the specimen (see Figure 1.60). As with the other hat-shaped geometry, the crack tip seems to grow by a coalescence of damage generated along its path.

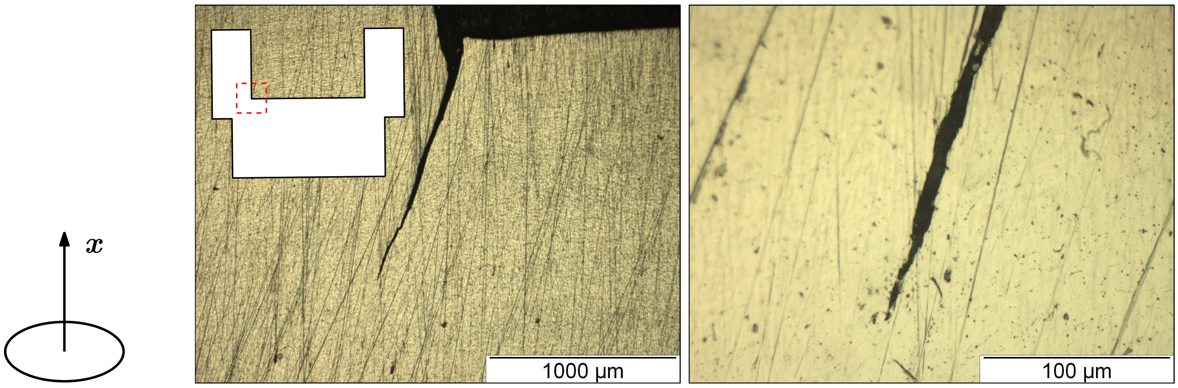

(a) $\dot{u} = 0.5\,\mathrm{mm/min}$ (x50) (b) $\dot{u} = 0.5\,\mathrm{mm/min}$ (x500)

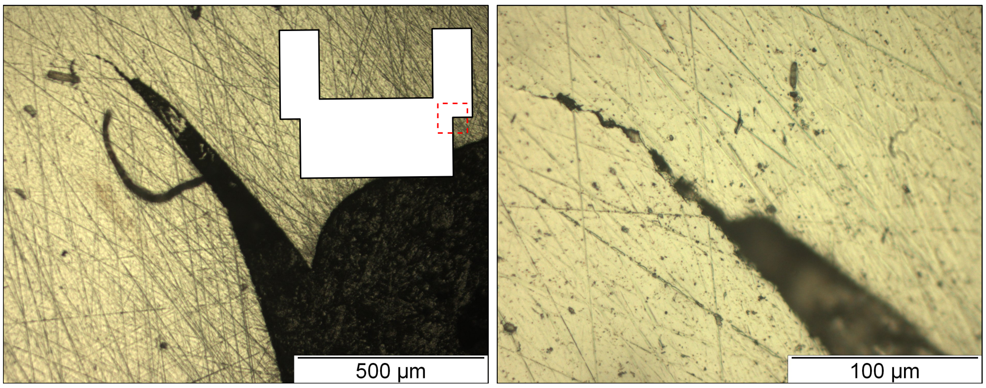

(c) $\dot{u} = 5 \times 10^3\,\mathrm{mm/s}$ (x100) (d) $\dot{u} = 5 \times 10^3\,\mathrm{mm/s}$ (x500)

Figure 1.59: Couque hat-shaped specimens after partial fracture. $T = 25\,^{\circ}\mathrm{C}$ and $x \equiv ND$.

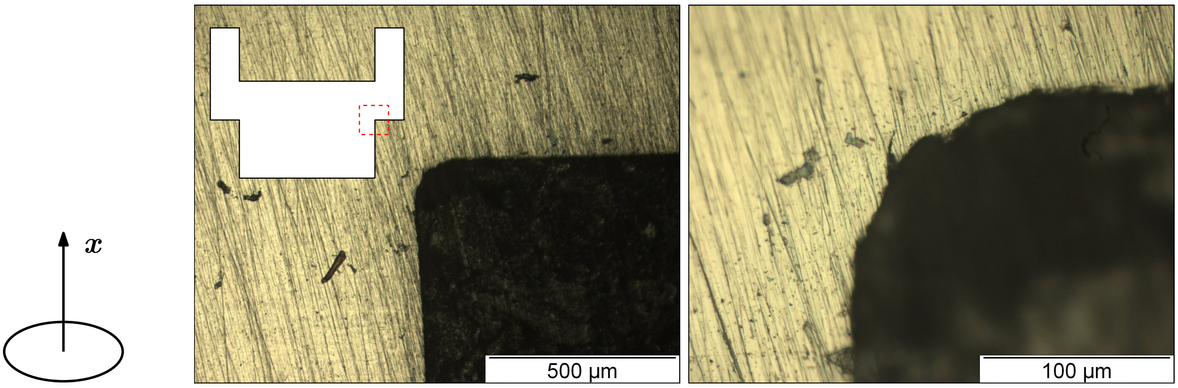

(a) $\dot{u} = 5\,\mathrm{mm/min}$ (x50) (b) $\dot{u} = 5\,\mathrm{mm/min}$ (x500)

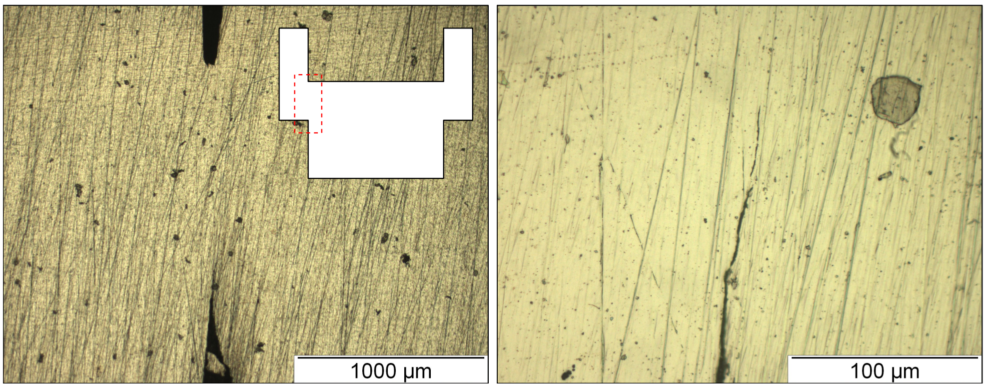

(c) $\dot{u} = 5 \times 10^3\,\mathrm{mm/s}$ (x100) (d) $\dot{u} = 5 \times 10^3\,\mathrm{mm/s}$ (x500)

Figure 1.60: Meyers hat-shaped specimens after partial fracture. $T = 25\,°\mathrm{C}$ and $x \equiv ND$.

1.6 Concluding remarks

This chapter summarized the results of an extensive experimental characterization of the Ti-6Al-4V alloy considered for the fan blade leading edge of aircraft engines. In order to emulate all the conditions found in a ballistic event on the engine several sample geometries as well as various experimental set-ups were employed.

Even though the cold rolled bimodal Ti-6Al-4V investigated here exhibits strong local texture (in the form of “macrozones”), but only a weak global texture, its mechanical behavior is nonetheless orthotropic and a significant tension-compression strength differential is measured.

The material hardening is dependent on three variables: the plastic strain, the plastic strain rate and the temperature, a rise of the latter promoting softening. The rate-dependent hardening exhibits a nearly linear evolution with respect to the plastic strain rate in logarithm scale. This viscous component does not show any anisotropy nor strain dependence. Although an influence of temperature on viscosity was observed, it will be neglected in subsequent modeling, because of its limited impact in the quasi-static regime, and the lack of data in the dynamic regime. In addition, the effect of temperature on the kinematic hardening has not been addressed in this chapter.

Load reversal tests in tension-compression showed that the rate-independent part of the material hardening is due to isotropic and kinematic contributions. These two components were roughly estimated to have the same importance in the hardening.

Finally, the damage and fracture mechanisms were analysed using SEM as well as optical observations of broken or non broken specimens.

Damage, in the form of cavities, nucleated mostly at α/β interfaces was found near the fracture surfaces. The latter were often inclined by 45° into the thickness of tension specimens. Depending on the loading conditions, shear-driven strain localization and damage, leading to slanted fracture with limited necking, or more diffuse, triaxiality-driven cavities nucleation, growth and coalescence leading to fracture with more substantial necking was observed. A higher amount of damage was detected at high temperatures but no clear conclusions could be drawn on the influence of strain rate or the orientation.

CHAPTER 2

Constitutive modeling

Abstract

In this chapter, a constitutive model is built within the irreversible thermodynamics framework at finite strain. The key aspects regarding (i) anisotropic plasticity, (ii) isotropic and kinematic hardening laws and (iii) viscoplastic formulation are presented to reproduce the behavior of the Ti-6Al-4V previously characterized. Finally, a model constant calibration using the Z-set software is carried out.

Contents

2.1 Introduction

The extensive experimental campaign detailed in the previous section has evidenced that the Ti-6Al-4V grade under consideration is subject to significant (i) anisotropic plasticity which manifests through loading direction dependence, kinematic hardening and strength differential, (ii) isotropic strain hardening, (iii) rate dependence and (iv) thermal softening. Starting from the experimental observations, a constitutive model accounting for the above mentioned effects is built within the irreversible thermodynamics framework. More generally, the aim of the present work is to develop a constitutive model able to describe the behavior of metals and alloys within a wide range of strain, strain rate, temperature and loading path. It is noted that a phenomenological approach is developed in this paper instead of the polycrystalline formalism as proposed by e.g. Zhang et al. [12] or Mayeur and McDowell [11].

The proposed constitutive model is calibrated using Z-set commercial software. Such identification is divided in several stages in order to ensure a satisfactory convergence. With these results, the applicability of the model is then discussed.

2.2 Some existing constitutive models

A dedicated review of the current strategies for building a suitable constitutive model describing plasticity and further damage is first presented.

Preliminary considerations

There are two main approaches that can be followed when describing the transformation of a medium: the Lagrangian point of view involving material quantities and Eulerian point of view involving spatial quantities. In the former, the quantities involved are expressed with respect to the reference configuration where as in the latter, the quantities are expressed with respect to the current one. The Eulerian perspective is adopted here since it is more adapted to history and path dependent mechanisms such as plasticity.

However, by following the Eulerian approach, the objectivity (frame independence) of the rate equations must be ensured. For a second order tensor $\underline{\underline{a}}$, the rate operator $\overset{\square}{\cdot}$ is used to satisfy objectivity. The symbol $\square$ represents the type of objective rate chosen.

$$\overset{\square}{\underline{\underline{a}}} = \dot{\underline{\underline{a}}} - \tilde{\underline{\underline{\Omega}}}\,\underline{\underline{a}} + \underline{\underline{a}}\,\tilde{\underline{\underline{\Omega}}} \tag{2.1}$$

where $\tilde{\underline{\underline{\Omega}}}$ is the spin involved in the rotation between the reference and the current configurations. If there is a consensus about the need for objective rates, there is no consesus about the spin to apply. Several approximations can thus be found in literature, see e.g. the comparison of objective rates made by Szabo and Balla [66] for a hypo-elastic isotropic material. Table 2.1 summarizes some of the more popular objective rates.

As explained in Schieck and Stumpf [71], the Jaumann definition can be considered a sufficiently accurate rate under moderate elastic and plastic strains since the oscillations start to occur at large strain.

Table 2.1: Summary of some objective derivatives

Jaumann [67]	$\overset{\nabla}{\underline{\underline{a}}} = \dot{\underline{\underline{a}}} - \underline{\underline{w}}\,\underline{\underline{a}} + \underline{\underline{a}}\,\underline{\underline{w}}$
Green-Naghdi [68]	$\overset{\triangle}{\underline{\underline{a}}} = \dot{\underline{\underline{a}}} - \underline{\underline{\Omega}}\,\underline{\underline{a}} + \underline{\underline{a}}\,\underline{\underline{\Omega}}$
Truesdell [69]	$\overset{\circ}{\underline{\underline{a}}} = \dot{\underline{\underline{a}}} - \underline{\underline{l}}\,\underline{\underline{a}} - \underline{\underline{a}}\,\underline{\underline{l}}^T + \underline{\underline{a}}\,tr(\underline{\underline{l}})$
Sowerby and Chu [70]	$\overset{\diamond}{\underline{\underline{a}}} = \dot{\underline{\underline{a}}} - \underline{\underline{\Omega}}_E\,\underline{\underline{a}} + \underline{\underline{a}}\,\underline{\underline{\Omega}}_E$

2.2.1 Behavior

In this section are presented some constitutive models or parts of constitutive models aiming at describing anisotropic plasticity, isotropic hardening and temperature and rate dependence.

2.2.1.1 Anisotropic plasticity

In literature, anisotropic plasticity has been largely addressed from both microstructure and phenomenological perspectives. This work is focused on the latter and a review of some of the most notable anisotropic criteria are summarized in Table 2.2. Anisotropic plasticity implies a loss of coaxiality between the strain rate and the stress. It thus involves the effect of (i) orientation, (ii) strength differential and (iii) Bauschinger effect.

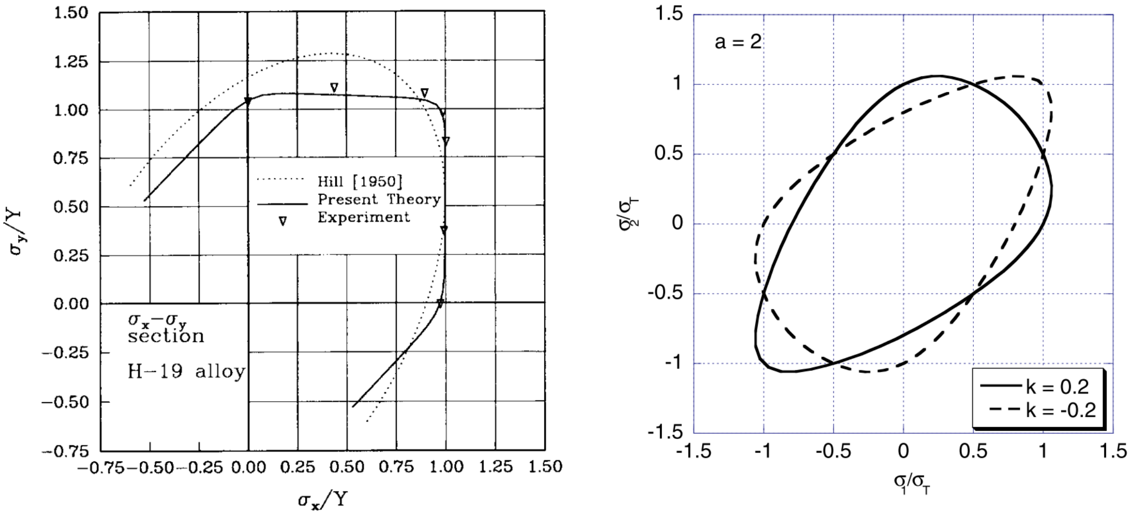

(a) Yield locus in case of orthotropy after Karafillis and Boyce [72]

(b) Yield locus in case of Strength Differential after Cazacu et al. [73]

Figure 2.1: Anisotropic yield surface criteria

Orthotropy

Hill's criterion [74] has been widely used to model the plastic behaviour of orthotropic materials due to its simplicity [75–77]. It consists in incorporating a fourth order tensor in the equivalent stress in order to make the yield stress dependent on the orientation. Plastic anisotropy evolving with strain has also been addressed by Baltov and Sawcsuk [78] by defining the fourth order tensor as a polynomial decomposition of notably the strain invariants [79]. Karafillis and Boyce [72] proposed a linear transformation of the stress tensor itself to induce orthotropy in plastic yielding without compromising the convexity of the yield function [80] (see Figure 2.1a). Some examples of this strategy can be seen in [81–85]. Moreover, a generalized version of the Karafillis and Boyce yield surface was later proposed by Bron and Besson [86] to improve the description of plastic anisotropy.

Strength-differential

A second aspect contributing to the anisotropy of the material is the strength differential between tension and compression. To model this effect, some authors have proposed asymmetric yield criteria including the third invariant of the stress tensor [87 ; 88]. Khan et al. proposed a criterion that manages to independently include the orthotropy, by means of the Hill criterion, and the asymmetry, by introducing a function depending on the Lode parameter [20]. With this method, the strength differential is successfully captured with only one material coefficient. Similarly, the CPB06 yield criterion [73] can simultaneously capture the orthotropy and the strength differential by combining a linear transformation of the stress deviator tensor and a yield function of the principal stresses (see Figure 2.1b). The simplicity, applicability and accuracy of this last model has made it widely used as seen in [19 ; 23 ; 33]. Furthermore, distortional models such as the Homogeneous yield function-based Anisotropic Hardening (HAH) model [89] has been proven useful when considering an evolving anisotropy that continuously distorts and rotates the yield surface as it was later on successfully applied on titanium [90]. The main concept being the addition of a so called fluctuating component in the yield criterion which is function of a microstructure deviator (defining the current state in the stress tensor space) and some evolving material coefficients. A last example worth mentioning for the modeling of asymmetry was proposed by Longère [91] who included a definition of a viscous stress dependent on the hydrostatic pressure (while maintaining the plastic yield criterion pressure-independent). It is noteworthy that Longère model preserves the coaxiality between the stress and the strain rate.

Bauschinger effect

The third and last aspect characterizing the anisotropy of the present material is the kinematic hardening. A kinematic hardening-related internal variable was introduced in Prager's model to describe this effect [92]. In this approach,the backstress represents a translation of the yield surface as plasticity occurs. Initially, Prager's model considered an isochoric plasticity, and therefore, the kinematic evolution would not be linked with the first stress invariant, i.e. the hydrostatic pressure. However, later Ziegler's model [93] included a pressure dependent evolution of the kinematic variable by replacing the stress deviator $\underline{\underline{s}}$ for $\underline{\underline{\sigma}}$ in the complementary laws. Nonlinear extensions for the evolution of this variable were later on proposed by Armstrong and Frederick [94] and Chaboche [95]. Moreover, as kinematic hardening may produce transient effects and permanent softening, mixed coupled hardening models were also proposed in the literature to predict such effects [96–98]. Another alternative to reproduce the Bauschinger effect is through the above mentioned yield surface distortion of the HAH model. More precisely, Barlat et al. [89] proved that by choosing a homogeneous yield function containing the strength asymmetry, they could additionally reproduce a kinematic response in the material with the fluctuating component in the yield criterion. However, the notion of a kinematic variable and its hardening is lost is such model.

Table 2.2: Examples of anisotropic/orthotropic yield functions found in literature. $J_2\left(\underline{\underline{s}}\right)=\frac{1}{2}\underline{\underline{s}}:\underline{\underline{s}}$ with $\underline{\underline{s}}=\underline{\underline{\sigma}}+\frac{1}{3}p\underline{\underline{I}}$.

Model	Type	Expression
Mises	Isotropic	$\sigma_{eq}^2=\frac{3}{2}\underline{\underline{s}}:\underline{\underline{s}}=3J_2\left(\underline{\underline{s}}\right)$
Hill (1948)	Orthotropic	$\sigma_{eq}^2=\frac{1}{2}\underline{\underline{\sigma}}:\underline{\underline{\underline{\underline{H}}}}_{48}:\underline{\underline{\sigma}}$
Prager-Mises	Kinematic	$\sigma_{eq}^2=3J_2\left(\underline{\underline{s}}-\underline{\underline{X}}\right)$
Longère et al. [91]	Asymmetry (Co-axial)	$\sigma_{eq}^2=3J_2\left(\underline{\underline{s}}\right),\sigma_v=Y\left[\dot{\kappa}exp\left(\frac{V_ap}{k_BT}\right)\right]^{\frac{1}{n}}$
Baltov and Sawcsuk [78]	Orthotropic & Kinematic	$\sigma_{eq}^2=\frac{1}{2}\left(\underline{\underline{s}}-\underline{\underline{X}}\right):\underline{\underline{\underline{\underline{A}}}}_{BS}:\left(\underline{\underline{s}}-\underline{\underline{X}}\right)$
Karafillis and Boyce [72]	Orthotropic & Kinematic	$\sigma_{eq}^2=J_2\left(\underline{\underline{\underline{\underline{L}}}}_{KB}:\left(\underline{\underline{\sigma}}-\underline{\underline{X}}\right)\right)$
Cazacu et al. [73]	Orthotropic & Asymmetry	$\sigma_{eq}^a=\frac{1}{m_0^a}\left\{\sum_{p=1}^3\left(\lvert\Sigma_p\rvert-k\Sigma_p\right)^a\right\}$ $\underline{\underline{\Sigma}}=\underline{\underline{\underline{\underline{A}}}}_{CPB}:\underline{\underline{s}}$
Khan et al. [20]	Orthotropic & Asymmetry	$\sigma_{eq}^2=\left(\frac{1}{2}\underline{\underline{\sigma}}:\underline{\underline{\underline{\underline{H}}}}_{48}:\underline{\underline{\sigma}}\right)e^{-C(\theta+1)}$
Barlat et al. [89][1]	Kinematic & Asymmetry	$\sigma_{eq}^a=\left[\tilde{\sigma}_{eq}^a+\hat{\sigma}_h^a\left(\underline{\underline{h}}:\underline{\underline{s}}\right)\right]$

[1] Although this model does not explicitly treat orthotropy, it can successfully reproduced a full distorted anisotropic surface.

Adopting a 2D representation, the orthotropic Hill tensor takes the form of the 6x6 matrix

$$\underline{\underline{\underline{\underline{H}}}}_{48}=\begin{bmatrix}-G-H & H & G & & & \\ H & -F-H & F & & & \\ G & F & -F-G & & & \\ & & & N & & \\ & & & & L & \\ & & & & & M\end{bmatrix} \tag{2.2}$$

whereas Karafillis and Boyce [72] define it as

$$\underline{\underline{\underline{\underline{L}}}}_{KB}=C_{KB}F\begin{bmatrix}1 & \beta_1 & \beta_2 & & & \\ \beta_1 & \alpha_1 & \beta_3 & & & \\ \beta_2 & \beta_3 & \alpha_2 & & & \\ & & & \gamma_1 & & \\ & & & & \gamma_2 & \\ & & & & & \gamma_3\end{bmatrix} \quad \text{with} \quad \begin{cases}\beta_1=\dfrac{\alpha_2-\alpha_1-1}{2}\\ \beta_2=\dfrac{\alpha_1-\alpha_2-1}{2}\\ \beta_3=\dfrac{1-\alpha_1-\alpha_2}{2}\end{cases} \tag{2.3}$$

In both cases, six independent material constants are sufficient to describe orthotropic plasticity. As for Cazacu et al. model [73] the 6x6 matrix is expressed as

$$\underline{\underline{A}}_{CPB} = \begin{bmatrix} A_{11} & A_{12} & A_{13} & & & \\ A_{12} & A_{22} & A_{23} & & & \\ A_{13} & A_{23} & A_{33} & & & \\ & & & A_{44} & & \\ & & & & A_{55} & \\ & & & & & A_{66} \end{bmatrix} \tag{2.4}$$

which a priori needs the knowledge of 9 independent material coefficients. The choice of the approach to use is dependent on the behavior of the material.

2.2.1.2 Isotropic Hardening

For the isotropic hardening, the phenomenological Voce [99] and Swift [100] laws are widely considered (see Table 2.3). The main difference between both is that Voce stress saturates at large strain whereas Swift law keeps a positive hardening slope all along the deformatin process. Some materials require a linear combination of both to ensure a higher accuracy [47 ; 101].

Table 2.3: Isotropic yield functions

Voce [99]	$\sigma_y = \sigma_{y0} + Q\left(1 - exp\left(-b\kappa\right)\right)$
Swift [100]	$\sigma_y = \sigma_{y0} + K\left(\varepsilon_0 + \kappa\right)^n$

2.2.1.3 Temperature and strain rate hardening

The engineering-oriented Johnson-Cook constitutive model [102] is widely employed to describe the strain rate hardening and temperature softening. Yet, it scarcely fits the experimental behavior of HCP metals and some alternatives have been proposed to improve the agreement with experiments, see e.g. Khan et al. [103]. Cowper-Symonds' model [104] based on a power law is also widely used. These laws are commonly expressed in a multiplicative form of strain, strain rate and temperature contributions. Alternatively, the strain rate stress used by Norton [61] is expressed as an additive contribution. Table 2.4 shows the corresponding yield stress and the viscous contributions. As seen in a previous chapter, the viscous stress should not depend on strain.

Table 2.4: Viscoplastic yield functions and corresponding viscous additive component. $\bar{\sigma}_y\left(\kappa, \dot{\kappa}, T\right) = \sigma_y\left(\kappa, T\right) + \sigma_v\left(\kappa, \dot{\kappa}, T\right)$

Johnson-Cook [102]	$\bar{\sigma}_y\left(\kappa, \dot{\kappa}, T\right) = \left(A + B\kappa\right)\left(1 + C\ln\frac{\dot{\kappa}}{\dot{\kappa}_0}\right)\left(1 - \left(\frac{T-T_0}{T_m-T_0}\right)^m\right)$ $\sigma_v\left(\kappa, \dot{\kappa}, T\right) = C\ln\frac{\dot{\kappa}}{\dot{\kappa}_0}\left(A + B\kappa\right)\left(1 - \left(\frac{T-T_0}{T_m-T_0}\right)^m\right)$
Cowper-Symonds [104]	$\bar{\sigma}_y\left(\kappa, \dot{\kappa}, T\right) = \sigma_{y0}\left(\kappa, T\right)\left(1 + \left(\frac{\dot{\kappa}}{D}\right)^n\right)$ $\sigma_v\left(\kappa, \dot{\kappa}, T\right) = \sigma_{y0}\left(\kappa, T\right)\left(\frac{\dot{\kappa}}{D}\right)^n$
Norton [61]	$\bar{\sigma}_y\left(\kappa, \dot{\kappa}, T\right) = \sigma_{y0}\left(\kappa, T\right) + Y\dot{\kappa}^{1/n}$ $\sigma_v\left(\dot{\kappa}\right) = Y\dot{\kappa}^{1/n}$

2.2.2 Damage and fracture

When dealing with damage and ductile fracture, one can typically distinguish two approaches: the use of a damage indicator which does not alter the material properties and the use of a damage variable which deteriorates the material properties (see Figure 2.2).

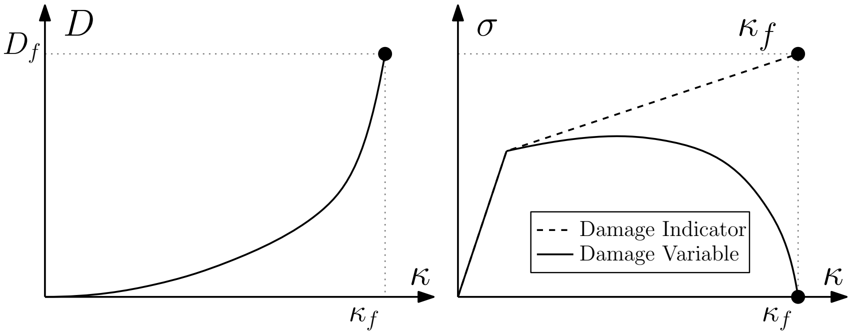

Figure 2.2: Damage approaches: indicator variable with no impact on the mechanical properties and damage variable with a deterioration of the material behavior until fracture. D is a damage-related quantity, D_f its value at fracture and κ_f the strain at fracture.

2.2.2.1 Damage indicator (no coupling)

When a damage indicator is used, there is no coupling between it and the elasto-plastic model. The properties of the material are not deteriorated at any instant of deformation until final rupture, occurring at $\kappa = \kappa_f$. This indicator is generally driven by a damage evolution law of the form

$$\dot{D} = f\left(\kappa, \dot{\kappa}\right) \tag{2.5}$$

For example in Xue [105], the evolution law is defined as

$$\dot{D} = \frac{m\kappa^{m-1}}{\kappa_f}\dot{\kappa} \rightarrow D_f = \int_0^{\kappa_f} \frac{m\kappa^{m-1}}{\kappa_f} d\kappa \tag{2.6}$$

where the fracture strain κ_f could depend on the strain rate, the stress triaxiality or the Lode parameter, i.e. $\kappa_f\left(\dot{\kappa}, \chi, \theta, \dots\right)$. Therefore, the fracture is heavily dependent on the loading path. For the simple case of a proportional loading and $m = 1$ and establishing $D_f = 1$, the expression reduces to a fracture locus surface $\kappa_f = \kappa_f\left(\dot{\kappa}, \chi, \theta, \dots\right)$ (see e.g. Figure 2.3a). The strain at rupture loci can be fitted experimentally as in Bao and Wierzbicki [106] or by means of a criterion as the Hosford-Coulomb [107] (see Bai and Wierzbicki [108] for an extensive comparison on fracture loci).

Alternatively, a recent extension from the Rice and Tracey [109] and Johnson-Cook [110] with a Lode parameter dependence in the evolution law is done in Defaisse et al. [111]

$$\dot{D} = \left[a\mathrm{exp}\left(b\chi\right) + c\left(1 - |L|p^d\right)\right]\dot{\kappa} \tag{2.7}$$

When D reaches the critical value D_f (e.g. $D_f = 1$), the resistance of the material suddenly drops to zero.

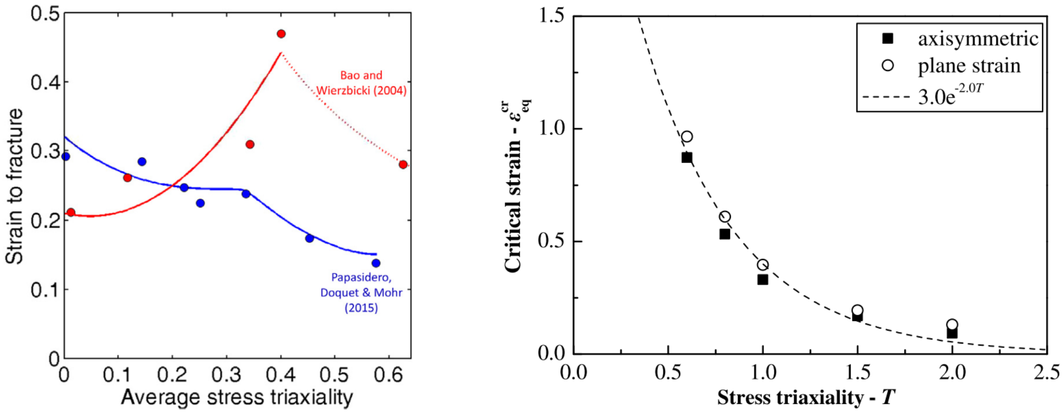

(a) Papasidero et al. [112] (b) Yan et al. [113]

Figure 2.3: Some fracture locus criteria: on the left, Bao and Wierzbicki is compared with the Hosford-Coulomb fracture locus for the initiation of fracture of a 2024 aluminum. On the right, a fracture locus is fitted for a Q345 steel, the exponential decay is characteristic of the Rice and Tracey and the Johnson-Cook loci.

2.2.2.2 Damage variable (coupling)

Conversely, one can consider the use of an internal variable whose evolution during loading has a direct impact on the material properties. The rupture of the material ocurring for a critical value of D_f of the damage variable D (e.g. $D_f = 1$) results in a progressive loss of the material resistance until zero (see the solid line in Figure 2.2). The increase in the damage variable may be related to the loss of stiffness, as done in the irreversible thermodynamics framework by Lemaitre [114] (elasto-damage coupling). In another way, the reduction in the plastic yield surface may be related to void concentration in the material (plastic-damage coupling), see eg. the Gurson [115] or the Rousselier [116] models.

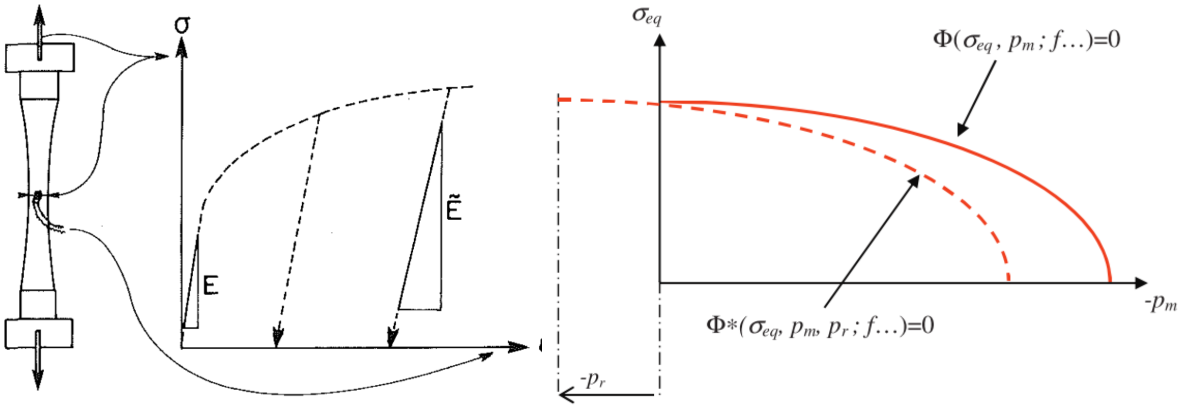

(a) Lemaitre [114] (b) Longère and Dragon [117]

Figure 2.4: On the left, Lemaitre uses the Young modulus variation as a damage variable $D = 1 - \frac{\tilde{E}}{E}$. On the right, Gurson coupled damage-plastic yield criteria is compared with Longère and Dragon [117] where a backstress-induced shift allows for the evolution of damage under zero stress triaxiality.

2.3 Constitutive Modeling

Kinematic considerations are first specified in the context of large elastic-plastic deformation. The general irreversible thermodynamics framework is then applied for phenomenologically describing the consequences of the underlying conservative and dissipative mechanisms. Eventually, constitutive equations are detailed for the Ti-6Al-4V grade under consideration.

In the present constitutive modeling, damage is not accounted for.

2.3.1 Finite strain framework

Moderately large elastic-plastic strains have been observed during the experimental campaign, implying a nonlinear geometric formulation. The deformation gradient $\underline{\underline{F}}$ describes the transformation from the initial (undeformed) configuration to the current (deformed) configuration of the particle coordinates of any point belonging to the material body. As suggested by Lee [118 ; 119], the deformation gradient $\underline{\underline{F}}$ may be multiplicatively decomposed into an elastic contribution $\underline{\underline{F}}^e$ and a plastic contribution $\underline{\underline{F}}^p$:

$$\underline{\underline{F}} = \frac{\partial \underline{x}}{\partial \underline{X}} = \underline{\underline{F}}^e \, \underline{\underline{F}}^p \tag{2.8}$$

where $\underline{X}$ and $\underline{x}\left(\underline{X}, t\right)$ represents the particle coordinates in the initial and current configurations, respectively. In this context, $\underline{\underline{F}}^e$ represents the transformation between the virtually elastically unstressed (intermediate) and current configurations, and $\underline{\underline{F}}^p$ the transformation between the initial and virtually elastically unstressed (intermediate) configurations.

We are here considering an intermediate configuration virtually unstressed by a pure elastic stretching $\underline{\underline{V}}^{e-1}$, yielding

$$\underline{\underline{F}} = \underline{\underline{V}}^e \, \underline{\underline{Q}} \, \underline{\underline{F}}^p \tag{2.9}$$

where $\underline{\underline{Q}}$ represents an orthogonal transformation (rotation). The velocity gradient $\underline{\underline{l}}$ accordingly reads (see Longère et al. [120])

$$\underline{\underline{l}} = \frac{\partial \underline{v}\left(\underline{x}\right)}{\partial \underline{x}} = \dot{\underline{\underline{F}}} \, \underline{\underline{F}}^{-1} = \overset{\nabla}{\underline{\underline{V}}}{}^e \, \underline{\underline{V}}^{e-1} + \underline{\underline{W}} + \underline{\underline{V}}^e \dot{\underline{\underline{F}}}{}^p \, \underline{\underline{F}}^{p-1} \underline{\underline{V}}^{e-1} \tag{2.10}$$

where $\underline{v}$ is the particle velocity and where $\underline{\underline{W}} = \dot{\underline{\underline{Q}}} \, \underline{\underline{Q}}^T$ represents the rate of the orthogonal transformation. The decomposition of the deformation gradient $\underline{\underline{l}}$ into a symmetric part $\underline{\underline{d}}$ and a skew-symmetric part $\underline{\underline{w}}$, viz. $\underline{\underline{l}} = \underline{\underline{d}} + \underline{\underline{w}}$, yields

$$\begin{cases} \underline{\underline{d}} = \left[l\right]^S = \underline{\underline{d}}^e + \underline{\underline{d}}^p \\ \underline{\underline{w}} = \left[l\right]^{SS} = \underline{\underline{W}} + \underline{\underline{w}}^e + \underline{\underline{w}}^p \end{cases} \tag{2.11}$$

where

$$\begin{cases} \underline{\underline{d}}^e = \left[\overset{\nabla}{\underline{\underline{V}}}{}^e \, \underline{\underline{V}}^{e-1}\right]^S \\ \underline{\underline{w}}^e = \left[\overset{\nabla}{\underline{\underline{V}}}{}^e \, \underline{\underline{V}}^{e-1}\right]^{SS} \end{cases} ; \quad \begin{cases} \underline{\underline{d}}^p = \left[\underline{\underline{V}}^e \dot{\underline{\underline{F}}}{}^p \, \underline{\underline{F}}^{p-1} \underline{\underline{V}}^{e-1}\right]^S \\ \underline{\underline{w}}^p = \left[\underline{\underline{V}}^e \dot{\underline{\underline{F}}}{}^p \, \underline{\underline{F}}^{p-1} \underline{\underline{V}}^{e-1}\right]^{SS} \end{cases} \tag{2.12}$$

yielding the following expression for the rotation rate $\underline{\underline{W}}$

$$\underline{\underline{W}} = \dot{\underline{\underline{Q}}}\,\underline{\underline{Q}}^T = \underline{\underline{w}} - \left(\underline{\underline{w}}^e + \underline{\underline{w}}^p\right) \tag{2.13}$$

Moreover, the objective derivative $\overset{\triangledown}{\underline{\underline{a}}}$ of any second order tensor $\underline{\underline{a}}$ reads

$$\overset{\triangledown}{\underline{\underline{a}}} = \dot{\underline{\underline{a}}} - \underline{\underline{W}}\,\underline{\underline{a}} + \underline{\underline{a}}\,\underline{\underline{W}} \tag{2.14}$$

Under small elastic strain assumption, Equation 2.12 reduces to

$$\begin{cases} \underline{\underline{d}}^e = \overset{\triangledown}{\underline{\underline{V}}}{}^e \\ \underline{\underline{w}}^e = 0 \end{cases} ; \begin{cases} \underline{\underline{d}}^p = \left[\dot{\underline{\underline{F}}}{}^p\,\underline{\underline{F}}^{p-1}\right]^S \\ \underline{\underline{w}}^p = \left[\dot{\underline{\underline{F}}}{}^p\,\underline{\underline{F}}^{p-1}\right]^{SS} \end{cases} \tag{2.15}$$

In addition, assuming tentatively negligible effect of the spin $\underline{\underline{w}}^p$ in regards with the spin $\underline{\underline{w}}$ (see the assumption of moderate plastic strain in Schieck and Stumpf [71]), Equation 2.13 reduces to

$$\underline{\underline{W}} = \underline{\underline{w}} \tag{2.16}$$

where the assumption of negligible effects of anisotropy is also used [121].

According to the decomposition of the deformation gradient $\underline{\underline{F}}$ in Equation 2.9, when working with respect to the current configuration, it is needed to use the Zaremba-Jaumann objective derivative. Alternatively, it is possible to work with respect to the $\underline{\underline{Q}}$-rotated or co-rotational configuration, by means of a push forward and a pull back rotations [122 ; 123]. The latter method is used in the following. The rate equations of the constitutive model are consequently formulated by using time derivatives with respect to the co-rotational frame:

$$\dot{\underline{\underline{a}}}_Q = \underline{\underline{Q}}^T\,\overset{\triangledown}{\underline{\underline{a}}}\,\underline{\underline{Q}} \tag{2.17}$$

For example the Cauchy stress would read in the context of temperature independent hypo-elasticity as

$$\overset{\triangledown}{\underline{\underline{\sigma}}} = \underline{\underline{\underline{\underline{C}}}} : \underline{\underline{d}}^e \quad \rightarrow \quad \dot{\underline{\underline{\sigma}}}_Q = \underline{\underline{\underline{\underline{C}}}}_Q : \dot{\underline{\underline{\varepsilon}}}{}^e_Q \tag{2.18}$$

In the sequel, the subscript $\cdot_Q$ is dropped for simplicity.

2.3.2 Irreversible thermodynamics framework

Constitutive state laws and complementary laws respectively derived from the state and dissipation potentials are expressed in this subsection.

2.3.2.1 State potential and constitutive state laws

The internal variable procedure is herein applied within the irreversible thermodynamics framework to model the thermo-mechanical behavior of the Ti-6Al-4V grade under consideration. The instantaneous state of the material is assumed to be well described via the Helmholtz free energy Ψ whose arguments are the absolute temperature T, the elastic strain tensor $\underline{\underline{\varepsilon}}^e$, the isotropic hardening variable (also called cumulated plastic strain) κ, and the kinematic hardening variable $\underline{\underline{\alpha}}$. Therefore, the Helmholtz state potential can be decomposed into four parts: a recoverable energy Ψ_e, a purely thermal part Ψ_T and two stored energies corresponding to the isotropic and kinematic hardening contributions, Ψ_{pI} and Ψ_{pK}, see [124]. Considering tentatively state uncoupling between the two mechanisms of plasticity and between them and elasticity, the Helmholtz free energy Ψ is taken of the form

$$\Psi\left(\underline{\underline{\varepsilon}}^e, \kappa, \underline{\underline{\alpha}}; T\right) = \Psi_e\left(\underline{\underline{\varepsilon}}^e; T\right) + \Psi_T\left(T\right) + \Psi_{pI}\left(\kappa; T\right) + \Psi_{pK}\left(\underline{\underline{\alpha}}\right) \tag{2.19}$$

where Ψ_{pK} is taken temperature independent. The specific contributions to the state potential are defined as

$$\left\{\begin{aligned} \rho\Psi_e\left(\underline{\underline{\varepsilon}}^e; T\right) &= \frac{1}{2}\underline{\underline{\varepsilon}}^e : \underline{\underline{\underline{\underline{C}}}} : \underline{\underline{\varepsilon}}^e - \alpha K\left(T - T_0\right)\mathrm{trace}(\underline{\underline{\varepsilon}}^e) \\ \rho\Psi_T &= -\frac{\rho c}{2T_0}\Delta T^2 \\ \rho\Psi_{pI}\left(\kappa; T\right) &= h\left(\kappa\right) g\left(T\right) \\ \rho\Psi_{pK}\left(\underline{\underline{\alpha}}\right) &= \frac{1}{3}C\underline{\underline{\alpha}} : \underline{\underline{\alpha}} \end{aligned}\right. \tag{2.20}$$

where ρ is the mass density, $\underline{\underline{\underline{\underline{C}}}}$ is the elasticity stiffness fourth order tensor, with $C_{ijkl} = \lambda\delta_{ij}\delta_{kl} + \mu\left(\delta_{ik}\delta_{jl} + \delta_{il}\delta_{jk}\right)$, λ and μ being the Lamé coefficients, K the bulk modulus, with $K = \lambda + \frac{2}{3}\mu$, α the thermal dilatation coefficient, T_0 the initial temperature, and c is the specific heat. $h\left(\kappa\right)$ and $g\left(T\right)$ are the stored energy of cold work and the thermal softening function, respectively, and the scalar C is a kinematic hardening-related parameter.

The thermodynamic forces derived from the state potential with respect to their conjugate variables are given by the constitutive state laws defined below.

$$\left\{\begin{aligned} \underline{\underline{\sigma}} = \rho\left.\frac{\partial\Psi}{\partial\underline{\underline{\varepsilon}}^e}\right|_{\kappa,\underline{\underline{\alpha}},T} &= \rho\left.\frac{\partial\Psi_e}{\partial\underline{\underline{\varepsilon}}^e}\right|_{T} = \underline{\underline{\underline{\underline{C}}}} : \underline{\underline{\varepsilon}}^e - \alpha K\left(T - T_0\right)\underline{\underline{I}} \\ \rho s = -\rho\left.\frac{\partial\Psi}{\partial T}\right|_{\underline{\underline{\varepsilon}}^e,\kappa,\underline{\underline{\alpha}}} &= -\rho\left(\left.\frac{\partial\Psi_e}{\partial T}\right|_{\underline{\underline{\varepsilon}}^e} + \frac{\partial\Psi_T}{\partial T} + \left.\frac{\partial\Psi_{pI}}{\partial T}\right|_{\kappa}\right) \\ &= \alpha K\mathrm{trace}\left(\underline{\underline{\varepsilon}}^e\right) + \frac{\rho c}{T_0}\Delta T - h\left(\kappa\right)g'\left(T\right) \\ r = \rho\left.\frac{\partial\Psi}{\partial\kappa}\right|_{\underline{\underline{\varepsilon}}^e,\underline{\underline{\alpha}},T} &= \rho\left.\frac{\partial\Psi_{pI}}{\partial\kappa}\right|_{T} = h'\left(\kappa\right)g\left(T\right) \\ \underline{\underline{X}} = \rho\left.\frac{\partial\Psi}{\partial\underline{\underline{\alpha}}}\right|_{\underline{\underline{\varepsilon}}^e,\kappa,T} &= \rho\left.\frac{\partial\Psi_{pK}}{\partial\underline{\underline{\alpha}}}\right|_{T} = \frac{2}{3}C\underline{\underline{\alpha}} \end{aligned}\right. \tag{2.21}$$

where $\underline{\underline{\sigma}}$ is the Cauchy stress tensor, s the entropy, r the isotropic hardening force and $\underline{\underline{X}}$ the kinematic hardening force.

Finally, the Gibbs relation reads

$$\rho\dot{\Psi} = \underline{\underline{\sigma}} : \dot{\underline{\underline{\varepsilon}}}^e + r\dot{\kappa} + \underline{\underline{X}} : \dot{\underline{\underline{\alpha}}} - \rho s\dot{T} \tag{2.22}$$

2.3.2.2 Dissipation and complementary laws

Injecting the Gibbs relation into Clausius-Duhem inequality and using $\dot{\underline{\underline{\varepsilon}}} = \dot{\underline{\underline{\varepsilon}}}^e + \dot{\underline{\underline{\varepsilon}}}^p$ yields the following expression for the intrinsic dissipation

$$\begin{aligned} \mathcal{D} &= \underline{\underline{\sigma}} : \dot{\underline{\underline{\varepsilon}}} - \rho\left(\dot{\Psi} + s\dot{T}\right) \\ &= \underline{\underline{\sigma}} : \dot{\underline{\underline{\varepsilon}}}^p - r\dot{\kappa} - \underline{\underline{X}} : \dot{\underline{\underline{\alpha}}} \quad \geq 0 \end{aligned} \tag{2.23}$$

which involves force-related quantities $A = \left(\underline{\underline{\sigma}}, r, \underline{\underline{X}}\right)$ and flux-related quantities $\dot{a} = \left(\dot{\underline{\underline{\varepsilon}}}^p, -\dot{\kappa}, -\dot{\underline{\underline{\alpha}}}\right)$. In the context of the normality rule, the dissipation may be rewritten in the following form

$$\mathcal{D} = A\dot{a} = A\dot{\lambda}\frac{\partial F}{\partial A} \geq 0 \tag{2.24}$$

where F is the plastic potential meeting the required conditions of positiveness and convexity and where $\dot{\lambda}$ is the positive plastic multiplier. In the context of rate dependent non-associated plasticity, $\dot{\lambda}$ is assumed to derive from a dissipation potential $\Omega\left(f\right)$, viz. $\dot{\lambda} = \partial\Omega/\partial f$, where f represents the yield function.

The yield function f and plastic potential F are written of the form

$$\begin{aligned} f\left(\underline{\underline{\sigma}}, r, \underline{\underline{X}}, ...\right) &= \sigma_{eq}\left(\underline{\underline{\sigma}}, \underline{\underline{X}}, ...\right) - \sigma_y\left(r, ...\right) = \sigma_v\left(\dot{\kappa}, ...\right) \geq 0 \\ F\left(\underline{\underline{\sigma}}, r, \underline{\underline{X}}, ...\right) &= f + \hat{f}\left(\underline{\underline{X}}\right) \end{aligned} \tag{2.25}$$

where σ_{eq} is the transformed equivalent stress accounting for the different sources of plastic anisotropy, σ_y the rate independent yield stress, σ_v the strain rate induced overstress or viscous stress, and where ... represents other arguments defined later. $\hat{f}\left(\underline{\underline{X}}\right)$ is a function involving non-linearity in kinematic hardening in a non-associated plasticity formulation.

In this work, the Perzyna approach is employed allowing the positiveness of the yield function in Equation 2.25 [62]. An alternative method for modeling is by means of a viscoplastic consistent formulation that includes the viscous component as a strain rate depending isotropic hardening [125]. However, both approaches can be proven to yield an equivalent conclusion as pointed out by Heeres et al. [126].

The normality rule accordingly yields

$$\begin{cases} \dot{\underline{\underline{\varepsilon}}}^p = \dot{\lambda}\dfrac{\partial F}{\partial \underline{\underline{\sigma}}} = \dot{\lambda}\dfrac{\partial \sigma_{eq}}{\partial \underline{\underline{\sigma}}} = \dot{\lambda}\underline{\underline{n}} \quad \text{with} \quad \underline{\underline{n}} = \dfrac{\partial \sigma_{eq}}{\partial \underline{\underline{\sigma}}} \\ \dot{\kappa} = -\dot{\lambda}\dfrac{\partial F}{\partial r} = -\dot{\lambda}\dfrac{\partial f}{\partial r} = \dot{\lambda} \\ \dot{\underline{\underline{\alpha}}} = -\dot{\lambda}\dfrac{\partial F}{\partial \underline{\underline{X}}} = -\dot{\lambda}\left(\dfrac{\partial f}{\partial \underline{\underline{X}}} + \dfrac{\partial \hat{f}}{\partial \underline{\underline{X}}}\right) = \dot{\lambda}\underline{\underline{m}} \quad \text{with} \quad \underline{\underline{m}} = -\left(\dfrac{\partial \sigma_{eq}}{\partial \underline{\underline{X}}} + \dfrac{\partial \hat{f}}{\partial \underline{\underline{X}}}\right) \end{cases} \tag{2.26}$$

These laws are completed by the temperature rise coming from adiabatic self-heating under high strain rate loading assuming negligible contributions of thermo-elastic and thermo-plastic couplings [127]. Temperature rise is estimated from dissipation in Equation 2.23, see Longère and Dragon [128], according to

$$\rho c\dot{T} \simeq \mathcal{D} = \underline{\underline{\sigma}} : \dot{\underline{\underline{\varepsilon}}}^p - r\dot{\kappa} - \underline{\underline{X}} : \dot{\underline{\underline{\alpha}}} \geq 0 \tag{2.27}$$

2.3.3 Constitutive equations

Quantities introduced in the previous subsection are now specified for the material under consideration in agreement with the experimental observations.

2.3.3.1 Transformed equivalent stress σ_{eq}

Plastic anisotropy entails a loss of coaxiality between the plastic strain rate and the stress deviator. As the plastic strain rate is derived from the transformed equivalent stress according to the normality rule (see Equation 2.26), the plastic anisotropy effects are accounted for in the expression of the transformed equivalent stress. It is reminded that in the present case plastic anisotropy manifests through (i) loading direction dependence, (ii) kinematic hardening, and (iii) strength differential.

We are here considering the transformed equivalent stress σ_{eq} as a function of three variables, namely the current Cauchy stress second order tensor $\underline{\underline{\sigma}}$, the back stress second order tensor $\underline{\underline{X}}$, and a fourth order tensor accounting for the texture-induced orthotropy $\underline{\underline{\underline{\underline{A}}}}$.

$$\sigma_{eq} = \sigma_{eq}\left(\underline{\underline{\sigma}}, \underline{\underline{X}}; \underline{\underline{\underline{\underline{A}}}}\right) \tag{2.28}$$

In addition, the plastic transformation can be further considered isochoric as it is thought that the origin comes mainly form slipping and twinning mechanisms which do not involve a volume change in the material. Therefore, only the deviatoric part of the stress state is supposed to play a role in the modeling of plasticity.

$$\underline{\underline{\sigma}} = -p\underline{\underline{I}} + \underline{\underline{s}} \tag{2.29}$$

Each source of anisotropy is first studied independently of the others and then a combination of the three sources is proposed.

Texture-induced initial orthotropy: $\underline{\underline{X}} = \underline{\underline{0}}$

Following Karafillis and Boyce [72], we introduce the transformed stress $\underline{\underline{\Sigma}} = \underline{\underline{\underline{\underline{A}}}} : \underline{\underline{\sigma}}$ also denoted as the Isotropy Plasticity Equivalent (IPE) stress. The fourth order tensor $\underline{\underline{\underline{\underline{A}}}}$ is a linear multiplicative operator involving potential plastic orthotropy. In the case of an isotropic material, the operator reduces to the identity tensor, viz. $\underline{\underline{\underline{\underline{A}}}} = \underline{\underline{\underline{\underline{I}}}}$. As a consequence, the transformed stress reads

$$\sigma_{eq}\left(\underline{\underline{\sigma}}, \underline{\underline{X}}; \underline{\underline{\underline{\underline{A}}}}\right) = \sigma_{eq}\left(\underline{\underline{\Sigma}}, \underline{\underline{X}}\right) \tag{2.30}$$

Table 2.5 reports two definitions of the transformed equivalent stress aiming at accounting for anisotropic plasticity: (i) by incorporating the tensor $\underline{\underline{\underline{\underline{A}}}}$ directly in the expression of the equivalent stress, as proposed by Hill [74], and (ii) by incorporating it at the stress level, as proposed by Karafillis and Boyce [72] (see also Table 2.2).

The fourth order tensor accounting for the orthotropic behavior can be simplified as a 6x6 matrix according to major and minor symmetries while stress second order tensors are reduced to vectors according to Voigt or Bechterew notations.

Table 2.5: Definitions of transformed equivalent stress in the case of orthotropic plasticity.

Hill (1948)	**K&B (1993)**
$\sigma_{eq}^2 = \frac{1}{2}\underline{\underline{\sigma}} : \underline{\underline{\underline{\underline{A}}}} : \underline{\underline{\sigma}}$	$\underline{\underline{\Sigma}} = \underline{\underline{\underline{\underline{A}}}} : \underline{\underline{\sigma}}$ $\sigma_{eq}^2 = \dfrac{1}{2}\underline{\underline{\Sigma}} : \underline{\underline{\Sigma}}$

$$\underline{\underline{\underline{\underline{A}}}} = \begin{bmatrix} A_{11} & A_{12} & A_{13} & & & \\ A_{12} & A_{22} & A_{23} & & & \\ A_{13} & A_{23} & A_{33} & & & \\ & & & A_{44} & & \\ & & & & A_{55} & \\ & & & & & A_{66} \end{bmatrix} \tag{2.31}$$

In Hill criterion [74] one has

$$\begin{cases} A_{11} = -\left(A_{12} + A_{13}\right) \\ A_{22} = -\left(A_{12} + A_{23}\right) \\ A_{33} = -\left(A_{13} + A_{23}\right) \end{cases} \tag{2.32}$$

Accordingly, 6 independent coefficients are sufficient for the description of orthotropy [72]. The Karafillis and Boyce [72] approach is used throughout this work. The notion of a transformed stress deviator has been widely applied to many yield criteria (see [73 ; 82 ; 83]).

Kinematic hardening-induced evolving anisotropy $\underline{\underline{\underline{\underline{A}}}} = \underline{\underline{\underline{\underline{I}}}}$

The approach commonly adopted when dealing with kinematic plastic hardening is to consider the translation of the yield surface by means of the deviatoric back stress $\underline{\underline{X}}$. For instance, the transformed equivalent stress would read

$$\sigma_{eq}^2 = \frac{3}{2}\left(\underline{\underline{s}} - \underline{\underline{X}}\right) : \left(\underline{\underline{s}} - \underline{\underline{X}}\right) = \frac{3}{2}\underline{\underline{\hat{s}}} : \underline{\underline{\hat{s}}} \tag{2.33}$$

where $\underline{\underline{\hat{s}}} = \left(\underline{\underline{s}} - \underline{\underline{X}}\right)$

Strength differential-induced initial anisotropy $\underline{\underline{\underline{\underline{A}}}} = \underline{\underline{\underline{\underline{I}}}}$ & $\underline{\underline{X}} = \underline{\underline{0}}$

The strength differential between tension and compression can be assumed to be a type of anisotropy. As mentioned in the introduction, CPB06 [73], Khan [20] and Longère [91] propose different methods for describing this effect. In this study, the CPB06 model [73] is chosen as it allows for a simple definition of the yield surface without resorting to the Lode angle or a coupling with the viscous component. The CPB06 isotropic yield surface adds a strength differential parameter k to the definition in Karafillis and Boyce [72] resulting in the form

$${\sigma_{eq}}^a = \frac{1}{{m_0}^a}\left\{\left(|S_1| - kS_1\right)^a + \left(|S_2| - kS_2\right)^a + \left(|S_3| - kS_3\right)^a\right\} \tag{2.34}$$

where S_p are the eigenvalues of the stress tensor $\underline{\underline{\sigma}}$, k is the main parameter defining the material asymmetry, a is a shape parameter of the yield surface, see Hosford [129] and m_0 is a model constant.

The Karafillis and Boyce [72] generalized yield criterion can be recovered for $k = 0$ (and the Mises criterion with $a = 2$). The CPB06 criterion in Equation 2.34 can thus be considered as an extended distortion (without a rotation) of such surface.

Complete transformed equivalent stress $\underline{\underline{\underline{\underline{A}}}} \neq \underline{\underline{\underline{\underline{I}}}}$ & $\underline{\underline{X}} \neq \underline{\underline{0}}$

In order to couple kinematic hardening and plastic orthotropy, two approaches can be considered, see Table 2.6. Following Baltov and Sawczuk [78], the back stress is first subtracted from the deviatoric stress tensor and the Hill criterion is then applied. Alternatively, Karafillis and Boyce [72] make use of their linear operator to transform the difference between the stress tensor and the back force.

On the other hand, coupling plastic orthotropy and strength differential may be achieved following CPB06 [73] approach. Indeed, the authors apply a linear transformation to the stress deviator: Σ_p is defined as the eigenvalues of the transformed tensor $\underline{\underline{\Sigma}} = \underline{\underline{\underline{\underline{A}}}} : \underline{\underline{s}}$ which replaces $\underline{\underline{s}}$ in Equation 2.34, see Table 2.6. The authors initially proposed a symmetric definition of the 6x6 matrix representation of the tensor $\underline{\underline{\underline{\underline{A}}}}$ as in Equation 2.31, although further simplifications using a Hill-like matrix can be made to model the orthotropy as found in Stewart and Cazacu [130].

We are here coupling kinematic hardening, plastic orthotropy and strength differential by combining Karafillis and Boyce [72] and CPB06 [73] methods. For that purpose, we are defining the transformed stress eigenvalues as follows, see Table 2.6.

$$\begin{aligned} \hat{\Sigma}_p &= eig(\hat{\underline{\underline{\Sigma}}}); \\ \hat{\underline{\underline{\Sigma}}} &= \underline{\underline{\underline{\underline{A}}}} : \left(\underline{\underline{s}} - \underline{\underline{X}}\right) \end{aligned} \tag{2.35}$$

Therefore, the complete anisotropic criterion reads

$$\sigma_{eq}{}^a = \frac{1}{m_0{}^a} \left\{ \left(|\hat{\Sigma}_1| - k\hat{\Sigma}_1\right)^a + \left(|\hat{\Sigma}_2| - k\hat{\Sigma}_2\right)^a + \left(|\hat{\Sigma}_3| - k\hat{\Sigma}_3\right)^a \right\} \tag{2.36}$$

The constant m_0 is defined such that the equivalent stress is equal to the uniaxial stress in tension (compression) if $k > 0$ ($k < 0$).

$$m_0{}^a = \left[\frac{2}{3}(1 - |k|)\right]^a + 2\left[\frac{1}{3}(1 + |k|)\right]^a \tag{2.37}$$

The coefficients A_{55} and A_{66} are herein assumed to be 1 due to the lack of information for shear along the normal direction (an alternative approach is to consider $A_{44} = A_{55} = A_{66}$ as done by Tuninetti and Habraken [33]). The capabilities of such yield stress criterion can be easily appreciated in Figure 2.5 which represents the yield surface in plane stress conditions.

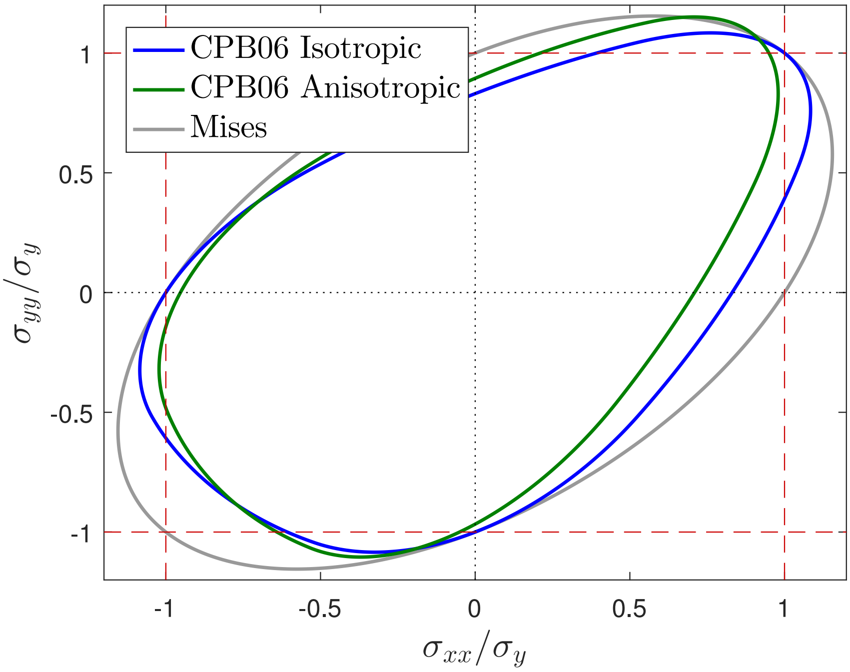

Figure 2.5: Distorted yield surface

Table 2.6: Anisotropic criteria

B&S (1965)	**K&B (1993)**	**CPB06**	**Present approach**
$\hat{\underline{\underline{s}}} = \underline{\underline{s}} - \underline{\underline{X}}$ $\sigma_{eq}^2 = \frac{1}{2}\hat{\underline{\underline{s}}} : \underline{\underline{\underline{\underline{A}}}} : \hat{\underline{\underline{s}}}$	$\hat{\underline{\underline{\Sigma}}} = \underline{\underline{\underline{\underline{A}}}}\left(\underline{\underline{\sigma}} - \underline{\underline{X}}\right)$ $\sigma_{eq}^2 = \frac{1}{2}\hat{\underline{\underline{\Sigma}}} : \hat{\underline{\underline{\Sigma}}}$	$\Sigma_p = eig(\underline{\underline{\Sigma}})$ $\underline{\underline{\Sigma}} = \underline{\underline{\underline{\underline{A}}}} : \underline{\underline{s}}$ $\sigma_{eq} = \sigma_{eq}\left(\Sigma_p, k\right)$	$\hat{\Sigma}_p = eig(\hat{\underline{\underline{\Sigma}}})$ $\hat{\underline{\underline{\Sigma}}} = \underline{\underline{\underline{\underline{A}}}} : \left(\underline{\underline{s}} - \underline{\underline{X}}\right)$ $\sigma_{eq} = \sigma_{eq}\left(\hat{\Sigma}_p, k\right)$

2.3.3.2 Viscous stress σ_v

Regarding the rate dependent formulation, the experimental results show the existence of a strain rate induced overstress independent of the anisotropy axes and plastic strain and whose temperature dependence within the temperature range of interest has been tentatively neglected. The Norton-Perzyna law is proposed to describe such behavior [61 ; 62].

$$\sigma_v = Y_v \dot{\kappa}^{1/n_v} \tag{2.38}$$

where Y_v and n_v are material coefficients.

By following the approach in Perzyna [62], the potential described in Equation 2.24 is accordingly of the form

$$\Omega\left(f\right) = \frac{1}{n_v + 1}\langle\frac{f}{Y_v}\rangle^{n_v+1} \tag{2.39}$$

Indeed, by applying the normality rule, the Norton law in Equation 2.38 is retrieved

$$\dot{\kappa} = \dot{\lambda} = \frac{\partial\Omega}{\partial f} = \langle\frac{f}{Y_v}\rangle^n = \langle\frac{\sigma_v}{Y_v}\rangle^n \tag{2.40}$$

2.3.3.3 Rate independent yield stress σ_y

The radius of the elasticity domain is defined as a temperature dependent initial threshold stress $\sigma_{y0}(T)$ plus the stress related to the isotropic hardening r(κ, T). Both the initial threshold stress and isotropic hardening force are assumed to depend on temperature according to the same thermal softening function $g(T)$:

$$\sigma_y = \sigma_{y0}(T) + r(\kappa, T) = g(T)\, R(\kappa) \tag{2.41}$$

Strain hardening

For the definition of the isotropic hardening, the Swift (power) law and the Voce (exponential with saturation) law are widely used (see [47 ; 101] for a linear combination of both). For the material under consideration, some initial constant calibration (see Figure 2.10 later) from the monotonic tests have shown that Swift law fits well the experimental curves. On the other hand, Chun et al. [96] and Carbonnière [97] have shown that a coupling between isotropic and kinematic hardening is well described by adding a negative Voce-type exponential law in the expression of the strain hardening function.

Therefore, a combination of Swift and (negative) Voce expressions is herein considered in view of coupling isotropic and kinematic hardening. The adopted forms for the strain hardening function $h'(\kappa)$ in Equation 2.21 and radius $R(\kappa)$ in Equation 2.41 read

$$\begin{aligned} h'(\kappa) &= Q_0\,(\varepsilon_0 + \kappa)^n - \frac{C}{D}\left(1 - exp\left(-D\kappa\right)\right) \\ R(\kappa) &= R_0 + h'(\kappa) \end{aligned} \tag{2.42}$$

where R_0, Q_0, ε_0 and n are the Swift law-related positive material constants and C and D are (negative) Voce law-related constants.

Thermal softening

As previously evidenced by the experimental campaign, the thermal softening function $g(T)$ is of the form

$$g(T) = 1 - \langle \frac{T - T_{ref}}{T_m - T_{ref}} \rangle^{m_T} \tag{2.43}$$

where T_m is the melting point and T_{ref} and m_T material constants.

2.3.3.4 Complementary laws

Following the decomposition made in Equation 2.26, the plastic strain rate is expressed as

$$\dot{\underline{\underline{\varepsilon}}}^p = \dot{\kappa}\frac{\partial \sigma_{eq}}{\partial \underline{\underline{\sigma}}} = \dot{\kappa}\underline{\underline{n}} \tag{2.44}$$

where $\underline{\underline{n}} = \partial \sigma_{eq} / \partial \underline{\underline{\sigma}}$ represents the yield direction. It can be shown that the explicit expression for $\underline{\underline{n}}$ is (see Appendix A)

$$\underline{\underline{n}} = \sum_{p=1}^{3}\left[\frac{1}{m_0^a}\left(\frac{|\hat{\Sigma}_p| - k\hat{\Sigma}_p}{\sigma_{eq}}\right)^{a-1}\left(sgn\left(\hat{\Sigma}_p\right) - k\right)\right]\underline{\underline{\underline{\underline{J}}}} : \underline{\underline{\underline{\underline{A}}}} : \left(\underline{v}_p \otimes \underline{v}_p\right) \tag{2.45}$$

where $\underline{v}_p$ is the eigenvector corresponding to the eigenvalue $\hat{\Sigma}_p$. The outer product $\cdot \otimes \cdot$ is here used and $\underline{\underline{\underline{J}}}$ is the fourth order tensor projecting $\underline{\underline{\sigma}}$ onto its deviatoric plane $\underline{\underline{s}}$. The deviator operator $\underline{\underline{\underline{J}}}$ is defined in the index form as

$$J_{ijkl} = \left[\frac{1}{2}\left(\delta_{ik}\delta_{jl} + \delta_{il}\delta_{jk}\right) - \frac{1}{3}\delta_{ij}\delta_{kl}\right] \tag{2.46}$$

To describe nonlinear kinematic hardening, function $\hat{f}\left(\underline{\underline{X}}\right)$ in Eq 2.25 is taken of the form (see [92])

$$\hat{f}\left(\underline{\underline{X}}\right) = \frac{3D}{4C}\underline{\underline{X}} : \underline{\underline{X}} \tag{2.47}$$

The rate of the kinematic hardening variable in Equation 2.26 accordingly reads

$$\dot{\underline{\underline{\alpha}}} = -\dot{\kappa}\left(\frac{\partial f}{\partial \underline{\underline{X}}} + \frac{3D}{2C}\underline{\underline{X}}\right) = \dot{\kappa}\underline{\underline{m}} \tag{2.48}$$

It can be easily shown that $\partial\sigma_{eq}/\partial\underline{\underline{X}} = -\underline{\underline{n}}$. With this expression, the normal tensor $\underline{\underline{m}}$ recovers the non linear definition seen in Armstrong and Frederick [94] and Chaboche [95]:

$$\begin{aligned} \underline{\underline{m}} &= \underline{\underline{n}} - \frac{3D}{2C}\underline{\underline{X}} \\ \dot{\underline{\underline{\alpha}}} &= \dot{\underline{\underline{\varepsilon}}}^p - D\dot{\kappa}\underline{\underline{\alpha}} \end{aligned} \tag{2.49}$$

It is noteworthy that the material constants C and D coincide with the Voce law constants in Equation 2.42.

Regarding the evolution of temperature, injecting the different expressions in Equations 2.44 and 2.49 into Equation 2.27 yields the following expression form for the temperature rise

$$\dot{T} = \frac{1}{\rho c}\left(\sigma_{eq} - r + \frac{2}{3}CD\underline{\underline{\alpha}} : \underline{\underline{\alpha}}\right)\dot{\kappa} \tag{2.50}$$

As mentioned previously, the temperature rise is usually estimated via the inelastic heat fraction β, also known as the Taylor-Quinney coefficient [63], defined as the fraction of the plastic work rate converted into heat, or

$$\dot{T} = \frac{\beta}{\rho c}q\dot{\kappa} \tag{2.51}$$

The coefficient β is often arbitrarily assumed constant with a value typically ranging from 0.8 to 1.0 without much physical motivation to back it up [125] and despite many experimental evidences of its dependence on strain and even strain rate and temperature itself (see Macdougall and Harding [36]). As done in Longère [32], this coefficient may be deduced consistently from the constitutive model. In the present case, it reads

$$\beta = \frac{\mathcal{D}}{q\dot{\kappa}} = \frac{\left[\sigma_{eq} - r + \frac{3D}{2C}\left(\underline{\underline{X}} : \underline{\underline{X}}\right)\right]}{q} \tag{2.52}$$

This expression for β intrinsically accounts for potential dependence on strain, strain rate and temperature and is used in the sequel.

2.3.4 Summary of the constitutive equations

Rate equations of the constitutive model are summarized below.

Constitutive state laws

$$\begin{cases} \dot{\underline{\underline{\sigma}}} = \underline{\underline{\underline{\underline{C}}}} : \dot{\underline{\underline{\varepsilon}}}^{e} - \alpha K \dot{T} \underline{\underline{I}} \\ \dot{\underline{\underline{X}}} = \dfrac{2}{3} C \dot{\underline{\underline{\alpha}}} \\ \dot{r} = h''\left(\kappa\right) g\left(T\right) \dot{\kappa} + h'\left(\kappa\right) g'\left(T\right) \dot{T} \end{cases} \tag{2.53}$$

with $C_{ijkl} = \lambda \delta_{ij} \delta_{kl} + \mu \left(\delta_{ik}\delta_{jl} + \delta_{il}\delta_{jk}\right)$ and

$$\begin{cases} h\left(\kappa\right) = \dfrac{Q_0}{n+1}\left(\varepsilon_0 + \kappa\right)^{n+1} - \dfrac{C}{D^2}\left(D\kappa + exp\left(-D\kappa\right)\right) \\ g\left(T\right) = 1 - \langle \dfrac{T - T_{ref}}{T_m - T_{ref}} \rangle^{m_T} \end{cases} \tag{2.54}$$

Yield function

$$f\left(\hat{\underline{\underline{\Sigma}}}, k, r\right) = \sigma_{eq}\left(\hat{\Sigma}_p, k\right) - \left[R_0 g\left(T\right) + r\left(\kappa, T\right)\right] = \sigma_v\left(\dot{\kappa}\right) \geq 0 \tag{2.55}$$

where

$$\begin{aligned} \sigma_{eq}^{a}\left(\hat{\Sigma}_p, k\right) &= \frac{1}{{m_0}^{a}}\left\{\left(|\hat{\Sigma}_1| - k\hat{\Sigma}_1\right)^{a} + \left(|\hat{\Sigma}_2| - k\hat{\Sigma}_2\right)^{a} + \left(|\hat{\Sigma}_3| - k\hat{\Sigma}_3\right)^{a}\right\} \\ \hat{\Sigma}_p &= eig(\hat{\underline{\underline{\Sigma}}}) \\ \hat{\underline{\underline{\Sigma}}} &= \underline{\underline{\underline{\underline{A}}}} : \left(\underline{\underline{s}} - \underline{\underline{X}}\right) \end{aligned} \tag{2.56}$$

where the anisotropy matrix is as defined in Equation 2.31.

Complementary laws

$$\begin{cases} \dot{\kappa} = \langle \dfrac{f}{Y_v} \rangle^{n_v} \\ \dot{\underline{\underline{\epsilon}}}^{p} = \dot{\kappa} \underline{\underline{n}} \\ \dot{\underline{\underline{\alpha}}} = \dot{\underline{\underline{\epsilon}}}^{p} - D\dot{\kappa}\underline{\underline{\alpha}} \\ \dot{T} = \dfrac{\beta q}{\rho c} \dot{\kappa} \end{cases} \tag{2.57}$$

where

$$\begin{cases} \underline{\underline{n}} = \displaystyle\sum_{p=1}^{3} \left[\frac{1}{m_0^{a}} \left(\frac{|\hat{\Sigma}_p| - k\hat{\Sigma}_p}{\sigma_{eq}}\right)^{a-1} \left(sgn\left(\hat{\Sigma}_p\right) - k\right)\right] \underline{\underline{\underline{\underline{J}}}} : \underline{\underline{\underline{\underline{A}}}} : \left(\underline{v}_p \otimes \underline{v}_p\right) \\ \beta = \dfrac{\sigma_{eq} - r + \frac{2}{3} C D \underline{\underline{\alpha}} : \underline{\underline{\alpha}}}{q} \\ q = \sqrt{\dfrac{3}{2} \underline{\underline{s}} : \underline{\underline{s}}} \end{cases} \tag{2.58}$$

with $J_{ijkl} = \frac{1}{2}\left(\delta_{ik}\delta_{jl} + \delta_{il}\delta_{jk}\right) - \frac{1}{3}\delta ij\delta_{kl}$.

Initial conditions

$$\begin{cases} \underline{\underline{\varepsilon}}^p\left(0\right) = \underline{\underline{0}} \\ \underline{\underline{X}}\left(0\right) = \underline{\underline{0}} \\ r\left(0\right) = 0 \\ T\left(0\right) = T_0 \end{cases} \tag{2.59}$$

Material constants

Elasticity: $E = 110\,\mathrm{GPa}$, $\nu = 0.3$

Anisotropy (9): $a, k, A_{11}, A_{22}, A_{33}, A_{44}, A_{12}, A_{23}, A_{13}, A_{55} = A_{66} = 1$

Viscosity (2): Y_v, n_v

Hardening (6): $R_0, Q_0, \varepsilon_0, n, C, D$

Temperature (2): $m_T, T_{ref}, T_m \simeq 1600\,°\mathrm{C}$

2.4 Material coefficients calibration

The commercial software Z-set is chosen to carry out the identification of the material coefficients. Three stages are considered for the calibration of the material parameters: (i) 9 coefficients for the anisotropy (using the von Mises criterion as the starting point of the optimization, i.e. $a = 2$, $k = 0$ and $A_{ij} = I_{ij}$), (ii) 2 coefficients for the viscosity (once the anisotropy has been identified) and finally (iii) 8 coefficients for the hardening identification. The three-step calibration plus the post-verification is depicted in Figure 2.6.

A volume element under uniaxial tension and compression at various strain rates along various directions is considered for the calibration in Z-set. The inverse-problem identification of the material constants is performed using a gradient-based optimization method [131]. In particular, the Levenberg-Marquardt algorithm [132] is employed for the least-square minimization between the numerical and experimental results:

$$\mathcal{C}\left(\underline{p}\right) = \frac{1}{2}\sum_{i=1}^{T}\sum_{j=1}^{N} w_j\left(\sigma_j^{EXP}\left(t_i\right) - \sigma_j^{NUM}\left(\underline{p}, t_i\right)\right)^2 \tag{2.60}$$

where $\mathcal{C}$ is the cost function to minimize, $\underline{p}$ the set of material constants to identify and the subscripts i and j are used to denote different times and tests respectively. For confidentiality reason, the values of the coefficients are not given here. Regarding the weight parameter w_j, it is chosen to have a value of 1 for the tests at room temperature and quasi-static regime and a value of 1/3 for high temperature and high strain rate simulations.

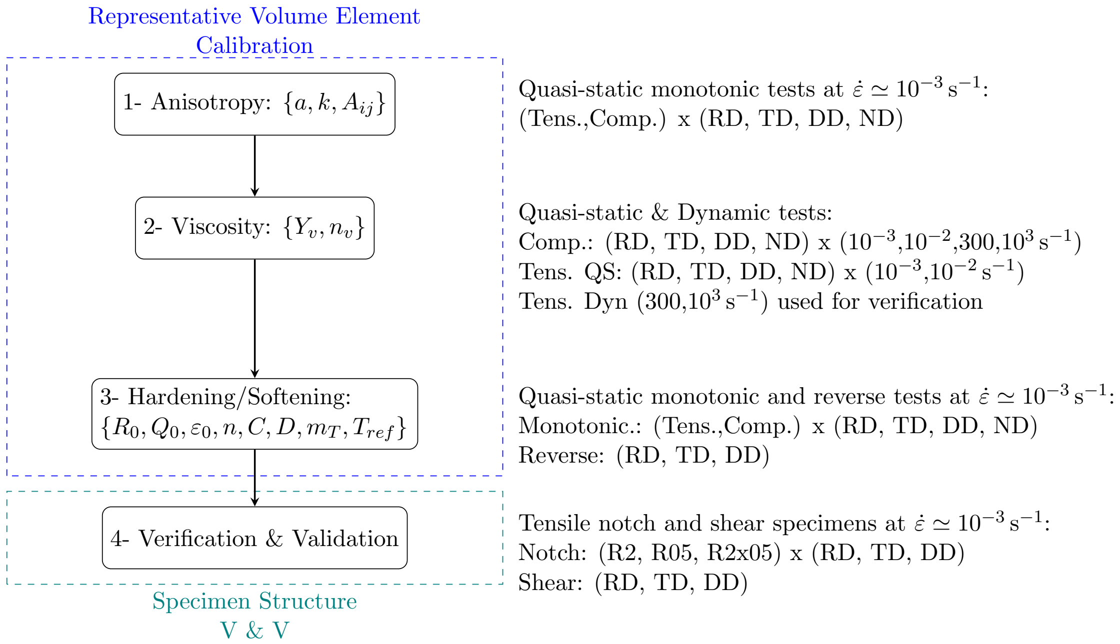

Figure 2.6: Flow chart of the 3-step calibration + verification procedure.

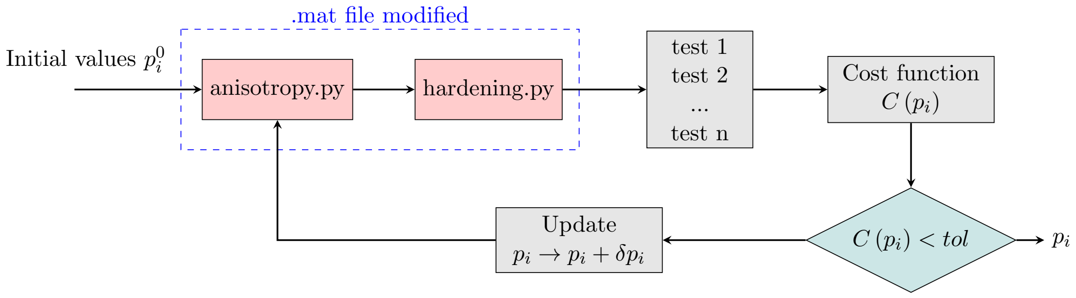

Figure 2.7: Inverse identification flowchart.

2.4.1 Preliminary considerations

Figure 2.7 shows a more precise flow chart of the algorithm used to calibrate the material coefficients. The calibration takes some initial input parameters as starting coefficients given by the user. Two python scripts are employed to modify the material, in the form of a text file, in terms of anisotropy matrix and hardening evolution in the optimization loop. Several numerical simulations on a representative volume element are carried out and compared to the experimental data. The calibration has been reached when the cost function $C\left(\underline{p}\right)$ in Equation 2.60 converges to a minimum value. Otherwise, an update of the material coefficients is done as an attempt to better fit the experimental data.

The representative volume element is depicted in Figure 2.8. It is a node-less material element with one integration point. Denoted in the Z-set manual as 'rve3d', it allows to directly impose a total deformation on the element and to output the related stress [133].

2.4.1.1 Strain range of the experimental curves to be used

Conventionally, the uniaxial loading is only assured before the onset of necking which involves a non-uniform triaxial stress state. The beginning of necking is identified with

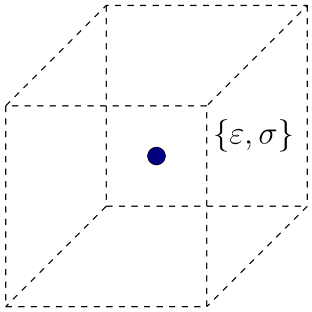

Figure 2.8: Representative Volume Element employed for the material calibration.

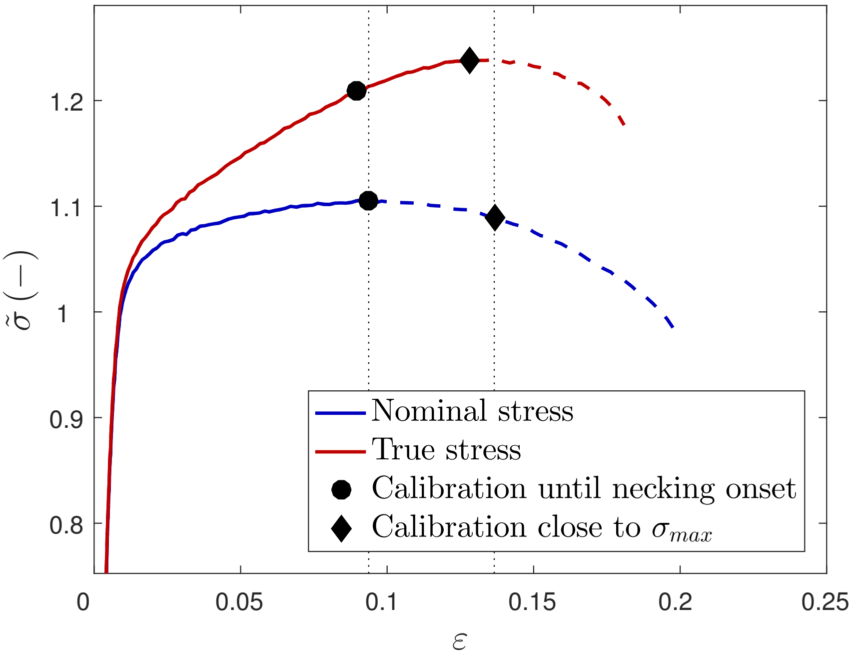

Figure 2.9: Stress vs. strain. Portion of the curves used in the calibration. $\dot{\varepsilon} \simeq 10^{-3}\,\mathrm{s}^{-1}$, $T = 25\,°\mathrm{C}$ and Rolling direction RD.

a maximum nominal stress value (following the Considère instability criterion [134]) as marked in Figure 2.9. However, by employing this method with an early necking offset, subsequent simulations using the smooth flat tension specimen are not only unable to reproduce a correct striction but they also yield an indefinite hardening in the nominal stress (largely different from the experimental data). In an attempt to reduce this effect, the limit strain of the curve employed during the calibration was extended in order to widen the strain range. The new limit was set close to the maximum true stress. As seen in Figure 2.9, this extra segment allowed the calibration to predict a more realistic hardening. This method was applied for all tension tests.

2.4.1.2 Choice of the anisotropic matrix

Regarding the 6x6 matrix used to transform the stress, two definitions can be here considered. On the one hand, a 6x6 matrix, denoted here as full matrix, defined as in Equation 2.31 comprises 9 independent parameters. It is to be noted that the coefficients A_{55} and A_{66} related to the shear along the normal direction are not calibrated and taken as one (see Equation 2.61). On the other hand, a reduced matrix containing only six coefficients (Equation 2.62), as the Hill criterion does, is employed considering the additional constrain $A_{i1}+A_{i2}+A_{i3}=1$ with $i=1,2,3$ from Equation 2.32 (see for instance, Stewart and Cazacu [130]). The full matrix definition is chosen for the material under consideration but the reduced form of the orthotropic matrix is here used for comparison purposes.

$$\underset{=}{A}_{full} = \begin{bmatrix} A_{11} & A_{12} & A_{13} & & & \\ A_{12} & A_{22} & A_{23} & & & \\ A_{13} & A_{23} & A_{33} & & & \\ & & & A_{44} & & \\ & & & & 1 & \\ & & & & & 1 \end{bmatrix} \quad (7\,\text{coeff.}) \tag{2.61}$$

$$\underset{=}{A}_{red} = \begin{bmatrix} 1-A_{12}-A_{13} & A_{12} & A_{13} & & & \\ A_{12} & 1-A_{12}-A_{23} & A_{23} & & & \\ A_{13} & A_{23} & 1-A_{13}-A_{23} & & & \\ & & & A_{44} & & \\ & & & & 1 & \\ & & & & & 1 \end{bmatrix} \quad (4\,\text{coeff.}) \tag{2.62}$$

Regarding the latter definition in Equation 2.62. The calibration package in Z-set offers several optimization algorithms accounting for constraints, however the Levenberg-Marquardt is not one of those [135]. It is needed to enforce this constraint by using the python script "*anisotropy.py*" in Figure 2.7. Before running the simulations and after the previous iteration update, the material file is modified accordingly with this script. With this method, only 4 anisotropy materials are calibrated for the reduced matrix.

2.4.1.3 Choice of the isotropic hardening

Before identifying the second order tensor modelling the anisotropy, one experimental curve is employed to find a temporary simple hardening law which can help identifying all the uniaxial experiments. Figure 2.10 shows a comparison of the Swift (power), Voce (exponential) and extended Voce (exponential plus a linear term) applied in the present material (see Table 2.3). The main inconvenient with the Voce law is the saturation which clearly does not follow the behaviour of the experimental data. The Voce plus linear term allows to better fit the results globally although greater errors are detected on the initial yield of the material (plus indefinite hardening at larger strains). Finally, the Swift law seems to provide the best fit of the experimental results.

2.4.1.4 Choice of the kinematic hardening

Regarding the kinematic hardening, two approaches were first tested: (i) an uncoupled isotropic and kinematic strategy where the C in Equation 2.54 is zero and (ii) a coupled strategy where such coefficient equals that of the kinematic hardening expression. Figure 2.11 shows the improvements made by coupling both types of hardening. By doing so, both the initial yield and the load reversal can be well reproduced without a significant loss of accuracy.

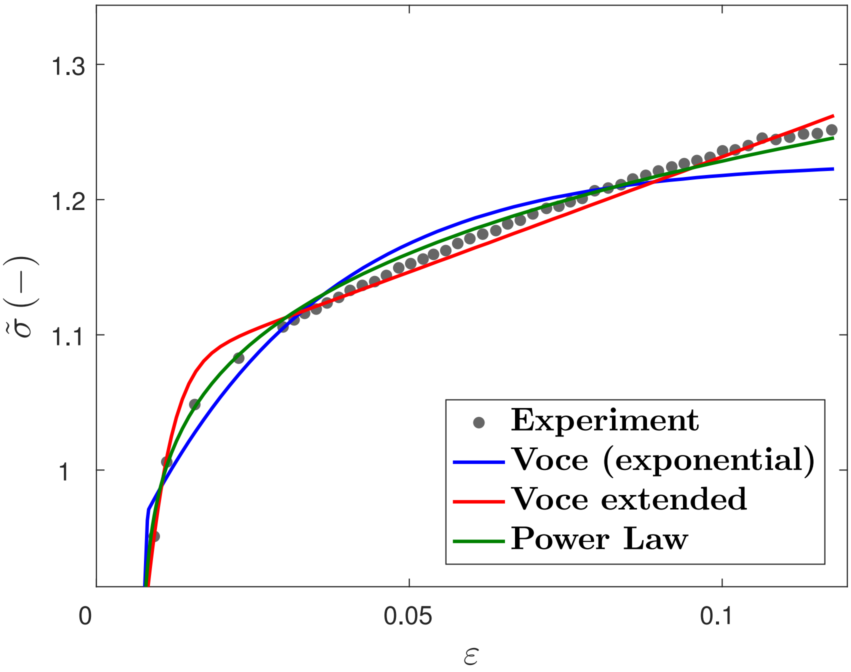

Figure 2.10: Stress vs. strain. Isotropic hardening laws comparison with the experimental data. $\dot{\varepsilon} \simeq 10^{-3}\,\mathrm{s}^{-1}$, $T = 25\,°\mathrm{C}$ and Rolling direction RD.

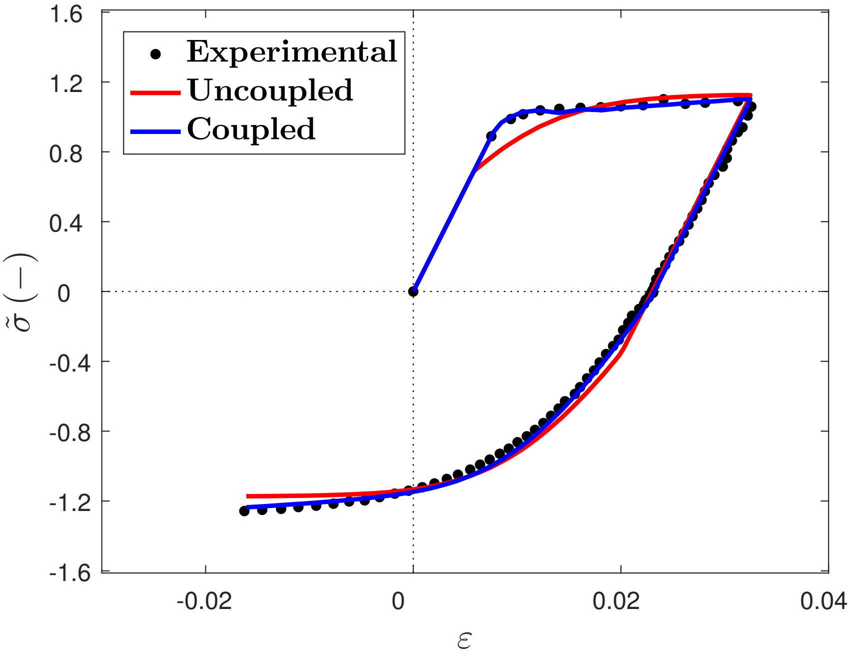

Figure 2.11: Stress vs. strain. Kinematic hardening laws comparison with the experimental data. $\dot{\varepsilon} \simeq 10^{-3}\,\mathrm{s}^{-1}$, $T = 25\,°\mathrm{C}$ and Rolling direction RD.

2.4.2 Step 1: Identification of the anisotropic plasticity related coefficients

In this first step, see Figure 2.6, coefficient k and the $\underline{\underline{A}}$ matrix components in Equation 2.61 are fitted (the value of a has been initially considered 2 and subsequent optimizations showed no significant impact on the calibration). For that purpose, the stress-strain tension and compression curves from the monotonic quasi-static tests run at $10^{-3}\,\mathrm{s}^{-1}$ are used.

A 6-substep procedure is followed in this Step 1 to identify the anisotropic plasticity related coefficients, see Figure 2.12. During the first substeps (1 to 3), the reduced matrix form is first considered due to the low number of coefficients involved. The first three diagonal terms (the off-side terms are defined by the constraint above mentioned) together with the strength differential parameter are first calibrated using the rolling RD, transverse TD and normal ND directions and the hardening values from Figure 2.10 in the preliminary section. Afterwards, the fourth diagonal term A_{44}, with the role of transforming the shear stress component, is identified. A full anisotropy matrix taking 7 coefficients plus the strength differential parameter k is calibrated using the reduced matrix results as the starter point for the calibration (substep 4). Finally, in substep 5, the hardening coefficients are re-identified and as a last substep, the new full and reduced matrix are again identified.

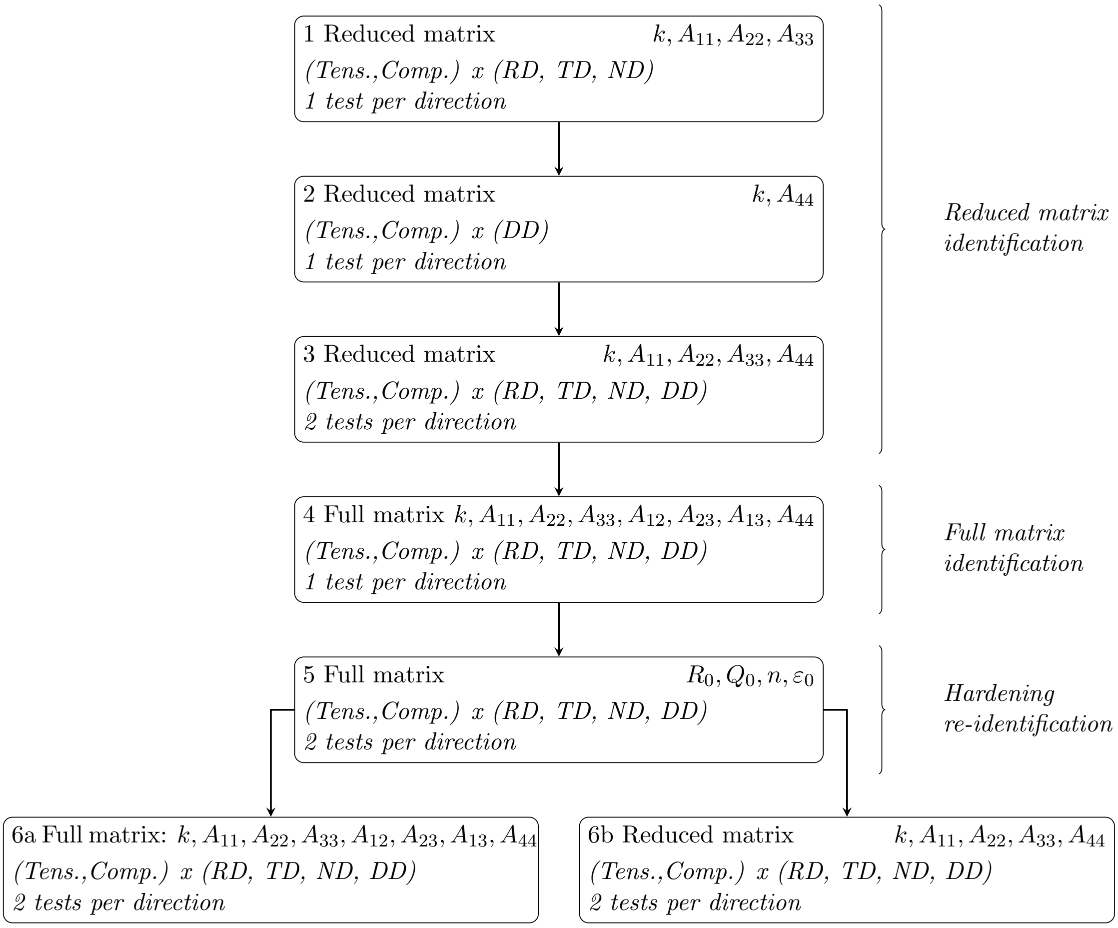

Figure 2.12: Anisotropic plasticity identification stages in step 1 (see Figure 2.6).

Figure 2.13 shows the result of the last step of the calibration considering both types of anisotropy matrices. Overall, the tension-compression differential is well captured as well as the orthotropy for both types of loadings. Differences between both types of matrices are mostly subtle except for the normal direction ND where the simple matrix produces a comparatively worse performance.

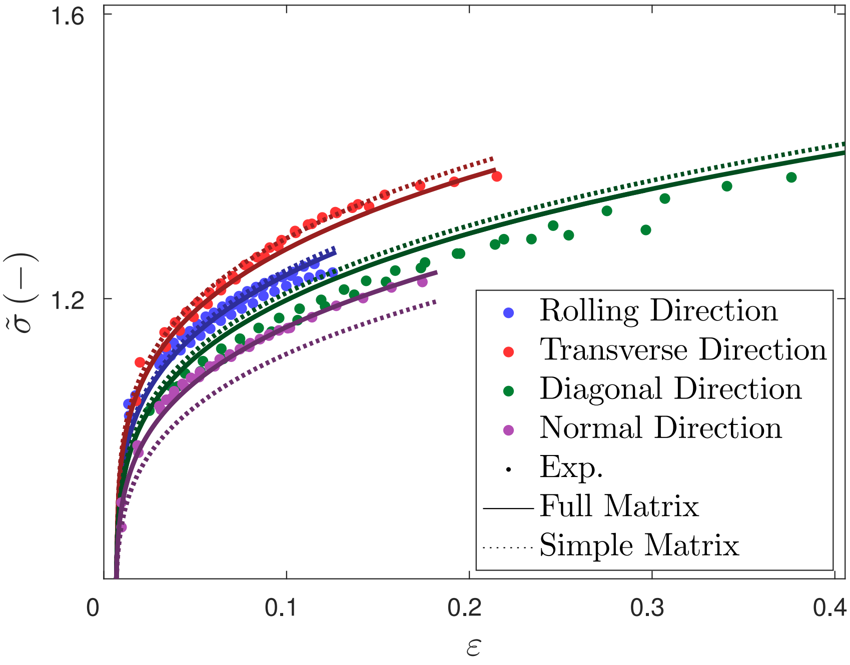

(a) Tension

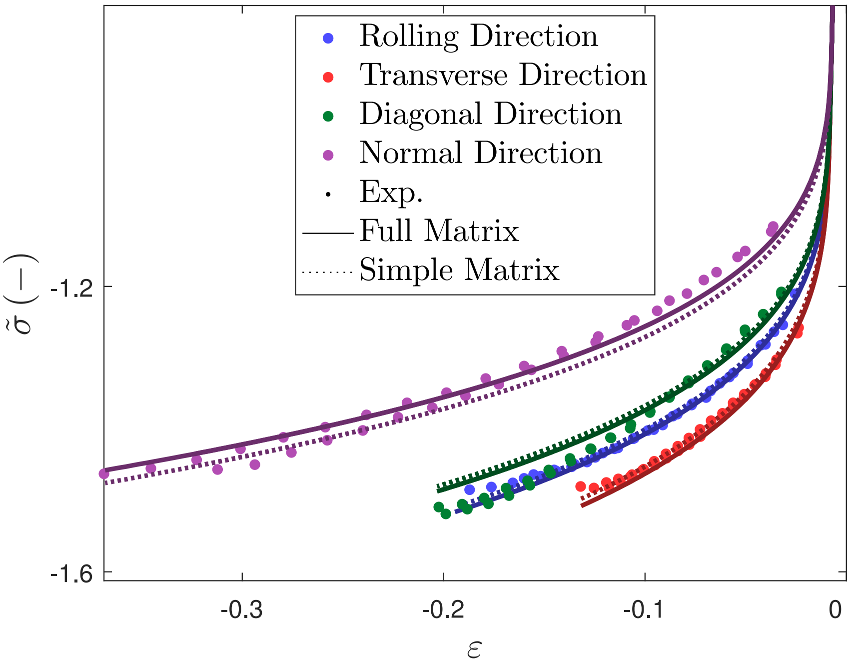

(b) Compression

Figure 2.13: Stress vs. strain. Anisotropic plasticity identification from step 1 (see Figure 2.6). $\dot{\varepsilon} \simeq 10^{-3}\,\mathrm{s}^{-1}$ and $T = 25\,°\mathrm{C}$.

The yield surface from both calibrations are plotted together with the experiment data in the TD-RD plane in Figure 2.14. The results are normalized with the yield stress. It can be seen that (i) the experimental anisotropy is overall well captured using both anisotropy strategies and (ii) no major differences are found between both surfaces except for the normal direction, where the calibrated surfaces is worse identified as above mentioned.

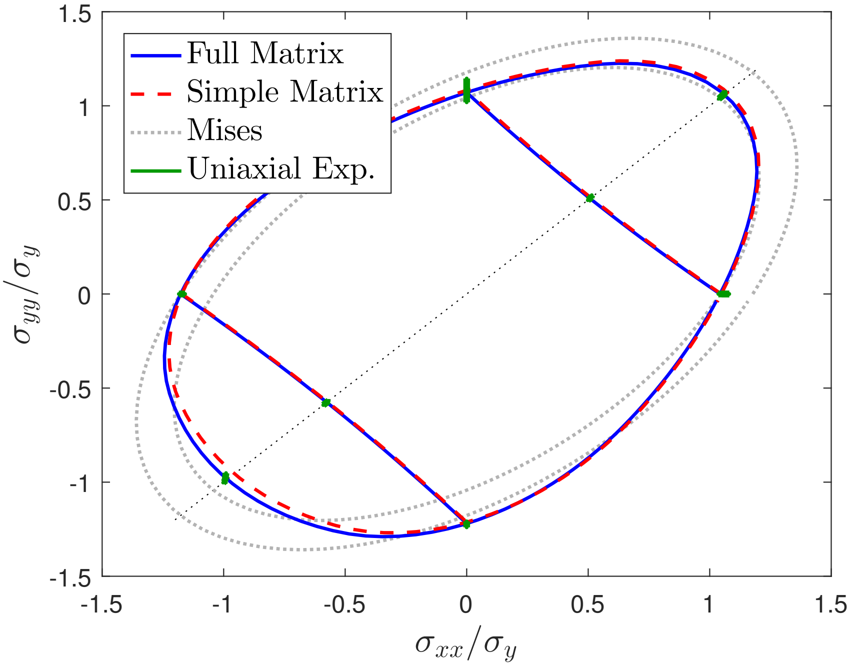

Figure 2.14: Calibrated yield locus in the $(TD - RD)$ plane from step 1 (see Figure 2.6). $\dot{\varepsilon} \simeq 10^{-3}\,\mathrm{s}^{-1}$ and $T = 25\,°\mathrm{C}$.

2.4.3 Step 2: Identification of the viscoplasticity related coefficients

The viscosity coefficients Y_v and n_v from Equation 2.57 are identified in this second step. As seen with the high strain rate tension test in Figure 1.23, the combined effect of self-heating induced softening at high strain rate and the poor camera resolution is responsible for a poor measurement of the hardening curves. For this reason, the viscosity identification uses only compression stress-strain curves from monotonic quasi-static and dynamic loading plus the tension curves in the quasi-static regime. Figure 2.15 shows a comparison with the identified numerical viscous model with the experimental data. Norton-Perzyna law in Equation 2.38 proves itself the right approximation to reproduce the overstress observed in the experiments.

Moreover, the tension yield stress in the dynamic regime (at low strains, i.e. before significant self-heating induced softening) which is not used for identification is well estimated.

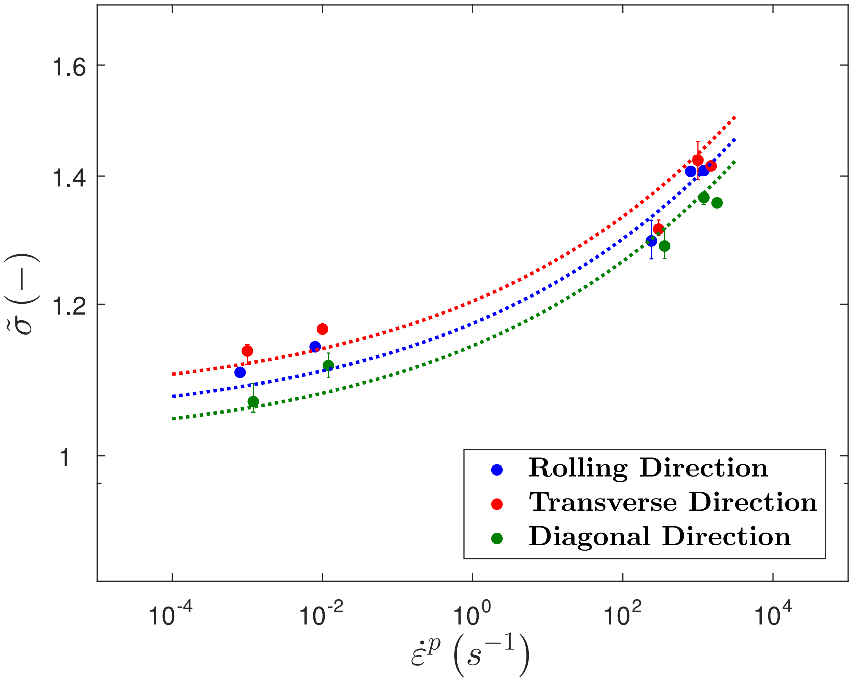

(a) Tension

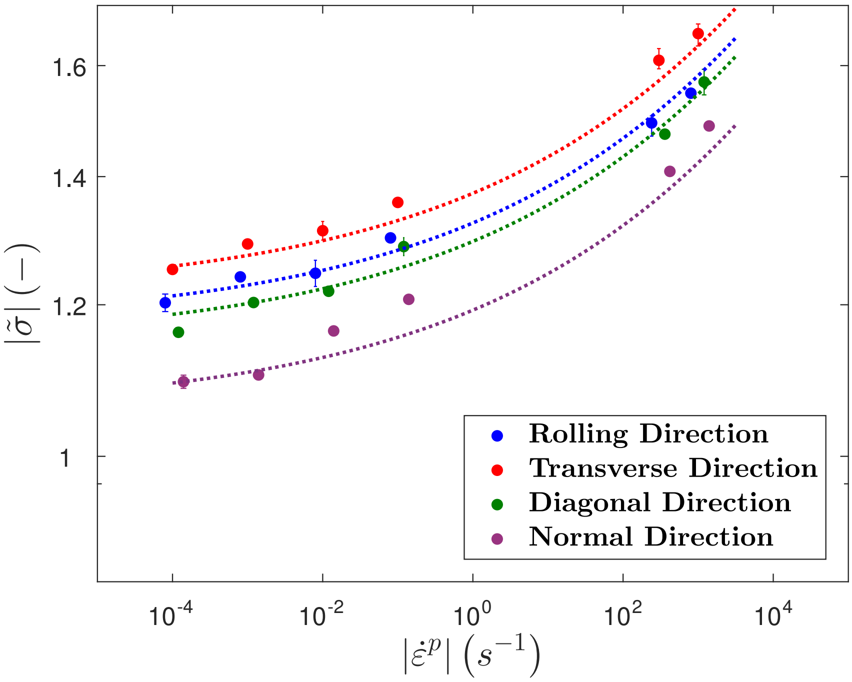

(b) Compression

Figure 2.15: Stress at 2 % plastic strain vs. plastic strain rate. Calibration of the strain rate dependence from step 2 (see Figure 2.6). $T = 25\,°\mathrm{C}$.

Figure 2.16 shows the results of the calibration along the rolling direction. It can be seen that the stress is well captured as well as its hardening for all the strain rate regimes.

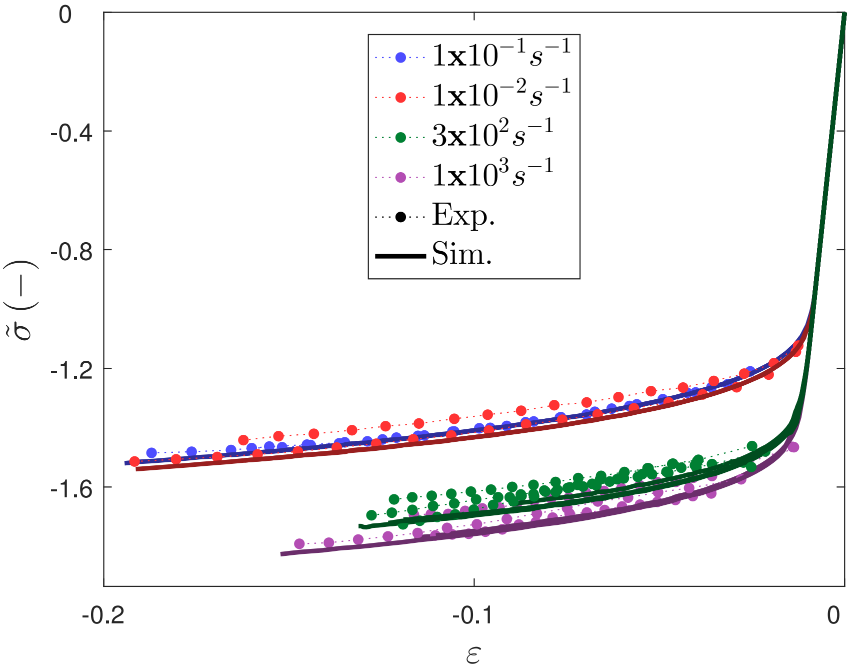

Figure 2.16: Stress vs. strain. Viscous stress comparison after calibration from step 2 (see Figure 2.6). $T = 25\,°\mathrm{C}$ and Rolling direction RD.

2.4.4 Step 3: Identification of the hardening and softening related coefficients

The last part of the identification is the mixed isotropic and kinematic hardening and thermal softening coefficients $R_0, K, n, C, D, m_T, T_{ref}$ from Equation 2.54. In order to ensure convergence to an optimal calibration, a 4-substep procedure was followed: first only the tension-compression along the rolling RD and transverse TD direction was used for the calibration. Secondly, the uniaxial experimental data were later added. The reverse loading along the diagonal direction DD and the uniaxial loading along the diagonal DD as well as the normal ND direction were considered (see Figure 2.17) in a third stage. Finally, the thermal softening related coefficients are calibrated.

Figure 2.18 summarizes the prediction capability of the model were both the monotonic and the reversed loadings are well fitted at room temperature.

Finally, the thermal softening is identified by fixing all the previous material coefficients. In order not to distort the results at room temperature a higher weight is imposed at this temperature. As shown in Equation 2.54, the thermal softening function uses three coefficients: the melting temperature of the material T_m, a reference temperature T_{ref} and the exponent coefficient m_T. Two approaches were used for the calibration of the temperature effect: an identification of m_T with $T_{ref} = 25\,°\mathrm{C}$ (Figure 2.19a) and an extended calibration fitting both m_T with T_{ref} (Figure 2.19b). The results show an overall satisfactory tendency for the tension loading with a slightly worse prediction for the compression. By fixing $T_{ref} = 25\,°\mathrm{C}$ no major errors are induced.

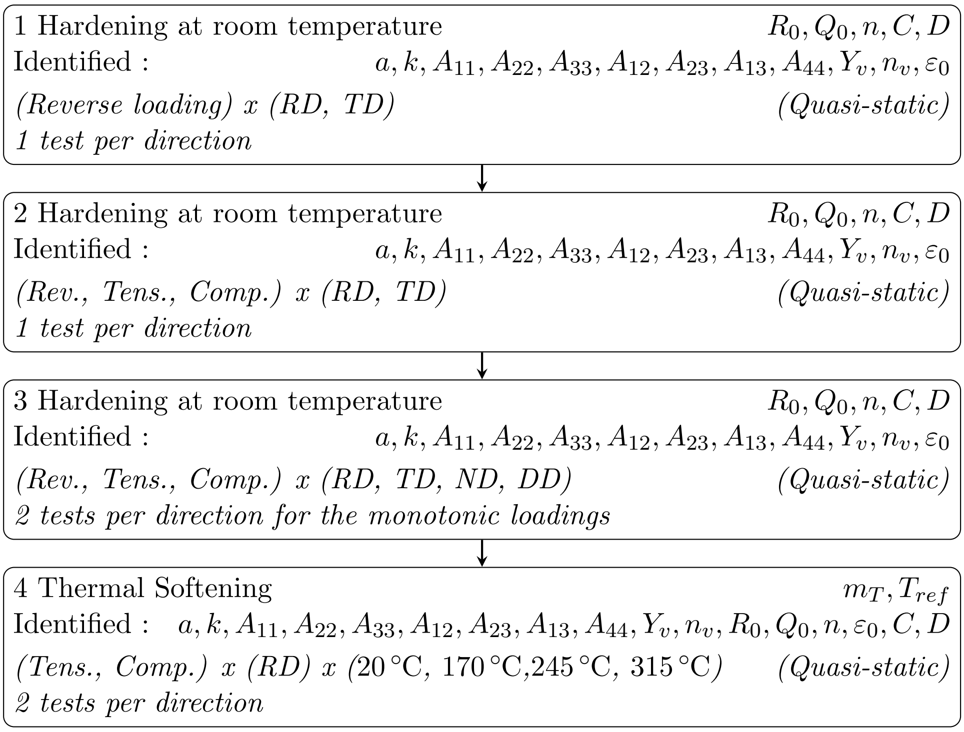

1 Hardening at room temperature R_0, Q_0, n, C, D
Identified : $a, k, A_{11}, A_{22}, A_{33}, A_{12}, A_{23}, A_{13}, A_{44}, Y_v, n_v, \varepsilon_0$
(Reverse loading) x (RD, TD) *(Quasi-static)*
1 test per direction

2 Hardening at room temperature R_0, Q_0, n, C, D
Identified : $a, k, A_{11}, A_{22}, A_{33}, A_{12}, A_{23}, A_{13}, A_{44}, Y_v, n_v, \varepsilon_0$
(Rev., Tens., Comp.) x (RD, TD) *(Quasi-static)*
1 test per direction

3 Hardening at room temperature R_0, Q_0, n, C, D
Identified : $a, k, A_{11}, A_{22}, A_{33}, A_{12}, A_{23}, A_{13}, A_{44}, Y_v, n_v, \varepsilon_0$
(Rev., Tens., Comp.) x (RD, TD, ND, DD) *(Quasi-static)*
2 tests per direction for the monotonic loadings

4 Thermal Softening m_T, T_{ref}
Identified : $a, k, A_{11}, A_{22}, A_{33}, A_{12}, A_{23}, A_{13}, A_{44}, Y_v, n_v, R_0, Q_0, n, \varepsilon_0, C, D$
*(Tens., Comp.) x (RD) x (*20 °C, 170 °C,245 °C, 315 °C*)* *(Quasi-static)*
2 tests per direction

Figure 2.17: Hardening identification stages from step 3 (see Figure 2.6).

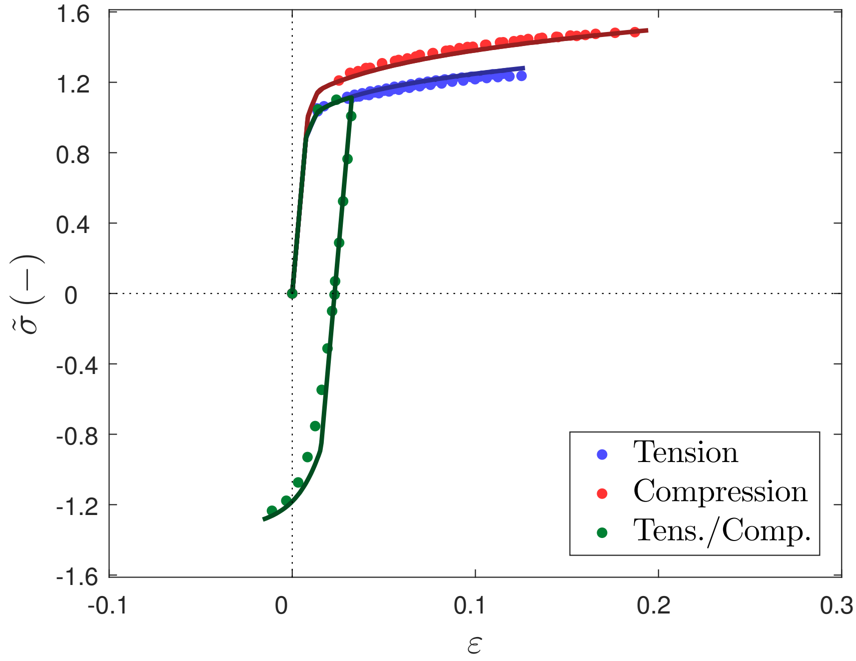

Figure 2.18: Stress vs. strain. Hardening calibration stages from step 3 (see Figure 2.6). $\dot{\varepsilon} \simeq 10^{-3}\,\mathrm{s}^{-1}$, $T = 25\,°\mathrm{C}$ and Rolling direction RD.

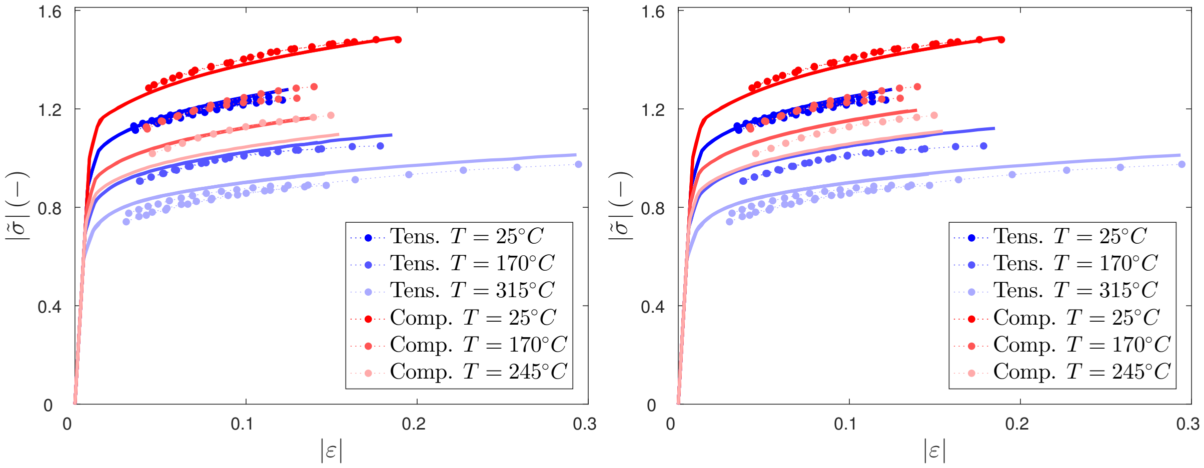

(a) $T_{ref} = 25\,°\mathrm{C}$ (b) T_{ref} to be calibrated

Figure 2.19: Stress vs. strain. Calibration of the thermal softening function from step 3 (see Figure 2.6). $\dot{\varepsilon} \simeq 10^{-3}\,\mathrm{s}^{-1}$ and Rolling direction RD.

It is noteworthy that the temperature used during the experiments are greater than or equal to the room temperature. For temperatures lower than $T_{ref} = 25\,°\mathrm{C}$, the thermal softening would not be defined. Under these conditions, the thermal softening function shall be 1 for temperatures lower than the reference temperature.

2.4.5 Comments

As explained in the Preliminary Considerations section 2.4.1, two anisotropy matrices were proposed. In Table 2.7, a comparison of the optimization error between both matrices during the three main stages in the calibration is shown. Initially, the cost function error is approximately 60 % higher for the reduced matrix identification. However, as the viscosity as well as the hardening are further identified, this difference is appreciably reduced as the errors concerning the anisotropy become less important to the accumulated error of the complete model calibration (anisotropy+viscoplastic+hardening).

Table 2.7: Comparison of the cost function after each stage for both types of matrices.

Stage	N° tests	Error Difference
Anisotropy	17	+59.63 %
Viscosity	61	+3.46 %
Hardening	20	+6.52 %

The three-step calibration strategy from Figure 2.6 has allowed the identification of the material by small groups of coefficients minimizing the risk of initial value dependence.

2.5 Concluding remarks

The extensive experimental campaign detailed in the previous section has evidenced that the Ti-6Al-4V grade under consideration is subject to significant (i) anisotropic plasticity which manifests through loading direction dependence, kinematic hardening and strength differential, (ii) isotropic strain hardening, (iii) rate dependence and (iv) thermal softening. The irreversible thermodynamics framework combined with a finite strain formulation has been here employed to build a constitutive model that reproduces the mechanical behavior observed in the previous chapter.

The plastic yielding condition is defined through a yield criterion and a plastic potential accounting for the anisotropy of the material (non associated plasticity). This is done with an extended definition of the equivalent stress proposed by Karafillis and Boyce [72] and Cazacu et al. [73].

The additional complementary laws used to close the problem are the Norton viscoplastic law, a non-linear coupled mixed hardening and a consistent temperature evolution related to the plastic dissipation.

The model has been satisfactorily identified by using the uniaxial tension and compression experimental data, leaving the notched, tension-induced shear and hat-shaped specimens for verification purposes. Due to the large quantity of material constants present in the model, a three-step identification procedure has been carried out. The anisotropy was first calibrated followed by the viscous component and final hardening contribution (thermal softening included). Although the error slightly increases as new coefficients are considered in the model, the overall performance reproduces all the experimental data. Some deviations may be found related to the viscosity at high strain rates as well as high temperatures.

Accounting for damage and/or localization is to be considered in future works.

CHAPTER 3

Numerical simulation

Abstract

The implementation of the numerical version of the model as a user material subroutine in the commercial finite element code LS-DYNA is here presented. The constitutive model previously proposed is integrated employing an explicit time integration scheme and the elastic prediction-plastic correction method is detailed. Simulations on Representative Volume Elements (RVE) are carried out to compare the performance of the subroutine coded in LS-DYNA with respect to another software (Z-set). Finite Element models of the geometries utilized during the experimental campaign are carried out to asses the validity of the numerical model at the scale of a structure with respect to experimental data.

Contents

3.1 Introduction

This section aims at showing the numerical procedure used to implement the material constitutive equations as a user material subroutine in a commercial finite element code (LS-DYNA). As a preamble, a few comments are done regarding the numerical strategies available in literature. Afterwards, an explicit time integration algorithm of the constitutive rate equations is proposed. A verification on two levels is then conducted: first at the representative volume element scale, where the code performance (in LS-DYNA) is compared to Z-set commercial software (previously used for the material constants calibration); second, at the specimen level, where validation is made by comparing the different experimental results with the corresponding numerical simulations. Finally, some conclusions on the code's applicability are drawn.

The Finite Element explicit code LS-DYNA has been chosen for the implementation of the constitutive models as it is largely used in the industry. Explicit codes are well suited for solving initial-boundary value problems involving high speed phenomena such as the bird strike ingestion [136]. In addition, LS-DYNA allows for the definition of user coded constitutive models and the coupling with other formulations such as the SPH (Smoothed-Particle Hydrodynamics) elements.

3.2 Some comments on the numerical integration

An initial-boundary value problem (IBVP) involving spatial quantities may be written in the condensed form:

$$\text{Equilibrium Eq.} \qquad \underline{\underline{M}}\,\dot{\underline{v}} + \underline{F}^{int}\left(\underline{x}, \underline{v}, t\right) - \underline{F}^{ext}\left(\underline{x}, \underline{v}, t\right) = 0 \quad \text{on} \quad \Omega \tag{3.1a}$$

$$\text{Kinematic Eq.} \qquad \underline{\underline{l}} = \frac{\partial \underline{v}\left(\underline{x}\right)}{\partial \underline{x}} \quad \text{on} \quad \Omega \tag{3.1b}$$

$$\text{Constitutive Eq.} \qquad \overset{\nabla}{\underline{\underline{\sigma}}} = \mathcal{L}\left(\underline{\underline{l}}\right) \quad \text{on} \quad \Omega \tag{3.1c}$$

$$\text{Boundary Cond.} \qquad \underline{v} = \underline{v}^{g} \quad \text{on} \quad \partial\Omega_u \quad \text{and} \quad \underline{\underline{\sigma}} \cdot \underline{n} = \underline{T}_g \quad \text{on} \quad \partial\Omega_T \tag{3.1d}$$

$$\text{Initial Cond.} \qquad \mathcal{X}\left(t = 0\right) = \mathcal{X}_0 \tag{3.1e}$$

where $\underline{x}$ is the position, $\underline{v}$ the velocity and t the time. $\mathcal{L}(\cdot)$ is a generic constitutive function, Ω the whole volume under consideration, $\partial\Omega$ its boundary. Finally, $\underline{n}$ is the normal to the boundary, $\underline{v}^g$ is a prescribed velocity field on the boundary and $\underline{T}^g$ a prescribed force on the boundary.

When complex geometries or/and loadings are involved, the solution to this problem is obtained by numerical means. The above mentioned equations have then to be discretized in space and in time.

3.2.1 Spatial discretization

The Finite Element method, well adapted to solve the IBVP involving structures, is chosen here for the spatial discretization [137]. The field variables, like the displacement, are approximated as

$$\underline{u}\left(\underline{x},t\right) \simeq \underline{\tilde{u}}\left(\underline{x},t\right) = \underline{\underline{N}}\left(\underline{x}\right)\underline{\hat{u}}\left(t\right) \tag{3.2}$$

where the continuous displacement $\underline{u}$ is assumed to be approximated by the discrete one $\underline{\tilde{u}}$ which is computed through interpolation of the displacements $\underline{\hat{u}}\left(t\right)$ at the nodes with an interpolation function $\underline{\underline{N}}\left(\underline{x}\right)$, the definition of which is dependent on the element formulation.

The mass matrix $\underline{\underline{M}}$, the internal and external forces F^{int} and F^{ext} in Equation 3.1a can be rewritten involving the previous notation as [137]

$$\begin{cases} \underline{\underline{M}} = \displaystyle\int_{\Omega} \rho \underline{\underline{N}}^{T}\left(\underline{x}\right)\underline{\underline{N}}\left(\underline{x}\right) d\Omega \\ \underline{F}^{int} = \displaystyle\int_{\Omega} \rho \underline{\underline{B}}^{T}\left(\underline{x}\right) : \underline{\sigma} d\Omega \\ \underline{F}^{ext} = \displaystyle\int_{\Omega} \rho \underline{\underline{N}}^{T}\left(\underline{x}\right)\underline{\hat{b}} d\Omega + \int_{\partial\Omega} \underline{\underline{N}}^{T}\left(\underline{x}\right)\underline{\hat{t}} dS \end{cases} \tag{3.3}$$

where the operator $\underline{\underline{\underline{B}}}$ is built from the partial derivations of the shape functions so that $\underline{\varepsilon} = \underline{\underline{\underline{B}}}\,\underline{\hat{u}}$. $\underline{\hat{b}}$ and $\underline{\hat{t}}$ are the body and surface forces at the nodes respectively.

The solution to these integrals is generally solved numerically using the Gaussian quadrature, i.e. it is approximated by a weighted sum of the function to integrate at specific points g as

$$\int_{-1}^{1} f\left(x\right) dx \simeq \sum_{g=1}^{GP} w_g f\left(x_g\right) \tag{3.4}$$

By using g-points of the Gaussian quadrature, the integration yields an exact solution for polynomials of a degree of $2g-1$. For instance, in the case of an eight-node 3D solid element, eight Gauss or integration points are sufficient to obtain an exact integration of a linear shape function.

Three 3D solid element types are available in LS-DYNA (see [138]):

elform 1 Reduced integration (R), i.e. a single integration point located at the center of the element

elform 2 Selectively reduced (S/R) integration 8-node solid element (8 integration points but assumption of constant pressure throughout the element)

elform 3 Fully integrated (F) quadratic 8-node with nodal rotation (equivalent of a 20-node quadratic element)

The reduced integration formulation (R) has the lowest computational cost. It is easily subject to hourglass (spurious deformation modes) but prevents any shear locking (stiffer numerical solution) ocurring in coarse meshes. The selectively reduced (S/R) formulation uses eight integration nodes, implying a higher computational time. However, with this strategy, the pressure is considered constant throughout the element avoiding volume locking [139]. Finally, the quadratic 8-node solid element (F) considers the nodal rotations as extra degrees of freedom [140]. This last formulation sensibly increases the computational cost and it can be subject to volume locking near incompressible states.

In the present work, the second formulation, i.e. S/R fomulation, is used as a compromise between time efficiency and precision. However, a comparison of the different formulations will be later shown.

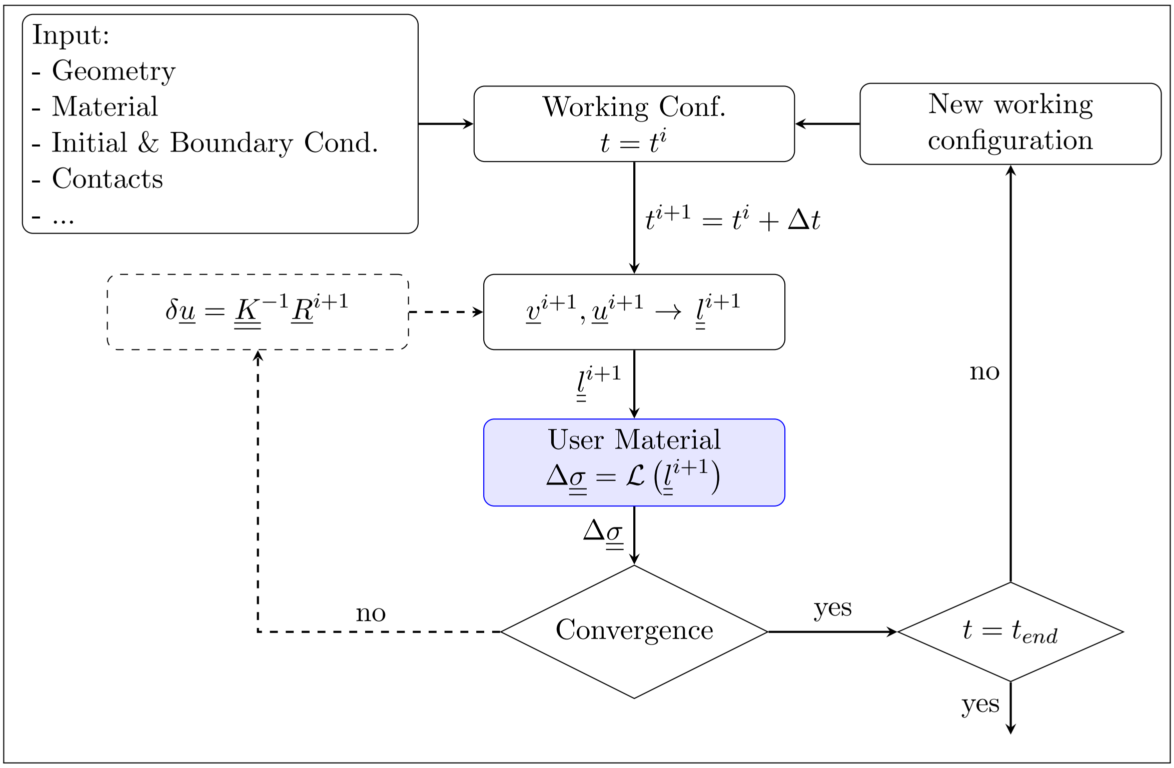

Figure 3.1: Flow chart for the time integration of the equilibrium and constitutive equations (LS-DYNA).

3.2.2 Time discretization

Regarding the time discretization, the Finite Difference method is employed. Figure 3.1 shows a schematic flowchart of the algorithm used to integrate the solution at every time increment. The algorithm comprises first, an integration of the equilibrium equation where the velocity/displacement field, and hence, the strain rate/strain field is computed. Secondly, the integration of the constitutive equations is done by updating the stress field (blue box in Figure 3.1). This chapter is focused on the latter with the proposition of an explicit user-coded material for the LS-DYNA software that takes as input the strain field computed from the equilibrium equations and gives as output an updated stress.

3.2.2.1 Time integration of the equilibrium equations

Motivated by the Taylor series expansion, numerical schemes such as Newmark's provide a numerical approximation of the displacement as a function of its derivatives and second derivatives at a given discretized time instants t^i [141].

$$\begin{cases} \underline{v}^{i+1} = \underline{v}^i + \Delta t \left[(1-\gamma)\, \dot{v}^i + \gamma \dot{v}^{i+1} \right] \\ \underline{x}^{i+1} = \underline{x}^i + \Delta t \underline{v}^i + \Delta t^2 \left[\left(1 - \dfrac{\beta}{2} \right) \dot{v}^i + \beta \dot{v}^{i+1} \right] \end{cases} \tag{3.5}$$

where Δt is the time increment and β and γ are numerical coefficients of the algorithm. For values $\beta = 1/4$ and $\gamma = 1/2$ the algorithm is implicit and unconditionnaly stable [141]. For $\beta = \gamma = 0$ an explicit expression is obtained.

LS-DYNA uses the explicit Central Difference Scheme (CDS) defined as [138]

$$\begin{cases} \underline{v}^{i+\frac{1}{2}} = \underline{v}^{i-\frac{1}{2}} + \Delta t \dot{\underline{v}}^{i} \\ \underline{x}^{i+1} = \underline{x}^{i} + \Delta t \underline{v}^{i+\frac{1}{2}} \end{cases} \tag{3.6}$$

Contrary to implicit schemes, the central difference scheme is conditionally stable and the time increment must satisfy the Courant–Friedrichs–Lewy condition [142].

$$\Delta t < \Delta t_{CFL} = \frac{l_e}{\tilde{c}} \tag{3.7}$$

where l_e is a characteristic length (typically the minimum element size) and $\tilde{c}$ the maximum wave speed defined as

$$\tilde{c} = \sqrt{\frac{E\left(1-\nu\right)}{\rho\left(1+\nu\right)\left(1-2\nu\right)}} \tag{3.8}$$

By default, the commercial software LS-DYNA uses an explicit integration of the rate equations although an implicit formulation is also available.

3.2.2.2 Time integration of the rate constitutive equations

Regarding the time integration of the rate constitutive equations, two aspects are worth considering: the numerical method, i.e. explicit/implicit, and the frame indifference, i.e. the objectivity notably.

As explained in Longere [123] there are two main methods to integrate the rate quantities: by working in the current configuration or by working in a Q-rotated frame.

Global frame objective update

The time integration is directly done in the current configuration using Equation 2.14

$$\dot{\underline{\underline{\sigma}}} = \overset{\nabla}{\underline{\underline{\sigma}}} + \underline{\underline{W}}\,\underline{\underline{\sigma}} - \underline{\underline{\sigma}}\,\underline{\underline{W}} \tag{3.9}$$

where the spin $\underline{\underline{W}}$ has been approximated here to the skew-symmetric part of the velocity gradient $\underline{\underline{\omega}}$ (see Equation 2.16). The term corresponding to the objective rate can be directly computed from the constitutive equations (see Hughes and Winget [122]). The time derivative has then the form

$$\dot{\underline{\underline{\sigma}}} = \mathcal{L}\left(\underline{\underline{d}}\right) + \underline{\underline{\omega}}\,\underline{\underline{\sigma}} - \underline{\underline{\sigma}}\,\underline{\underline{\omega}} \tag{3.10}$$

After discretization of Equation 3.10, the stress update between two time increments $t^i \rightarrow t^{i+1}$ is composed of the sum of two components as

$$\begin{aligned} \underline{\underline{\sigma}}^{i+1} &= \underline{\underline{\sigma}}^{i} + \Delta \underline{\underline{\sigma}}^{PC} + \underline{\underline{r}}^{*} \\ &= \underline{\underline{\sigma}}^{i} + \Delta t \mathcal{L}\left(\underline{\underline{l}}^{i}\right) + \left(\underline{\underline{\omega}}^{*}\underline{\underline{\sigma}}^{*} - \underline{\underline{\sigma}}^{*}\underline{\underline{\omega}}^{*}\right) \end{aligned} \tag{3.11}$$

where the first term is computed by means of a prediction-correction algorithm (see the method in Section 3.3) and the second is an *objective correction*. The instant $\cdot^{*}$ can refer to the previous time step t^i, the next one t^{i+1} or something in between $i+\alpha$ with $\alpha \in [0,1]$. In the case of LS-DYNA, the known time instant t^i is chosen for the objective integration.

Local frame objective update

In the case of a material having frame dependent properties, it can be more convenient to work in the Q-rotated frame (see Vadillo et al. [125]). With this approach the variables such as the stress or strain tensors are rotated before the material integration and rotated back after the stress update with a rotation $\underline{\underline{Q}}$. With this strategy, the constitutive equations are expressed as

$$\dot{\underline{\underline{\sigma}}}_Q = \underline{\underline{Q}}^T \overset{\nabla}{\underline{\underline{\sigma}}} \underline{\underline{Q}} = \underline{\underline{Q}}^T \mathcal{L}\left(\underline{\underline{l}}\right) \underline{\underline{Q}} \tag{3.12}$$

For the case where $\overset{\nabla}{\underline{\underline{\sigma}}} = \underline{\underline{\underline{\underline{C}}}} : \underline{\underline{d}}$, the above equation can be rewritten as

$$\dot{\underline{\underline{\sigma}}}_Q = \underline{\underline{\underline{\underline{C}}}}_Q : \underline{\underline{d}}_Q \tag{3.13}$$

where both the stress tensor, strain tensor and the tangent operator $\underline{\underline{\underline{\underline{C}}}}$ have been rotated to a reference configuration.

If the spin $\underline{\underline{W}}$ is explicitly known but not $\underline{\underline{Q}}$, the rotation matrix is related to its spin tensor as

$$\dot{\underline{\underline{Q}}} = \underline{\underline{W}}\,\underline{\underline{Q}} \tag{3.14}$$

The integration of which can be done as [123]

$$\underline{\underline{Q}}^{n+1} = \underline{\underline{K}}^{n+\alpha} \underline{\underline{Q}}^{n} \quad \text{with} \quad \underline{\underline{Q}}^{0} = \underline{\underline{I}} \tag{3.15}$$

where the tensor $\underline{\underline{K}}$ is function of the spin as

$$\underline{\underline{K}}^{n+\alpha} = \left[\underline{\underline{I}} - \frac{1}{2}\underline{\underline{\omega}}^{n+\alpha}\Delta t\right]^{-1} \left[\underline{\underline{I}} + \frac{1}{2}\underline{\underline{\omega}}^{n+\alpha}\Delta t\right] \tag{3.16}$$

where the parameter α is generally taken as $1/2$ (mid-point rule).

Therefore, the stress update rotation would be composed of three steps:

Rotation to reference frame $\underline{\underline{\sigma}}^n_Q = \underline{\underline{Q}}^{nT} \underline{\underline{\sigma}}\, \underline{\underline{Q}}^n$, $\Delta\underline{\underline{\varepsilon}}_Q = \underline{\underline{Q}}^{nT} \Delta\underline{\underline{\varepsilon}}\, \underline{\underline{Q}}^n$ and other frame-dependent variables.

Integration in the local frame $\underline{\underline{\sigma}}^{n+1}_Q = \underline{\underline{\sigma}}^n_Q + \Delta\underline{\underline{\sigma}}_Q = \underline{\underline{\sigma}}^n_Q + \mathcal{L}_Q\left(\Delta\underline{\underline{\varepsilon}}_Q\right)$ and $\underline{\underline{Q}}^{n+1} = \underline{\underline{K}}^{n+\alpha} \underline{\underline{Q}}^n$

Rotation to global frame $\underline{\underline{\sigma}}^{n+1} = \underline{\underline{Q}}^{n+1} \underline{\underline{\sigma}}^{n+1}_Q \underline{\underline{Q}}^{n+1T}$ and other frame dependent variables.

3.3 Numerical implementation

Figure 3.2 shows the flowchart of the algorithm followed in the user material proposed here. The numerical time integration of the constitutive equations takes place in the co-rotational frame. This means a push forward operation has been previously performed [123]. The strategy used to integrate the equations is based on a two-step elastic prediction-plastic correction algorithm [143].

In case of elasto-plastic evolution, the method followed for the stress integration is the predictor-corrector algorithm. The linear (elastic) stress is first calculated followed by a (plastic) correction, if needed, by means of return algorithms aiming at ensuring the plastic yield condition [143]. Although the elastic prediction is usually straight forward, the plastic correction is generally a non linear problem and various strategies can be adopted.

For instance, in the case of rate independent plasticity, the stress update from an elastic prediction to a projected solution onto the yield surface reduces to a root-finding problem of the type

$$f\left(\sigma^{n+1}\right) = 0 \tag{3.17}$$

which can be integrated by using implicit [144], explicit [145 ; 146] or mixed schemes [147]. A comparison of some stress integration algorithms can be seen in Safaei et al. [148].

For rate dependent problems, a consistent formulation of the type $\tilde{f} = f - \sigma_v = 0$ can be similarly solved as explained above [125]. Alternatively, the internal variable can be directly integrated from the Perzyna formulation [62]

$$\dot{\kappa} = \tilde{f}\left(\sigma^{n+1}\right) \tag{3.18}$$

In this chapter, an integration of the Perzyna approach is presented. An explicit strategy is employed as it has been done with the equilibrium equations by LS-DYNA.

The user material main input provided by LS-DYNA is the total strain increment $\Delta\underline{\underline{\varepsilon}}$ between times t^i and t^{i+1} deduced from the equilibrium equations. In the present case, it can be composed of four different contributions: (i) elastic $\Delta\underline{\underline{\varepsilon}}^e$, (ii) plastic $\Delta\underline{\underline{\varepsilon}}^p$, (iii) strain related to temperature under isothermal conditions $\Delta\underline{\underline{\varepsilon}}^T_{iso}$, i.e. a global external temperature, and (iv) due to the adiabatic self-heating of the material $\Delta\underline{\underline{\varepsilon}}^T_{adia}$:

$$\Delta\underline{\underline{\varepsilon}} = \Delta\underline{\underline{\varepsilon}}^e + \Delta\underline{\underline{\varepsilon}}^p + \frac{1}{3}\Delta\varepsilon^T_{iso}\underline{\underline{I}} + \frac{1}{3}\Delta\varepsilon^T_{adia}\underline{\underline{I}} \tag{3.19}$$

Furthermore, it can be split in a volumetric part (not playing a role in the viscoplastic problem here defined) and a deviatoric part.

$$\begin{cases} \Delta\varepsilon_v = trace\left(\Delta\underline{\underline{\varepsilon}}\right) = trace\left(\Delta\underline{\underline{\varepsilon}}^e\right) + \Delta\varepsilon^T_{iso} + \Delta\varepsilon^T_{adia} \\ \Delta\underline{\underline{\varepsilon}}_{dev} = \Delta\underline{\underline{\varepsilon}}^e_{dev} + \Delta\underline{\underline{\varepsilon}}^p_{dev} \end{cases} \tag{3.20}$$

The constitutive rate equations in Equation 2.53 in Chapter 2, can be accordingly expressed with this volumetic/deviatoric splitting as

$$\begin{cases} \dot{p} = -K\dot{\varepsilon}_v + 3\alpha K\dot{T} = K\left(\dot{\varepsilon}^T - \dot{\varepsilon}_v\right) \\ \dot{\underline{\underline{s}}} = 2\mu\dot{\underline{\underline{\varepsilon}}}^e_{dev} \end{cases} \quad \rightarrow \quad \begin{cases} \Delta p = K\left(\Delta\varepsilon^T_{iso} + \Delta\varepsilon^T_{adia} - \Delta\varepsilon_v\right) \\ \Delta\underline{\underline{s}} = 2\mu\Delta\underline{\underline{\varepsilon}}^e_{dev} \end{cases} \tag{3.21}$$

where $\dot{\varepsilon}^T = 3\alpha\dot{T} = 3\alpha\left(\dot{T}_{iso} + \dot{T}_{adia}\right)$ and therefore, the related thermal strain increments are $\Delta\varepsilon^T_{iso} = 3\alpha\Delta T_{iso}$ and $\Delta\varepsilon^T_{adia} = 3\alpha\Delta T_{adia}$.

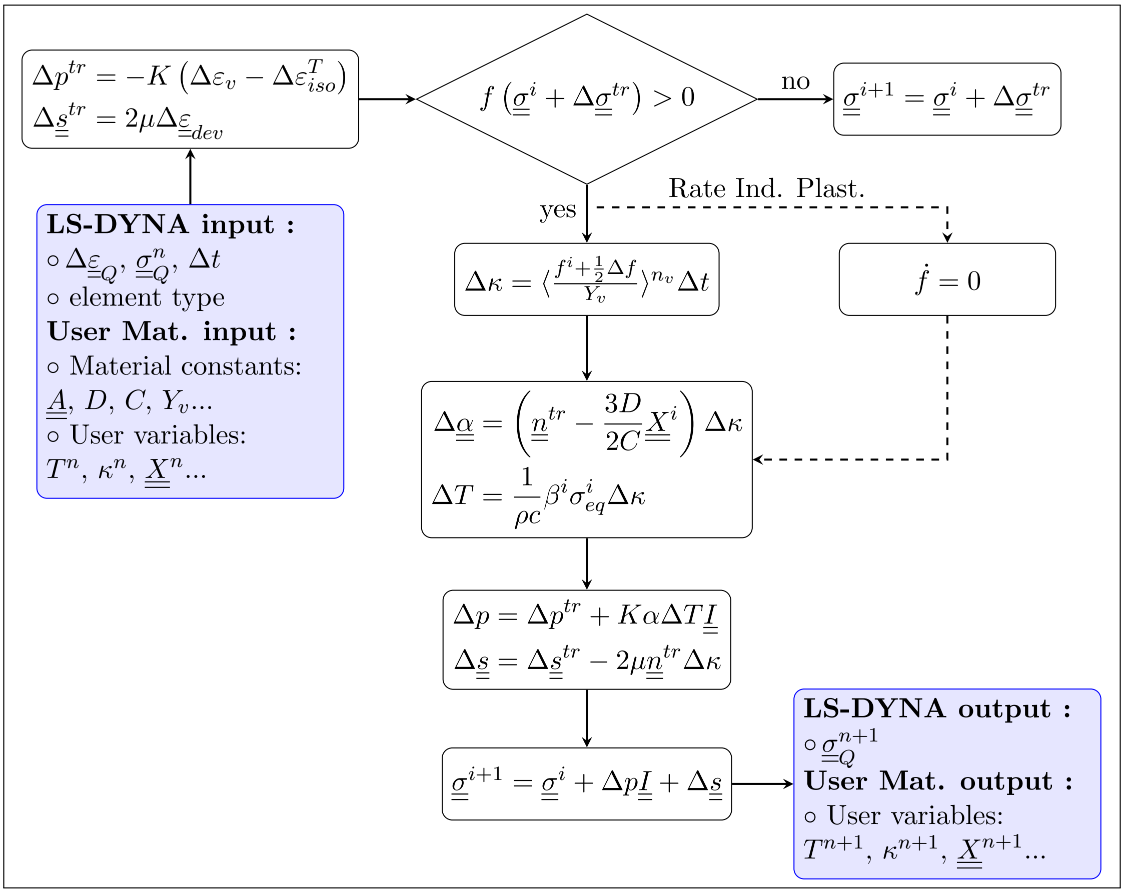

Figure 3.2: Flow chart of the time integration of the rate constitutive equations. The Q notation is dropped within the algorithm. Note that the rate independent plasticity and viscoplasticity formulations are allowed.

Elastic prediction: $\Delta\underline{\underline{\varepsilon}}^p = \Delta\varepsilon^T_{adia}\underline{\underline{I}} = \underline{\underline{0}}$ **and** $\Delta\varepsilon^T_{iso} = 3\alpha\left(T^{i+1}_{iso} - T^i_{iso}\right)$

In the scenario where such time increment is purely elastic, the plastic strain as well as the adiabatic thermal component are zero $\Delta\underline{\underline{\varepsilon}}^p = \frac{1}{3}\Delta\varepsilon^T_{adia}\underline{\underline{I}} = \underline{\underline{0}}$. However, the isothermal strain increment is related to the increment in the external temperature $\Delta\varepsilon^T_{iso} = 3\alpha\left(T^{i+1}_{iso} - T^i_{iso}\right)$. The constitutive rate equations discretized in Equation 3.21 can be explicitly calculated and the stress can be updated as

$$\begin{cases} \Delta p = -K\Delta\varepsilon^e_v = -K\left(\Delta\varepsilon_v - \Delta\varepsilon^T_{iso}\right) \\ \Delta\underline{\underline{s}} = 2\mu\Delta\underline{\underline{\varepsilon}}^e_{dev} = 2\mu\Delta\underline{\underline{\varepsilon}}_{dev} \end{cases} \xrightarrow[\text{prediction}]{\text{elastic}} \begin{cases} p^{trial} = p^i + \Delta p \\ \underline{\underline{s}}^{trial} = \underline{\underline{s}}^i + \Delta\underline{\underline{s}} \end{cases} \tag{3.22}$$

The validity of the elastic increment is verified. If $f\left(\underline{\underline{s}}^{trial}\right) < 0$ from Equation 2.55, the updated stress becomes the solution for the next increment $\underline{\underline{\sigma}}^{i+1} = \underline{\underline{\sigma}}^{trial}$.

Plastic correction $\Delta\underline{\underline{\varepsilon}}^p \neq \underline{\underline{0}}, \Delta\varepsilon^T_{adia} \neq \underline{\underline{0}}$

If the yield function is lower than zero, the increment is elastic and the constitutive equations have been successfully integrated. Otherwise, the increment is elastic-viscoplastic and a correction must be made.

Two cases are here considered in the user material: a viscoplastic formulation (where the material constant Y_v from Equation 2.57 is not zero in the user material) and rate independent plasticity (where the input variable $Y_v = 0$ in the user material).

The plastic correction entails a return mapping algorithm where the stress is corrected based on an estimated plastic strain. Equation 3.21 is used to integrate the stress as a function of the strain components as

$$\begin{aligned} p^{n+1} &= p^n + K\left(\Delta^T_{iso} + \Delta^T_{adia} - \Delta\varepsilon_v\right) \\ &= p^{trial} + K\alpha\Delta T\left(\Delta\kappa\right) \\ \underline{\underline{s}}^{n+1} &= \underline{\underline{s}}^n + 2\mu\left(\Delta\varepsilon - \Delta\varepsilon^p\right) \\ &= \underline{\underline{s}}^{trial} - 2\mu\underline{\underline{n}}^*\Delta\kappa \end{aligned} \tag{3.23}$$

where the notation $\cdot^*$ refers to the arbitrary instant at which the normal direction is calculated. In the code, the normal direction will be considered at the instant after the elastic prediction $\underline{\underline{n}}^{trial}$. As seen in Potts and Gens [149], the errors induced by this choice has a negligible influence on the return mapping of the stress state.

· *Rate Dependent Plasticity*

The plastic correction is carried out with a direct integration of the Perzyna formulation in Equation 2.57 (see [62]). The yield surface value to be used here is a first order approximation based on its value at the time instant $t^{i+1/2}$.

$$\dot{\kappa} = \langle\frac{f}{Y_v}\rangle^{n_v} \rightarrow \Delta\kappa = \langle\frac{f^{i+1/2}}{Y_v}\rangle^{n_v}\Delta t = \langle\frac{f^i + \frac{1}{2}\Delta f}{Y_v}\rangle^{n_v}\Delta t \tag{3.24}$$

In order to integrate Equation 3.24, an approximation of the yield surface increment is done by expanding its partial derivatives with respect to its arguments and using Equation 3.23.

$$\begin{aligned}\Delta f &= \frac{\partial f}{\partial \underline{\underline{\sigma}}} : \Delta \underline{\underline{\sigma}} + \frac{\partial f}{\partial \underline{\underline{X}}} : \Delta \underline{\underline{X}} + \frac{\partial f}{\partial \kappa}\Delta \kappa + \frac{\partial f}{\partial T}\Delta T \\ &= \underline{\underline{n}} : \Delta \underline{\underline{s}}^{trial} \\ &- \left(2\mu \underline{\underline{n}} : \underline{\underline{n}} + g'\left(T^i\right) R\left(\kappa^i\right) \left.\frac{\partial T}{\partial \kappa}\right|^i + g\left(T^i\right) R'\left(\kappa^i\right) + \underline{\underline{n}} : \frac{\partial \underline{\underline{X}}}{\partial \kappa}\right) \Delta \kappa_0\end{aligned} \tag{3.25}$$

where $\underline{\underline{n}} : \Delta \underline{\underline{\sigma}}^{trial} = \underline{\underline{n}} : \Delta \underline{\underline{s}}^{trial}$ is taken since the normal direction is deviatoric. An initial estimation of the plastic strain increment is here defined as

$$\Delta \kappa_0 = \langle \frac{f^i}{Y_v} \rangle^{n_v} \Delta t \tag{3.26}$$

The partial derivative of the temperature with respect to the plastic strain is obtained by using the reduced heat expression in Equation 2.27.

$$\left.\frac{\partial T}{\partial \kappa}\right|^i = \frac{\beta^i \sigma^i_{vm}}{\rho c} \tag{3.27}$$

· *Rate Independent Plasticity*

A rate independent plasticity subroutine is also considered as an alternative to the viscoplastic formulation when the viscous coefficient Y_v is zero. The plastic multiplier is integrated by means of the consistent condition of the yield surface as

$$\begin{aligned}\dot{f} = 0 \rightarrow \Delta f &= \frac{\partial f}{\partial \underline{\underline{\sigma}}} : \Delta \underline{\underline{\sigma}} + \frac{\partial f}{\partial \underline{\underline{X}}} : \Delta \underline{\underline{X}} + \frac{\partial f}{\partial \kappa}\Delta \kappa + \frac{\partial f}{\partial T}\Delta T \\ &= \underline{\underline{n}} : \left(\Delta \underline{\underline{s}}^{trial} - 2\mu \Delta \kappa \underline{\underline{n}}\right) - \underline{\underline{n}} : \left(\frac{2}{3} C \underline{\underline{n}} \Delta \kappa - D \underline{\underline{X}} \Delta \kappa\right) - H_R \Delta \kappa = 0\end{aligned} \tag{3.28}$$

where

$$H_R = g'\left(T^i\right) R\left(\kappa^i\right) \left.\frac{\partial T}{\partial \kappa}\right|^i + g\left(T^i\right) R'\left(\kappa^i\right) \tag{3.29}$$

The rate independent plastic increment can then be expressed as

$$\Delta \kappa = \frac{\underline{\underline{n}}^{trial} : \Delta \sigma^{trial}}{\left(2\mu + \frac{2}{3} C\right) \underline{\underline{n}}^{trial} : \underline{\underline{n}}^{trial} - D \underline{\underline{n}}^{trial} : \underline{\underline{X}} + H_R} \tag{3.30}$$

An important accumulated error can result from such explicit integration. In order to reduce its effects, Halilovic et al. [145] proposed an explicit scheme that could remarkably decrease the integration error. In addition, they later showed that the accuracy obtained was comparable to the Backward Euler scheme with a sensibly lower computational cost [150]. The consistency condition was replaced by a condition that ensured the yield surface function would remain zero at the next instant.

$$f^i + \Delta f = 0 \tag{3.31}$$

In the exact problem, the value f^i is zero and hence, the same condition is integrated. As the surface value in the current instant deviates from zero, its correction would take place at the next increment. Therefore, the plastic multiplier can be expressed as

$$\Delta\kappa = \frac{f^i + \underline{\underline{n}}^{trial} : \Delta\sigma^{trial}}{\left(2\mu + \frac{2}{3}C\right) \underline{\underline{n}}^{trial} : \underline{\underline{n}}^{trial} - D\underline{\underline{n}}^{trial} : \underline{\underline{X}} + H_R} \tag{3.32}$$

where the only additional computational cost is the allocation of f^i.

Once the cumulative equivalent plastic strain κ is integrated, the rest of the state variables, i.e., the kinematic variable and the temperature can be updated. A discrete approximation of Equations 2.48 and 2.51 as well as Equation 2.49 is considered:

$$\begin{cases} \Delta\underline{\underline{\alpha}} = \left(\underline{\underline{n}}^{trial} - \frac{3D}{2C}\underline{\underline{X}}^i\right)\Delta\kappa \\ \Delta T = \frac{1}{\rho c}\beta^i \sigma^i_{eq}\Delta\kappa \end{cases} \tag{3.33}$$

Finally the update of the stress state is performed by means of a correction where the plastic strain and thermal increment contributions are subtracted as in Equation 3.23.

$$\begin{cases} \Delta p = \Delta p^{trial} + K\Delta\varepsilon_v^T \underline{\underline{I}} = \Delta p^{trial} + K\alpha\Delta T\underline{\underline{I}} \\ \Delta\underline{\underline{s}} = \Delta\underline{\underline{s}}^{trial} - 2\mu\Delta\underline{\underline{\varepsilon}}^p_{dev} = \Delta\underline{\underline{s}}^{trial} - 2\mu\underline{\underline{n}}^{trial}\Delta\kappa \end{cases} \tag{3.34}$$

Application

Figure 3.3 shows the resulting stress integration of a representative volume element under a constant uniaxial velocity for both rate dependent and rate independent plasticity formulations.

Regarding the viscoplastic simulation, the first order approximation manages to delay instabilities when the imposed strain increments are large (a high strain rate is imposed). Figure 3.3a shows a comparison between the forward Euler integration (using the yield function at the time instant t^n) and the first order approximation just described. When compared to the Z-set implicit solution, where convergence to the exact solution is presumed, the forward Euler shows instabilities for very high strain rates. Some slight oscillations can be observed on the stress-strain curve as well as some larger ones when computing the plastic strain rate. Therefore, a first-order approximation of the yield surface at time $t^{n+1/2}$ provides a much closer and more stable solution with respect to the implicit one without recurring to a computationally costly implicit loop.

Another way of keeping the solution stable may consist in reducing the too large strain increment imposed by the code by scaling it inside the user material subroutine as done in Longère et al. [151] and Dorothy and Longère [65].

Regarding the rate independent plasticity, the advantages of the explicit scheme motivated from Halilovic et al. [145] are shown in Figure 3.3b where the accumulated error is controlled at the expense of some oscillations in the computation of the strain rate.

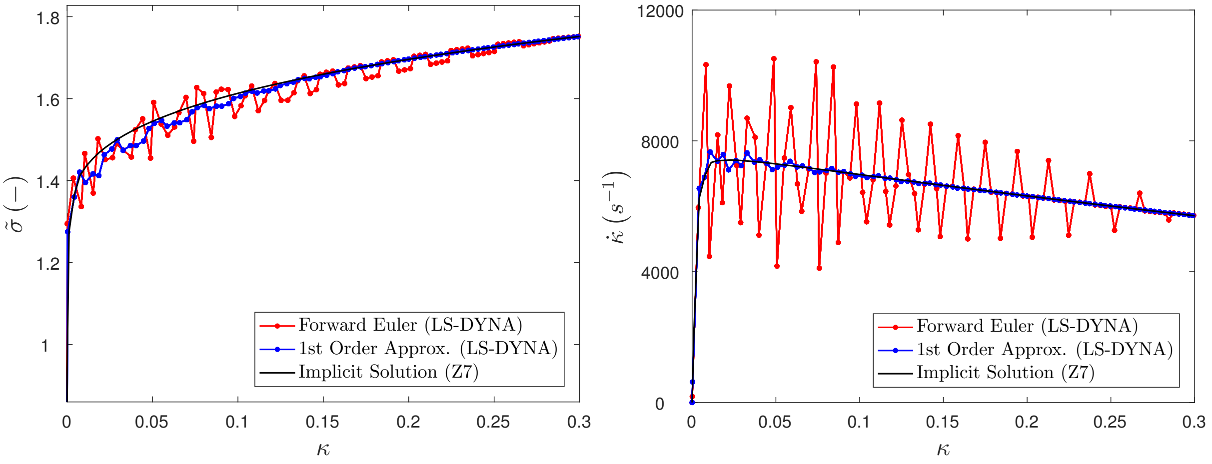

(a) Rate Dependent Plasticity

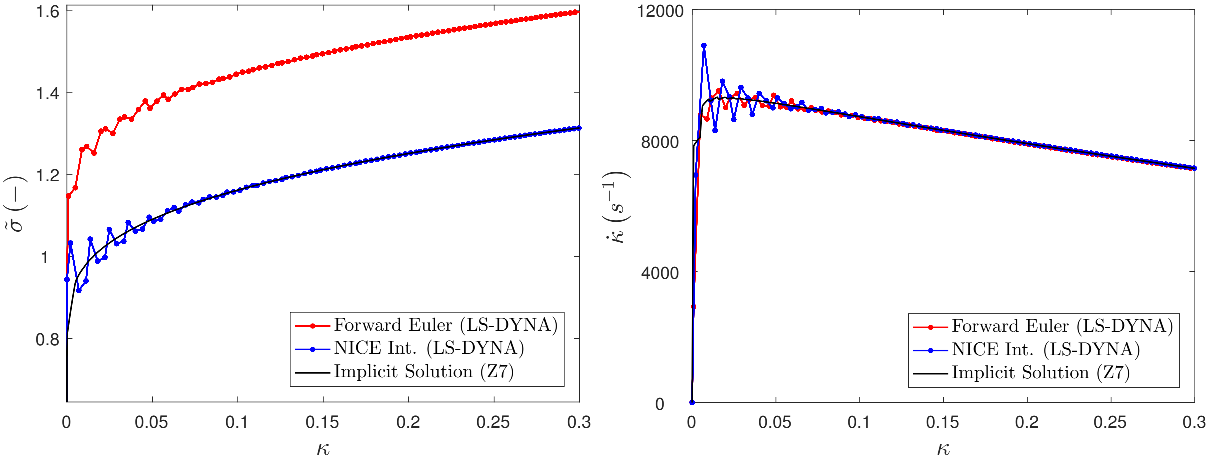

(b) Rate Independent Plasticity

Figure 3.3: Stress vs plastic strain. Uni-dimensional integration of the constitutive equations for an RVE with an imposed displacement. The simulation is done at a loading rate close to the stability limits of the explicit integration.

3.4 Verification of the model at the RVE scale

This section presents a series of simulations at the Representative Volume Element scale. The calibration from Chapter 2) is used. First, a comparison of the implemented user material in LS-DYNA with Z-set is done to verify the algorithm presented above. Secondly, the Lankford coefficients are post-processed from a simulation in an RVE with the user material as a first verification of the material model performances. Table 3.1 summarizes the main features used for each of the two finite element codes.

Table 3.1: LS-DYNA and Z-set main features.

	LS-DYNA	Z-set
Equilibrium Int.	Explicit	Implicit (Newton-Raphson)
Constitutive Eq.	User Material	Included
Constitutive Int.	Explicit	Implicit-θ [152]
Element-type	Selectively Reduced Int.: elform 2	Full integration

3.4.1 Comparison of various loadings

In a first attempt to test the validity of the coded subroutine, some simple loading cases on a representative volume element (eight-node solid element) are considered.

Case 1: Uniaxial tension, compression and simple shear

Case 2: Uniaxial reversed loading

Case 3: Combined multi-directional loading

Case 4: Combined multi-directional loading with relaxed boundary conditions

Case 1: Uniaxial tension, compression and simple shear

The loading conditions are depicted in Figure 3.4. The tension and compression cases considered a vertical imposed displacement along the upper face as seen in Figure 3.4a (there were no restrictions for the remaining degrees of freedom in such face). The symmetry conditions on three faces were additionally imposed. As for the tension-induced shear loading, a transverse displacement on the upper face with a constrained vertical motion is applied (see Figure 3.4b). Likewise for this case, one symmetry plane is taken into account. A fixed condition is set at the base of the element as well as the vertical displacement on the upper face.

Figure 3.5 shows the comparison between the explicit integration performed by the LS-DYNA subroutine and the implicit one by Z-set for the three loading cases above described. Both codes yield the same result in the cases of viscoplasticity as well as rate independent plasticity. The same isotropic and kinematic hardening constants are used for both cases. However, the viscoplastic simulation comprises a strain rate induced overstress, hence the higher values in stress.

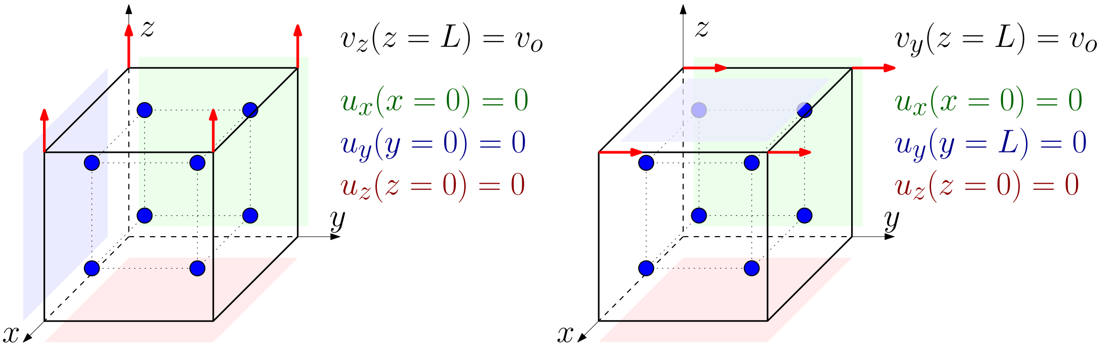

(a) Uniaxial loading

(b) Simple shear loading

Figure 3.4: Uniaxial and simple shear loading cases on a representative volume element ($v_0 = 10^3$ mm/s).

Case 2: Uniaxial reversed loading

The kinematic hardening is also verified by imposing a tension-then-compression loading on the element. The same loading conditions as in Figure 3.4a are imposed. Figure 3.6 shows no disparities between the results of both software for both plastic formulations.

Case 3: Combined multi-directional loading

A more complex type of loading is also considered to assess the kinematic and orthotropic properties during subsequent changes in loading directions. Three consecutive displacements along the three main directions are sequentially imposed. The boundary conditions remain the same as those depicted in Figure 3.4a. Additionally the remaining degrees of freedom corresponding to the moving face are restricted. Figure 3.7 shows the evolution of a representative volume element which can be summarized as follows

1. Imposed velocity of 10^3 mm s^{-1} for 5×10^{-4} s along the x-axis with restricted motion along the y and z-dimensions
2. Imposed velocity of 10^3 mm s^{-1} for 5×10^{-4} s along the y-axis with restricted motion along the x and y-dimensions
3. Imposed velocity of 10^3 mm s^{-1} for 5×10^{-4} s along the z-axis with restricted motion along the x and y-dimensions

The boundary conditions are defined in the material coordinates for simplicity.

Both the viscoplastic and the rate independent solutions are compared against the implicit solution provided by Z-set. Because of the restricted degrees of freedom during the loading, the pressure in the element rapidly increases. Since the plasticity considered in this work is pressure-independent, the solution to such loading will be elastically dominated (Figure 3.8).

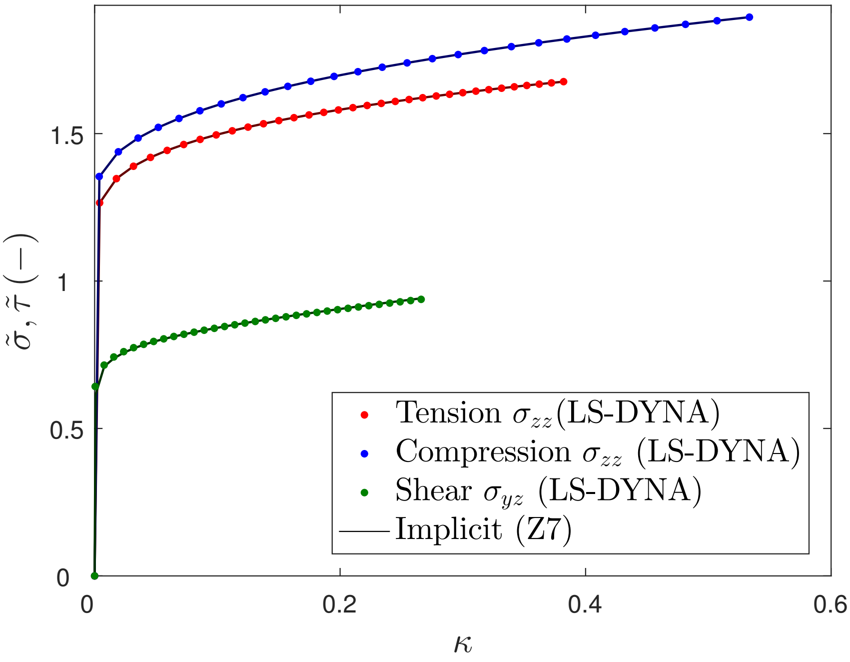

(a) Rate Dependent Plasticity.

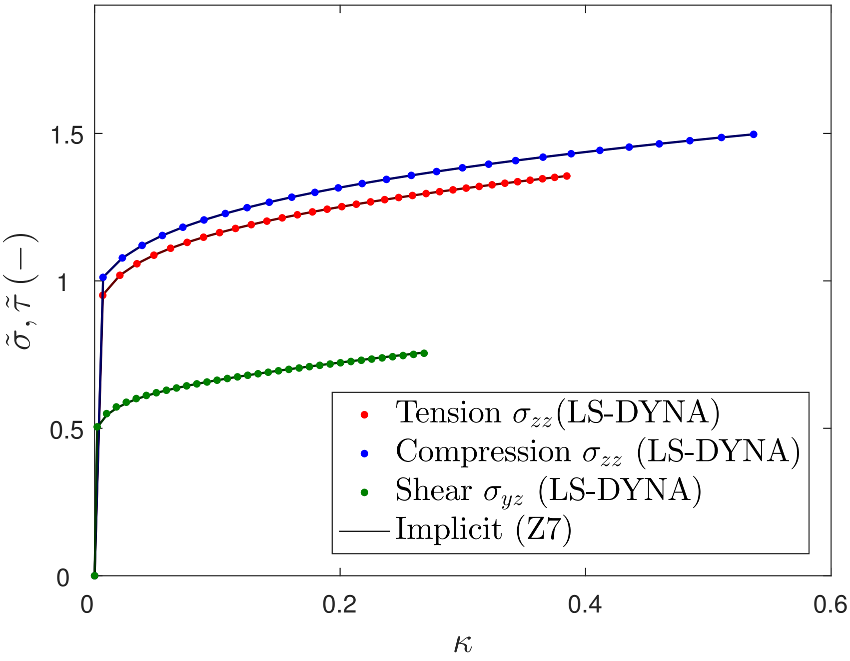

(b) Rate Independent Plasticity.

Figure 3.5: Stress vs. plastic strain. Tension, compression and shear. Rate dependent and rate independent plasticity formulations. LS-DYNA (explicit) and Z-set (implicit) comparison at $\dot{\kappa} \simeq 800\,\mathrm{s}^{-1}$ and $T = 25\,^{\circ}\mathrm{C}$.

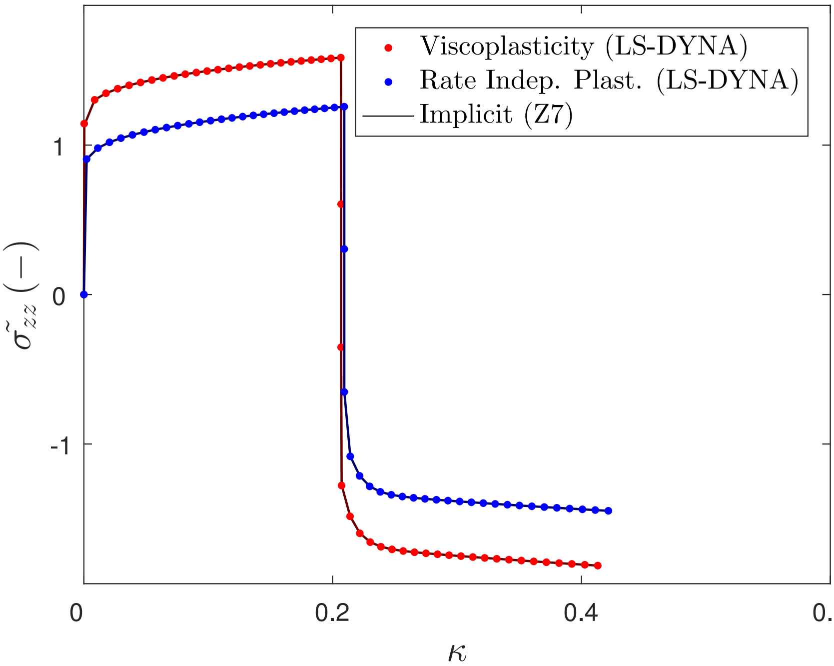

Figure 3.6: Stress vs. plastic strain. Tension-then-compression. LS-DYNA (explicit) and Z-set (implicit) comparison at $\dot{\kappa} \simeq 800\,\mathrm{s}^{-1}$ and $T = 25\,°\mathrm{C}$.

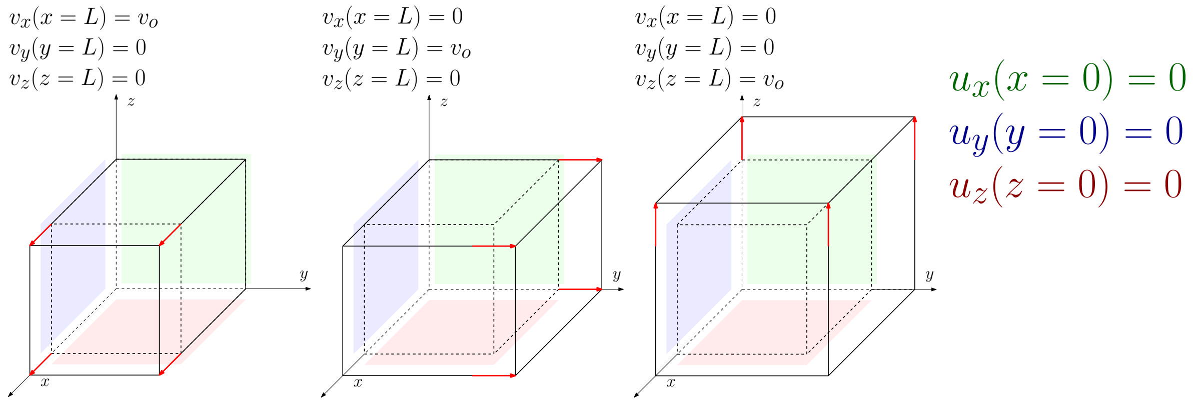

Figure 3.7: Deptiction of a combined loading along the three dimensions with restricted boundary conditions on the remaining degrees of freedom.

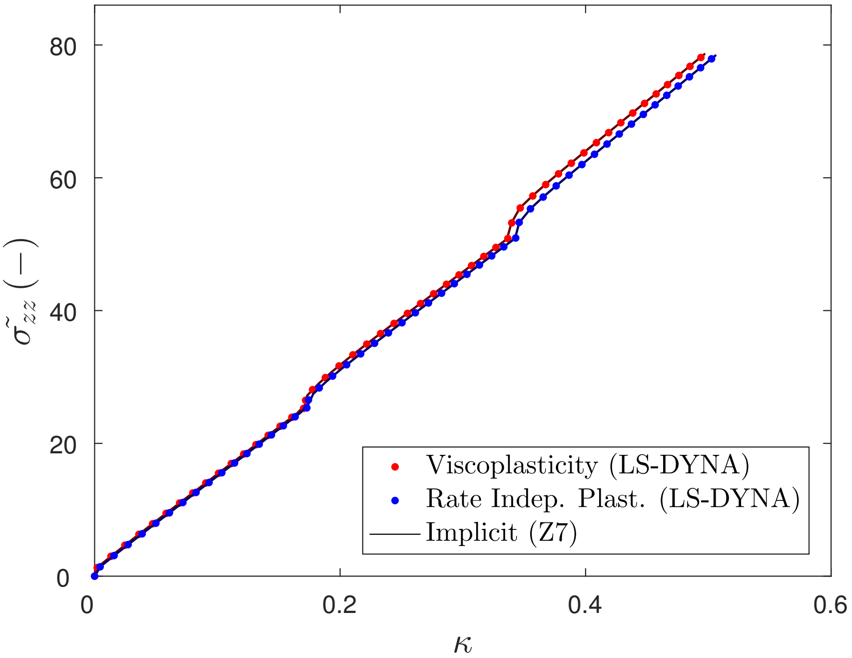

Figure 3.8: Stress vs. plastic strain. Tension loading along x, y and z with tight boundary conditions (see Figure 3.7). LS-DYNA (explicit) and Z-set (implicit) comparison at $\dot{\kappa} \simeq 800\,\mathrm{s}^{-1}$ and $T = 25\,°\mathrm{C}$.

Case 4: Combined multi-directional loading with relaxed boundary conditions
A last loading combining imposed displacements along several directions was also simulated. For this case, the boundary constraints were relaxed in order to avoid an excessive presence of the hydro-static pressure. The loading, shown in Figure 3.9, can be summarized as follows:

1. Imposed velocity of $10^3\,\mathrm{mm\,s^{-1}}$ for $5 \times 10^{-4}\,\mathrm{s}$ along the x-axis while allowing transverse displacement on the loaded face
2. Imposed velocity of $10^3\,\mathrm{mm\,s^{-1}}$ for $5 \times 10^{-4}\,\mathrm{s}$ along the y-axis with the x-displacement restricted on the loaded face
3. Imposed velocity of $10^3\,\mathrm{mm\,s^{-1}}$ for $5 \times 10^{-4}\,\mathrm{s}$ along the z-axis with the remaining degrees of freedom restricted

The results of such simulation are plotted in Figure 3.10. The stress components in the x as well as the y-direction are here considered. During the first stage of the loading, σ_{xx} becomes non-zero and it accordingly evolves as plastic deformation is imposed. Afterwards, the loading along the y-direction implies a σ_{yy} component and a relaxation of σ_{xx} due to the volume reduction provoked by the weak boundary conditions. Finally, as the displacement along the z-direction is imposed and the motion along the other dimensions restricted, the volume increase of the element produces a sudden increase in the stress tensor components (through the hydro-static pressure). Such increase has been cut in Figure 3.10 to keep the previous evolution visible.

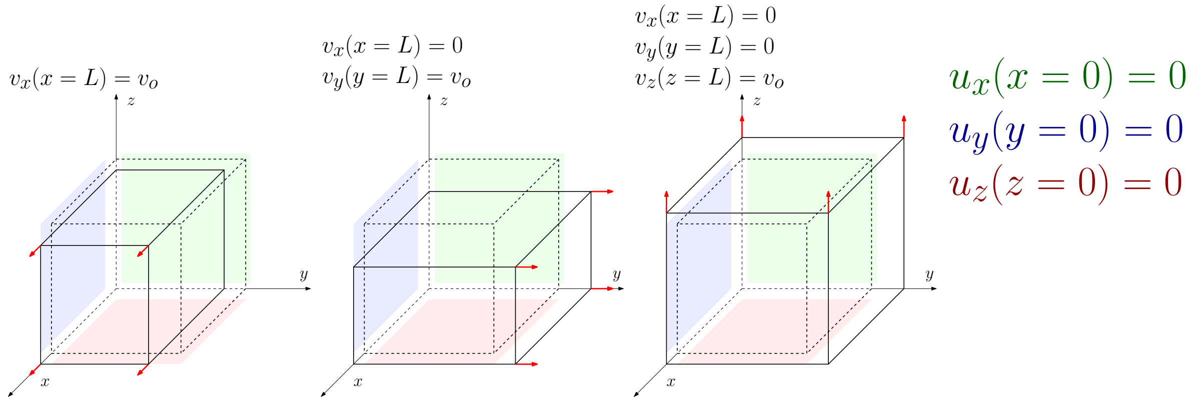

Figure 3.9: Deptiction of a combined loading along the three dimensions with relaxed boundary conditions on the remaining degrees of freedom.

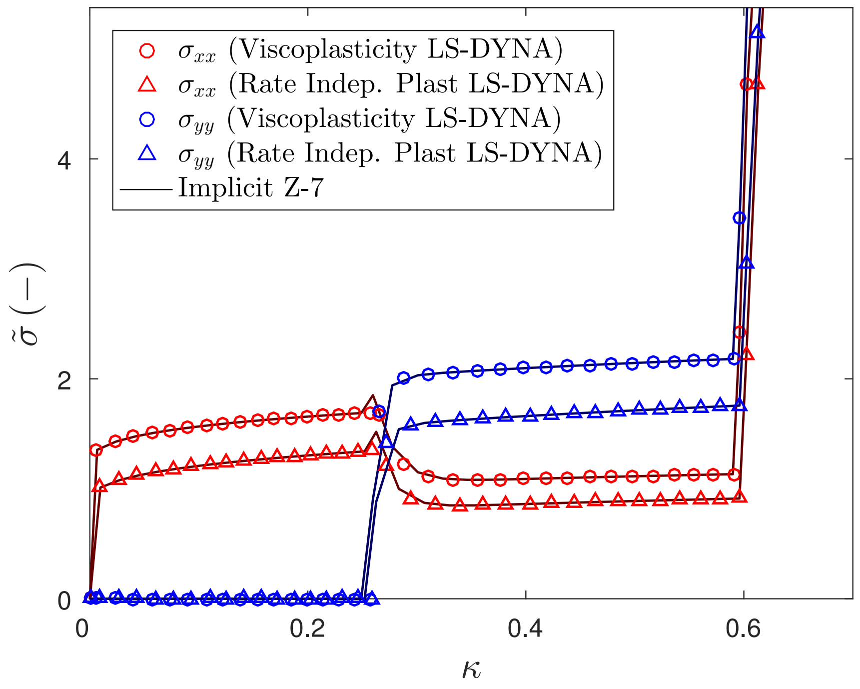

Figure 3.10: Stress vs. plastic strain. Tension loading along x, y and z with relaxed boundary conditions (see Figure 3.9). LS-DYNA (explicit) and Z-set (implicit) comparison at $\dot{\kappa} \simeq 800\,\mathrm{s}^{-1}$ and $T = 25\,°\mathrm{C}$.

Assessment

As seen from the different loading cases on an RVE, the user material subroutine has proven to correctly integrate the constitutive equations. Despite of the high loading rate in the element, the explicit subroutine has followed the implicit solution given by the Z-set software.

3.4.2 Comparison of the computed and measured Lankford coefficients

The second part of this section consists in a comparison of the Lankford coefficients. It is reminded that they have not been used in the calibration procedure. Two different estimations of the Lankford coefficients were done. The first estimation of the Lankford coefficients, r_θ, was defined in Equation 1.2 as the width $\varepsilon_{transverse}$ to thickness ε_{normal} total strain ratio. Considering isochoric deformation (rough assumption since the elastic strain is not isochoric) as measured in the experiments, they read

$$r_\theta = \frac{\varepsilon_{transverse}}{\varepsilon_{normal}} = -\frac{\varepsilon_{transverse}}{\varepsilon_{axial} + \varepsilon_{transverse}} \tag{3.35}$$

where ε_{axial} is the strain measured along the loading direction.

A second definition is the width to thickness plastic strain ratio. Since the loading is uniaxial, the plastic strain rate ratio can be considered

$$r_\theta^p = \frac{\dot{\varepsilon}^p_{transverse}}{\dot{\varepsilon}^p_{normal}} = \frac{\varepsilon^p_{transverse}}{\varepsilon^p_{normal}} = \frac{n_{transverse}}{n_{normal}} \tag{3.36}$$

where $\underline{\underline{n}}$ is the yield surface normal.

Figure 3.11 shows the superimposition for the four directions (under tension uniaxial loading) of the experimental measurements with the numerical simulation. It is clearly appreciated that the experimental scatter is considerably higher than the differences with respect to the numerical solutions. In addition, both definitions of the Lankford coefficients yield almost identical values at large strain amounts (for very small strains, the elastic components play a bigger role, as expected).

Figure 3.12 shows a comparison of the computed evolution of the Lankford coefficients for loadings along various directions. The orthotropy is evident being the normal direction the one with the highest Lankford value and the rolling direction the lowest one.

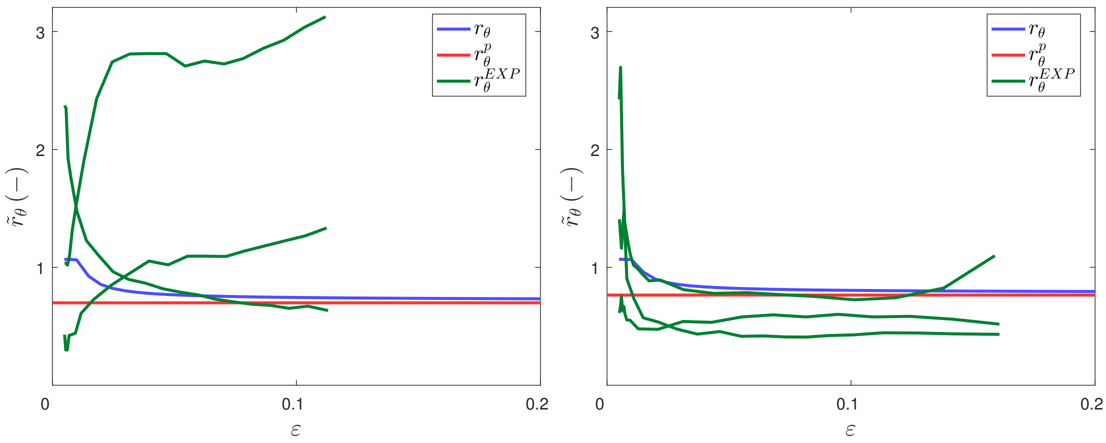

(a) Rolling Direction (b) Transverse Direction

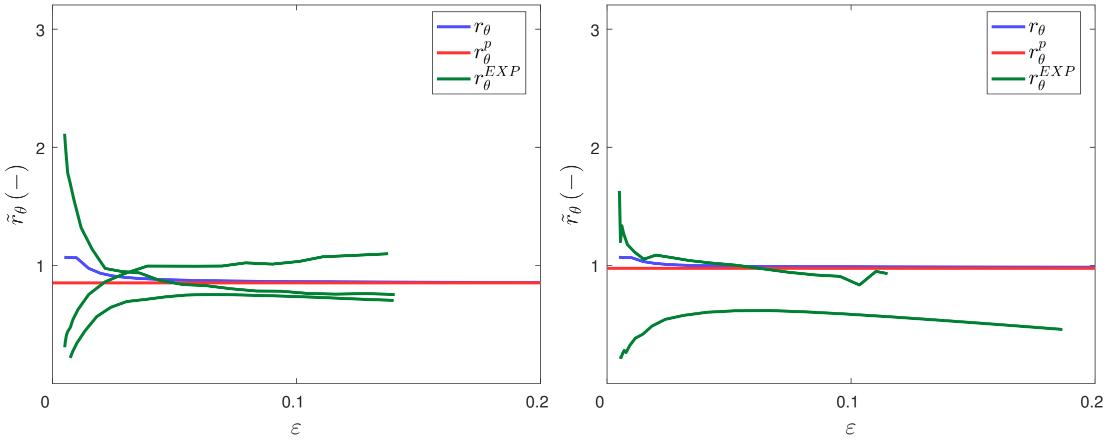

(c) Diagonal Direction (d) Normal Direction

Figure 3.11: Lankford coefficient vs. strain. Experimental vs. numerical comparison of uniaxial tension. $\dot{\varepsilon} \simeq 10^{-3}\,\mathrm{s}^{-1}$ and $T = 25\,°\mathrm{C}$.

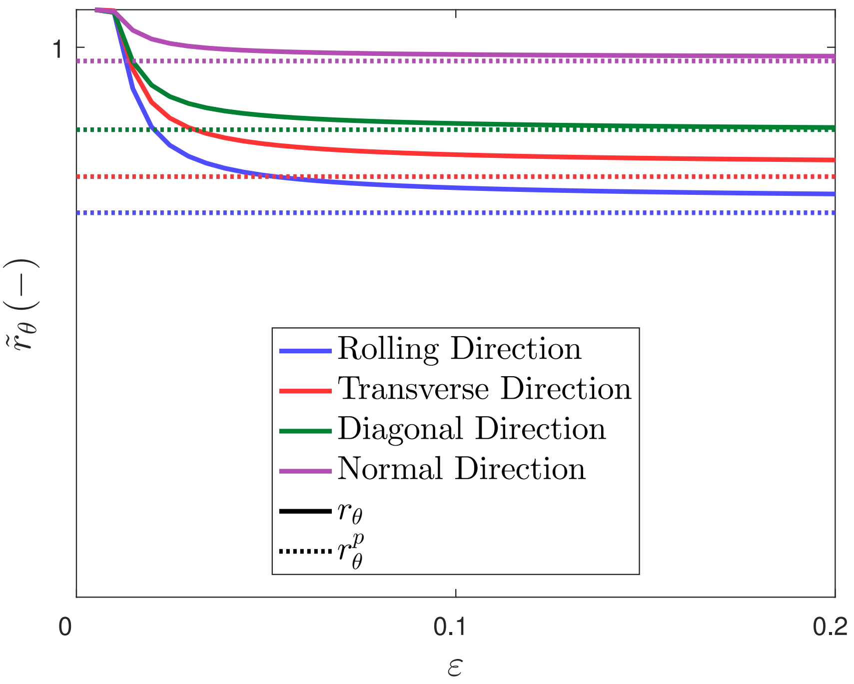

Figure 3.12: Lankford coefficient vs. strain. Numerical comparison of the plastic and total width to thickness strain ratio. $\dot{\varepsilon} \simeq 10^{-3}\,\mathrm{s}^{-1}$ and $T = 25\,°\mathrm{C}$.

3.5 Verification of the model at the specimen scale

Numerical simulations of various loading cases are presented below:

i Uniaxial tension loading

ii Triaxial tension loading (see [27 ; 77])

iii Tension-induced shear (see [27 ; 47])

iv Uniaxial compression loading

v Shear-compression loading (see [65 ; 151])

It is to be noted that the triaxial (ii), tension-induced shear (iii) and shear-compression (v) cases were not used for the calibration of the material constants. The viscoplastic formulation will be considered for all the simulations.

After a first comparison with the experiments, a discussion of the different finite element models in terms of accuracy, mesh or element type is followed.

3.5.1 Experimental vs. numerical results comparison

A comparison is here made by superimposing the applied vs. computed load and the measured vs. computed nominal strain (from an extensometer with the same gauge length) for the different specimens. Numerical simulations are done employing LS-DYNA with the user material subroutine presented above. Specimens are originally meshed using 8-node solid elements of an average size of 100 µm. The element-type formulation *elform*

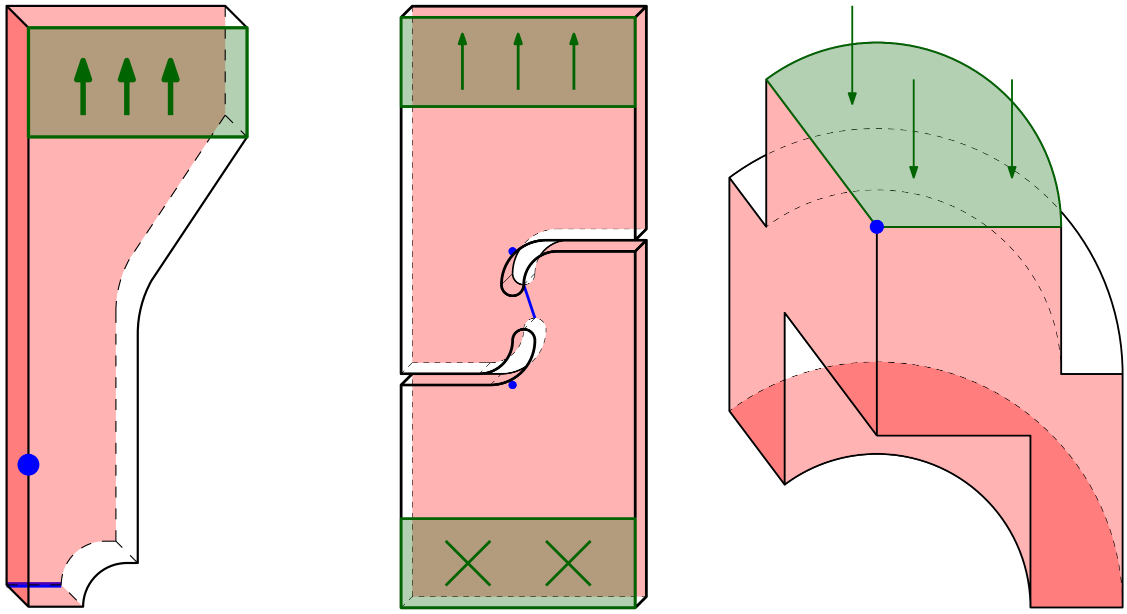

(a) Notched tension (b) Tension-induced shear (c) Shear-compression

Figure 3.13: Geometries and boundary conditions for the different configurations tested. The green areas represent the imposed displacement (or fixture) and the red zones represent the symmetry conditions. Displacement is indicated by blue markers and the parts where internal variables are extracted are indicated by blue lines for the tension specimens. A symmetry condition is imposed at the base of the hat-shaped specimen to let it move along that plane.

2 is chosen: 8 integration points with a reduced integration for the hydrostatic pressure. The effect of this choice will be discussed later in Section 3.5.2.

Figure 3.13 shows a drawing with the main boundary conditions imposed for the different specimens. In the case of quasi-static simulations, only one eighth of the tension specimens (Figures 1.17b, 1.17c, 1.17d and 1.17e) is considered in the FEM model due to symmetry properties (one half for the tension-induced shear specimen in Figure 1.17a). Similarly, one eighth is also considered for the compression cylindrical specimen (see Figure 1.18b) and one quarter for the hat-shaped geometries (Figures 1.18a and 1.18c).

However, for high strain rate loading, the symmetry property along the cross section area is dropped for both the tension and compression type of loadings. The different geometries are loaded by applying the machine imposed displacement corresponding to the experimental campaign. Post-processing of these simulations would then read the displacement at the location of the experimental extensometer as well as the internal variables at the cross-section for analysis.

One important limitation when simulating the quasi-static (but rate dependent) conditions is the time increment. In order to ensure a stable explicit integration of the dynamic equations, a maximum time increment is imposed by the CFL condition in Equation 3.7 [142]. The necessary time step to consider is thus the smallest from all the elements in the mesh. In addition, the stiffer the material is and the finer its mesh, the smaller the required time step and the longer the simulation (see Equations 3.7 and 3.8). Therefore, as the mesh is refined the computational cost will be augmented due to (i) an increase in the number of elements and (ii) an increased number of time increments

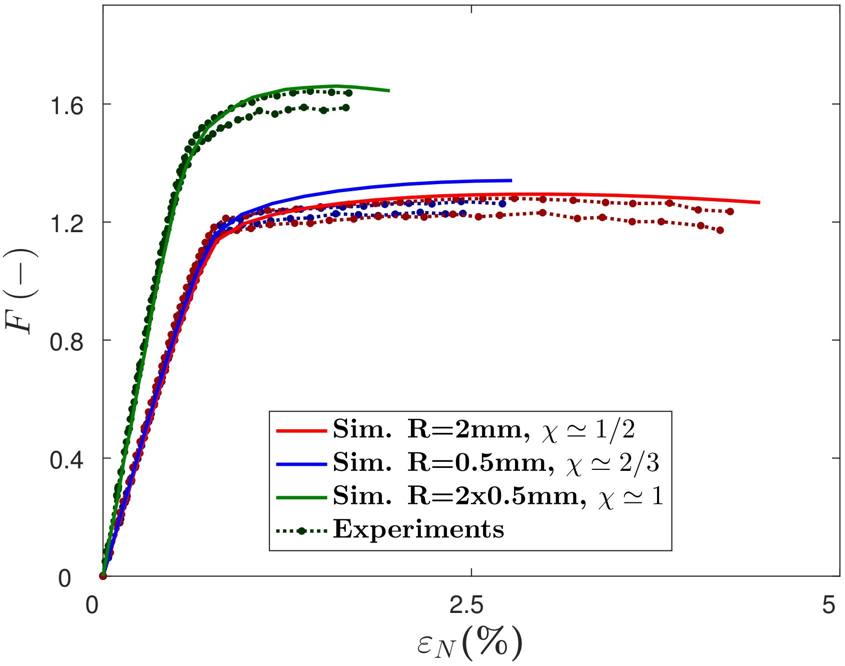

Figure 3.14: Force vs. strain. Numerical and experimental comparison of notched flat tension specimens at $v = 1.6 \times 10^{-3}$ mm/s. $T = 25$ °C and Transverse direction TD.

inversely proportional to the mesh size.

In order to reduce the computational time of quasi-static simulations, mass-scaling is applied to the mesh [153]. It consists in the addition of mass to the model to increase the density and decrease the celerity defined in Equation 3.8 and therefore increase the maximum time increment. An alternative would be to set a lower Young's modulus but it would considerably alter the mechanical behavior.

The mass added to the model is such that it ensures a stable integration for a given time step imposed prior to the simulation (the step size imposed was of the order of 10^{-3} s for a simulation lasting ≃500 s). Notwithstanding, the increase in mass can imply an important increase of the kinetic energy which should be negligible for a quasi-static simulation. The mass-scaling is controlled with the parameter *DT2MS* in the control card **CONTROL_ TIMESTEP* [153].

3.5.1.1 Triaxial tension loading on notched flat specimens

The triaxial tension loading is obtained by applying a tension loading on the notched specimens from Figures 1.17c, 1.17d and 1.17e in Chapter 1. These geometries allow for the verification of the plastic behavior at very positive triaxialities by means of three types of notches in the flat specimens: a single notch of 2 mm ($\chi \simeq 1/2$) and 0.5 mm ($\chi \simeq 2/3$) and a double-notch of 2 mm × 5 mm ($\chi \simeq 1.0$).

Figure 3.14 shows the performance of the model with respect to the experimental curves (see Figure 1.28a). For the three notched geometries with positive triaxiality, the force as well as the hardening up to necking is correctly predicted with only a slight overestimation, especially for the 0.5 mm radius notch (with an estimated $\chi \simeq 2/3$). However, this disparity remains lower than the experimental scatter.

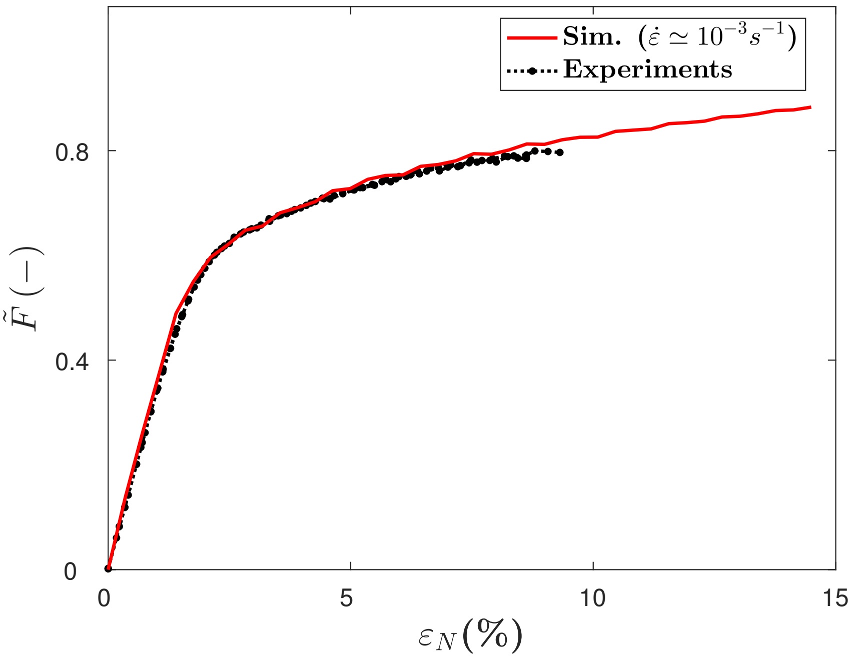

Figure 3.15: Force vs. strain. Numerical and experimental comparison of the tension-induced shear specimen at $v = 1.6 \times 10^{-3}$ mm/s. $T = 25\,°\mathrm{C}$ and Transverse direction TD.

3.5.1.2 Tension-induced shear loading

The tension-induced shear loading is obtained with the specimen from Figure 1.17a in Chapter 1. The largest fracture strain is expected for this specimen.

Figure 3.15 shows a comparison with the experimental curve. As opposed with the notched specimen under high triaxialities, the tension-induced shear specimen simulation matches satisfactorily the experimental curve until fracture.

3.5.1.3 Shear-compression loading

A shear-compression loading with negative triaxialities is performed with the Couque and Meyers specimens from Figures 1.18a and 1.18c in Chapter 1 respectively.

Figure 3.16 shows the hat shaped specimens simulated at a quasi-static loading rate. The force-displacement curves are plotted with the elastic component removed. The reason is the difficulty to measure the correct stiffness on experimental compression tests. Regarding Meyers geometry, the stress triaxiality ratio is expected to be weak and negative ($\chi \simeq -1/5$). The agreement with the experimental results is relatively satisfactory with only a slight overestimation of the force. On the other hand, the results from the Couque geometry ($\chi \simeq -1/2$) show that the simulated load is sensibly higher than the experimental one.

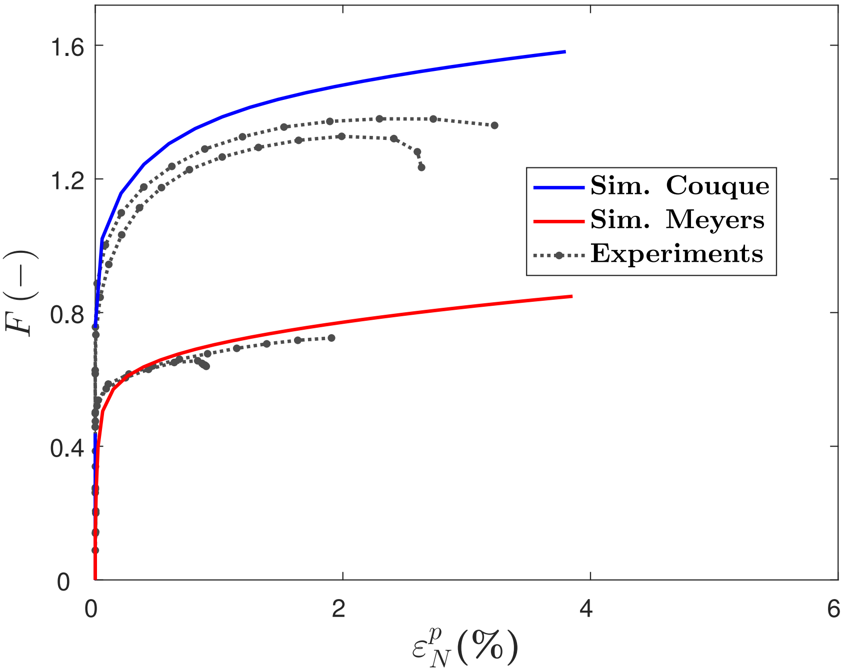

Figure 3.16: Force vs. strain. Numerical and experimental comparison of shear-compression specimens at quasi-static loading rate $v = 8 \times 10^{-3}$ mm/s. $T = 25\,°\mathrm{C}$ and Normal direction ND.

3.5.2 Analysis and discussion

A thorough discussion of the results regarding mass scaling, mesh dependence and disparities with the experiments is presented.

3.5.2.1 Effect of mass-scaling

Table 3.2 summarizes the maximum values of kinetic energy and internal energy as well as the mass scaling employed for the subsequent simulations. It can be verified that the ratio between the kinetic energy (times the mass scaling) and the internal energy remains close to zero for all the specimens tested.

Table 3.2: Maximum value of kinetic and internal energy in the LS-DYNA viscoplastic simulations.

Specimen	Kinetic Energy (N mm)	Internal Energy (N mm)	Mass Scaling	Energy Ratio
Flat tension	2.8×10^{-12}	1.5×10^{3}	4.9×10^{-9}	$\simeq 0\,\%$
Compression	7.8×10^{-13}	1.5×10^{4}	2.4×10^{-9}	$\simeq 0\,\%$
Notch $N = 2$ mm	2.6×10^{-13}	9×10^{2}	1.7×10^{12}	0.05 %
Notch $N = 0.5$ mm	2.6×10^{-13}	8.8×10^{2}	1.7×10^{12}	0.05 %
Double Notch	3.4×10^{-13}	4.3×10^{2}	7.7×10^{11}	0.06 %
Shear	3.8×10^{-12}	2.3×10^{3}	4.7×10^{8}	0.05 %

3.5.2.2 Mesh size sensitivity

Regarding the mesh size sensitivity, an initial average element size of 100 µm was initially considered for all the simulations. The convergence in the solution with mesh density is verified with a coarser (200 µm) and a finer mesh size (50 µm). This has been done for:

i Uniaxial tension loading

ii Triaxial tension loading

iii Tension-induced shear

The mesh size sensitivity is studied in terms of plastic strain κ, stress triaxiality ratio χ and the Lode parameter L. The latter is defined as

$$L = \frac{2\sigma_2 - \sigma_1 - \sigma_3}{\sigma_1 - \sigma_3} \tag{3.37}$$

where σ_i are the eigenvalues sorted in descending order.

An alternative expression of the stress triaxiality ratio (in Equation 1.1) can be defined with the equivalent stress. This definition would consider the orthotropy, kinematic hardening and strength differential:

$$\tilde{\chi} = -\frac{p}{\sigma_{eq}\left(A, \underline{\underline{X}}, k\right)} \neq -\frac{p}{q} = \chi \tag{3.38}$$

Uniaxial tension specimen

Figure 3.17 shows the force-displacement curves of the smooth tension specimen for a quasi-static loading considering three mesh densities (shown in Figure 3.19) and three different LS-DYNA element-type formulations.

As previously mentioned in Section 3.2.1, the reduced (R) and the selectively reduced (S/R) integration avoid shear locking problems which translates in a lower mesh dependence. On the other hand, the curves using the quadratic (F) element (8-node with nodal rotations) yield different results for each mesh due to some volume locking. As the mesh becomes finer, the results converge towards the other element formulations. In this work, the S/R integration element (*elform 2*) is considered as the optimal formulation. It provides with a reasonable computational cost and does not require an hourglass control as with the R element. In addition, by considering eight integration points, the local precision in the model is considerably higher.

Figure 3.18 shows the local spatial distribution of evolving plastic strain, stress triaxiality and Lode parameter (as defined in Equations 1.1 and 3.37) along a line in the zone of interest and at the nominal strain amount corresponding to the vertical line in Figure 3.17. It can be seen that, for the type of element considered (S/R) no mesh dependence is observed as similarly seen on the force-displacement curves (Figure 3.17).

Local observations of the finite element simulations are also carried out to further study the mesh dependence. Figure 3.19 shows one eighth of the specimen simulated for the three mesh densities considered at an advance state of deformation. The S/R element formulation has been used. As the mesh becomes finer, the resolution of the field measure

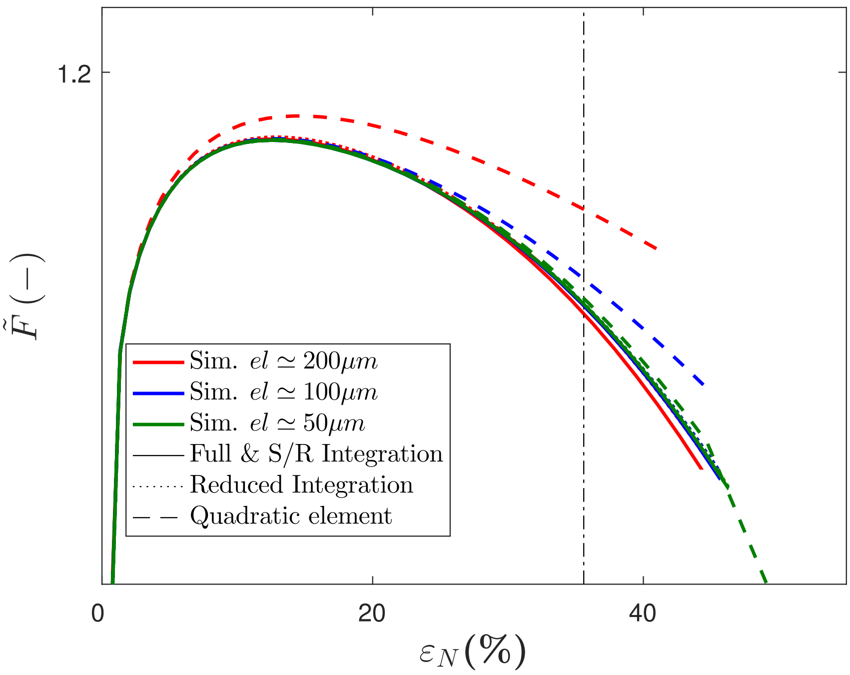

Figure 3.17: Force vs. nominal total axial strain. Mesh size sensitivity comparison of a smooth flat tension specimen at $\dot{\varepsilon} \simeq 10^{-3}\,\mathrm{s}^{-1}$ and $T = 25\,°\mathrm{C}$. Three mesh densities are considered: 200 µm, 100 µm and 50 µm, and three element-type formulations: elform 1, 2 and 3.

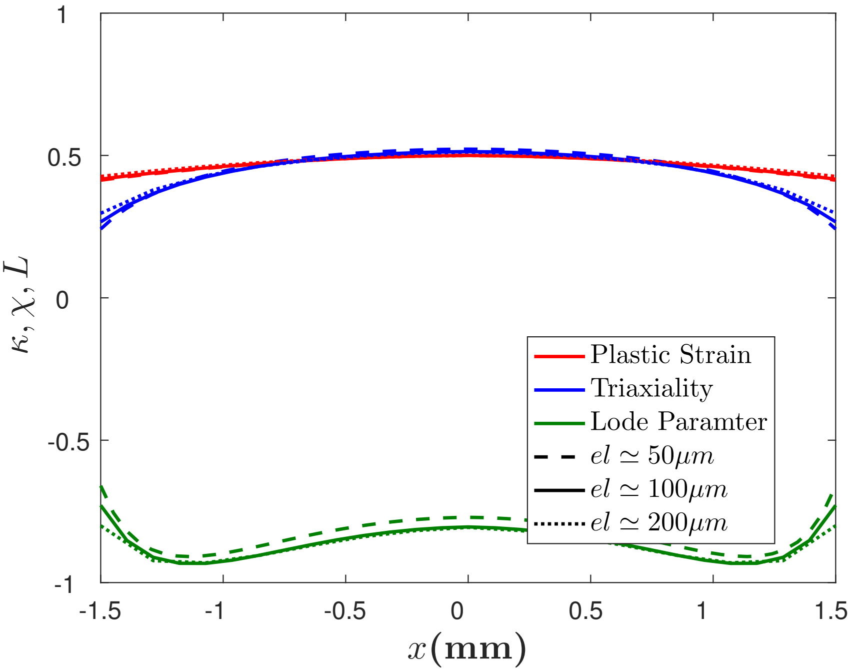

Figure 3.18: Mesh size sensitivity at the local level at the cross section of the smooth flat tension specimen. The S/R element is chosen. The spatial measurements are taken at $\varepsilon \simeq 35\,\%$ (as marked in Figure 3.17 with a vertical line).

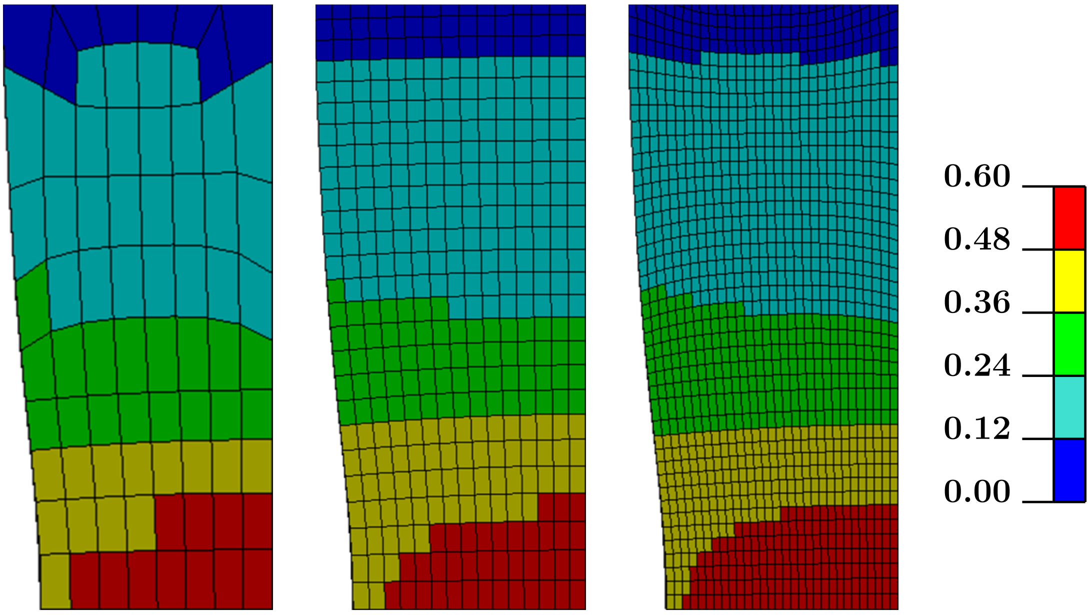

(a) *size* $\simeq$ 200 µm. (b) *size* $\simeq$ 100 µm. (c) *size* $\simeq$ 50 µm.

Figure 3.19: Plastic strain field for three mesh densities using a selectively reduced element formulation (*elform 2*) on the smooth flat tension specimen.

is better. Apart from that, there are not great disparities among the three meshes as accordingly seen in Figure 3.17.

As performed with the representative volume element, a comparison between the software LS-DYNA and Z-set is also carried out for the quasi-static smooth flat tension specimen to asses the performance of the subroutine at the structure scale. The 8-node full integration solid element is here employed in Z-set and the quadratic element (F) in LS-DYNA. Figure 3.20 shows the curves for both software using three different mesh sizes. It is interesting to note the similar mesh dependence among the two codes whose element are subject to volume locking. For the coarser mesh, the LS-DYNA quadratic element shows a slightly closer performance towards the converged result due to the enriched formulation of the nodal rotations. As the mesh is refined, their mesh dependence is quasi-similar converging to the same result as the two other element formulations (see Figure 3.17).

A comparison of the computational time of the simulations in Figure 3.20 is summarized in Table 3.3. For these simulations run in the quasi-static regime (not suited for the LS-DYNA explicit code), the LS-DYNA simulation under-performs Z-set in terms of computational time. However, as the mesh density becomes finer, the amount of time to run the simulations becomes comparable for both software. This is mainly due to the MPP parallel process available in LS-DYNA, however, this is not the object of the chapter. In any respect, the LS-DYNA explicit code would prove a better option as the loading rate of the mechanical problem increases.

Regarding the tests at a high loading rate, the tension specimen is simulated for two mesh densities (using the S/R elements). Figure 3.21 shows a comparison between the numerical output and the experimental data. Independently of the mesh size, the numerical solution is very oscillatory. A smoothing of such curve by averaging every three consecutive points, yields a similar behavior as the experimental results. Two reasons

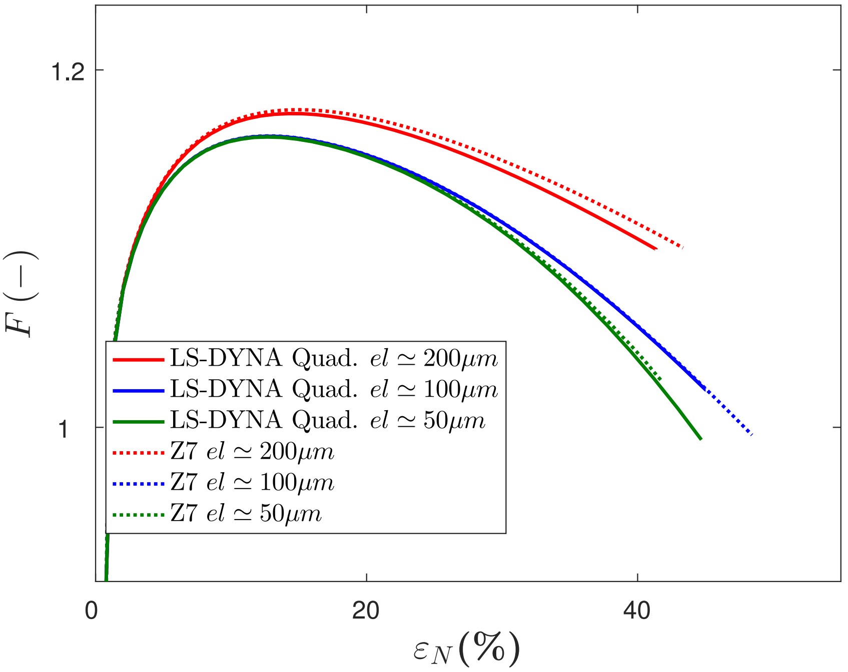

Figure 3.20: Force vs. strain. LS-DYNA vs. Z-set comparison of a smooth flat tension specimen. $\dot{\varepsilon} \simeq 10^{-3}\,\mathrm{s}^{-1}$ and $T = 25\,°\mathrm{C}$. The former uses a full integrated solid element and the latter a quadratic 8-node element (with nodal rotations).

Table 3.3: LS-DYNA (explicit, F-element, 32 MPP cores) and Z-set (implicit, Full Integration, 4 SMP cores) computational time for various mesh densities.

	LS-DYNA	Z-set	LS-DYNA/Z-set
$el \simeq 200\,\mu\mathrm{m}$	$\simeq 30\,\mathrm{min}$	$\simeq 6\,\mathrm{min}$	5
$el \simeq 100\,\mu\mathrm{m}$	$\simeq 4\,\mathrm{h}$	$\simeq 1.5\,\mathrm{h}$	2.66
$el \simeq 50\,\mu\mathrm{m}$	$\simeq 8\,\mathrm{h}$	$\simeq 8.5\,\mathrm{h}$	0.94

could explain this numerical noise. First, the mesh might not be smooth enough involving great variations in the size of the elements (bigger ones in the specimen head and smaller ones in the zone of interest) that could distort the propagation of waves. Secondly, these mechanical waves produced from a rapid loading keep bouncing between the boundaries. This last effect may be fixed by including the output pressure bar so that the wave can be mechanically transferred outside of the specimen.

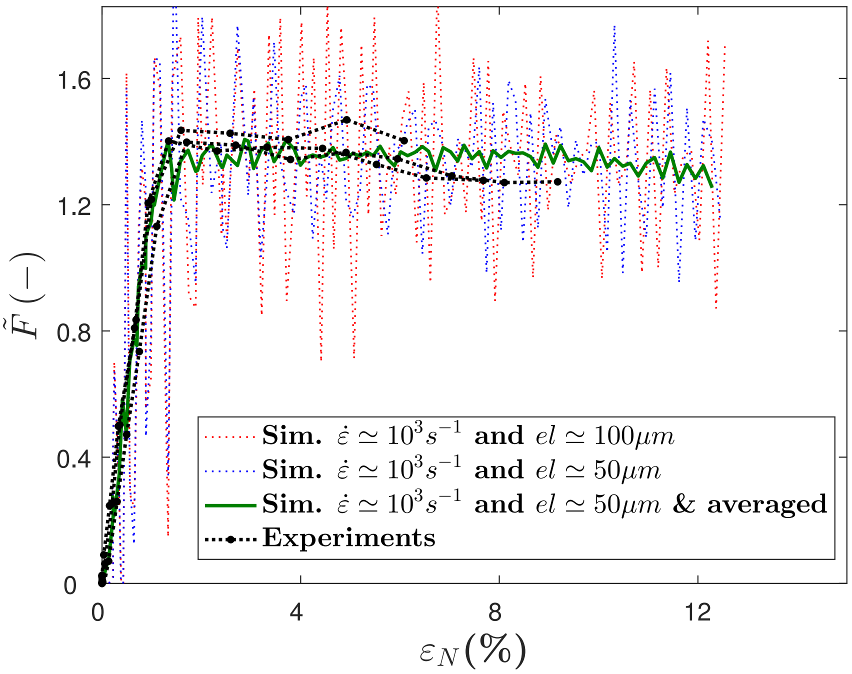

Figure 3.21: Force vs. nominal total axial strain. Mesh size sensitivity comparison of a smooth flat tension specimen at $\dot{\varepsilon} \simeq 10^3\,\mathrm{s}^{-1}$ and $T = 25\,°\mathrm{C}$. Two mesh densities are considered: 100 µm and 50 µm. The oscillatory behavior is found for the two different mesh densities.

Triaxial tension specimen

Figure 3.22 shows the results using two different mesh sizes of 50 µm and 100 µm for the notches of $R = 2\,\mathrm{mm}$ and $R = 0.5\,\mathrm{mm}$. Due to high triaxialities, the mesh is more dependent on volume deformation as compared with the smooth specimens. However, the strain range covered by the experimental curves shows no effect of the element size on the global scale, i.e. the force-displacement curves. In addition, the plastic strain κ, stress triaxiality χ and the Lode parameter L read along the width crossing the notches converge for the mesh size considered, i.e. 100 µm.

The local field measurements in Figure 3.23 obtained at an advance stage of deformation do not show any important differences with respect to the element size either, the finer mesh providing with a higher precision. It is interesting to note how the smaller notched specimen have a higher amount of plastic deformation along the whole cross-section. This characteristic will be re-discussed at the end of the chapter in the context of the strain to fracture.

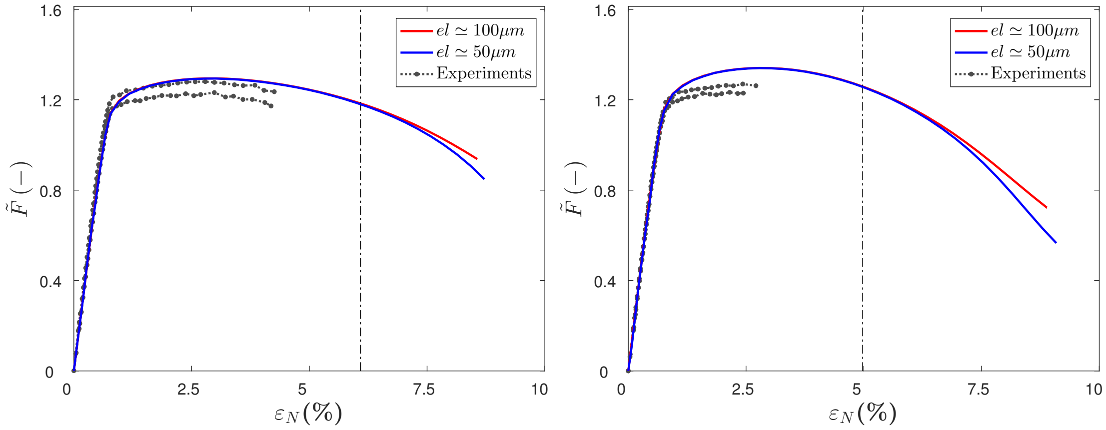

(a) $R = 2\,\mathrm{mm}$ (global)　(b) $R = 0.5\,\mathrm{mm}$ (global)

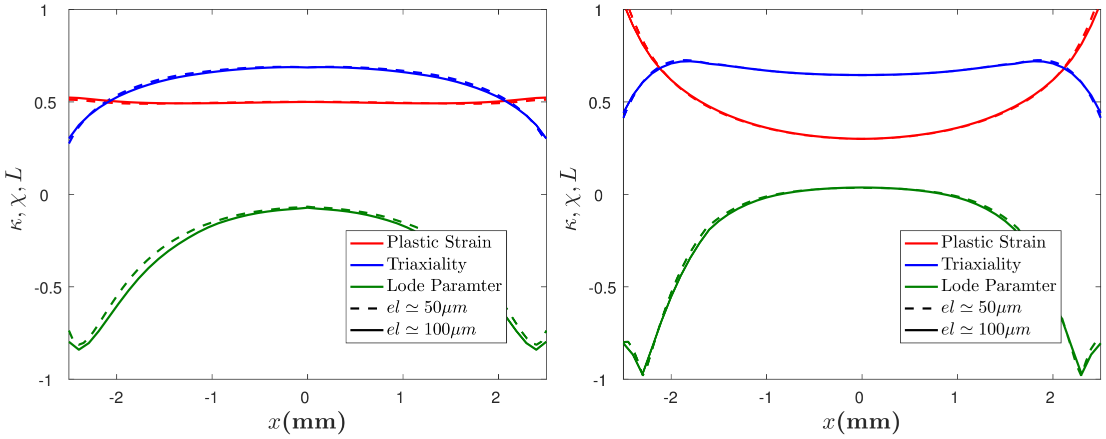

(c) $R = 2\,\mathrm{mm}$ (local)　(d) $R = 0.5\,\mathrm{mm}$ (local)

Figure 3.22: Above: Force vs. strain. Below: Mesh size sensitivity at the local level at the cross section of the notch flat tension specimens (S/R element). The spatial measurements shown below are taken at $\varepsilon \simeq 6\,\%$ and $\varepsilon \simeq 5\,\%$ (marked on the respective Figures above with a vertical line). $v = 1.6 \times 10^{-3}\,\mathrm{mm/s}$ and $T = 25\,°\mathrm{C}$.

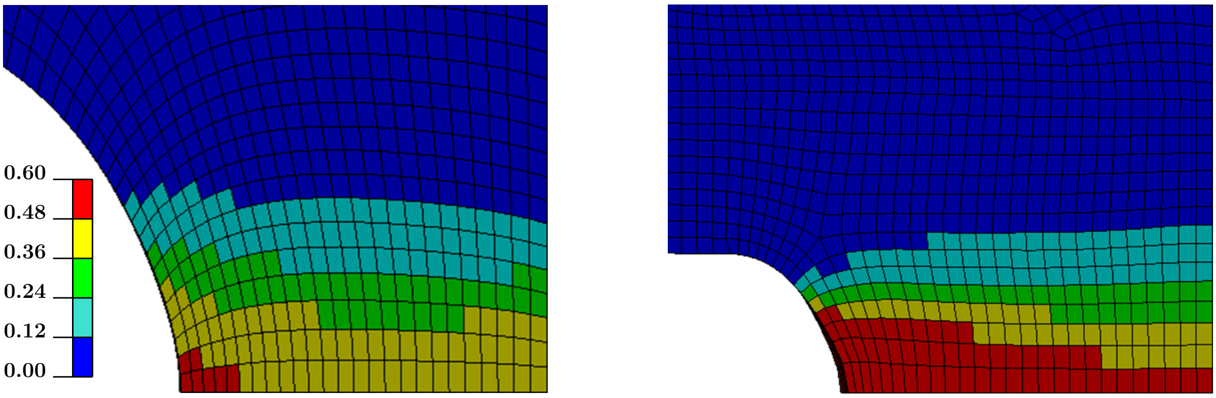

(a) $R = 2\,\mathrm{mm}$ (Coarse).

(b) $R = 0.5\,\mathrm{mm}$ (Coarse).

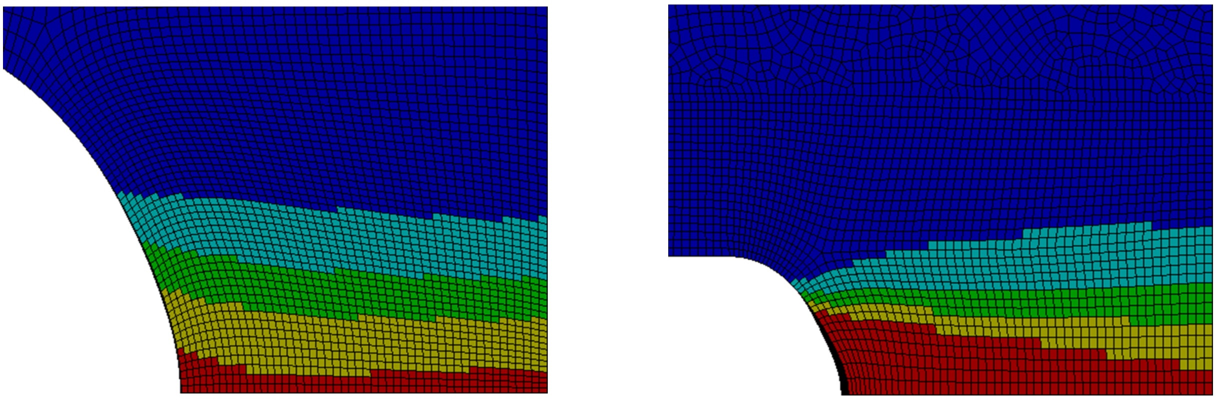

(c) $R = 2\,\mathrm{mm}$ (Fine).

(d) $R = 0.5\,\mathrm{mm}$ (Fine).

Figure 3.23: Plastic strain fields for two mesh densities using a S/R element formulation (*elform 2*) on the notch flat tension specimens (both geometries are compared at the same instant of imposed displacement).

Tension-induced shear specimen

The mesh size sensitivity for the tension-induced shear specimen is shown in Figure 3.24a. Interestingly enough, as the mesh is refined, an oscillatory behavior appears similar to the one observed in the dynamic smooth tension specimen in Figure 3.21. The reason might again be the mesh non-homogeneity where large differences in the size and shape of elements would produce unwanted bounding elastic waves.

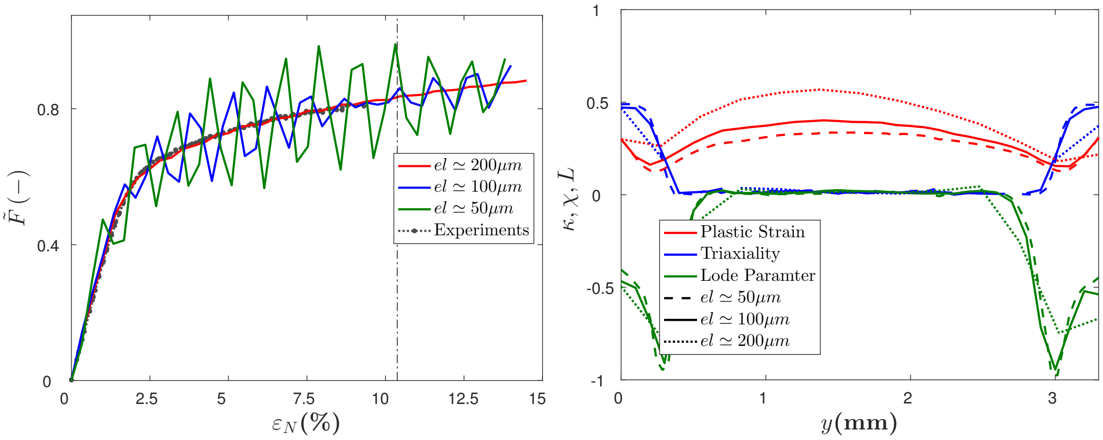

(a) Global mesh dependence.

(b) Local mesh dependence.

Figure 3.24: Left: Force vs. nominal total axial strain. Right: Mesh size sensitivity at the local level at the cross section of the tension-induced shear specimen (S/R element). The spatial measurements on the right are taken at $\varepsilon \simeq 10\,\%$ (marked on the left Figure with a vertical line). $v = 1.6 \times 10^{-3}\,\mathrm{mm/s}$ and $T = 25\,°\mathrm{C}$.

The oscillatory response from the simulation comes from very small oscillations in the force output of the nodes belonging to the boundary condition in the head of the specimen. However, the plastic strain κ, the stress triaxiality ratio χ and the Lode parameter L do not present such behavior as observed in Figure 3.24b. Additionally, the predicted values are weakly dependent on the element size, except maybe for the plastic strain, in which a too rough mesh produces larger errors. It is assumed that an element size of 100 µm is enough for a converged solution.

Figure 3.25 shows the local field for the three meshes considered. At an arbitrary instant t_0 (top figures), plastic flow first starts close to (but not in) the notches. However, as time passes, such strain is concentrated in a band joining both edges. Neither the amount of plastic deformation nor the width of such band are heavily dependent on the element size. Although plastic strains are eventually developed at the notches, the larger amounts of strain are localized near the center under shear loading. Therefore, by assuming a good correlation with the experimental results from Figure 3.15, it is expected that subsequent damage and fracture would initiate near the center as wished. However, as stated above, the more the mesh is refined in the zone of interest, the more chaotic the arrangement of the elements and the bigger the difference in size, which could explain the oscillatory response on the force. Due to the large size of the tension-induced shear specimen model, where the symmetry along the loading direction is no longer possible, the global element size is limited. Therefore, further local refinements in the mesh would only contribute to increase the disparity between element sizes.

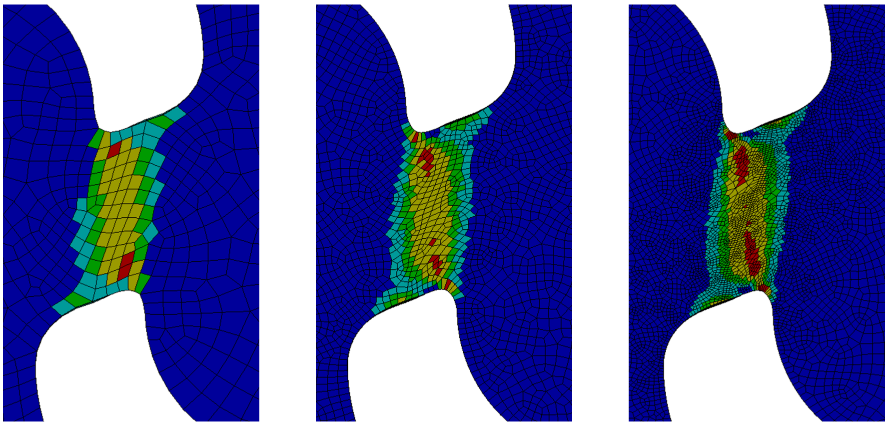
Plastic strain map κ

(a) *size* $\simeq 250\,\mu\text{m}$
$t = t_0$

(b) *size* $\simeq 100\,\mu\text{m}$
$t = t_0$

(c) *size* $\simeq 50\,\mu\text{m}$
$t = t_0$

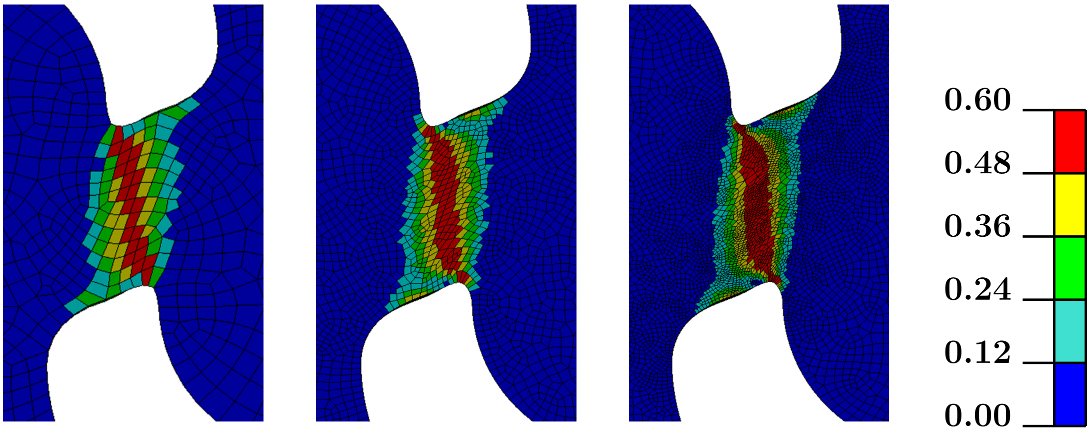
Plastic strain map κ

(d) *size* $\simeq 250\,\mu\text{m}$
$t_1 > t_0$

(e) *size* $\simeq 100\,\mu\text{m}$
$t_1 > t_0$

(f) *size* $\simeq 50\,\mu\text{m}$
$t_1 > t_0$

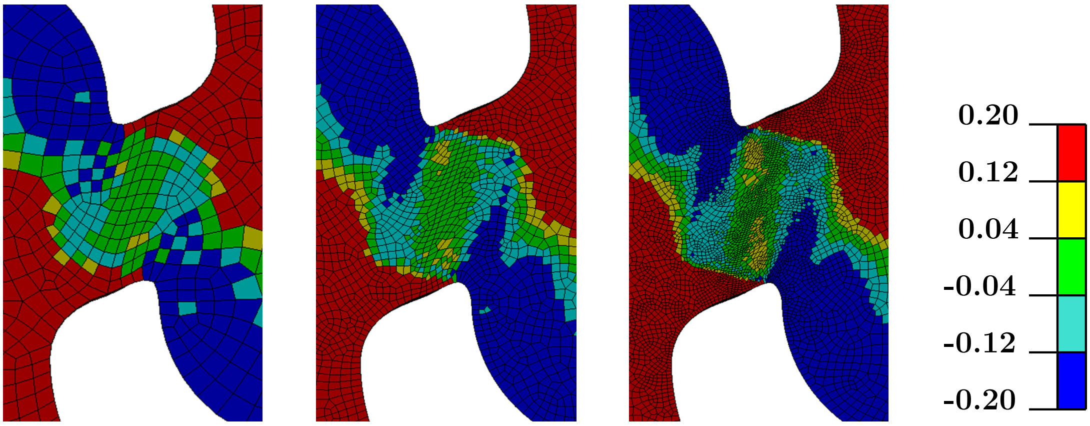
Stress triaxiality map χ

(g) χ, *size* $\simeq 250\,\mu\text{m}$
$t_1 > t_0$

(h) χ, *size* $\simeq 100\,\mu\text{m}$
$t_1 > t_0$

(i) χ, *size* $\simeq 50\,\mu\text{m}$
$t_1 > t_0$

Figure 3.25: Plastic strain and stress triaxiality fields for three mesh densities using a selectively reduced element formulation (*elform 2*) on the tension-induced shear specimen.

3.5.2.3 Discrepancies with experiments

The discrepancies observed in the triaxial tension and the shear-compression simulations are here commented.

Triaxial tension loading

Even though the error between the numerical and experimental curves is smaller than the experimental scatter, the triaxial simulation yields a higher force than the experimental result (see Figure 3.14). If the source of such difference was purely experimental, such general overestimation would not exist for all the cases. Three possible reasons could be behind this disparity: the mesh size, the specimen dimension variations and the yield surface. Regarding the former, it has been shown in Figure 3.22 that the results are not dependent on the mesh density for the strain range measured in the experiments.

The specimens tested may have some deviations from the nominal geometry that can have an impact on the measured force. For instance, a lower tolerance in the notch radius may imply samples machined with a sufficiently close but lower radii producing a higher cross-section area which translates into a smaller nominal force.

Figure 3.26 compares two simulations for two different cross-sections (the nominal cross section and one increased by 5 %). It can be seen that this small variation may induce differences in the measured force similar to the current experimental-numerical gap. Nonetheless, a 5 % variation in the cross section dimension is considerably higher than the tolerances specified. Plus, the measurements later on made on the specimens showed deviations from the nominal geometry of less than 1 % (including the measurement error per se). In addition, it can be seen in the numerical results that the modification of the cross-section would underestimate the initial yield which was otherwise well captured.

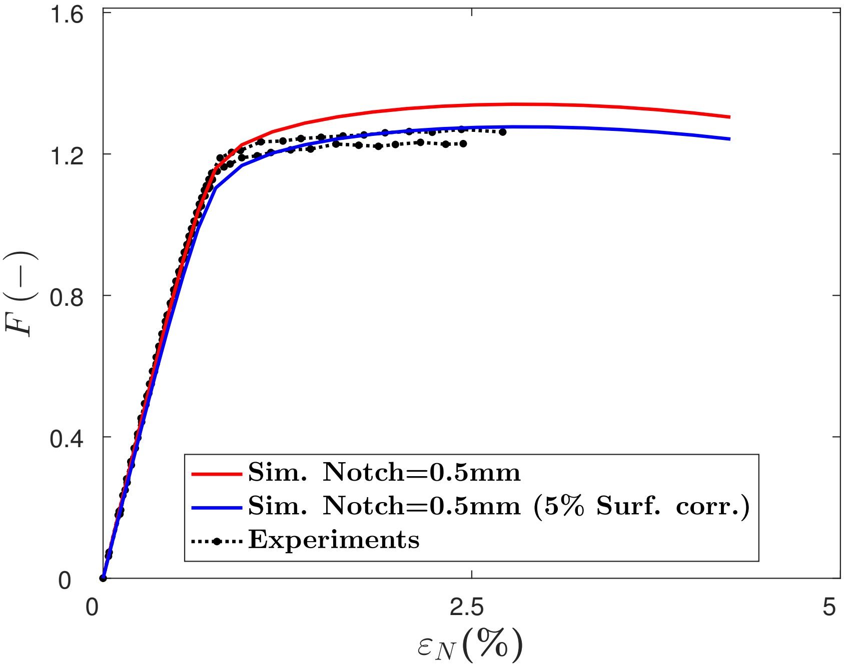

Figure 3.26: Force vs. nominal total axial strain. Numerical and experimental comparison of a notched flat tension specimen of $R = 0.5\,\text{mm}$ at $v = 1.6 \times 10^{-3}\,\text{mm/s}$ and $T = 25\,°\text{C}$. The nominal surface used in the simulation is A_0 and $1.05A_0$.

The last reason for the disparity with the experiments here considered corresponds to a potential incomplete calibration of the yield surface. Figure 3.27 shows the yield surface under plane stresses. The initial calibration captures the eight different uniaxial states. Moreover, the stress states simulated at the center of the notched specimens are accordingly placed (the double notched is not shown because it does not have a plane stress state). In addition, two arbitrary yield surfaces (in dashed lines) can be considered by inducing slight modifications of the anisotropy coefficients. They are roughly obtained by raw visual modification of the material parameters, one is considered to have very small modifications from the initial calibration whereas the other one involves larger variations in the anisotropy coefficients. These new surfaces would still match the experimental results (the identification would not have a unique solution). The flattening induced by these curves on the positive part of the yield surface, where the notch specimens are placed, might allow to reduce the initial overestimation observed in the simulations. However, these modifications would provoke big discrepancies in the normal direction under compression.

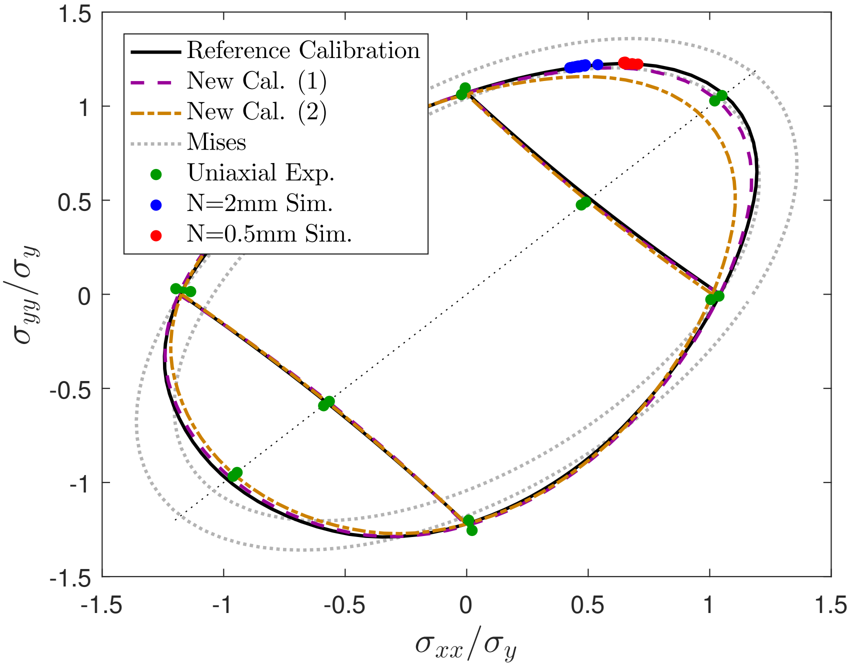

Figure 3.27: Yield loci for three different calibrations at $T = 25\,°\mathrm{C}$. For simplicity the kinematic and viscous components of the stress have been subtracted and the values have been normalized with respect to the rate independent isotropic hardening. The normal direction under tension (compression) is represented with its equivalent biaxial compression (tension) state since the yield criterion is pressure independent. Regarding the diagonal direction, the tensor components with respect to the rolling and transverse directions are accordingly plotted (the shear component is therefore not plotted).

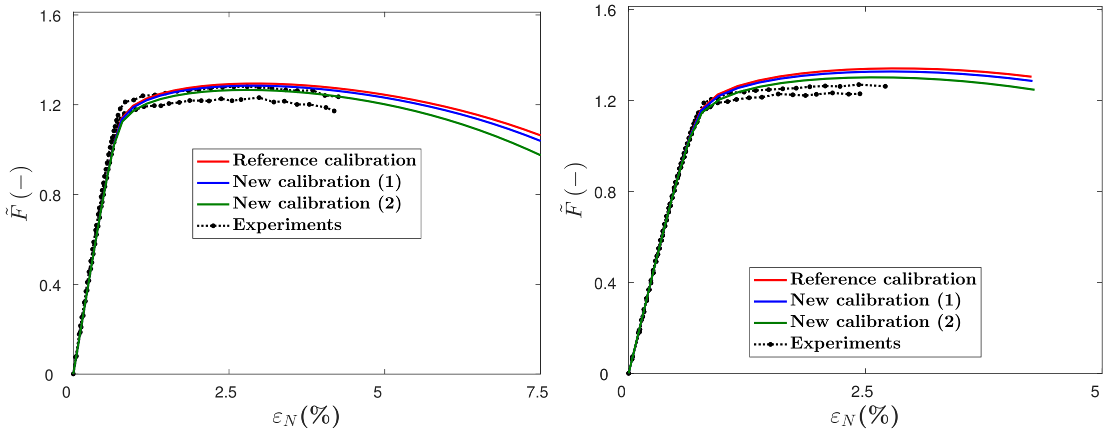

(a) $R = 2\,\mathrm{mm}$ (b) $R = 0.5\,\mathrm{mm}$

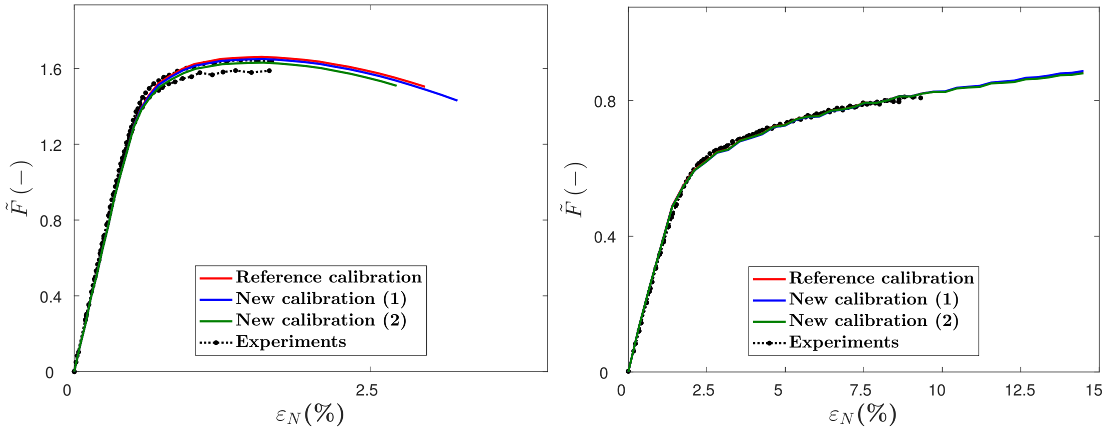

(c) $R = 2\,\mathrm{mm} \times 0.5\,\mathrm{mm}$ (d) Tension-induced shear

Figure 3.28: Force vs. nominal total axial strain. Numerical and experimental comparison of the notched flat tension specimens and tension-induced shear specimen at $v = 1.6 \times 10^{-3}\,\mathrm{mm/s}$ and $T = 25\,°\mathrm{C}$. The yield loci from Figure 3.27 is used.

Hence, with the results from Figure 3.27, it is shown that the uniaxial tests alone do not seem sufficient for the complete identification of the surface. The notched specimens might serve to this purpose by including their experimental curves in the calibration process. However due to the high experimental scattering observed and the long simulation time of these specimens, it is doubtful that an improvement worth considering would be obtained.

Figure 3.28 compares three different material calibrations corresponding each to one of the yield surfaces depicted in Figure 3.27 for the three notch tension and the tension-induced shear geometries. The flattening of the yield surface manages to get the wanted effect of lowering the numerical force estimation except for the shear case, where no apparent effect is visible. The yield locus sensitivity is much more apparent for the $R = 0.5\,\mathrm{mm}$ notched specimen where the deviations from experiments were initially larger. However, the simulated force remains still overestimated after a strong modification of the anisotropy surface which compromise the behavior under the normal direction. This might justify the role of hydro-static pressure on the plastic problem, not as a damage-driving factor but as a necessary variable for the plastic criterion under high stress triaxialities.

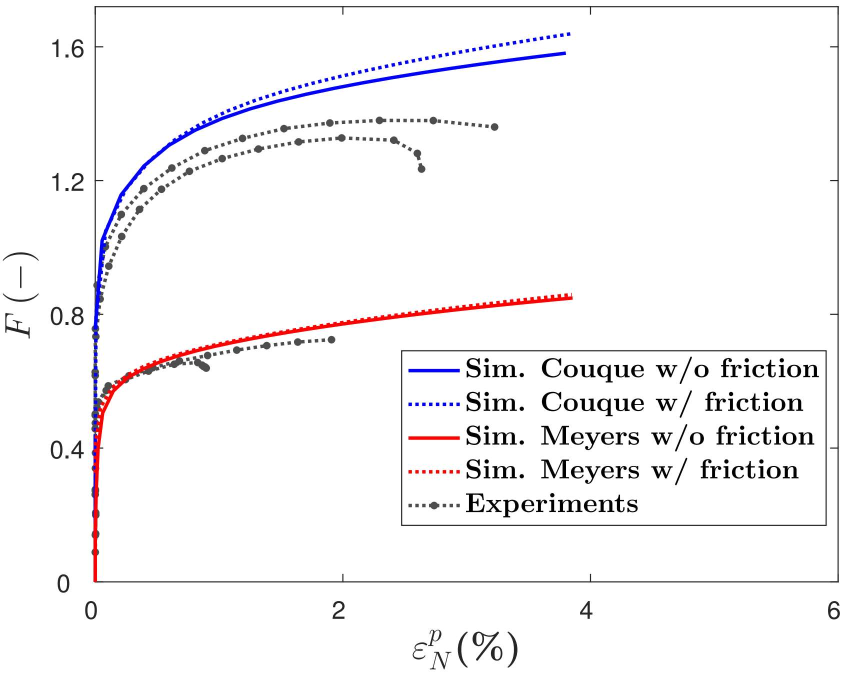

Figure 3.29: Force vs. nominal total axial strain. Numerical and experimental comparison of shear-compression specimens at quasi-static loading rate $v = 8 \times 10^{-3}$ mm/s and $T =$ 25 °C. Transverse displacement is restricted at the base of the specimen in one of the simulations.

Shear-compression loading

The simulations shown in Figure 3.16 have overestimated the experimental force measurements. The mesh sensitivity have proven to be negligible for the smooth, notched and tension-induced shear specimens and therefore it is not considered here.

Figure 3.29 shows a new comparison of the simulations with two extreme boundary conditions. The first case considers no friction between the specimen and the machine grips (as simulated in Figure 3.16). Since some lubricant was used during the experimental campaign, this case is expected to be close to reality. For the second case, a simulation assuming complete friction (no transverse displacement) with respect to the machine is also carried out.

For the Meyers geometry there is practically no difference. However, for the Couque geometry, the difference between both boundary conditions is more noticeable as the compression induces an outward force. Even though the strong friction case is not realistic, it is considered as an upper limit in our modeling. However, it is not sufficient to explain the disparity with the experimental results. It can be concluded that the current model can not reproduce the mechanical behavior under very negative stress triaxiality ratios.

3.6 Complementary comments

Some final aspects aspects such as the loading paths and the self-heating induced softening at high strain rates are here discussed.

3.6.1 Loading paths

The loading path may be described through the stress triaxiality ratio evolution that the different specimens have undergone as plastic deformation evolves. It can provide with an insight on how damage and subsequent fracture can occur as a function of the stress state. Six of the above geometries are considered: the (i) flat and (ii-iv) notched and (v) tension-induced shear specimens and the (vi) simple compression geometry. The hat-shaped specimens have been left out of the study due to the disparity between numerical and experimental results which should be further analyzed.

Figure 3.30 shows the different loading paths. They were extracted from simulations with an element size of approximately 100 µm of the S/R type. Such size was assumed to yield converged results for the range of strains considered here. The element whose loading path has been plotted is the innermost element in the cross-section of the considered specimens, i.e. the furthest point from the notches or edges. The choice is done assuming the more important stress triaxiality χ values are found away from any free surface. However, the notched geometry of radius $R = 0.5$ mm has a loading path from an element close to the notches (as justified by the microscropic observations and corroborated below).

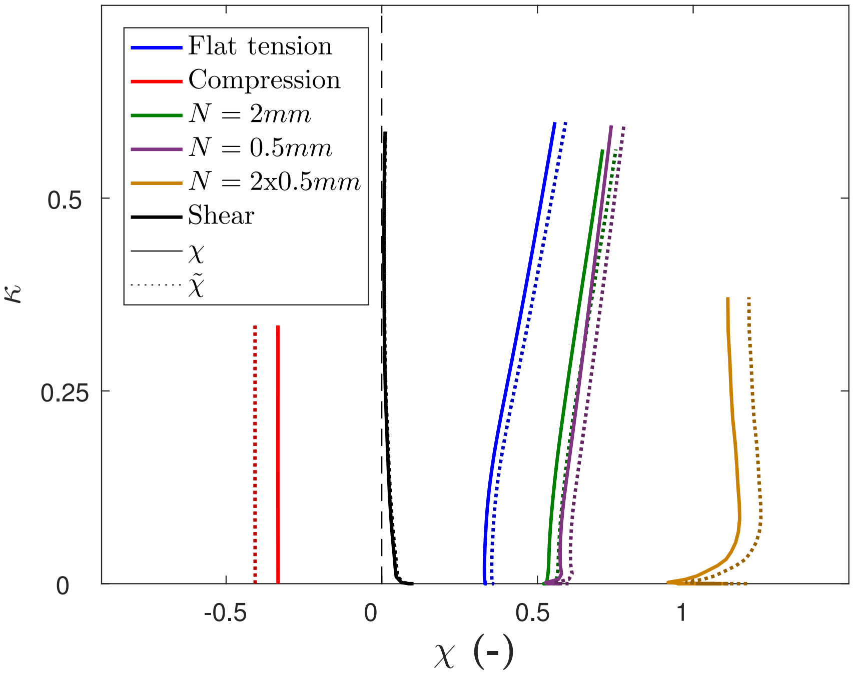

Figure 3.30: Loading paths for the different geometries. $\dot{\varepsilon} \simeq 10^{-3}\,\text{s}^{-1}$, $T = 25\,°\text{C}$ and Transverse direction TD. From left to right: simple compression, tension-induced shear, flat tension, simple notched ($R = 2$ mm and $R = 0.5$ mm) and double notched specimens. Definitions for the stress triaxiality can be found in Equations 1.1 and 3.38.

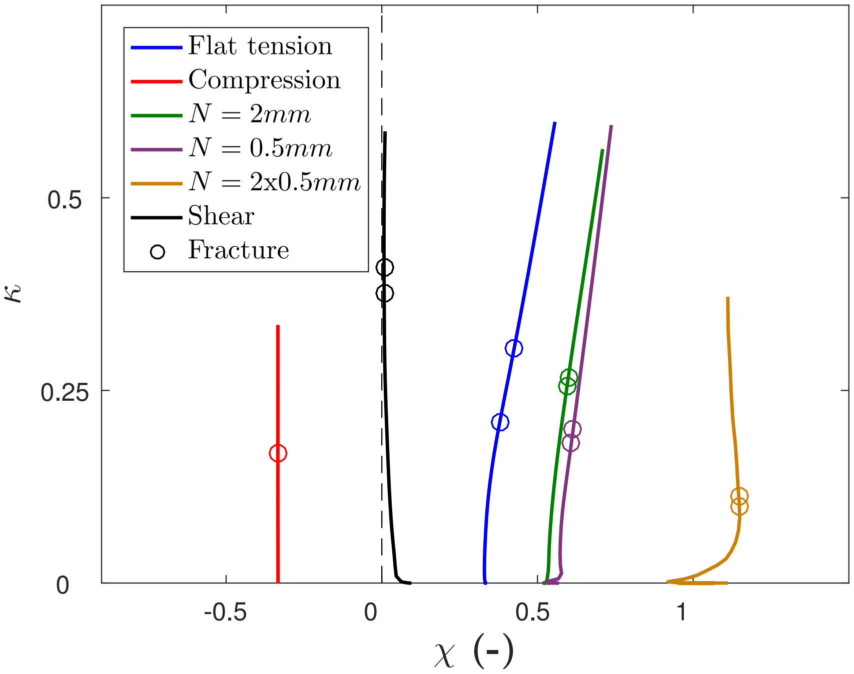

Figure 3.31: Loading paths for the different geometries. $\dot{\varepsilon} \simeq 10^{-3}\,\mathrm{s}^{-1}$, $T = 25\,°\mathrm{C}$ and Transverse direction TD (stress triaxiality from Equation 1.1). From left to right: simple compression, tension-induced shear, flat tension, simple notched ($R = 2\,\mathrm{mm}$ and $R = 0.5\,\mathrm{mm}$) and double notched specimens. The dots indicate an estimate of the plastic strain at fracture.

Depending on the definition used for the stress triaxility ratio in Equations 1.1 and 3.38, the loading paths may appreciably change (see Figure 3.30). For instance, $\tilde{\chi}$ in compression is slightly more negative ($\tilde{\chi} < \chi \simeq -1/3$). Conversely, the tension specimens present higher values of triaxiality. However, no big discrepancies are seen for the shear conditions. The first definition χ (Equation 1.1) is retained for the rest of the section.

According to Figure 3.30, regarding the notched specimens, the stress triaxiality χ are comparatively more positive than for the flat tension geometry, as expected. Both simple notches of $R = 2\,\mathrm{mm}$ and $R = 0.5\,\mathrm{mm}$ yield relatively close results. On the other hand, the double notched specimen reaches very positive triaxiality values ($\chi > 1$) which results in a low ductility as observed in the experiments. Surprisingly enough, after some initial plastic deformation, the loading path becomes proportional with values close 1.2. Finally, the tension-induced shear specimen deforms under near pure shear stress.

Additionally, Figure 3.31 displays an estimation of the points at which the different geometries fail. In order to find those points, the experimental nominal strain at fracture measured with the extensometer is compared with the virtual extensometer placed in the simulation. The instant at which the specimen is supposed to fail is used to read the plastic strain on the studied element (the innermost element with the higher triaxiality ratio, not necessarily the most deformed element). It is recalled that the element used in the $R = 0.5\,\mathrm{mm}$ notched specimen is not placed in the center but close to the edges.

The fracture points show a tendency towards smaller strain to fracture whenever the triaxiality increases in terms of absolute values. This result is appreciably different from the known fracture yield locus obtained by Bao and Wierzbicki [106 ; 154] where the

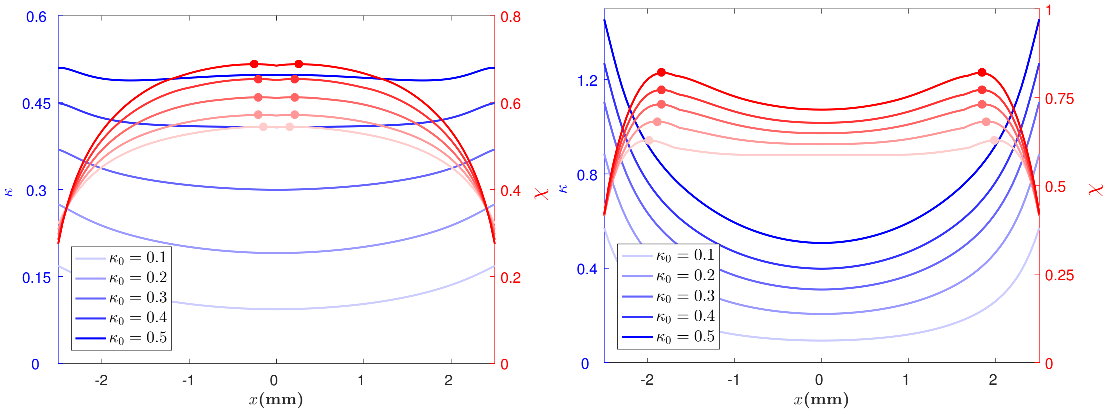

(a) $R = 2\,\mathrm{mm}$. (b) $R = 0.5\,\mathrm{mm}$.

Figure 3.32: Plastic strain and stress triaxiality ratio vs. the lateral coordinate of the simple notch specimens at several instants. $\dot{\varepsilon} \simeq 10^{-3}\,\mathrm{s}^{-1}$ and $T = 25\,°\mathrm{C}$ and stress triaxiality from Equation 1.1. The dots indicate the maximum value of stress triaxiality.

maximum strain to fracture is found under uniaxial tension loading with a local minimum under shear loading (see Figure 2.3a in Chapter 2). Three features are highlighted and briefly discussed: (i) consistent decrease in the strain to fracture under positive stress triaxiality ratios, (ii) largest strain to fracture under shear loading and (iii) low strain to fracture under negative stress triaxialities.

Positive stress triaxiality ratios

Regarding the positive stress triaxiality range, the strain to fracture decreases as the stress triaxiality χ becomes more positive (see Figure 3.31). This result is in accord with Rice and Tracey [109]/Johnson-Cook [110] fracture loci.

In Figure 3.32 are plotted the plastic strain and the stress triaxiality ratio along the width of both simple notched specimens at several strain amounts (the notch being the extremes in the graph).

Concerning the bigger notch ($R = 2\,\mathrm{mm}$ and lower stress triaxiality χ), the maximum values of stress triaxiality are seen at the center of the sample and it quickly decreases near the notch edges. As for the plastic strain, it is relatively constant irrespective of the position in the sample (especially at large strain). On the other hand, the inverse scenario is seen for the smaller notch ($R = 0.5\,\mathrm{mm}$ and higher stress triaxiality χ). The stress triaxiality can be considered quasi-constant in most part of the sample (the maximum values are found close to the edges) whereas the plastic strain is substantially higher near the notches where it reaches up to three times the level found at the center.

It can be speculated that for the former specimen, fracture would occur at the center where triaxiality is appreciably higher. Contrarily, the fracture of the small notched tension specimen is likely to occur near (although not exactly at) the edges of the sample where plastic strain and triaxiality reach the highest values. These conclusions are in good agreement with the microscope observations done in Chapter 1, particularly in Figures 1.44 and 1.45. In these micrographs, fracture for the $R = 2\,\mathrm{mm}$ notch seems to emanate from the center as opposed with the $R = 0.5\,\mathrm{mm}$ notch that seem to show a spread of damage from the edges.

Nil stress triaxiality ratios

The second feature worth noting is the relatively high plastic deformation at fracture under shear with respect to the flat tension test, see Figure 3.31. It can be due to the fact that under shear conditions, void nucleation and growth mechanisms are limited with respect to other loadings involving higher stress triaxiality χ.

Negative stress triaxiality ratios

Last aspect to point out is the low strain to fracture for uniaxial compression, see Figure 3.31. An early unstable fracture has been observed for the compression specimens (see Figure 1.21 in Chapter 1). The reasons behind are thought to be entirely different as with positive triaxialities. The broken specimens show a clear shear band that, although filled with elongated dimples, might be explained by a localization before damage of the material. This is in close agreement with the works of Lee and Lin [43 ; 46] where their compression specimens also failed by development of a shear band with dimples inside. Although they remarked a shear strain localization, they did not claim a premature failure of their sample as it has been evidenced here. Therefore, when considering a fracture criterion for this material, both localization and void damage are two important aspects to take into account. Failure would thus occur when one of the two processes would take place, the order of which is thought to be extremely dependent on the stress triaxiality ratio.

3.6.2 Influence of the inelastic heat fraction β

The self-heating induced softening is here evaluated first on a Representative Volume Element (see Figure 3.4a) and then on the uniaxial tension and compression specimens at high strain rates.

Three cases are compared for three different values of the inelastic heat fraction:

$\beta = 0$ No self-heating is considered

$\beta = 0.8$ The induced self-heating is simulated using an arbitrary constant value of the Taylor-Quinney coefficient as seen in literature

$\beta = \beta(\mathcal{D})$ The induced self-heating is based on the plastic dissipation

Uniaxial tension loading on an RVE

Figure 3.33 shows the softening obtained when considering adiabatic conditions under uniaxial tension.

The computed increase in temperature with a consistent β reaches 140 °C. The inelastic heat fraction computed throughout the simulation starts at 0.9, slightly increases and then finally slowly approaches the value of 0.8. The stress-strain curves for both adiabatic curves in Figure 3.33 are relatively similar. However, it can be seen that the estimation of temperature by both methods diverges by an amount which becomes non negligible at large strain.

Uniaxial tension smooth specimen

Figure 3.34 shows the superimposition of experimental and computed load/strain curves for the monotonic tension specimens. The finite element model used is equivalent to that described for the notched tension specimen in Figure 3.13a. It can be verified that the quasi-static loading is well captured until necking coherently with the results of the identification in the previous chapter (see Figure 2.17). On the other hand the dynamic tension tests are simulated by considering both isothermal and adiabatic conditions using a consistent β. It can be observed that with the latter, the thermal softening produces a better match with the experimental data.

Uniaxial compression specimen

Figure 3.35 shows the superimposed numerical simulations and experimental curves regarding simple compression tests. The finite element model used is equivalent to that described for the shear-compression specimen in Figure 3.13c. As with the hat-shape specimens, the force-displacement curves are plotted with the elastic component removed. The adiabatic conditions using a consistent β considered for the dynamic simulation prove a better performance at capturing the temperature-dependent hardening rate. However, the stress level is overall underestimated for both regimes. The sources for such disparities mostly resides in the calibration stage. Indeed, Figures 2.15 and 2.18 show slight underestimations with respect to experiments.

The friction effect was not evaluated in the simple compression case since the rupture occurs at an early state of deformation and the observations made for both broken and non-broken specimens showed no sign of barreling.

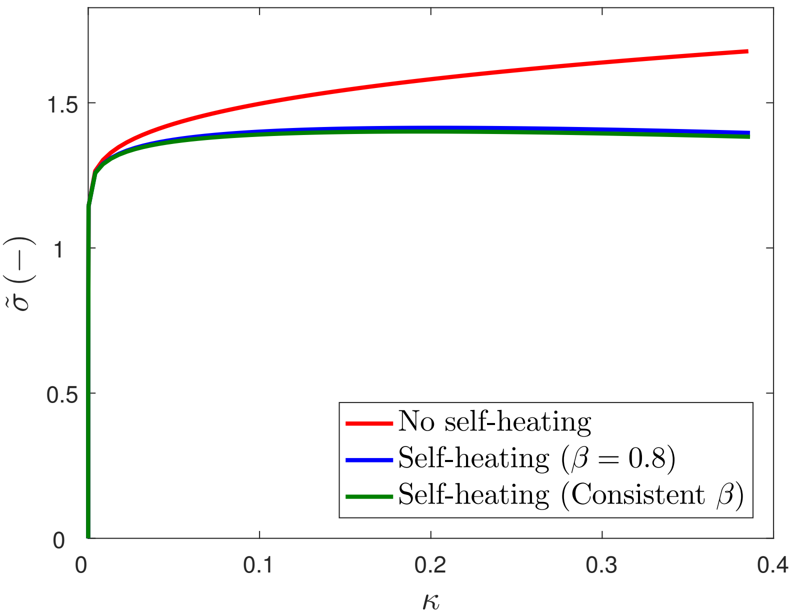

(a) Stress vs. plastic strain.

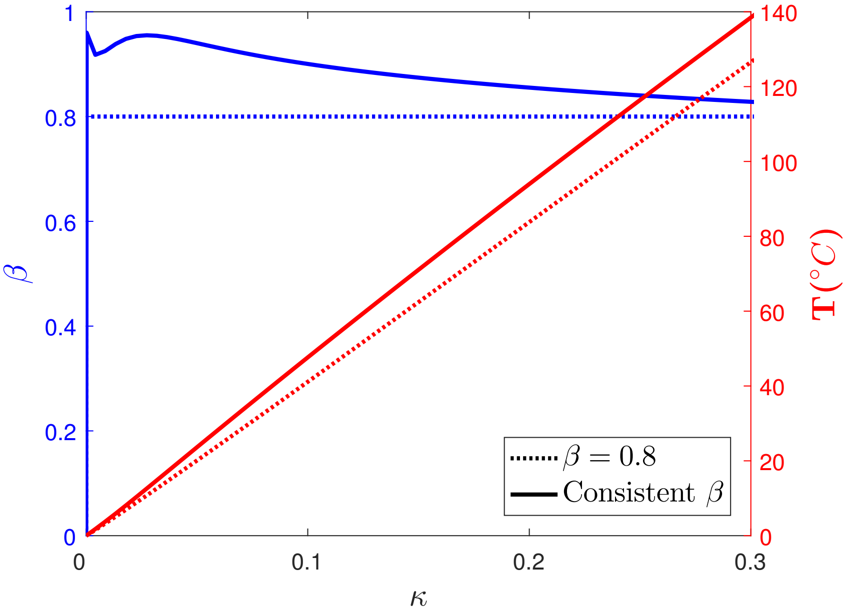

(b) Inelastic heat fraction and temperature vs. plastic strain.

Figure 3.33: Uniaxial simulation on an RVE. Plastic dissipation induced self-heating at $\dot{\kappa} \simeq 10^3\,\mathrm{s}^{-1}$ and $T = 25\,^\circ\mathrm{C}$.

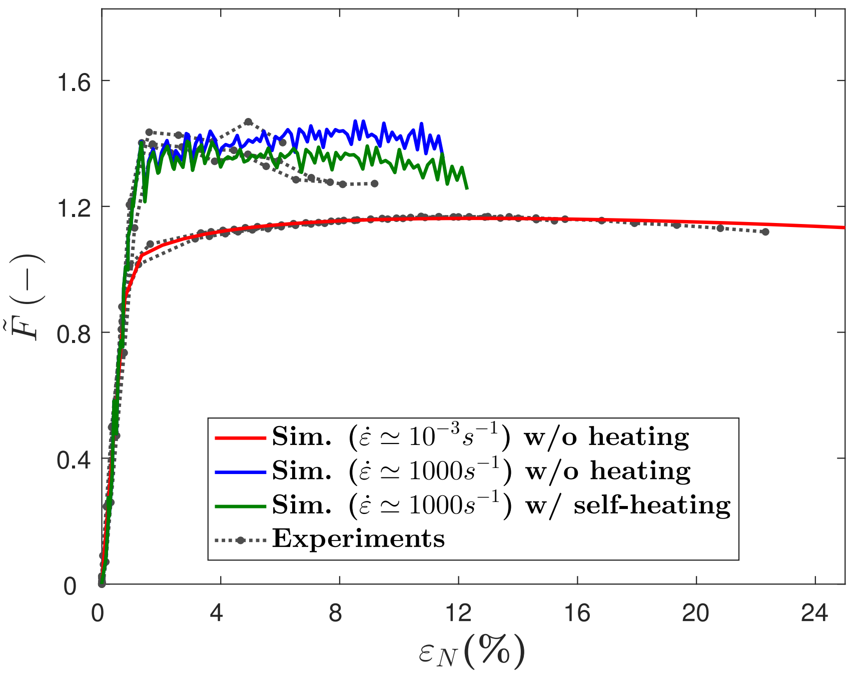

Figure 3.34: Force vs. nominal total axial strain. Numerical and experimental comparison of a smooth flat tension specimen at $T = 25\,°\mathrm{C}$ and Transverse direction. The inelastic self-heating induced softening is compared.

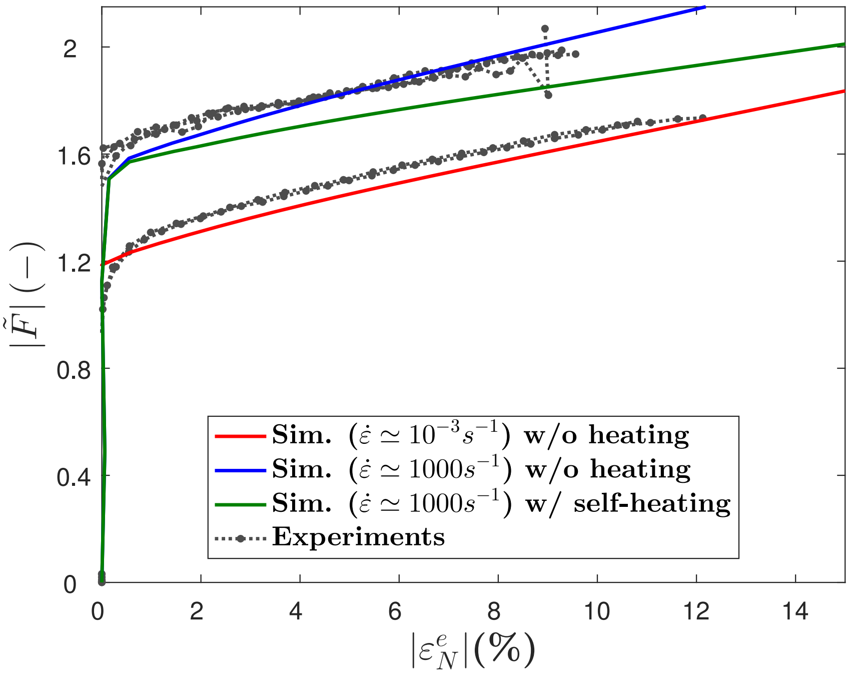

Figure 3.35: Force vs. nominal total axial strain. Numerical and experimental comparison of uniaxial compression at $T = 25\,°\mathrm{C}$ and Transverse direction. The inelastic self-heating induced softening is compared.

3.7 Concluding remarks

This chapter has focused on the numerical implications of the constitutive model previously presented: (i) the user material algorithm used, (ii) its comparison with an existing commercial code, (iii) the model verification at the specimen scale.

Within an explicit time integration scheme, the plastic strain increment is directly deduced from the viscoplastic Norton-Perzyna formulation. A first order scheme of the integration has been shown to delay instabilities and reduce incremental errors. The variables, namely the stress, the temperature and the kinematic stress are updated in a Q-rotated frame to ensure objectivity. A verification at the RVE scale with the implicit Z-set software shows a good agreement for various types of simple loadings.

The user material and the model performance on the different specimens show satisfactory results. Nevertheless, some disparities have been found and should be addressed in the future. They include (i) the slight overestimation in the notched flat tension specimens, (ii) the larger one in the hat-shaped geometries and (iii) the underestimation in uniaxial compression.

The first two deviations are thought to be explained by the yield surface employed. It has been initially assumed that the yield locus definition is pressure independent yet discrepancies arise for larger values of this variable (positive and negative). Regarding the simple compression specimens, the differences with the experimental data mainly come from the calibration stages. The anisotropy and viscosity were first fixed before identifying the hardening of the material.

Finally, the simulations have also provided interesting results concerning the loading paths for a future modeling of the failure of the material. A decrease in the strain to fracture is observed as the material is tested to higher triaxialities (positive and negative). For positive triaxilities, the fracture is thought to originate from diffuse damage mechanisms. For negative triaxialities, a localisation of strain is speculated. Therefore, two fracture loci could be considered in further work.

Conclusions and perspectives

General conclusion

This work focuses on a Ti-6Al-4V titanium alloy known for its high strength-to-weight ratio and good toughness [1] and accordingly considered as a promising candidate for the leading edge of multicomponent fan blades.

The constitutive modeling of Ti-6Al-4V titanium alloy under consideration has been conducted paying attention to three important aspects: (i) the experimental characterization, (ii) the constitutive modeling and (iii) its numerical implementation and verification.

Experimental characterization

In order to emulate all the conditions found in a ballistic event on aircraft engines, several sample geometries as well as various experimental set-ups have been employed in an extensive experimental campaign. The latter consisted in tension, compression and shear tests performed at various low and high strain rates and temperatures, and under monotonic as well as alternate loading path. Three sources of anisotropy have been found during the characterization: weak textured-induced orthotropy, kinematic hardening and strength asymmetry. In addition, strain and strain rate isotropic hardening and thermal softening have been evidenced and quantified. Although the strain rate induced overstress does not exhibit any anisotropy, a temperature dependence is observed (tentatively neglected). Regarding the temperature sensitivity, its effect is taken into account for potential self-heating induced thermal softening that can occur under rapid loadings.

Concerning the damage of the material, the causes of fracture are far from being clear. While loadings performed at positive triaxiality ratios have shown evidence of diffuse damage in the form of voids, early failure in the form of shear band is observed for negative stress triaxialities.

Constitutive modeling

A model accounting for all this features has been accordingly proposed. Concerning the anisotropy, it consists in a combination of the yield criteria proposed by Cazacu et al. [73] and Karafillis and Boyce [72] to describe strength differential, and coupled orthotropy-kinematic hardening. In addition, the isotropic hardening has been coupled with the kinematic hardening in order to better reproduce the onset of plastic flow during load reversal following the approach of Carbonnière et al. [97]. The Norton-Perzyna [61 ; 62] formulation correctly predicts the flow stress dependence on the loading rate. As for the temperature, its effect is included in the isotropic hardening with a softening function.

Regarding self-heating under adiabatic conditions, a consistent approach based on the plastic dissipation is used for the computation of the temperature rise.

Given the large number of parameters (strain, strain rate, temperature, loading orientation, strength asymmetry, isotropic and kinematic hardening) it accounts for, this model is expected to apply to a wide range of engineering materials without significant modifications of its structure. In particular, a change in the titanium alloy thermo-mechanical treatment is expected to result in a change in some material constant values and not in the model itself.

An identification of the proposed model on an RVE, using the experimental data from uniaxial tension and compression tests at various strain rates and temperatures has been carried out. The model shows a satisfying capability of reproducing the features observed in the experimental campaign.

Numerical implementation

The model has been implemented as a user material subroutine in the commercial finite element computation code LS-DYNA and its performances have been evaluated at the structure scale considering notched and shear specimens.

The user material and the model performance on the different specimens show satisfying results. The modeling of adiabatic self-heating at high speed loadings matches accordingly the strain hardening rate observed during the dynamic tests. Nevertheless, some disparities have been found with experiments as the stress triaxiality becomes high (in absolute value).

Finally, the simulations have also provided interesting results concerning the loading paths for a future modeling of the failure of the material. A decrease in the strain to fracture is observed as the material is tested at higher triaxialities (positive and negative). For positive triaxilities, the fracture is thought to originate from diffuse damage mechanisms. However, for negative triaxialities, a localisation of strain is speculated. Therefore, two fracture loci could be considered in further work.

Future works

Some perspectives regarding the experimental characterization, the constitutive modeling and its numerical implementation are worth considering in the short and long term.

Experimental characterization

In the short term, the temperature characterization of the material behavior should be extended. In the present work, the effect of high temperatures has been considered only on the isotropic hardening; lower temperatures should also be considered, e.g. the range ($-50\,^{\circ}$C-25 °C). Moreover, temperature sensitivity could be included in the viscous component, after a more systematic characterization. In addition, the effect of temperature on kinematic hardening could be studied.

Second, the diffuse damage vs. localization scenarios must be addressed. Although both types of fracture occur in the present Ti-6Al-4V, it is necessary to discern which one precedes which and under which conditions one scenario is favored over the other. Real time monitoring of the strain field by DIC in tension-induced shear specimens during quasi static tests (possibly, in a SEM to get a high imaging resolution) might provide some useful elements, although it would be limited to the surface. To get information concerning the volume, *in situ* tests on a synchrotron beamline with computed micro-tomography or laminography would be more appropriate.

In the long term, the present characterization of this material should be compared with other Ti-6Al-4V microstructures induced by different thermo-mechanical processes. This would allow to extend the knowledge on this alloy and to assess the impact of the microstructure and forming processes on the mechanical properties.

Last, it would be interesting to run dynamic tests with temperature measurements to assess the validity of the inelastic heat fraction based evaluation.

Constitutive modeling

In the short term, the strain rate-induced overstress must account for temperature. Indeed by considering the extended yield stress $\bar{\sigma}_y = \sigma_y + \sigma_v$, Figure 1.34 showed a decrease in $\bar{\sigma}_y$ and σ_v as temperature is increased. However, only the strain rate independent yield stress was assumed to depend on temperature $\sigma_y = \sigma_y (T, ...)$. A formulation of the type $\bar{\sigma}_y (T, ...) = g (T) R (...) + \tilde{g} (T) \sigma_v (...)$ could be pursued.

The disparities found in the model with respect to experiments at high stress triaxialities $|\chi| \gg 1/3$ should be further investigated. Assuming that such discrepancies are not coming from experimental scatter (non negligible in the present material), an extended calibration using notched specimens may help to fully identify the anisotropic plasticity matrix. However, it is strongly suspected that a pressure-independent yield criterion is insufficient. The stress triaxiality χ or the Lode parameter L might be necessary to correctly capture the anisotropic plasticity. For instance, the hydrostatic-pressure was taken into consideration in the expression of the strain rate-induced overstress in Longere [91].

Linked with further investigation on diffuse damage and localization proposed in the experimental characterization, the choice of a damage simulation strategy, be it through a damage indicator or a damage variable should be done. The current work has shown no correlation with the experimental fracture loci reported by Bao and Wierzbicki [106] nor with the compression experiments on Ti-6Al-4V done in Longère and Dragon [37] (where they did not obtain an early failure under compression) which suggests that no universal fracture locus can be postulated.

Numerical implementation

Even though a mesh sensitivity and element type formulation analysis have been carried out in the present work, the user subroutine should be tested on a wider range of finite element formulations, such as shell formulation or unstructured meshes, due to the constraints that might be imposed for the finite element model (for reasons unrelated to the material but strongly connected to the bird strike problem), e.g. the imposition of a minimum element size or the use of a certain type of elements in the simulation.

As for the spatial discretization when attempting to reproduce crack formation (initiation and propagation), alternative formulations might be needed to be used to ensure mesh objectivity notably of the crack path, as e.g. XFEM (see Wolf et al. [155]).

In the long term, the material model should be tested on a bigger scale. First, in the deep drawing problem for instance, where abundant examples are available in literature, to compare the performance with existing models. Later on, it could be implemented in the bird strike finite element model in order to assess the improvements done with the advanced modeling developed in this work.

Bibliography

[1] G. Welsch, R. Boyer, and E. W. Collings, *Materials Properties Handbook: Titanium Alloys.* Materials properties handbook, ASM International, 1993. *3 citations in pages 1, 8, et 141*

[2] C. Leyens and M. Peters, *Titanium and titanium alloys: fundamentals and applications.* John Wiley & Sons, 2003. *2 citations in pages 8 et 9*

[3] R. Boyer, "An overview on the use of titanium in the aerospace industry," *Materials Science and Engineering: A*, vol. 213, pp. 103–114, aug 1996. *Cited in page 8*

[4] C. Zheng, F. Wang, X. Cheng, K. Fu, J. Liu, Y. Wang, T. Liu, and Z. Zhu, "Effect of microstructures on ballistic impact property of Ti–6Al–4V targets," *Materials Science and Engineering: A*, vol. 608, pp. 53–62, jul 2014. *2 citations in pages 8 et 10*

[5] K. Le Biavant, S. Pommier, and C. Prioul, "Local texture and fatigue crack initiation in a Ti-6Al-4V titanium alloy," *Fatigue & Fracture of Engineering Materials & Structures*, vol. 25, pp. 527–545, 2002. *2 citations in pages 9 et 15*

[6] D. G. Prakash, R. Ding, R. J. Moat, I. Jones, P. J. Withers, J. Q. da Fonseca, and M. Preuss, "Deformation twinning in Ti-6Al-4V during low strain rate deformation to moderate strains at room temperature," *Materials Science and Engineering A*, vol. 527, no. 21-22, pp. 5734–5744, 2010. *2 citations in pages 9 et 11*

[7] F. Coghe, W. Tirry, L. Rabet, D. Schryvers, and P. Van Houtte, "Importance of twinning in static and dynamic compression of a Ti-6Al-4V titanium alloy with an equiaxed microstructure," *Materials Science and Engineering A*, vol. 537, no. 2012, pp. 1–10, 2012. *Cited in page 9*

[8] G. I. Taylor, "Plastic strain in metals," *Journal of the Institute of Metals*, vol. 62, pp. 307–324, 1938. *Cited in page 9*

[9] M. H. Yoo, "Slip, twinning, and fracture in hexagonal close-packed metals," *Metallurgical Transactions A*, vol. 12, no. 3, pp. 409–418, 1981. *Cited in page 9*

[10] V. Hasija, S. Ghosh, M. J. Mills, and D. S. Joseph, "Deformation and creep modeling in polycrystalline Ti–6Al alloys," *Acta Materialia*, vol. 51, pp. 4533–4549, sep 2003. *2 citations in pages 9 et 10*

[11] J. Mayeur and D. McDowell, "A three-dimensional crystal plasticity model for duplex Ti–6Al–4V," *International Journal of Plasticity*, vol. 23, pp. 1457–1485, sep 2007. *2 citations in pages 9 et 64*

[12] M. Zhang, J. Zhang, and D. McDowell, "Microstructure-based crystal plasticity modeling of cyclic deformation of Ti–6Al–4V," *International Journal of Plasticity*, vol. 23, pp. 1328–1348, aug 2007. *2 citations in pages 9 et 64*

[13] P. G. Partridge, "The crystallography and deformation modes of hexagonal close-packed metals," *Metallurgical Reviews*, vol. 12, pp. 169–194, jan 1967. *Cited in page 9*

[14] J. C. Williams, R. G. Baggerly, and N. E. Paton, "Deformation behavior of HCP Ti-Al alloy single crystals," *Metallurgical and Materials Transactions A*, vol. 33, no. 3, pp. 837–850, 2002. *Cited in page 9*

[15] M. A. Lowden and W. B. Hutchinson, "Texture strengthening and strength differential in titanium-6Al-4V," *Metallurgical Transactions A*, vol. 6, no. 2, pp. 441–448, 1975. *3 citations in pages 11, 15, et 18*

[16] G. Gilles, W. Hammami, V. Libertiaux, O. Cazacu, J. Yoon, T. Kuwabara, A. Habraken, and L. Duchêne, "Experimental characterization and elasto-plastic modeling of the quasi-static mechanical response of TA-6 V at room temperature," *International Journal of Solids and Structures*, vol. 48, pp. 1277–1289, may 2011. *Cited in page 11*

[17] H. P. Lee, C. Esling, and H. J. Bunge, "Development of the Rolling Texture in Titanium," *Textures Microstruct.*, vol. 7, 1988. *2 citations in pages 11 et 15*

[18] S. Zaefferer, "A study of active deformation systems in titanium alloys: dependence on alloy composition and correlation with deformation texture," *Materials Science and Engineering: A*, vol. 344, pp. 20–30, mar 2003. *2 citations in pages 11 et 15*

[19] V. Tuninetti, G. Gilles, O. Milis, T. Pardoen, and A. Habraken, "Anisotropy and tension–compression asymmetry modeling of the room temperature plastic response of Ti–6Al–4V," *International Journal of Plasticity*, vol. 67, pp. 53–68, apr 2015. *3 citations in pages 11, 12, et 66*

[20] A. S. Khan, S. Yu, and H. Liu, "Deformation induced anisotropic responses of Ti–6Al–4V alloy Part II: A strain rate and temperature dependent anisotropic yield criterion," *International Journal of Plasticity*, vol. 38, pp. 14–26, nov 2012. *4 citations in pages 11, 66, 67, et 76*

[21] B. Revil-Baudard, O. Cazacu, P. Flater, and G. Kleiser, "Plastic deformation of high-purity α-titanium: Model development and validation using the Taylor cylinder impact test," *Mechanics of Materials*, vol. 80, pp. 264–275, jan 2015. *Cited in page 11*

[22] F. Kabirian and A. S. Khan, "Anisotropic yield criteria in σ-τ Stress space for materials with yield asymmetry," *International Journal of Solids and Structures*, 2015. *Cited in page 11*

[23] D. Steglich, X. Tian, and J. Besson, "Mechanism-based modelling of plastic deformation in magnesium alloys," *European Journal of Mechanics, A/Solids*, vol. 55, pp. 289–303, 2016. *2 citations in pages 11 et 66*

[24] G. Kleiser, B. Revil-Baudard, O. Cazacu, and C. L. Pasiliao, "Plastic deformation of polycrystalline molybdenum: Experimental data and macroscopic model accounting for its anisotropy and tension–compression asymmetry," *International Journal of Solids and Structures*, vol. 75-76, pp. 287–298, dec 2015. *Cited in page 11*

[25] I. Jones and W. B. Hutchinson, "Stress-state dependence of slip in Titanium-6Al-4V and other H.C.P. metals," *Acta Metallurgica*, vol. 29, no. 6, pp. 951 – 968, 1981. *Cited in page 11*

[26] W. F. Hosford and T. J. Allen, "Twinning and directional slip as a cause for a strength differential effect," *Metallurgical Transactions*, vol. 4, no. 5, pp. 1424–1425, 1973. *Cited in page 11*

[27] T. Tancogne-Dejean, C. C. Roth, U. Woy, and D. Mohr, "Probabilistic fracture of Ti-6Al-4V made through additive layer manufacturing," *International Journal of Plasticity*, vol. 78, pp. 145–172, 2016. *3 citations in pages 11, 12, et 115*

[28] L. Zhonghua and G. Haicheng, "Bauschinger effect and residual phase stresses in two ductile-phase steels: Part I. The influence of phase stresses on the Bauschinger effect," *Metallurgical Transactions A*, vol. 21, no. 2, pp. 717–724, 1990. *Cited in page 12*

[29] L. Zhonghua and G. Haicheng, "Bauschinger effect and residual phase stresses in two ductile-phase steels: Part II. The effect of microstructure and mechanical properties of the constituent phases on Bauschinger effect and residual phase stresses," *Metallurgical Transactions A*, vol. 21, no. 2, pp. 725–732, 1990. *Cited in page 12*

[30] A. L. Helbert, X. Feaugas, and M. Clavel, "The influence of the back stress (X) and the hardening rate (dX/x epsilon(peq)) on void nucleation in alpha/beta titanium alloys," *Journal De Physique Iv*, vol. 6, no. C6, pp. 101–111, 1996. *3 citations in pages 12, 38, et 39*

[31] K. Minnaar and M. Zhou, "An analysis of the dynamic shear failure resistance of structural metals," *Journal of the Mechanics and Physics of Solids*, vol. 46, no. 10, pp. 2155–2170, 1998. *Cited in page 12*

[32] P. Longère, "Respective/combined roles of thermal softening and dynamic recrystallization in adiabatic shear banding initiation," *Mechanics of Materials*, vol. 117, pp. 81–90, feb 2018. *4 citations in pages 12, 13, 41, et 80*

[33] V. Tuninetti and A. Habraken, "Impact of anisotropy and viscosity to model the mechanical behavior of Ti–6Al–4V alloy," *Materials Science and Engineering: A*, vol. 605, pp. 39–50, may 2014. *5 citations in pages 12, 13, 34, 66, et 77*

[34] S. Seo, O. Min, and H. Yang, "Constitutive equation for Ti-6Al-4V at high temperatures measured using the SHPB technique," *International Journal of Impact Engineering*, vol. 31, no. 6, pp. 735–754, 2005. *Cited in page 13*

[35] J. Galán López, P. Verleysen, and J. Degrieck, "Thermal Effects During Tensile Deformation of Ti-6Al-4V at Different Strain Rates," *Strain*, vol. 49, 2013. *Cited in page 13*

[36] D. Macdougall and J. Harding, “A constitutive relation and failure criterion for Ti6Al4V alloy at impact rates of strain,” *Journal of the Mechanics and Physics of Solids*, vol. 47, pp. 1157–1185, apr 1999. *2 citations in pages 13 et 80*

[37] P. Longère and A. Dragon, “Dynamic vs. quasi-static shear failure of high strength metallic alloys: Experimental issues,” *Mechanics of Materials*, vol. 80, no. PB, pp. 203–218, 2015. *4 citations in pages 13, 14, 59, et 143*

[38] J. Peirs, P. Verleysen, J. Degrieck, and F. Coghe, “The use of hat-shaped specimens to study the high strain rate shear behaviour of Ti–6Al–4V,” *International Journal of Impact Engineering*, vol. 37, pp. 703–714, jun 2010. *2 citations in pages 14 et 59*

[39] A. L. Helbert, X. Feaugas, and M. Clavel, “Effects of microstructural parameters and back stress on damage mechanisms in α/β titanium alloys,” *Acta Materialia*, vol. 46, no. 3, pp. 939–951, 1998. *3 citations in pages 14, 43, et 48*

[40] P. Lefranc, V. Doquet, M. Gerland, and C. Sarrazin-Baudoux, “Nucleation of cracks from shear-induced cavities in an α/β titanium alloy in fatigue, room-temperature creep and dwell-fatigue,” *Acta Materialia*, vol. 56, no. 16, pp. 4450–4457, 2008. *2 citations in pages 14 et 39*

[41] H. V. Arrieta and H. D. Espinosa, “The role of thermal activation on dynamic stress-induced inelasticity and damage in Ti-6Al-4V,” *Mechanics of Materials*, vol. 33, no. 10, pp. 573–591, 2001. *Cited in page 14*

[42] H. Margolin and Y. Mahajan, “Void formation, void growth and tensile fracture in Ti-6AI-4V,” *Metallurgical Transactions A*, vol. 9, no. 6, pp. 781–791, 1978. *Cited in page 14*

[43] W.-S. Lee and M.-T. Lin, “The effects of strain rate and temperature on the compressive deformation behaviour of Ti-6Al-4V alloy,” *Journal of Materials Processing Technology*, vol. 71, pp. 235–246, nov 1997. *3 citations in pages 14, 50, et 136*

[44] Z. Zhang, D. E. Eakins, and F. P. Dunne, “On the formation of adiabatic shear bands in textured HCP polycrystals,” *International Journal of Plasticity*, vol. 79, pp. 196–216, 2016. *Cited in page 14*

[45] S. Nemat-Nasser, W. G. Guo, V. F. Nesterenko, S. S. Indrakanti, and Y. B. Gu, “Dynamic response of conventional and hot isostatically pressed Ti-6Al-4V alloys: Experiments and modeling,” *Mechanics of Materials*, vol. 33, no. 8, pp. 425–439, 2001. *Cited in page 14*

[46] W.-S. Lee and C.-F. Lin, “Plastic deformation and fracture behaviour of Ti–6Al–4V alloy loaded with high strain rate under various temperatures,” *Materials Science and Engineering: A*, vol. 241, pp. 48–59, jan 1998. *2 citations in pages 14 et 136*

[47] C. C. Roth and D. Mohr, “Determining the strain to fracture for simple shear for a wide range of sheet metals,” *International Journal of Mechanical Sciences*, vol. 149, pp. 224–240, dec 2018. *4 citations in pages 19, 68, 79, et 115*

[48] J. Peirs, P. Verleysen, and J. Degrieck, "Novel Technique for Static and Dynamic Shear Testing of Ti6Al4V Sheet," *Experimental Mechanics*, pp. 729–741, 2012. *Cited in page 19*

[49] S. Thuillier and P. Manach, "Comparison of the work-hardening of metallic sheets using tensile and shear strain paths," *International Journal of Plasticity*, vol. 25, pp. 733–751, may 2009. *Cited in page 19*

[50] H. Couque, "A hydrodynamic hat specimen to investigate pressure and strain rate dependence on adiabatic shear band formation," *J. Phys. IV France*, vol. 110, pp. 423–428, 2003. *3 citations in pages 19, 20, et 30*

[51] M. A. Meyers, V. F. Nesterenko, J. C. LaSalvia, and Q. Xue, "Shear localization in dynamic deformation of materials: microstructural evolution and self-organization," *Materials Science and Engineering: A*, vol. 317, no. 1-2, pp. 204–225, 2001. *3 citations in pages 19, 20, et 30*

[52] R. Hill, *The mathematical theory of plasticity.* Oxford university press, 1950. *Cited in page 21*

[53] B. Hopkinson, "X. A method of measuring the pressure produced in the detonation of high, explosives or by the impact of bullets," *Philosophical Transactions of the Royal Society of London. Series A, Containing Papers of a Mathematical or Physical Character*, vol. 213, no. 497-508, pp. 437–456, 1914. *Cited in page 22*

[54] H. Kolsky, "An Investigation of the Mechanical Properties of Materials at very High Rates of Loading," *Proc. Phys. Soc. London, Sect. B*, vol. 676, no. 62, pp. 676–700, 1949. *Cited in page 22*

[55] H. Zhao and G. Gary, "On the use of SHPB techniques to determine the dynamic behavior of materials in the range of small strains," *International Journal of Solids and Structures*, vol. 33, pp. 3363–3375, sep 1996. *Cited in page 22*

[56] G. Gary and H. Zhao, "Étude expérimentale du comportement dynamique des matériaux," *Mécanique & Industries*, vol. 1, pp. 15–26, jan 2000. *Cited in page 22*

[57] M. Dunand, G. Gary, and D. Mohr, "Load-Inversion Device for the High Strain Rate Tensile Testing of Sheet Materials with Hopkinson Pressure Bars," *Experimental Mechanics*, vol. 53, 2013. *Cited in page 22*

[58] C. C. Roth, G. Gary, and D. Mohr, "Compact SHPB System for Intermediate and High Strain Rate Plasticity and Fracture Testing of Sheet Metal," *Experimental Mechanics*, vol. 55, pp. 1803–1811, nov 2015. *Cited in page 22*

[59] M. Zhou and S. Park, "Separation of Elastic Waves in Split Hopkinson Bars Using One-point Strain Measurements," *Experimental Mechanics*, vol. 39, no. 4, pp. 287–294, 1999. *Cited in page 22*

[60] J. Dickson, J. Boutin, and L. Handfield, "A comparison of two simple methods for measuring cyclic internal and effective stresses," *Materials Science and Engineering*, vol. 64, pp. L7–L11, may 1984. *Cited in page 32*

[61] F. Norton, *The Creep of Steel at High Temperatures*. McGraw-Hill Book Company, 1929. *4 citations in pages 41, 68, 78, et 141*

[62] P. Perzyna, "Fundamental Problems in Viscoplasticity," *Advances in Applied Mechanics*, vol. 9, pp. 243–377, jan 1966. *6 citations in pages 41, 74, 78, 101, 103, et 141*

[63] G. I. Taylor and H. Quinney, "The latent energy remaining in a metal after cold working," *Proceedings of the Royal Society of London. Series A, Containing Papers of a Mathematical and Physical Character*, vol. 143, no. 849, pp. 307–326, 1934. *2 citations in pages 41 et 80*

[64] H. Hooputra, H. Gese, H. Dell, and H. Werner, "A comprehensive failure model for crashworthiness simulation of aluminium extrusions," *International Journal of Crashworthiness*, vol. 9, pp. 449–464, 2004. *Cited in page 50*

[65] H. L. Dorothy and P. Longère, "Unified modelling of adiabatic shear banding and subsequent micro-voiding driven dynamic failure of viscoplastic solids," *International Journal of Impact Engineering*, vol. 132, no. June, p. 103322, 2019. *3 citations in pages 59, 105, et 115*

[66] L. Szabó and M. Balla, "Comparison of some stress rates," *International Journal of Solids and Structures*, vol. 25, pp. 279–297, jan 1989. *Cited in page 64*

[67] G. Jaumann, "Geschlossenes system physikalischer und chemischer differentialgesetze," in *Sitzungsberichte der Akademie der Wissenschaften, Wien 120*, pp. 385–530, 1911. *Cited in page 65*

[68] A. E. Green and P. M. Naghdi, "A general theory of an elastic-plastic continuum," *Archive for Rational Mechanics and Analysis*, vol. 18, no. 4, pp. 251–281, 1965. *Cited in page 65*

[69] C. Truesdell, "The Simplest Rate Theory of Pure Elasticity," *Communications on Pure and Applied Mathematics*, vol. 8, no. 1, pp. 123–132, 1955. *Cited in page 65*

[70] R. Sowerby and E. Chu, "Rotations, stress rates and strain measures in homogeneous deformation processes," *International Journal of Solids and Structures*, vol. 20, no. 11-12, pp. 1037–1048, 1984. *Cited in page 65*

[71] B. Schieck and H. Stumpf, "The appropriate corotational rate, exact formula for the plastic spin and constitutive model for finite elastoplasticity," *International Journal of Solids and Structures*, vol. 32, pp. 3643–3667, dec 1995. *2 citations in pages 64 et 72*

[72] A. Karafillis and M. Boyce, "A general anisotropic yield criterion using bounds and a transformation weighting tensor," *Journal of the Mechanics and Physics of Solids*, vol. 41, pp. 1859–1886, dec 1993. *8 citations in pages 65, 66, 67, 75, 76, 77, 94, et 141*

[73] O. Cazacu, B. Plunkett, and F. Barlat, "Orthotropic yield criterion for hexagonal closed packed metals," *International Journal of Plasticity*, vol. 22, no. 7, pp. 1171–1194, 2006. *8 citations in pages 65, 66, 67, 76, 77, 94, 141, et 159*

[74] R. Hill, "A theory of the yielding and plastic flow of anisotropic metals," *Proceedings of the Royal Society of London. Series A. Mathematical and Physical Sciences*, vol. 193, no. 1033, pp. 281–297, 1948. *3 citations in pages 65, 75, et 76*

[75] D. Mohr, M. Dunand, and K. H. Kim, "Evaluation of associated and non-associated quadratic plasticity models for advanced high strength steel sheets under multiaxial loading," *International Journal of Plasticity*, vol. 26, no. 7, pp. 939–956, 2010. *Cited in page 65*

[76] A. Taherizadeh, D. E. Green, and J. Yoon, "A non-associated plasticity model with anisotropic and nonlinear kinematic hardening for simulation of sheet metal forming," *International Journal of Solids and Structures*, 2015. *Cited in page 65*

[77] X. Li, C. C. Roth, and D. Mohr, "Machine-learning based temperature- and rate-dependent plasticity model: Application to analysis of fracture experiments on DP steel," *International Journal of Plasticity*, 2019. *2 citations in pages 65 et 115*

[78] A. Baltov and A. Sawczuk, "A rule of anisotropic hardening," *Acta Mechanica*, vol. 1, no. 2, pp. 81–92, 1965. *3 citations in pages 65, 67, et 77*

[79] J. Boehler, *Applications of Tensor Functions in Solid Mechanics.* CISM International Centre for Mechanical Sciences, Springer Vienna, 2014. *Cited in page 66*

[80] R. T. Rockafellar, *Convex analysis.* Princeton, N.J. : Princeton University Press, 1970. *Cited in page 66*

[81] F. Barlat, D. Lege, and J. Brem, "A six-component yield function for anisotropic materials," *International Journal of Plasticity*, vol. 7, pp. 693–712, jan 1991. *Cited in page 66*

[82] F. Barlat, R. Becker, Y. Hayashida, Y. Maeda, M. Yanagawa, K. Chung, J. Brem, D. Lege, K. Matsui, S. Murtha, and S. Hattori, "Yielding description for solution strengthened aluminum alloys," *International Journal of Plasticity*, vol. 13, pp. 385–401, jan 1997. *2 citations in pages 66 et 76*

[83] F. Barlat, J. Brem, J. Yoon, K. Chung, R. Dick, D. Lege, F. Pourboghrat, S.-H. Choi, and E. Chu, "Plane stress yield function for aluminum alloy sheets—part 1: theory," *International Journal of Plasticity*, vol. 19, pp. 1297–1319, sep 2003. *2 citations in pages 66 et 76*

[84] J. Yoon, F. Barlat, R. Dick, K. Chung, and T. J. Kang, "Plane stress yield function for aluminum alloy sheets—part II: FE formulation and its implementation," *International Journal of Plasticity*, vol. 20, pp. 495–522, mar 2004. *Cited in page 66*

[85] G. Gilles, O. Cazacu, W. Hammami, A. Habraken, and L. Duchêne, "Experimental and numerical study of TA-6 V mechanical behavior in different monotonic loading conditions at room temperature," *Procedia IUTAM*, vol. 3, pp. 100–114, jan 2012. *Cited in page 66*

[86] F. Bron and J. Besson, "A yield function for anisotropic materials Application to aluminum alloys," *International Journal of Plasticity*, vol. 20, pp. 937–963, apr 2004. *Cited in page 66*

[87] O. Cazacu and F. Barlat, “A criterion for description of anisotropy and yield differential effects in pressure-insensitive metals,” *International Journal of Plasticity*, vol. 20, pp. 2027–2045, nov 2004. *Cited in page 66*

[88] J. Yoon, Y. Lou, J. Yoon, and M. V. Glazoff, “Asymmetric yield function based on the stress invariants for pressure sensitive metals,” *International Journal of Plasticity*, vol. 56, pp. 184–202, may 2014. *Cited in page 66*

[89] F. Barlat, J. J. Gracio, M.-G. Lee, E. F. Rauch, and G. Vincze, “An alternative to kinematic hardening in classical plasticity,” *International Journal of Plasticity*, vol. 27, pp. 1309–1327, sep 2011. *2 citations in pages 66 et 67*

[90] N. Manopulo, C. Raemy, and P. Hora, “A flexible modelling approach for capturing plastic anisotropy and strength differential effects exhibited by commercially pure titanium,” *International Journal of Solids and Structures*, vol. 151, pp. 91–98, 2018. *Cited in page 66*

[91] P. Longère, A.-G. Geffroy, B. Leblé, and A. Dragon, “Modeling the Transition between Dense Metal and Damaged (Microporous) Metal Viscoplasticity,” *International Journal of Damage Mechanics*, vol. 21, no. 7, pp. 1020–1063, 2012. *4 citations in pages 66, 67, 76, et 143*

[92] J. Lemaitre and J. Chaboche, *Mechanics of Solid Materials.* Cambridge University Press, 1994. *2 citations in pages 66 et 80*

[93] H. Ziegler, “A Modification of Prager’s hardening rule,” *Quarterly of Applied Mathematics*, vol. 17, no. 1, pp. 55–65, 1959. *Cited in page 66*

[94] P. J. Armstrong and C. O. Frederick, *A mathematical representation of the multiaxial Bauschinger effect*, vol. 731. Central Electricity Generating Board [and] Berkeley Nuclear Laboratories˜. . . , 1966. *2 citations in pages 66 et 80*

[95] J. Chaboche, “Time-independent constitutive theories for cyclic plasticity,” *International Journal of Plasticity*, vol. 2, pp. 149–188, jan 1986. *2 citations in pages 66 et 80*

[96] B. Chun, J. Jinn, and J. Lee, “Modeling the Bauschinger effect for sheet metals, part I: theory,” *International Journal of Plasticity*, vol. 18, pp. 571–595, oct 2002. *2 citations in pages 66 et 79*

[97] J. Carbonnière, S. Thuillier, F. Sabourin, M. Brunet, and P. Y. Manach, “Comparison of the work hardening of metallic sheets in bending-unbending and simple shear,” *International Journal of Mechanical Sciences*, vol. 51, no. 2, pp. 122–130, 2009. *3 citations in pages 66, 79, et 141*

[98] S. Zang, C. Guo, S. Thuillier, and M. Lee, “A model of one-surface cyclic plasticity and its application to springback prediction,” *International Journal of Mechanical Sciences*, vol. 53, pp. 425–435, jun 2011. *Cited in page 66*

[99] E. Voce, “A practical strain hardening function,” *Metallurgia*, vol. 51, pp. 219–226, 1955. *Cited in page 68*

[100] W. Swift, “Length changes in metals under torsional overstrain,” *Engineering*, vol. 163, p. 253, 1947. *Cited in page 68*

[101] C. C. Roth and D. Mohr, “Ductile fracture experiments with locally proportional loading histories,” *International Journal of Plasticity*, vol. 79, pp. 328–354, apr 2016. *2 citations in pages 68 et 79*

[102] G. R. Johnson and W. H. Cook, “A constitutive model and data for metals subjected to large strains, high strain rates and high temperatures,” in *Proceedings 7th International Symposium on Ballistics*, (The Hague), pp. 541–547, 1983. *Cited in page 68*

[103] A. S. Khan, Y. Sung Suh, and R. Kazmi, “Quasi-static and dynamic loading responses and constitutive modeling of titanium alloys,” *International Journal of Plasticity*, vol. 20, pp. 2233–2248, dec 2004. *Cited in page 68*

[104] G. R. Cowper and P. S. Symonds, “Strain-hardening and strain-rate effects in the impact loading of cantilever beams,” tech. rep., Brown Univ Providence Ri, 1957. *Cited in page 68*

[105] L. Xue, “Damage accumulation and fracture initiation in uncracked ductile solids subject to triaxial loading,” *International Journal of Solids and Structures*, 2007. *Cited in page 69*

[106] Y. Bao and T. Wierzbicki, “On fracture locus in the equivalent strain and stress triaxiality space,” *International Journal of Mechanical Sciences*, vol. 46, pp. 81–98, jan 2004. *3 citations in pages 69, 134, et 143*

[107] D. Mohr and S. J. Marcadet, “Micromechanically-motivated phenomenological Hosford–Coulomb model for predicting ductile fracture initiation at low stress triaxialities,” *International Journal of Solids and Structures*, vol. 67-68, pp. 40–55, aug 2015. *Cited in page 69*

[108] Y. Bai and T. Wierzbicki, “A comparative study of three groups of ductile fracture loci in the 3D space,” *Engineering Fracture Mechanics*, 2015. *Cited in page 69*

[109] J. R. Rice and D. M. Tracey, “On the ductile enlargement of voids in triaxial stress fields*,” *Journal of the Mechanics and Physics of Solids*, vol. 17, pp. 201–217, jun 1969. *2 citations in pages 69 et 135*

[110] G. R. Johnson and W. H. Cook, “Fracture characteristics of three metals subjected to various strains, strain rates, temperatures and pressures,” *Engineering Fracture Mechanics*, vol. 21, pp. 31–48, jan 1985. *2 citations in pages 69 et 135*

[111] C. Defaisse, M. Mazière, L. Marcin, and J. Besson, “Ductile fracture of an ultra-high strength steel under low to moderate stress triaxiality,” *Engineering Fracture Mechanics*, vol. 194, pp. 301–318, may 2018. *Cited in page 69*

[112] J. Papasidero, V. Doquet, and D. Mohr, “Ductile fracture of aluminum 2024-T351 under proportional and non-proportional multi-axial loading: Bao–Wierzbicki results revisited,” *International Journal of Solids and Structures*, vol. 69-70, pp. 459–474, sep 2015. *Cited in page 70*

[113] S. Yan, X. Zhao, and W. Aihui, “Ductile Fracture Simulation of Constructional Steels Based on Yield-to-Fracture Stress-Strain Relationship and Micromechanism-Based Fracture Criterion,” *Journal of Structural Engineering*, vol. 144, p. 4018004, 2018. *Cited in page 70*

[114] J. Lemaitre, “A Continuous Damage Mechanics Model for Ductile Fracture,” *Journal of Engineering Materials and Technology*, vol. 107, pp. 83–89, jan 1985. *Cited in page 70*

[115] A. L. Gurson, “Porous rigid-plastic materials containing rigid inclusions: yield function, plastic potential, and void nucleation,” 1976. *Cited in page 70*

[116] G. Rousselier, “Ductile fracture models and their potential in local approach of fracture,” *Nuclear Engineering and Design*, vol. 105, pp. 97–111, dec 1987. *Cited in page 70*

[117] P. Longère and A. Dragon, “Description of shear failure in ductile metals via back stress concept linked to damage-microporosity softening,” *Engineering Fracture Mechanics*, vol. 98, pp. 92–108, jan 2013. *Cited in page 70*

[118] E. H. Lee and D. T. Liu, “Finite-strain elastic—plastic theory with application to plane-wave analysis,” *Journal of applied physics*, vol. 38, no. 1, pp. 19–27, 1967. *Cited in page 71*

[119] E. Lee, “Elastic-Plastic Deformation at Finite Strains,” *Journal of Applied Mechanics*, vol. 36, no. 1, pp. 1–6, 1969. *Cited in page 71*

[120] P. Longere, A. Dragon, H. Trumel, T. De Resseguier, X. Deprince, and E. Petitpas, “Modelling adiabatic shear banding via damage mechanics approach,” *Archives of Mechanics*, vol. 55, pp. 3–38, jan 2003. *Cited in page 71*

[121] J. Mandel, “Equations constitutives et directeurs dans les milieux plastiques et viscoplastiques,” *International Journal of Solids and Structures*, vol. 9, pp. 725–740, jun 1973. *Cited in page 72*

[122] T. Hughes and J. Winget, “Finite rotation effects in numerical integration of rate constitutive equations arising in large-deformation analysis,” *International Journal for Numerical Methods in Engineering*, vol. 15, no. 12, pp. 1862–1867, 1980. *2 citations in pages 72 et 99*

[123] P. Longère, “Numerical integration of rate constitutive equations in presence of large strains and rotations,” *Mechanics Research Communications*, vol. 95, pp. 61–66, jan 2019. *3 citations in pages 72, 99, et 100*

[124] B. Halphen and Q. S. Nguyen, “Sur les Matériaux Standard Généralisés,” *Journal de Mécanique*, vol. 14, no. 1, pp. 39–63, 1975. *Cited in page 73*

[125] G. Vadillo, R. Zaera, and J. Fernández-Sáez, “Consistent integration of the constitutive equations of Gurson materials under adiabatic conditions,” *Computer Methods in Applied Mechanics and Engineering*, vol. 197, pp. 1280–1295, feb 2008. *4 citations in pages 74, 80, 100, et 101*

[126] O. M. Heeres, A. S. Suiker, and R. de Borst, “A comparison between the Perzyna viscoplastic model and the Consistency viscoplastic model,” *European Journal of Mechanics - A/Solids*, vol. 21, pp. 1–12, jan 2002. *Cited in page 74*

[127] P. Longère and A. Dragon, “Inelastic heat fraction evaluation for engineering problems involving dynamic plastic localization phenomena,” *Journal of Mechanics of Materials and Structures - J MECH MATER STRUCT*, vol. 4, pp. 319–349, feb 2009. *Cited in page 74*

[128] P. Longère and A. Dragon, “Evaluation of the inelastic heat fraction in the context of microstructure-supported dynamic plasticity modelling,” *International Journal of Impact Engineering*, vol. 35, pp. 992–999, sep 2008. *Cited in page 74*

[129] W. F. Hosford, “A Generalized Isotropic Yield Criterion,” *Journal of Applied Mechanics*, vol. 39, no. 2, pp. 607–609, 1972. *2 citations in pages 77 et 159*

[130] J. B. Stewart and O. Cazacu, “Analytical yield criterion for an anisotropic material containing spherical voids and exhibiting tension–compression asymmetry,” *International Journal of Solids and Structures*, vol. 48, pp. 357–373, jan 2011. *2 citations in pages 77 et 85*

[131] A. Andrade-Campos, S. Thuillier, P. Pilvin, and F. Teixeira-Dias, “On the determination of material parameters for internal variable thermoelastic–viscoplastic constitutive models,” *International Journal of Plasticity*, vol. 23, pp. 1349–1379, aug 2007. *Cited in page 82*

[132] D. W. Marquardt, “An algorithm for least-squares estimation of nonlinear parameters,” *Journal of the society for Industrial and Applied Mathematics*, vol. 11, no. 2, pp. 431–441, 1963. *Cited in page 82*

[133] Z-set, “Z-set package: Non-linear material & structure analysis suite.,” 2013. *Cited in page 83*

[134] M. Considére, “M{é}moire sur l’emploi du fer et de l’acier dans les constructions,” in *Annales des Ponts et Chaussées*, pp. 574–775, 1885. *Cited in page 84*

[135] Z-set, “Materials manual,” 2013. *Cited in page 85*

[136] J. Sun, K. Lee, and H. Lee, “Comparison of implicit and explicit finite element methods for dynamic problems,” *Journal of Materials Processing Technology*, vol. 105, pp. 110–118, sep 2000. *Cited in page 96*

[137] K.-J. Bathe, *Finite element procedures.* Klaus-Jurgen Bathe, 2014. *2 citations in pages 96 et 97*

[138] LSTC, *LS-DYNA Theory Manual.* 2018. *2 citations in pages 97 et 99*

[139] D. S. Malkus and T. Hughes, “Mixed finite element methods — Reduced and selective integration techniques: A unification of concepts,” *Computer Methods in Applied Mechanics and Engineering*, vol. 15, pp. 63–81, jul 1978. *Cited in page 97*

[140] S. M. Yunus, T. P. Pawlak, and R. D. Cook, “Solid elements with rotational degrees of freedom: Part 1—hexahedron elements,” *International Journal for Numerical Methods in Engineering*, vol. 31, no. 3, pp. 573–592, 1991. *Cited in page 97*

[141] N. M. Newmark, “A method of computation for structural dynamics,” *Journal of the Engineering Mechanics Division*, vol. 85, no. 3, pp. 67–94, 1959. *Cited in page 98*

[142] R. Courant, K. Friedrichs, and H. Lewy, “{U}ber die partiellen Differenzengleichungen der mathematischen Physik,” *Mathematische annalen*, vol. 100, no. 1, pp. 32–74, 1928. *2 citations in pages 99 et 116*

[143] J. C. Simo and T. J. Hughes, *Computational inelasticity*, vol. 7. Springer Science & Business Media, 2006. *2 citations in pages 100 et 101*

[144] M. Ortiz and J. Simo, “An analysis of a new class of integration algorithms for elastoplastic constitutive relations,” *International Journal for Numerical Methods in Engineering*, vol. 23, no. 3, pp. 353–366, 1986. *Cited in page 101*

[145] M. Halilovič, M. Vrh, and B. Štok, “NICE—An explicit numerical scheme for efficient integration of nonlinear constitutive equations,” *Mathematics and Computers in Simulation*, vol. 80, pp. 294–313, oct 2009. *3 citations in pages 101, 104, et 105*

[146] K. Ding, Q.-H. Qin, and M. Cardew-Hall, “Substepping algorithms with stress correction for the simulation of sheet metal forming process,” *International Journal of Mechanical Sciences*, vol. 49, pp. 1289–1308, nov 2007. *Cited in page 101*

[147] J. Oliver, A. Huespe, and J. Cante, “An implicit/explicit integration scheme to increase computability of non-linear material and contact/friction problems,” *Computer Methods in Applied Mechanics and Engineering*, vol. 197, pp. 1865–1889, apr 2008. *Cited in page 101*

[148] M. Safaei, M. Lee, and W. De Waele, “Evaluation of stress integration algorithms for elastic–plastic constitutive models based on associated and non-associated flow rules,” *Computer Methods in Applied Mechanics and Engineering*, vol. 295, pp. 414–445, oct 2015. *Cited in page 101*

[149] D. M. Potts and A. Gens, “A critical assessment of methods of correcting for drift from the yield surface in elasto-plastic finite element analysis,” *International Journal for Numerical and Analytical Methods in Geomechanics*, vol. 9, no. 2, pp. 149–159, 1985. *Cited in page 103*

[150] M. Vrh, M. Halilovič, and B. Štok, “Improved explicit integration in plasticity,” *International Journal for Numerical Methods in Engineering*, vol. 81, no. 7, pp. 910–938, 2010. *Cited in page 104*

[151] P. Longère, A. Dragon, H. Trumel, and X. Deprince, “Adiabatic shear banding-induced degradation in a thermo-elastic/ viscoplastic material under dynamic loading,” *International Journal of Impact Engineering*, vol. 32, no. 1-4, pp. 285–320, 2005. *2 citations in pages 105 et 115*

[152] M. Besson, J., G. Cailletaud, J. Chaboche, and S. Forest, *Non-Linear Mechanics of Materials*. Solid Mechanics and Its Applications, Springer Netherlands, 2009. *Cited in page 107*

[153] LSTC, *LS-DYNA Keyword User's Manual Volume I, LS-DYNA R9.0*, vol. I. 2016. *Cited in page 117*

[154] Y. Bao and T. Wierzbicki, "On the cut-off value of negative triaxiality for fracture," *Engineering Fracture Mechanics*, vol. 72, no. 7, pp. 1049–1069, 2005. *Cited in page 134*

[155] J. Wolf, P. Longère, J.-P. Crété, and J.-M. Cadou, "Strain localization in ductile materials: Assessment of three X-FEM-based enrichment methods," *Mechanics Research Communications*, vol. 99, pp. 1–7, jul 2019. *Cited in page 143*

APPENDIX A

Constitutive modelling details

A.1 Normal of the yield surface

This section aims to provide a detailed definition of the yield surface normal employed when considering the CPB06 model [73]. Its main purpose being its implementation in the user law subroutine in LS-DYNA. First, the yield surface normal for an isotropic material will be defined. The extended definition including the orthotropy will later be added. Finally, the second derivative of the yield surface is also shown as it is necessary for the estimation of the tangent matrix in implicit schemes.

A.1.1 Isotropic material exhibiting a strength differential

The anisotropic CPB06 yield surface proposed by Cazacu, Plunkett and Barlat [73] has the form

$$\sigma_{eq}{}^{a} = \frac{1}{m_0{}^{a}} \left\{ \left(|\hat{S}_1| - k\hat{S}_1 \right)^{a} + \left(|\hat{S}_2| - k\hat{S}_2 \right)^{a} + \left(|\hat{S}_3| - k\hat{S}_3 \right)^{a} \right\} \tag{A.1}$$

where m_0 is a constant such that the equivalent stress is equal to the uniaxial stress in tension (compression) if $k > 0$ ($k < 0$). $\hat{S}_p$ are the eigenvalues of the stress state considering the kinematic force, i.e.

$$\hat{S}_p = eig(\underline{\underline{\hat{s}}}) = eig(\underline{\underline{s}} - \underline{\underline{X}}) \tag{A.2}$$

k is the main parameter defining the tension/compression asymmetry and a is a shape parameter of the yield surface as the one found in the Hosford criterion [129].

$$m_0{}^{a} = \left[\frac{2}{3} \left(1 - |k| \right) \right]^{a} + 2 \left[\frac{1}{3} \left(1 + |k| \right) \right]^{a} \tag{A.3}$$

According to the normality rule, the yield surface normal $\underline{\underline{n}}$ is defined as the derivative of the yield function with respect to the stress tensor $\underline{\underline{\sigma}}$. Subsequently, it is also the derivative of the equivalent stress with respect to the stress. The chain rule is herein applied:

$$\underline{\underline{n}} = \frac{\partial f}{\partial \underline{\underline{\sigma}}} = \frac{\partial \sigma_{eq}}{\partial \underline{\underline{\sigma}}} = \sum_{p=1}^{3} \frac{\partial \sigma_{eq}}{\partial \hat{S}_p} \frac{\partial \hat{S}_p}{\partial \underline{\underline{\hat{s}}}} \frac{\partial \underline{\underline{\hat{s}}}}{\partial \underline{\underline{\sigma}}} \to n_{ij} = \sum_{p=1}^{3} \frac{\partial \sigma_{eq}}{\partial \hat{S}_p} \frac{\partial \hat{S}_p}{\partial \hat{s}_{kl}} \frac{\partial \hat{s}_{kl}}{\partial \sigma_{ij}} \tag{A.4}$$

The first term $\frac{\partial \sigma_{eq}}{\partial \hat{S}_p}$ corresponds to the derivative of the equivalent stress with respect to the eigenvalues of the effective stress deviator $\underline{\underline{s}} - \underline{\underline{X}}$. The second term $\frac{\partial \hat{S}_p}{\partial \hat{s}_{kl}}$ is the derivative of the eigenvalues with respect to the effective stress deviator (see Remark).

The last term $\frac{\partial \hat{s}_{kl}}{\partial \sigma_{ij}}$ is the derivative of the effective stress deviator with respect to the stress tensor.

$$\begin{cases} \dfrac{\partial \sigma_{eq}}{\partial \hat{S}_p} = \dfrac{\sigma_{eq}^{1-a}}{m_0^a} \left(|\hat{S}_p| - k\hat{S}_p \right)^{a-1} \left(\operatorname{sgn}\left(\hat{S}_p\right) - k \right) = \dfrac{1}{m_0^a} \left(\dfrac{|\hat{S}_p| - k\hat{S}_p}{\sigma_{eq}} \right)^{a-1} \left(\operatorname{sgn}\left(\hat{S}_p\right) - k \right) \\ \dfrac{\partial \hat{S}_p}{\partial \hat{s}_{kl}} = v_{p_k} v_{p_l} = \underline{v}_p \otimes \underline{v}_p \\ \dfrac{\partial \hat{s}_{kl}}{\partial \sigma_{ij}} = \dfrac{\partial s_{kl}}{\partial \sigma_{ij}} = \dfrac{\partial}{\partial \sigma_{ij}} \left(\sigma_{kl} - \dfrac{1}{3} \sigma_{pp} \delta_{kl} \right) = \dfrac{1}{2} \left(\delta_{ik}\delta_{jl} + \delta_{il}\delta_{jk} \right) - \dfrac{1}{3} \delta_{ij}\delta_{kl} = J_{ijkl} \end{cases} \tag{A.5}$$

where $\operatorname{sgn}(x) = 1$ if $x > 0$ and $\operatorname{sgn}(x) = -1$ otherwise.

Remark

The derivative of the eigenvalues with respect to its tensor, i.e. $\frac{\partial \hat{S}_p}{\partial \hat{s}_{kl}}$, can be calculated from the definition of the eigenvalue problem.

$$\hat{s}_{kl} v_{p_l} = \hat{S}_p v_{p_k} = \hat{S}_p I_{kl} v_{p_k} \tag{A.6}$$

By differentiating the above expression and pre-multiplying by the desired eigenvector, one has

$$\begin{aligned} d\hat{s}_{kl} v_{p_l} + \hat{s}_{kl} dv_{p_l} &= d\hat{S}_p v_{p_k} + \hat{S}_p dv_{p_k} \\ v_{p_k} d\hat{s}_{kl} v_{p_l} + v_{p_k} \hat{s}_{kl} dv_{p_l} &= v_{p_k} d\hat{S}_p v_{p_k} + v_{p_k} \hat{S}_p dv_{p_k} \\ v_{p_k} d\hat{s}_{kl} v_{p_l} + \hat{S}_p \cancelto{0}{v_{p_k} dv_{p_k}} &= d\hat{S}_p \cancelto{1}{v_{p_k} v_{p_k}} + \hat{S}_p \cancelto{0}{v_{p_k} dv_{p_k}} \\ v_{p_k} d\hat{s}_{kl} v_{p_l} &= d\hat{S}_p \end{aligned} \tag{A.7}$$

where the normality of the eigenvectors yields $v_{p_k} dv_{p_k} = 0$ and $v_{p_k} v_{p_k} = 1$

Therefore, the derivative of the eigenvalues with respect to its matrix is

$$\frac{\partial \hat{S}_p}{\partial \hat{s}_{kl}} = v_{p_k} v_{p_l} \tag{A.8}$$

The tensor notation of such expression takes the simple form

$$\frac{\partial \hat{S}_p}{\partial \underline{\underline{\hat{s}}}} = \underline{v}_p \otimes \underline{v}_p = \underline{v}_p \, \underline{v}_p^T \tag{A.9}$$

By assembling the three terms, the normal to the yield surface in the index notation is

$$
\begin{aligned}
n_{ij} =& \sum_{p=1}^{3} \left[\frac{1}{m_0^a} \left(\frac{|\hat{S}_p| - k\hat{S}_p}{\sigma_{eq}} \right)^{a-1} \left(\operatorname{sgn}\left(\hat{S}_p\right) - k \right) \right] \cdot \left[v_{p_k} v_{p_l} \right] \cdot J_{ijkl} \\
=& \sum_{p=1}^{3} \left[\frac{1}{m_0^a} \left(\frac{|\hat{S}_p| - k\hat{S}_p}{\sigma_{eq}} \right)^{a-1} \left(\operatorname{sgn}\left(\hat{S}_p\right) - k \right) \right] \cdot \left[v_{p_k} v_{p_l} \right] \cdot \left[\frac{1}{2} \left(\delta_{ik}\delta_{jl} + \delta_{il}\delta_{jk} \right) - \frac{1}{3}\delta_{ij}\delta_{kl} \right] \\
=& \sum_{p=1}^{3} \left[\frac{1}{m_0^a} \left(\frac{|\hat{S}_p| - k\hat{S}_p}{\sigma_{eq}} \right)^{a-1} \left(\operatorname{sgn}\left(\hat{S}_p\right) - k \right) \right] \cdot \left[v_{p_i} v_{p_j} - \frac{1}{3}\delta_{ij} \right]
\end{aligned}
\tag{A.10}
$$

Therefore, the intrinsic notation for the normal direction is of the form

$$
\underline{\underline{n}} = \sum_{p=1}^{3} \frac{1}{m_0^a} \left(\frac{|\hat{S}_p| - k\hat{S}_p}{\sigma_{eq}} \right)^{a-1} \left(\operatorname{sgn}\left(\hat{S}_p\right) - k \right) \left(\underline{v}_p \otimes \underline{v}_p - \frac{1}{3}\underline{\underline{I}} \right) \tag{A.11}
$$

Moreover, the fourth order projector tensor $\underline{\underline{\underline{J}}}$ presents major and minor symmetries. This allows for a further simplification of the normal definition using the Voigt notation ($\underline{\underline{\sigma}}^T = (\sigma_{xx},\, \sigma_{yy},\, \sigma_{zz},\, \sigma_{xy},\, \sigma_{yz},\, \sigma_{xz},\,)$). In this case, such normal will be expressed as a 6-element vector as

$$
n_i = \sum_{p=1}^{3} \left[\frac{1}{m_0^a} \left(\frac{|\hat{S}_p| - k\hat{S}_p}{\sigma_{eq}} \right)^{a-1} \left(\operatorname{sgn}\left(\hat{S}_p\right) - k \right) \right] \cdot V_j \cdot J_{ji} \tag{A.12}
$$

with

$$
\underline{\underline{J}} = \begin{bmatrix}
2/3 & -1/3 & -1/3 & & & \\
-1/3 & 2/3 & -1/3 & & & \\
-1/3 & -1/3 & 2/3 & & & \\
 & & & 1 & & \\
 & & & & 1 & \\
 & & & & & 1
\end{bmatrix} \tag{A.13}
$$

and where V_j is a 6-element vector coming from Voigt notation of the second order tensor $v_{p_k} v_{p_l}$

$$
\underline{V} = \begin{bmatrix} v_{p1}v_{p1} & v_{p2}v_{p2} & v_{p3}v_{p3} & v_{p1}v_{p2} & v_{p2}v_{p3} & v_{p1}v_{p3} & \end{bmatrix} \tag{A.14}
$$

The tensor form of such expression is therefore

$$
\underline{n} = \underline{\underline{J}} \sum_{p=1}^{3} \frac{1}{m_0^a} \left(\frac{|\hat{S}_p| - k\hat{S}_p}{\sigma_{eq}} \right)^{a-1} \left(\operatorname{sgn}\left(\hat{S}_p\right) - k \right) \underline{V} \tag{A.15}
$$

where the projector tensor can be taken out of the sum. This shows how the normal definition is forced to be a deviator as long as the derivative $\frac{\partial \underline{\underline{\hat{s}}}}{\partial \underline{\underline{\sigma}}}$ is considered. However, it is not co-rotational with the stress deviator as it is the case for the von Mises yield criterion.

A problem arises when repeated eigenvalues are present. If the matrix $\underline{\underline{\hat{s}}}$ is real and symmetric, it can be proven that its eigenvalues are real and the eigenvectors can form an orthonormal base. In more physical terms, it is possible to rotate the stress deviatoric tensor to the principal frame composed of the eigenvectors. If all the eigenvalues are the same value, any base is an orthogonal base and thus, an infinite number of eigenvectors exists. Likewise, if two eigenvalues are repeated, it can be proved there is an infinite number of combinations for its two respective eigenvectors. However, it shall be proved that the derivative of the eigenvalues will be unique for any combination of real eigenvalues.

Let an arbitrary orthonormal frame be composed of the set of vectors $\{\underline{v}_1, \underline{v}_2, \underline{v}_3\}$, it can be proved that the following condition is satisfied

$$\underline{v}_1 \otimes \underline{v}_1 + \underline{v}_2 \otimes \underline{v}_2 + \underline{v}_3 \otimes \underline{v}_3 = \underline{\underline{I}} \tag{A.16}$$

Furthermore, the Equation A.11 can be summarized as a scalar A_0, a scalar function depending on the eigenvalues $B_0\left(\hat{S}_p\right)$ and the eigenvector crossproduct $\underline{v}_p \otimes \underline{v}_p$.

$$\underline{\underline{n}} = A_0 \sum_{p=1}^{3} B_0\left(\hat{S}_p\right)\left(\underline{v}_p \otimes \underline{v}_p - \frac{1}{3}\underline{\underline{I}}\right) \tag{A.17}$$

with

$$\begin{cases} A_0 = \dfrac{1}{m_0^a} \\ B_0 = \left(\dfrac{|\hat{S}_p| - k\hat{S}_p}{\sigma_{eq}}\right)^{a-1}\left(\operatorname{sgn}\left(\hat{S}_p\right) - k\right) \end{cases} \tag{A.18}$$

Three cases are herein distinguished depending on the multiplicity of the eigenvalues (1 to 3).

Multiplicity of 1

If the multiplicity of the eigenvalue is 1, the problem is well posed and the uniqueness of the eigenvectors is satisfied.

Multiplicity of 2

For the case when one of the eigenvalues has a multiplicity of 2 (e.g the simple tension stress state). The yield surface normal can be expressed as

$$\underline{\underline{n}} = A_0 B_0\left(\hat{S}_r\right)\sum_{r=1}^{2}\left(\underline{v}_r \otimes \underline{v}_r\right) - \frac{2}{3}A_0 B_0\left(\hat{S}_r\right)\underline{\underline{I}} + A_0 B_0\left(\hat{S}_s\right)\left(\underline{v}_s \otimes \underline{v}_s\right) - \frac{1}{3}A_0 B_0\left(\hat{S}_s\right)\underline{\underline{I}} \tag{A.19}$$

Where the subscript $\cdot_s$ stands for the single unrepeated eigenvalue. Because the multiplicity of such eigenvalue is 1, its eigenvector is unique and well defined. The quantity corresponding to the repeated eigenvalue $\sum_{r=1}^{2}\left(\underline{v}_r \otimes \underline{v}_r\right)$ can, a priori, take and infinite amount of combinations. However, by using Equation A.16 and taking into account that the unrepeated eigenvalue has a unique eigenvector one has

$$\sum_{r=1}^{2} \underline{v}_r \otimes \underline{v}_r = \underline{\underline{I}} - \underline{v}_s \otimes \underline{v}_s \tag{A.20}$$

which is a unique quantity.

Multiplicity of 3

However, if the eigenvalue multiplicity is 3, i.e. they are all equal, the Equation A.17 can be simplified as

$$\underline{\underline{n}} = A_0 B_0 \left(\hat{S}_r\right) \sum_{r=1}^{3} \left(\underline{v}_r \otimes \underline{v}_r\right) - A_0 B_0 \left(\hat{S}_r\right) \underline{\underline{I}} \tag{A.21}$$

where the subscript $\cdot_r$ is used to denote a repeated eigenvalue. Therefore, any orthonormal basis chosen from the infinite combination of eigenvector ensures the uniqueness of the yield surface normal (see Equation A.16).

A.1.2 Anisotropic material exhibiting a strength differential

The extension to the anisotropic case is done by considering the stress linear transformation $\underline{\underline{\hat{\Sigma}}} = \underline{\underline{\underline{\underline{A}}}} \left(\underline{\underline{s}} - \underline{\underline{X}}\right) = \underline{\underline{\underline{\underline{A}}}}\,\underline{\underline{\hat{s}}}$. Hence, the equivalent stress has the following form

$$\sigma_{eq}{}^{a} = \frac{1}{m_0{}^{a}} \left\{ \left(|\hat{\Sigma}_1| - k\hat{\Sigma}_1\right)^{a} + \left(|\hat{\Sigma}_2| - k\hat{\Sigma}_2\right)^{a} + \left(|\hat{\Sigma}_3| - k\hat{\Sigma}_3\right)^{a} \right\} \tag{A.22}$$

where the eigenvalues of the transformed stress $\underline{\underline{\hat{\Sigma}}}$ are now considered.

Therefore, an additional stage is considered in the chain rule derivative.

$$\underline{\underline{n}} = \frac{\partial f}{\partial \underline{\underline{\sigma}}} = \frac{\partial \sigma_{eq}}{\partial \underline{\underline{\sigma}}} = \sum_{p=1}^{3} \frac{\partial \sigma_{eq}}{\partial \hat{\Sigma}_p} \frac{\partial \hat{\Sigma}_p}{\partial \underline{\underline{\hat{\Sigma}}}} \frac{\partial \underline{\underline{\hat{\Sigma}}}}{\partial \underline{\underline{\hat{s}}}} \frac{\partial \underline{\underline{\hat{s}}}}{\partial \underline{\underline{\sigma}}} \rightarrow n_{ij} = \sum_{p=1}^{3} \frac{\partial \sigma_{eq}}{\partial \hat{\Sigma}_p} \frac{\partial \hat{\Sigma}_p}{\partial \hat{\Sigma}_{mn}} \frac{\partial \hat{\Sigma}_{mn}}{\partial \hat{s}_{kl}} \frac{\partial \hat{s}_{kl}}{\partial \sigma_{ij}} \tag{A.23}$$

where three out of the four derivatives were already computed in the isotropic case. The new term is a fourth dimensional tensor that contains the information about the anisotropy expressed as

$$\frac{\partial \hat{\Sigma}_{mn}}{\partial \hat{s}_{kl}} = A_{mnkl} \tag{A.24}$$

Once again, by assembling all the terms together, one has

$$n_{ij} = \sum_{p=1}^{3} \left[\frac{1}{m_0^a} \left(\frac{|\hat{\Sigma}_p| - k\hat{\Sigma}_p}{\sigma_{eq}} \right)^{a-1} \left(\operatorname{sgn}\left(\hat{\Sigma}_p\right) - k \right) \right] \cdot \left[v_{p_m} v_{p_n} \right] \cdot A_{mnkl} \cdot \left[\frac{1}{2} \left(\delta_{ik}\delta_{jl} + \delta_{il}\delta_{jk} \right) - \frac{1}{3} \delta_{ij}\delta_{kl} \right] \tag{A.25}$$

The Voigt notation can be employed as the anisotropy matrix is defined with major and minor symmetries. Likewise, the fourth order projector tensor can also be reduced into a $6x6$. This simplifies the definition of the normal as

$$n_i = \sum_{p=1}^{3} \left[\frac{1}{m_0^a} \left(\frac{|\hat{\Sigma}_p| - k\hat{\Sigma}_p}{\sigma_{eq}} \right)^{a-1} \left(\operatorname{sgn}\left(\hat{\Sigma}_p\right) - k \right) \right] \cdot V_k \cdot A_{kj} \cdot J_{ji} \tag{A.26}$$

where V_k is a 6-element vector coming from Voigt notation of the second order tensor $v_{p_m} v_{p_n}$. The tensor form of the previous expression is

$$\underline{n} = \underline{\underline{J}}\,\underline{\underline{A}} \sum_{p=1}^{3} \frac{1}{m_0^a} \left(\frac{|\hat{\Sigma}_p| - k\hat{\Sigma}_p}{\sigma_{eq}} \right)^{a-1} \left(\operatorname{sgn}\left(\hat{\Sigma}_p\right) - k \right) \underline{V} \tag{A.27}$$

The only difference with respect to the isotropic case in Equation A.15 is the anisotropy matrix which is pre-multiplied to the expression before the projection in the deviatoric plane.

A.1.3 Second derivative of the yield surface function

The second derivative of the yield surface is necessary to assure a quadratic convergence in an implicit scheme. It is also necessary for the building of the consistent tangent matrix. The second derivative yields a fourth order tensor that can be reduced to a second order tensor when considering the Voigt notation.

As with the yield normal calculation, the chain rule is herein employed

$$\underline{\underline{\underline{\underline{N}}}} = \frac{\partial^2 \sigma_{eq}}{\left(\partial \underline{\underline{\sigma}}\right)^2} = \frac{\partial}{\partial \underline{\underline{\sigma}}} \left(\frac{\partial \sigma_{eq}}{\partial \underline{\underline{\sigma}}} \right) = \frac{\partial}{\partial \underline{\underline{\sigma}}} \left(\sum_{p=1}^{3} \frac{\partial \sigma_{eq}}{\partial \hat{\Sigma}_p} \frac{\partial \hat{\Sigma}_p}{\partial \underline{\underline{\hat{\Sigma}}}} \frac{\partial \underline{\underline{\hat{\Sigma}}}}{\partial \underline{\underline{\hat{s}}}} \frac{\partial \underline{\underline{\hat{s}}}}{\partial \underline{\underline{\sigma}}} \right) \tag{A.28}$$

The index notation is used in order to develop the previous equation

$$\begin{aligned}
N_{ijkl} &= \frac{\partial^2 \sigma_{eq}}{\partial \sigma_{ij} \partial \sigma_{kl}} = \frac{\partial}{\partial \sigma_{ij}} \left(\sum_{p=1}^{3} \frac{\partial \sigma_{eq}}{\partial \hat{\Sigma}_p} \frac{\partial \hat{\Sigma}_p}{\partial \hat{\Sigma}_{rs}} \frac{\partial \hat{\Sigma}_{rs}}{\partial \hat{s}_{mn}} \frac{\partial \hat{s}_{mn}}{\partial \sigma_{kl}} \right) \\
&= \sum_{p=1}^{3} \frac{\partial^2 \sigma_{eq}}{\partial \sigma_{ij} \partial \hat{\Sigma}_p} \frac{\partial \hat{\Sigma}_p}{\partial \hat{\Sigma}_{rs}} A_{rsmn} J_{mnkl} + \sum_{p=1}^{3} \frac{\partial \sigma_{eq}}{\partial \hat{\Sigma}_p} \frac{\partial^2 \hat{\Sigma}_p}{\partial \sigma_{ij} \partial \hat{\Sigma}_{rs}} A_{rsmn} J_{mnkl} \\
&= \sum_{p=1}^{3} \frac{\partial}{\partial \hat{\Sigma}_p} \left(\sum_{q=1}^{3} \frac{\partial \sigma_{eq}}{\partial \hat{\Sigma}_q} \frac{\partial \hat{\Sigma}_q}{\partial \hat{\Sigma}_{\tilde{r}\tilde{s}}} \frac{\partial \hat{\Sigma}_{\tilde{r}\tilde{s}}}{\partial \hat{s}_{\tilde{m}\tilde{n}}} \frac{\partial \hat{s}_{\tilde{m}\tilde{n}}}{\partial \sigma_{ij}} \right) \frac{\partial \hat{\Sigma}_p}{\partial \hat{\Sigma}_{rs}} A_{rsmn} J_{mnkl} \\
&+ \sum_{p=1}^{3} \frac{\partial \sigma_{eq}}{\partial \hat{\Sigma}_p} \frac{\partial}{\partial \hat{\Sigma}_{rs}} \left(\frac{\partial \hat{\Sigma}_p}{\partial \hat{\Sigma}_{\tilde{r}\tilde{s}}} \frac{\partial \hat{\Sigma}_{\tilde{r}\tilde{s}}}{\partial \hat{s}_{\tilde{m}\tilde{n}}} \frac{\partial \hat{s}_{\tilde{m}\tilde{n}}}{\partial \sigma_{ij}} \right) A_{rsmn} J_{mnkl} \\
&= \sum_{p=1}^{3} \sum_{q=1}^{3} \frac{\partial^2 \sigma_{eq}}{\partial \hat{\Sigma}_p \partial \hat{\Sigma}_q} \frac{\partial \hat{\Sigma}_q}{\partial \hat{\Sigma}_{\tilde{r}\tilde{s}}} \frac{\partial \hat{\Sigma}_p}{\partial \hat{\Sigma}_{rs}} A_{\tilde{r}\tilde{s}\tilde{m}\tilde{n}} J_{\tilde{m}\tilde{n}ij} A_{rsmn} J_{mnkl} \\
&+ \sum_{p=1}^{3} \frac{\partial \sigma_{eq}}{\partial \hat{\Sigma}_p} \frac{\partial^2 \hat{\Sigma}_p}{\partial \hat{\Sigma}_{rs} \partial \hat{\Sigma}_{\tilde{r}\tilde{s}}} A_{\tilde{r}\tilde{s}\tilde{m}\tilde{n}} J_{\tilde{m}\tilde{n}ij} A_{rsmn} J_{mnkl}
\end{aligned} \tag{A.29}$$

where only the terms $\frac{\partial^2 \sigma_{eq}}{\partial \hat{\Sigma}_p \partial \hat{\Sigma}_q}$ and $\frac{\partial^2 \hat{\Sigma}_p}{\partial \hat{\Sigma}_{rs} \partial \hat{\Sigma}_{\tilde{r}\tilde{s}}}$ are unknown. The first one can be directly derived from the results obtained in Equation A.5 using the anisotropic variables.

$$\frac{\partial \sigma_{eq}}{\partial \hat{\Sigma}_p} = \frac{1}{m_0^a} \left(\frac{|\hat{\Sigma}_p| - k\hat{\Sigma}_p}{\sigma_{eq}} \right)^{a-1} \left(\operatorname{sgn}\left(\hat{\Sigma}_p\right) - k \right) \tag{A.30}$$

Special attention must be made concerning the eigenvalues used for the derivation. Two cases are possible

$$\begin{cases} p = q \rightarrow \dfrac{\partial^2 \sigma_{eq}}{\partial \hat{\Sigma}_p \partial \hat{\Sigma}_q} & = \dfrac{a-1}{m_0^a} \left(\dfrac{|\hat{\Sigma}_p| - k\hat{\Sigma}_p}{\sigma_{eq}} \right)^{a-2} \left(\operatorname{sgn}\left(\hat{\Sigma}_p\right) - k \right) \left\{ \dfrac{\operatorname{sgn}\left(\hat{\Sigma}_p\right) - k}{\sigma_{eq}} - \dfrac{|\hat{\Sigma}_p| - k\hat{\Sigma}_p}{\sigma_{eq}^2} \dfrac{\partial \sigma_{eq}}{\partial \hat{\Sigma}_p} \right\} \\ & = \dfrac{a-1}{m_0^a} \dfrac{\left(|\hat{\Sigma}_p| - k\hat{\Sigma}_p\right)^{a-2} \left(\operatorname{sgn}\left(\hat{\Sigma}_p\right) - k \right)^2}{\sigma_{eq}^{a-1}} \left(1 - \dfrac{\left(|\hat{\Sigma}_p| - k\hat{\Sigma}_p\right)^a}{m_0^a \sigma_{eq}^a} \right) \\ p \neq q \rightarrow \dfrac{\partial^2 \sigma_{eq}}{\partial \hat{\Sigma}_p \partial \hat{\Sigma}_q} & = \dfrac{1-a}{m_0^a} \left(\dfrac{|\hat{\Sigma}_p| - k\hat{\Sigma}_p}{\sigma_{eq}} \right)^{a-2} \left(\dfrac{|\hat{\Sigma}_p| - k\hat{\Sigma}_p}{\sigma_{eq}^2} \dfrac{\partial \sigma_{eq}}{\partial \hat{\Sigma}_q} \right) \left(\operatorname{sgn}\left(\hat{\Sigma}_p\right) - k \right) \\ & = \dfrac{1-a}{m_0^a} \dfrac{\left(|\hat{\Sigma}_p| - k\hat{\Sigma}_p\right)^{a-1} \left(|\hat{\Sigma}_q| - k\hat{\Sigma}_q\right)^{a-1}}{\sigma_{eq}^{2a-1}} \left(\operatorname{sgn}\left(\hat{\Sigma}_p\right) - k \right) \left(\operatorname{sgn}\left(\hat{\Sigma}_q\right) - k \right) \end{cases} \tag{A.31}$$

The second term to calculate $\frac{\partial^2 \hat{\Sigma}_p}{\partial \hat{\Sigma}_{ij} \partial \hat{\Sigma}_{kl}}$ is the double derivative of an eigenvalue with respect to its matrix. From the conclusions in Equation A.8, the term can be expressed as the derivative of the eigenvectors

$$\frac{\partial^2 \hat{\Sigma}_p}{\partial \hat{\Sigma}_{ij} \partial \hat{\Sigma}_{kl}} = \frac{\partial}{\partial \hat{\Sigma}_{kl}} \left(\frac{\partial \hat{\Sigma}_p}{\partial \hat{\Sigma}_{ij}} \right) = \frac{\partial}{\partial \hat{\Sigma}_{kl}} \left(v_{p_i} v_{p_j} \right) \tag{A.32}$$

Therefore, the derivative of an eigenvector with respect to its matrix is needed. As formulated in Equation A.7, a similar procedure is followed by pre-multiplying by a different eigenvector.

$$\begin{aligned} d\hat{\Sigma}_{kl} v_{p_l} + \hat{\Sigma}_{kl} dv_{p_l} &= d\hat{\Sigma}_p v_{p_k} + \hat{\Sigma}_p dv_{p_k} \\ v_{q_k} d\hat{\Sigma}_{kl} v_{p_l} + v_{q_k} \hat{\Sigma}_{kl} dv_{p_l} &= v_{q_k} d\hat{\Sigma}_p v_{p_k} + v_{q_k} \hat{\Sigma}_p dv_{p_k} \\ v_{q_k} d\hat{\Sigma}_{kl} v_{p_l} + \hat{\Sigma}_q v_{q_k} dv_{p_k} &= d\hat{\Sigma}_p \cancelto{0}{v_{q_k} v_{p_k}} + \hat{\Sigma}_p v_{q_k} dv_{p_k} \\ v_{q_k} d\hat{\Sigma}_{kl} v_{p_l} &= \left(\hat{\Sigma}_p - \hat{\Sigma}_q \right) v_{q_k} dv_{p_k} \\ v_{q_k} dv_{p_k} &= v_{q_k} \frac{d\hat{\Sigma}_{kl} v_{p_l}}{\hat{\Sigma}_p - \hat{\Sigma}_q} \end{aligned} \tag{A.33}$$

the result is but the projection of the differential of an eigenvector with respect to either one of the other two directions left. Considering all the eigenvectors one has

$$dv_{p_i} = \sum_{q=1}^{q \neq p} \left(v_{q_k} \frac{d\hat{\Sigma}_{kl} v_{p_l}}{\hat{\Sigma}_p - \hat{\Sigma}_q} \right) v_{q_i} \tag{A.34}$$

It is noted that the projection of a normal eigenvector with respect to its direction is zero. Therefore, the third order tensor derivative is as follows

$$\frac{dv_{p_i}}{d\hat{\Sigma}_{kl}} = \sum_{q=1}^{q \neq p} \left(\frac{v_{q_k} v_{p_l}}{\hat{\Sigma}_p - \hat{\Sigma}_q} \right) v_{q_i} \tag{A.35}$$

By recovering the expression in Equation A.32 and introducing in it Equation A.35, one can obtain

$$\begin{aligned}\frac{\partial^2\hat{\Sigma}_p}{\partial\hat{\Sigma}_{ij}\partial\hat{\Sigma}_{kl}} =& \frac{\partial}{\partial\hat{\Sigma}_{kl}}\left(v_{p_i}v_{p_j}\right) = \frac{\partial v_{p_i}}{\partial\hat{\Sigma}_{kl}}v_{p_j} + v_{p_i}\frac{\partial v_{p_j}}{\partial\hat{\Sigma}_{kl}} \\ =& v_{p_j}\sum_{q=1}^{q\neq p}\left(\frac{v_{q_k}v_{p_l}}{\hat{\Sigma}_p-\hat{\Sigma}_q}\right)v_{q_i} + v_{p_i}\sum_{q=1}^{q\neq p}\left(\frac{v_{q_k}v_{p_l}}{\hat{\Sigma}_p-\hat{\Sigma}_q}\right)v_{q_j}\end{aligned} \tag{A.36}$$

It can be verified that such vector possesses both minor and major symmetries. Therefore, such vector can be simplified as a second order tensor.

As with the eigenvalue derivatives, a problem may arise when there is a multiplicity higher than 1. For that case, an infinite number of eigenvector can form an orthonormal basis. Thus, the uniqueness of the solution must be proved.

With a similar line of thought as previously shown for the normal uniqueness proof. The decomposition of the orthonormal basis from Equation A.16 can be differentiated as

$$\frac{\partial}{\partial\underline{\underline{\hat{\Sigma}}}}\left(\underline{v}_1\otimes\underline{v}_1\right) + \frac{\partial}{\partial\underline{\underline{\hat{\Sigma}}}}\left(\underline{v}_2\otimes\underline{v}_2\right) + \frac{\partial}{\partial\underline{\underline{\hat{\Sigma}}}}\left(\underline{v}_3\otimes\underline{v}_3\right) = \underline{\underline{O}} \tag{A.37}$$

where $\underline{\underline{O}}$ is the null matrix.

Should the multiplicity of an eigenvalue be higher than one, the expressions will take similar forms as A.21, and the sums of the derivatives of the eigenvectors will be uniquely defined.

$$\sum_{r=1}^{2}\frac{\partial}{\partial\underline{\underline{\hat{\Sigma}}}}\left(\underline{v}_r\otimes\underline{v}_r\right) = -\frac{\partial}{\partial\underline{\underline{\hat{\Sigma}}}}\left(\underline{v}_s\otimes\underline{v}_s\right) \tag{A.38}$$

where, once again, the subscript $\cdot_r$ and $\cdot_s$ stands for the repeated and unique eigenvalues respectively.

There is one last issue to solve and is the zero determinant obtained in Equation A.36 when the eigenvalues are repeated. The solution is to first identify the eigenvector with a multiplicity of 1 and calculate its derivative. Secondly, the derivative of the remaining eigenvectors will be half of that quantity calculated. This combination will ensure the property in Equation A.37 and the normal calculation will be unique.

$$\frac{\partial}{\partial\underline{\underline{\hat{\Sigma}}}}\left(\underline{v}_r\otimes\underline{v}_r\right) = -\frac{1}{2}\frac{\partial}{\partial\underline{\underline{\hat{\Sigma}}}}\left(\underline{v}_s\otimes\underline{v}_s\right) \tag{A.39}$$

The case where the multiplicity equals to 3 can be easily computed considering all the derivatives equal to zero.

$$\frac{\partial}{\partial\underline{\underline{\hat{\Sigma}}}}\left(\underline{v}_r\otimes\underline{v}_r\right) = 0 \qquad \text{for} \quad r = 1, 2, 3 \tag{A.40}$$

A.1.4 Yield surface normal for the case $a = 2$

A particularly simple definition of the yield surface normal (and its derivative) can be made when the shape material coefficient $a = 2$. For this case, the CPB06 model can be expressed similarly as the Hill criterion.

$$\begin{aligned}
{\sigma_{eq}}^{a} &= \frac{1}{{m_0}^{a}}\left\{\left(|\hat{\Sigma}_1| - k\hat{\Sigma}_1\right)^{a} + \left(|\hat{\Sigma}_2| - k\hat{\Sigma}_2\right)^{a} + \left(|\hat{\Sigma}_3| - k\hat{\Sigma}_3\right)^{a}\right\} \\
&= \frac{1}{{m_0}^{a}} \sum_{p=1}^{3} \left(|\hat{\Sigma}_p| - k\hat{\Sigma}_p\right)^{a} \\
&= \frac{1}{{m_0}^{2}} \sum_{p=1}^{3} \hat{\Sigma}_p^2 \left(1 + k^2 - 2ksng\left(\hat{\Sigma}_p\right)\right) \\
&= \frac{1}{{m_0}^{2}} \hat{\Sigma}_\alpha \tilde{A}_{\alpha\beta} \hat{\Sigma}_\beta
\end{aligned} \tag{A.41}$$

where $\tilde{A}_{\alpha\beta}$ is a diagonal matrix. The tilde is used here to distinguish the matrix from the one used to transform the stress deviator as anisotropy is included. A priori, this matrix does not seem constant with respect to the eigenvalues. However, the derivative $\partial \mathrm{sgn}\left(\hat{\Sigma}_p\right)/\partial\hat{\Sigma}_p$ equals zero everywhere except from the case where the eigenvalues is null. Nonetheless, for the case of a zero eigenvalue, the whole expression would be null.

$$\hat{\Sigma}_p \frac{A_{pp}}{\partial \hat{\Sigma}_p} \hat{\Sigma}_p = 0 \tag{A.42}$$

By expressing the eigenvalues as a matrix the result goes

$${\sigma_{eq}}^{2} = \frac{1}{{m_0}^{a}} \hat{\Sigma}_{\alpha\beta} \tilde{A}_{\alpha\beta\gamma\delta} \hat{\Sigma}_{\gamma\delta} \tag{A.43}$$

where Greek letter indices are used to remark that it is principal frame. The matrix $\tilde{A}_{\alpha\beta\gamma\delta}$ has a non zero element when $\alpha = \beta = \gamma = \delta$. Therefore, a possible way to define it is

$$\tilde{A}_{\alpha\beta\gamma\delta} = \left(1 + k^2 - 2k\mathrm{sgn}\left(\hat{\Sigma}_\alpha\right)\right) \delta_{\alpha\beta}\delta_{\alpha\gamma}\delta_{\alpha\delta} \tag{A.44}$$

Special attention must be made concerning the index notation of the eigenvalues matrix/vector. If only one index is used, it is considered as an array whereas two indices would mean that it is a matrix.

The result from A.41 is expressed with respect to the transformed tensor principal frame. Therefore a rotation defined by the eigenvectors is made to calculate the matrix with respect to the current frame.

$$\tilde{A}_{ijkl} = \tilde{A}_{\alpha\beta\gamma\delta} Q_{i\alpha} Q_{j\beta} Q_{k\gamma} Q_{l\delta} \tag{A.45}$$

where the rotation matrix is built using the corresponding eigenvectors as columns.

$$Q_{i\alpha} = v_{\alpha_i} \tag{A.46}$$

Note that Latin indices are used now for the expression of the matrix in the current frame as opposed to the principal frame where Greek indices are employed.

The matrix $\tilde{A}_{ijkl}$ controls the strength differential of the material and it is premultiplied and multiplied by the transformed deviator. In order to include the full anisotropy, the fourth-order anisotropic tensor is included in the formulation.

$$\begin{aligned}{\sigma_{eq}}^2 &= \frac{1}{{m_0}^a}\hat{\Sigma}_{\alpha\beta}\tilde{A}_{\alpha\beta\gamma\delta}\hat{\Sigma}_{\gamma\delta} \\ &= \frac{1}{{m_0}^a}\hat{\Sigma}_{ij}\tilde{A}_{ijkl}\hat{\Sigma}_{kl} \\ &= \frac{1}{{m_0}^a}\hat{s}_{ij}A_{ijkl}\tilde{A}_{klmn}A_{mnpq}\hat{s}_{pq} \\ &= \frac{1}{{m_0}^a}\hat{s}_{ij}\hat{A}_{ijkl}\hat{s}_{kl}\end{aligned} \tag{A.47}$$

where the fourth order tensor $\hat{A}_{ijkl}$ can now fully described the anisotropy within the material. As previously denoted, the tensor $\hat{s}_{ij}$ is the difference between the stress tensor deviator s_{ij} and the kinematic force X_{ij} (which is defined deviatoric as well).

All the fourth order tensors presented above have major and minor symmetries that would allow for a simplification of the equivalent stress by using a matrix.

$$\hat{A}_{ijkl} = A_{ijpq}Q_{p\alpha}Q_{q\beta}tildeA_{\alpha\beta\gamma\delta}Q_{m\gamma}Q_{n\delta}A_{mnkl} \quad \rightarrow \quad \hat{A}_{ij} = A_{ik}\tilde{Q}_{\alpha k}\tilde{A}_{\alpha\beta}\tilde{Q}_{\beta l}A_{lj} \tag{A.48}$$

The matrix A_{ij} is defined so as to linearly transform the stress deviator in Voigt notation.

$$\hat{\Sigma}_i = A_{ij}\hat{s}_j \tag{A.49}$$

Subsequently, the matrix $\tilde{Q}_{\alpha i}$ is a 3×6 matrix that rotates the 6-element transformed tensor (in Voigt notation) to the 3-element principal frame, i.e. the three eigenvalues.

$$\hat{\Sigma}_\alpha = \tilde{Q}_{\alpha i}\hat{\Sigma}_i \tag{A.50}$$

This 'rotation' matrix has the form

$$\begin{aligned}\tilde{Q}_{\alpha i} &= \begin{bmatrix} Q_{11}^2 & Q_{21}^2 & Q_{31}^2 & 2Q_{11}Q_{21} & 2Q_{21}Q_{31} & 2Q_{31}Q_{11} \\ Q_{12}^2 & Q_{22}^2 & Q_{32}^2 & 2Q_{12}Q_{22} & 2Q_{22}Q_{32} & 2Q_{32}Q_{12} \\ Q_{13}^2 & Q_{23}^2 & Q_{33}^2 & 2Q_{13}Q_{23} & 2Q_{23}Q_{33} & 2Q_{33}Q_{13} \end{bmatrix} \\ &= \begin{bmatrix} \underline{\underline{Q}}.\underline{\underline{Q}} \\ 2\underline{\underline{Q}}.\underline{\underline{Q}}\left([2,3,1],:\right) \end{bmatrix}^T\end{aligned} \tag{A.51}$$

The aforementioned notations allows for the expression of the yield surface as

$${\sigma_{eq}}^2 = \frac{1}{{m_0}^2}\hat{s}_i\hat{A}_{ij}\hat{s}_j \tag{A.52}$$

The derivative is therefore straight forward

$$\begin{aligned}\frac{\partial\sigma_{eq}}{\partial\sigma_{ij}} &= \frac{\partial\sigma_{eq}}{\partial\hat{s}_k}\frac{\partial\hat{s}_k}{\partial\hat{s}_{lm}}\frac{\partial\hat{s}_{lm}}{\partial\sigma_{ij}} \\ &= \left(\frac{1}{{m_0}^2}\frac{\hat{A}_{k\tilde{k}}\hat{s}_{\tilde{k}}}{\sigma_{eq}}\right)\cdot\tilde{I}_{klm}\cdot J_{lmij}\end{aligned} \tag{A.53}$$

where $\tilde{I}_{klm}$ is a third order tensor representing the transition from the deviator $\hat{s}_{lm}$ and its Voigt notation equivalent $\hat{s}_k$. By simplifying the normal definition expressing it as a 6-element vector, the result yields

$$n_i = \frac{1}{{m_0}^2} \frac{dev\left(\tilde{I}_{ik} \hat{A}_{k\tilde{k}} \hat{s}_{\tilde{k}}\right)}{\sigma_{eq}} \tag{A.54}$$

where $dev\left(\cdot\right)$ is the deviator operator in vector form. The matrix $\tilde{I}_{ik}$ reads

$$\tilde{I}_{ik} = \begin{bmatrix} 1 & 0 & 0 & 0 & 0 & 0 \\ 0 & 1 & 0 & 0 & 0 & 0 \\ 0 & 0 & 1 & 0 & 0 & 0 \\ 0 & 0 & 0 & 1/2 & 0 & 0 \\ 0 & 0 & 0 & 0 & 1/2 & 0 \\ 0 & 0 & 0 & 0 & 0 & 1/2 \end{bmatrix} \tag{A.55}$$